Plasma Self-organization and its Development on Liquid and Metal Anode Surfaces in Atmospheric Pressure DC Glow

by

Yao Elizabeth Kovach

A dissertation submitted in partial fulfillment
of the requirements for the degree of
Doctor of Philosophy
(Nuclear Engineering and Radiological Sciences)
in the University of Michigan
2020

Doctoral Committee:

Professor John E. Foster, Chair
Professor Fei Gao
Professor Maria C. Garcia, Escuela Politécnica Superior de Córdoba
Professor Mark J. Kushner

“Faith is to believe what you do not yet see; the reward for this faith is to see what you believe”

– *Saint Aurelius Augustine*

Yao E. Kovach

yaok@umich.edu

ORCID iD: 0000-0001-9393-5929

To both my Kovach and Li family

ACKNOWLEDGEMENTS

Before I entered the college of engineering at University of Michigan, I was in a music field. Piano was my primary instrument to perform melody self-organizations in major, minor and counterpoint with black and white keys. After I started my graduate research, I was fortunately worked and developed plasma self-organization as the topic for my dissertation. During the entire graduate career, I have honed great experiences with encouragement academically, professionally and personally. At the end of my graduate moment, please allow me to pay my highest tribute to the following individuals and resources that have supported me on this successful journey.

First, I would like to express my greatest gratitude to my advisor, Prof. John Foster. I deeply appreciated his passion for teaching not only on his professional knowledge and intelligences in sciences, also the beauty of his mentoring philosophy on every student is different by guiding us to shine by our own strengthens. As for the last five years working closely with Professor Foster, his excitement for research, sagaciousness in solving issues and having a natural keen appreciation for physics discovery has inspirited me throughout my academic growth. “Asking questions makes you an expert.”, “Keep working on the experiments, the physics will talk back to you.” were the wonderful examples that he has taught me and thus impacted my thinking and enlightened my creativity. I wouldn’t stand on where I am today without all of his help, in terms of guidance, patience, energy, immense knowledge and inspiration.

Secondly, I would like to sincerely thank the dissertation committee, Prof. Fei Gao, Prof. Maria C Garicia, and Prof. Mark Kushner, for the time they took out of their busy schedules to help me improve this thesis. More and particularly, for my thankfulness to Prof. Gao who introduced me to the material world with his expertise in nuclear materials. He has spent a lot of time to help me in solve problems, discussing as a friend, as well as encouraging and guiding me in the proper academic directions. I am grateful for the opportunity to have worked with Prof. Garicia, who trained me in optical emission spectroscopy, and also generously demonstrated and taught me data analysis, interpretation, and writing with her expert background in plasma physics. I have learned and enjoyed from Prof. Kushner's classes, especially in plasma chemistry, where I have gained some of the understanding and was able to apply it to these dissertation experiments.

I would like to acknowledgement the financial supports, resources, and collaborations that have made this work possible. This work was founded by the U.S. Department of Energy under the grant award DE-SC0018058. It was also supported by the Michigan Memorial Phoenix Project (MMPP) seed grant program. Part of the conference travelling was supported by the Rackham Graduate School. In calibration, some of this work was partially supported by the Lam Research with grant and adequate silicon wafers as material components. Another supported graduate fellowship I would like to express my thankfulness for was provided by the Michigan Institute for Plasma Science and Engineering (MIPSE).

During my last year Ph.D. studies, I had the opportunity to work at Los Alamos National Laboratory (LANL) under my thesis topic. Here, I would like to pay my special regards to the High Speed Imaging team from Subatomic Physics (P-25) division at LANL with their excellent fast camera technology support. Particularly, I would like to thank the team leader Dr. Jeph

Wang for his meticulous help when I was worked in his lab at LANL. In addition, thanks to the Department of Energy Office of Science Graduate Student Research (SCGSR) program award which was supported me with this great experience. This collaboration has resulted in an impact chapter that contributed for my thesis.

I would also like to delivery my appreciation with warm thanks to the generous offers on experimental parts and technique supports. Thanks to the Dellamar Manufacturing Company in Belleville Michigan for offering the copper, brass materials, as well as the technique supports of CNC and EDM machining. Thanks to the scientists Dr. Sun Kai and Dr. Feifei Zhang who has trained me step by step with the operations of all of the electron microscopy technologies at Michigan Center for Material Characterization. Without everyone's efforts, all of the remarkable results and discovery illustrated in this work will not be possible.

I would like to extend my acknowledgement to all of the members in the Plasma Science and Technology Laboratory at University of Michigan. Thanks to the past colleagues that who have had helped me to make this achievement possible: Sara Gucker, Kapil Sawlani, Neil Arthur, Selman Mujovics, Janis Lai, Adrian Lopez, and Kenneth Engeling (classmate since undergraduates). Thanks to the present colleagues for all of the time that we have improved together: Joe Groele, Ritz Raju, Jenny Smith, Nate Wirgau, Roxanne Pinsky, and Zimu Yang. I have learned so much from each of you through everyone's insightful work and absolutely enjoyed the fun time we have spent together. This is a great precious memory for me.

For all of my friends who has had supported, and encouraged me to get to this point. My special thanks belong to you. A warm regards I would like to send to Professor Gregory Yeh from the department of chemical engineering at University of Michigan, who also was my referral to enroll the undergraduate program at Nuclear Engineering department. Thank you for

your mentoring and getting me seeded. Mr. Tim Dooly, thank you for being part of our family. Your encouragement and what you have always believed on me are my best gifts.

In closing, my deepest thank you is to my dear Kovach and Li family. They are the strongest support I have had through all of my life challenges. Getting to this point and completing my Ph.D. would not have been possible without my family. I am very fortunate for all the support I have received over the years. Thanks to Jane Kovach who didn't get to see any of my graduation but always watching me. Thanks to my parents, brother, sister in law and two baby nieces. Most importantly, I would like to thank Louis Kovach. All gratitude counts for nothing in the face of what you have done for me. You have taught me everything new and changed my life!

Yao Elizabeth Kovach

September 2020

TABLE OF CONTENTS

LIST OF TABLES

LIST OF FIGURES

LIST OF APPENDICES

ABSTRACT

The concept of self-organization in nature has been pondered and written about since ancient times. Pattern formation derived from self-organization constitutes a complex phenomenon that is equally fascinating from an observational standpoint. Such phenomena appear in a broad range of systems including biological, chemical, and physical. Their occurrences have been associated with instability, symmetry breaking, bifurcation, and to the formation of dissipative structures. Recently, self-organized pattern structures studied using atmospheric pressure plasma sources are becoming an increasingly important topical area because of their applications ranging from environmental remediation to health care and material processing. A typical class of these weakly ionized plasma discharges is the 1 atm DC glow. To utilize the properties of this type of discharge requires demonstration of control which in turn requires some understanding of physical mechanisms underlying it occurrence. However, the origin of plasma self-organization is still poorly understood.

To extend the understanding on the mechanisms of self-organization formation in DC atmospheric pressure glows, the exploration of the parameter space of occurrence was carried out. Here the overarching objective was to understand the control parameters and associated responses thereby allowing for the establishment of a phenomenological model of this self-organization—which heretofore remains elusive. Such plasma self-organization arises on both solid and liquid anodes in pin to plane electrode geometries. An array of self-organization patterns cataloged along with their dependencies on parameters such as discharge current,

electrode separation, gas effects, and electrode conditions have been studied. Previously unreported threshold parameters for the pattern formations were recorded, as well as the unusual pattern morphologies.

Optical emission spectroscopy (OES) was used to spatially resolve the plasma characteristics in the plasma column and near anode region. It also facilitated estimation of the local electric field at the anode. Particular to the liquid anodes, the species distributions, plasma density, gas temperature, and local electric field were determined. The importance of water vapor in pattern formation was elucidated thus highlighting the role of local evaporation. In this study, it was found that the onset of pattern formation followed a dramatic increase in water vapor in the gas phase. Additionally, it was found that pattern morphology was dependent on the type of electrolyte used.

The observation of droplets in the gas phase was also discovered. Under the self-organization condition, it was observed that luminous high-speed particles were emitted from the plasma liquid interface near the center of the plasma attachment point. Apparently droplets are accelerating into the gas phase containing solution nanoparticles. The size and composition of these particles in the droplets was determined using the combination of a theoretical model, scanning electron microscopy (SEM) and energy dispersive X-ray spectroscopy (EDS) analysis. Secondly, the plasma attachment on a tungsten anode was found to produce nanostructures on the surface giving rise to tungsten fuzz morphologies as typically observed in fusion wall simulators. This suggests that similar physics might be present in both scenarios.

Overall this dissertation not only improves our fundamental understanding on the mechanisms of plasma self-organization, but it also provides an important basis for technological innovations that exploit self-organization in an array of arenas such as materials nanotechnology,

chemical synthesis, waste water treatment, and medicine. This work also serves to extend our understanding of key controlling parameters for self-organization and forms a basis for any future model development and validation.

CHAPTER I

Introduction

Self-organization is the spontaneous and purposeful formation of spatial, temporal, spatiotemporal structures or function in systems composed of few or many components. Critical to understanding the definition of self-organization is the meaning of the term pattern, which is an assembly consisting of parts. The process of self-organization patterns (SOPs) can be found in many other fields, such as chemical, biological, robotic, and cognitive systems [1-3]. The appearance of self-organization in plasma systems is ubiquitous. It has been claimed that self-organization is a universal mechanism in nature [4]. However, over several decades' research studies, the origin of self-organization formation remains unclear. This dissertation research aims to elucidate the nature of self-organization in a specific system — a DC glow with liquid and metal anodes — through the experimental investigation. Such efforts have shown that plasma self-organization can be studied from the aspect of a low temperature plasma physics, chemistry and nanotechnology.

In this chapter, a brief introduction on the background of self-organization from a general (Sec. 1.1) and plasma physics (Sec. 1.2) point of view are given, followed by the description of the dissertation overview in Sec. 1.3.

1.1 Self-organization in General

The term “Self-organizing” was first used by the German philosopher Immanuel Kant in 1790 to define the nature of living organisms [5]. Self-organization was introduced to the science field in 1947 by the English engineer W. Ross Ashby as discussed in a dynamic system [6]. In 1977, Nicolis and Prigogine (Nobel Prize in chemistry in 1977) applied non-equilibrium thermodynamics and in particular the concept of dissipative structures and the formation of self-organization patterns [7]. Dissipative structure formalism remains the dominant tool used to analyze self-organizing phenomena.

Self-organization refers to a broad range of pattern-formation processes in both physical and biological systems such as the skin pigmentation of animals, the crystallization of snow flakes, the shape of sand dunes, and fish joining in schools (Fig. 1.1). A key attribute of such organization is that its occurrence manifests due to attribute microscopic processes. In

Figure 1.1: The self-organization patterns in earth nature.

physics, self-organization occurs in open systems driven away from thermal equilibrium. These self-organized structures form patterns that do not require any controlling external force. They appear to produce order out of randomness [8, 9]. Various examples of patterns phenomena are studied in fluid dynamic and magneto hydrodynamic stability, including thermal convection and Taylor Couette flow [10-12]. Reacting chemical systems also manifest self-organizing behavior

both in space and time, such as that derived from the Belousov - Zkabotinsky reaction shown in Fig 1.2. [13].

Figure 1.2: The pattern waves resulting from Belousov-Zkabotinsky reaction [14].

1.2 Self-organization in Plasmas Physics

In plasma physics[1], self-organization is observed in phenomena ranging from plasmoids formation in low pressure, laboratory plasmas to large scaled structures in astrophysical processes of the universe. Processes underlying the self-organization remain poorly understood. Insight into such phenomena therefore not only advances basic plasma science but also enables a range of applications.

1.2.1 Fusion Plasma

A self-organization phenomenon is also observed in fusion plasma systems. Manifestations of such self-organization on the sun appear as intricate and dynamic architecture of structures such as the loops, arcade and filaments shown in Fig 1.3.

[1] The fundamental science background of plasma is provided in Appendix A.

Figure 1.3: Magnetized plasma loop on the surface of the sun by NASA.

In human-made fusion plasmas, self-organization manifests as density and velocity patterns in partially or fully ionized gases. In the 1980s, it became clear that the effects of self-organization play an important role in transport and must be incorporated into the fusion models [15]. For example, it was found that plasma self-organization is the main reason for the different dependencies of the ITER confinement time scaling on the toroidal and poloidal magnetic field. As can be seen from Fig.1.4, certain plasma configuration exhibit properties as self-organization

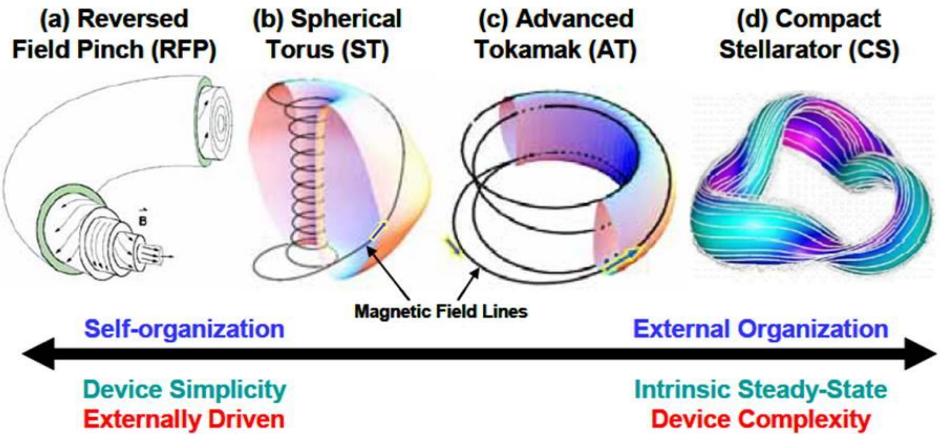

Figure 1.4: The magnetic topology of major U.S. magnetic fusion concept improvement experiments [16].

where the plasma alters an externally applied magnetic field in a way that improves the confinement properties needed for fusion [16].

1.2.2 Atmospheric Pressure Plasma

Non-thermal atmospheric pressure plasmas are partially ionized electrical discharges with high rates of collisions (1×10^{12} s^{-1}) leading to short physics time scales (1×10^{-9} s). Self-organization is also observed in atmospheric pressure plasmas. In general, there is a large range of methods to generate cold atmospheric pressure plasmas: (1) corona discharge, (2) dielectric barrier discharge (DBD), (3) spark discharges, (4) atmospheric pressure glow (APG), (5) atmospheric pressure plasma jets (APPJ), and (6) micro discharges.

By DBD we refer to those discharge configurations in which at least one electrode is covered with a dielectric, which limits current flow subsequent to breakdown leading to transitory discharges. DBD can be operated over a broad range of pressures from sub-atmospheric pressure to above 1 atm. Self-organization has been observed in such plasmas some of which is attributed to the memory effect associated with the deposition of charge on the dielectric surface by micro discharges. These processes are believed to contribute in part to self-organization as shown in figure 1.5. A spark discharge is a non-self-sustaining arc discharge where the streamer crosses the electrode gap leading to a return stroke and associated plasma column heating. In this case, if the current capacity of the discharge supply is large enough, localized heating of the electrodes will give rise to the formation of an arc. The APPJ is a non-thermal plasma discharge that manifests itself as a self-propagating ionization wave. The discharge itself is typically in the form of a luminous tapered plume. With ballasting it is possible to generate glow like discharges at 1 atm (APG). At sub-mm length scales, it is also possible to produce DC glow discharges. Such micro discharges are of interest for a variety of applications such as ozone generation and lighting. Under certain conditions, such as reduced pressure in inert gas, such discharges self-organize into a multitude of localized micro discharges

as can be seen in figure 1.5. In this work, we study a ballasted 1 atm DC glow with liquid and metal anodes. This discharge type is discussed in detail in chapter 2.

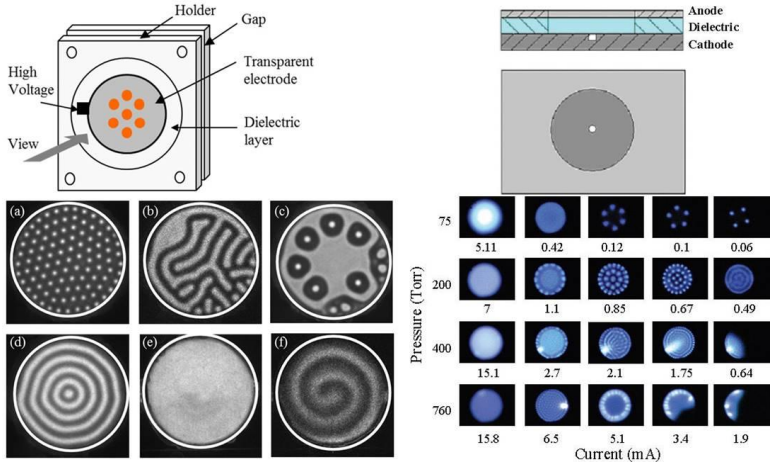

Figure 1.5: Patterns observed in DBD (left) at 500 Torr using helium (a-c) and neon (c-f) plasma [17] and self-organized xenon plasma pattern at various pressures observed in DC micro discharge (right) [18].

1.3 Dissertation Overview

1.3.1 Research Approach

The approach of this work is to utilize experiments to understand plasma conditions prevailing at the surface of liquid or metal anodes in an effort to obtain insight into the origin of self-organization. The effort will improve our fundamental understanding of plasma-surface interactions in atmospheric pressure glows via an investigation that combines comprehensive experimental measurements of the surface plasma and its coupling to the main plasma column. Fundamental research questions that will be addressed in this dissertation research include:

- What are the characteristics of the plasmas that form at the surface of both liquid and metal anodes in DC glows?

- Why do patterns form? Here the question's focus is not necessarily on the specific geometry of the patterns formed but rather, why is the pattern necessary for current continuity. Simply put, what role does the pattern play in completing the circuit?
- What is the origin of the geometrical differences between patterns that form on metal and liquid anodes?
- What is the potential distribution in the plasma column particularly near the electrode surface?
- What role does the liquid phase processes on self-organized pattern formation?
- Finally, as a development from direct SOP study, nanostructuring has been observed on the metal electrode surface, and a particle emission phenomenon has been observed from the liquid electrode surface. Given the discharge energy of ions and the relatively low electrode temperature, what is the mechanism for nanostructuring in a DC glow and can we control it? What is the driving force on the local liquid interface that causes particle emission? What are the physics behind both situations that might produce insight into self-organization formation on both electrode surfaces? Does particle or droplet emission provide useful insight into the magnitude of the local surface electric field?

Atmospheric pressure plasmas pose challenges in regards to making direct plasma measurements. Additionally, conditions in the solution for liquid electrodes tend to change as a function of time (pH, conductivity). Research published to date has suggested that solution conductivity can have a large effect on the behavior of anode attachments [9-12]. In many such studies however, this parameter is not fixed, rather only its starting value is set. Additionally, the plasma tends to deposit a great deal of heat into the liquid leading to evaporation. The role of the evaporated fluid on discharge behavior and pattern formation is not well understood. In this

regard, any comprehensive study must be capable of isolating these variables, ideally fixing the conditions in solution. The same can be said for the metal electrodes. In this case, surface temperature is likely quite important. Also, based on a limited SOP study on metal anode under 1 atm DC glow [13, 14], the measurement and control of this process are therefore another parameter that must be tracked. Past experimental investigations have largely focused on studying macroscopic conditions for which self-organization patterns emerges. Parameters of interest include current, voltage, solution conductivity, gas flow rate/mixtures, and electrode spacing. While this data give insights such as providing some sense of a parameter space for self-organization, it is difficult to infer the underlying mechanisms. In this dissertation, we propose the following experimental objectives:

- To experimentally measure plasma properties (density, gas temperature, the plasma potential, and excitation temperature) within the plasma column as well in the self-organized plasma structures.
- To characterize the occurrence of self-organization by mapping the parameter space (current, gap, liquid conductivity, initial surface conductivity).
- Determine the local electric field near the anode for both metal and liquid anodes.
- Quantify the time evolution of nanostructuring on anode surfaces as a function of gas type and electrode composition
- Quantify the velocity profile of droplet or particle emission
- Explore the impact of chemically driven convection on plasma patterning and thus self-organization sensitivity.

Addressing these objectives will greatly improve our understanding of mechanics of self-organization in 1 atm DC glows.

1.3.2 Scope

This thesis is organized as follows: In chapter 2, the 1 atm DC glow helium plasma source is described with the review on the state of art for SOPs. The typical application of such source is briefly discussed. In chapter 3, the theoretical background is provided with the description of SOP related low temperature plasma physics. The hypothetical mechanisms of pattern formation in reaction diffusion model and transport system are theoretically discussed. The methods of building and design of the experiments are explained in this chapter as well. Chapter 4 begins with a review of early experimental observations. In this work, the control parameter space is explored. The pattern behavior in response to these parameters for both liquid and solid anodes is documented. Chapter 5 summarizes the spectroscopic investigation of the plasma column using the optical emission spectroscopy (OES). Here spatial variations in gas temperature, electron density, excitation temperature, electric field and species emission are discussed. Chapter 6 explores pattern sensitivity to electrolyte type. Here 13 distinct electrolytes are studied. In chapter 7, we report on particle emission phenomena. Nanostructuring observed at surface of a solid electrode is discussed in chapter 8. In this latter case, the time evolution of anode nanostructure was studied. The observed nanostructured morphologies are similar to that observed in fusion tungsten fuzz studies. Key findings are summarized and perspective future work is speculated upon in chapter 9.

1.4 References

[1]. H. Haken, Synergetics, Synergetics – Introduction and Advanced Topics, Springer, Berlin, (2004).

[2]. H. Haken, Scholarpedia, 3(8):1401, (2008).

[3]. S. Camazine, J. L. Deneubourg, N. R. Franks, J. Sneyd, G. Theraulaz, and E. Bonabeau, Self-organization in Biological systems, Princeton University Press, Priceton, N.J., (2001).

[4]. W. J. Zhang, Self-organization: Theories and Methods, Chapter 1, Nova Science Publishers, INC., New York, (2013).

[5]. F. Paslack, Urgeschichte der Selbstorganisation, Vieweg, Braunschweig, (1991).

[6]. W. R. Ashby, Principles of the self-organizing dynamic system. Journal of General Psychology 37: 125 – 128 (1947).

[7]. G. Nicolis and I. Prigogine, Self-organization in Nonequilibrium Systems, Wiley, New York, (1977).

[8]. M. J. Aschwanden, F. Scholkmann, W. Béthune, W. Schmutz, V. Abramenko, M.C.M. Cheung, D. Müller, A. Benz, G. Chernov, A.G. Kritsuk, J. D. Scargle, A. Melatos, R.V. Wagoner, V. Trimble, and W. H. Green, Space Sci Rev 214:55, (2018).

[9]. H. Haken, series ed.: Springer Series in Synergetics, Springer, (1977).

[10]. P. G. Drazin and W. H. Reid, Hydrodynamic Stability, Cambridge: Cambridge University Press, (2004).

[11]. D. N. Riahi, Flow Instability, Boston, MA: WIT Press, (2000).

[12]. S. Chandrasekhar, Hydrodynamic and Hydromagnetic Stability, International Series of Monographs on Physics, Oxford: Dover, (1981).

[13]. M. Orlik, J. Solid State Electrochem 19: 3203-3206 (2015).

[14]. A. N. Zaikin and A. M. Zhabotinsky, Nature 225, 535–537 (1970).

[15]. Yu. N. Dnestrovskij, Self-Organization of Hot Plasmas, Springer Cham Heidelberg New York, Dordrecht London, (2013).

[16]. Plasma 2010 Committee Plasma Sicence: Advancing Knowledge in the national Interest, Washington DC, The National Academies Press, (2010).

[17]. T. Callegari, B Bernecker, and J. P. Poeuf, Plasma Sources Sci. Technol. 23 054003 (2014).

[18]. K. H. Schoenbach, M. Moselhy, and W. Shi, Plasma Sources Sci. Technol. 13 177 (2004).

CHAPTER II

Self-organization Patterns in 1 atm DC glows[2]

This chapter explores the range of experimental and phenomenological insight regarding the occurrence of plasma self-organization in a typical 1 atm DC glow source with liquid and metal anodes along with a literature review of the subject. Applications of self-organizing DC glow plasmas at 1 atm are also commented upon.

2.1 Atmospheric Pressure DC glow

Atmospheric pressure DC glows are fascinating plasma discharges that despite operating at 1atm in regular ambient air, they manifest all the general characteristics of a DC glow discharge[3] including the presence of a positive column structure and an anode dark space [1-3]. These features have been studied using metal and liquid electrodes that can be seen form Fig. 2.1. Typically, with increasing pressure, discharges tend to constrict and ultimately transition

[2] Portion of the text and discussion in this chapter have been previously published by J.E. Foster, Y.E. Kovach, J. Lai, and M. C. Garcia, "Self-organization in 1 atm DC glows with liquid anodes: current understanding and potential applications" Plasma Sources Sci. Technol. 29 034004 2020.

[3] Theoretical background of DC glow discharge is provided in chapter 3.

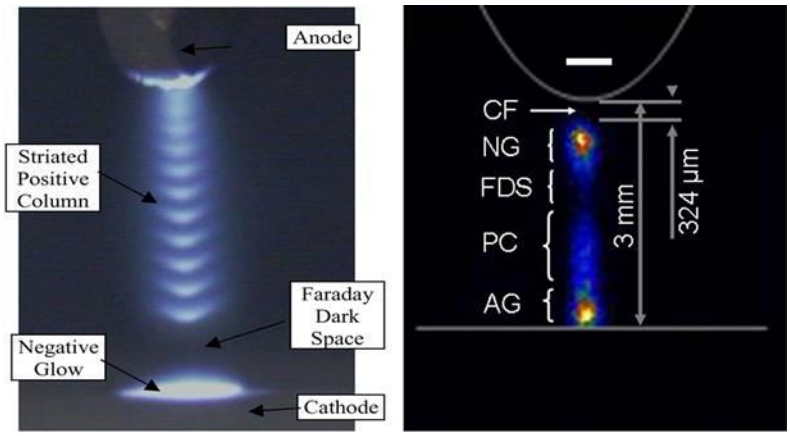

Figure 2.1: Examples of 1 atm DC glow studied using metal cathode (left [1]) and water anode (right [2]).

into an arc as the electron and heavy particles thermalize as the collision frequency increases. The transition to an arc discharge driven by the so-called thermal instability is avoided by the presence of inherent ballasting associated with gas flow rate and the presence of a resistive layer at the anode. These discharges are typically of the pin to plane configuration (Fig. 2.2a) where the planar electrode can be either solid or an electrolytic solution. In many experiments, gas flows through the pin electrode and contacts to the surface. Equally fascinating in such discharges is the appearance of self-organized, discrete plasma patterns forming on the surface of the anode electrode (Fig. 2.2b).

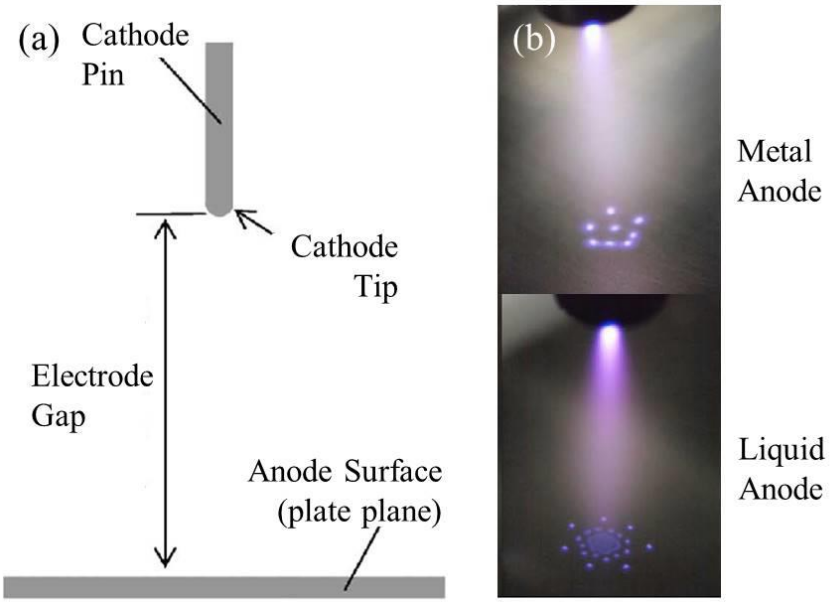

Figure 2.2: (a) A sketch of typical pin to plane geometry configuration applied to the self-organization in atmospheric pressure glow (not to scale). (b) Self-organization anode patterns were observed on the metal and liquid anode surfaces using helium flow in 1 atm DC glow [4].

The 1 atm DC glow under SOPs study is a stable continuous discharge regime with no pulses. The most common gas applied into such experimentation is the noble gas helium. It provides a uniform plasma discharge at high energy electronic excitation levels without electron energy losses due to vibrational excitation. Contraction and other instabilities at such high pressure are reduced by rapaid heat and mass transfer processes [5-8]. Usually, the spacing range between electrodes is from few mm to 1 cm with DC voltages ranging for 300 –1000 V, and DC currents up to few hundred mA [4]. At the anode surface where the discharge contacts, there is typically a luminous plasma attachment. This attachment for all practical purposes is an anode spot structure. Within the spot, the electric field is locally sufficient to drive ionization and excitation processes [9]. Above some threshold discharge current (30 mA), self-organization of the attachment at the anode surfaces is observed [4].

Although the observation of self-organization on metal electrodes at low pressure has been reported dating back to the late 1920s [10], it should be noted out that the study of SOPs on metal anodes in 1 atm DC glow is infrequent to date. Most of recent SOPs studied in 1 atm DC glow were focused on the case of using liquid anodes such as water and salt water [11-15]. This is usually due to the potential of novel fundamental understanding of the plasma state (liquid-gas-vapor phases) in plasma liquid model, as well as for their role in established and emerging applications.

2.1.1 1 atm DC Glows with Liquid

1 atm DC glow plasma with a liquid anode is a plasma discharge with a cathode (which may be either liquid or solid) and an anode consisting of a liquid electrolytic solution. There is usually an immersed physical collector electrode in the anode liquid that is coupled to the external circuit, which consists of a DC power supply and a ballast resistor (Fig 2.3). DC glows are stabilized here because the liquid electrolyte limits the current that the discharge can practically support.

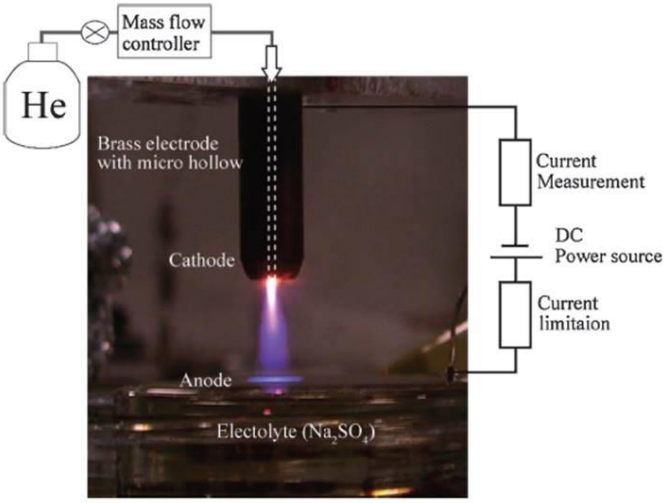

Figure 2.3: Electric circuit Setup of DC glow with liquid anode in 1 atm with helium flow [5].

The discharge glow can be generated with or without helium flow through the cathode. Here, the presence of helium can stabilize the discharge owing to its high thermal conductivity which can lead to gas cooling and high ionization potential, which reduces the ionization rate at a given effective electron distribution temperature. Both contribute to the mitigation of the ionization instability. Liquid evaporation at the anode also has a cooling effect. In such a discharge, the current is carried by ions in solution. In this respect, current continuity is driven by electron flow on the gas side of the discharge. It met at the interface with either positive ion flux or electron driven negative ion production as well as the transport of negative ions from the gas phase into the solution. In this regard, current continuity is complex when compared to simple anodic collection with a metal anode. What is so remarkable about discharges of this type is that owing to plasma interaction with the liquid, the liquid chemistry actually changes over time as can be characterized by monitoring solution pH, conductivity or ion concentration [16]. Additionally reduction reactions at the immersed anode lead to nanoparticle production in solution [17].

The other interesting but important phenomena of this 1 atm DC glow with a liquid electrode is that surface patterns are not been observed when the solution is biased negatively, suggesting the importance of electron injection into the liquid (which also drives electrochemical reduction processes at the interface) and pattern formation [2, 13, 18, 19]. Indeed, Richmonds et al showed that reduction of a model system (ferricyanide - $Fe(CN)_6^{3-}$ to ferrocyanide - $Fe(CN)_6^{4-}$) increased with increasing discharge current for a liquid anode. In that work it was suggested that only a fraction the electrons making it to the surface owing to the fact that in the reduction process is energy specific and in general the plasma electrons will have a distribution in energy.

2.2 SOP State of the Art

2.2.1 Theoretical Insight

In general, self-organization tends to result from competing effects and may be considered a consequence of instability or a multivalued equilibrium solution. These patterns have been observed in high-pressure discharges with both liquid and solid electrodes. In such discharges, the attachment at the anode is observed to transition from a uniform discharge spot at the anode to highly structured patterns that are either static or in motion. The theoretical basis for the spot formation has advanced in recent years with computational models actually replicating the self-organization at least in 2-D models. In this regard, no "new" physics is required to replicate their appearance computationally.

Theoretically, reaction-diffusion models have been used with limited success in at least qualitatively explaining observed self-organization phenomena [20]. Here self-organization results from competing effects where there is an activator and an inhibitor. For example, competition between current density, the activator, and the anode fall voltage, the inhibitor, can give rise to spot phenomena [21, 22]. Here, the anode voltage variations can drive stratification of the attachment at the anode ultimately leading to separation into spots. Local space charge also plays a key role in self-organization. In this case, the competition is between space charge and diffusion [23, 24]. Some of the theory of anode spot self-organization suggests the need for a resistive anode or Ohmic barrier at the anode surface. The Ohmic barrier would tend to regulate and thus stabilize the current flow and the resulting pattern [20, 25]. However, self-organization of anode spots has been experimentally observed also on bare anodes, which shows that the presence of a resistive anode is not a decisive condition for self-organization. Raizer and Mokrov [26] suggest that space charge can give rise to filamentation and thus the redistribution of the

electric field at the surface, which can lead to self-organization. Muller [25] suggests that pattern formation is a consequence of a bistable layer in contact with a resistive zone at the anode surface. The bistable layer is modeled as an S shaped current voltage characteristic. Here the formalism is again the reaction-diffusion equation. Metastable solutions associated with local minima in a generalized potential is associated with the observed anode patterns. Muller also asserts that Coulombic effects determine spot behavior on the surface. Anode spots tend to interact repulsively. The spatial distribution of plasma structures on the surface of the electrode, whether liquid or metal should therefore tend to form a pattern that minimizes the energy of the system. Muller used a generalized potential term associated with Coulombic interactions between plasma attachments to account for repulsion effects. Berezin [27] was able to show that the minimum energy configuration of localized charges such spots was not necessarily that in which all attachments were located at the circumference but rather above a certain spot number, subsequent attachments placed in the center minimized the energy. Such interactions invariably determine pattern spatial distribution.

2.2.2 Computational Insight

To the best of authors' knowledge, to date, the complete computational prediction of the SOPs in 1 atm DC glow discharges is absent, for metal and liquid anodes. Here both indirect modeling and partial modeling methods are summarized.

Trelles [28] using a time-dependent non-equilibrium model was able to show the formation of anode spots in a high current free burning arc discharge. The self-organization observed in this case is similar to the anode patterns observed in atmospheric pressure glows. This model suggests that anode cooling plays a key role in self-organization. The model suggests that heavy particle cooling at the anode, which lowers heavy particle temperature impacts plasma

conductivity and ultimately electron collection at anode. To maintain equilibrium, electron temperature must increase to maintain plasma conductivity. No chemical or electrode effects were included in model yet it reproduced the spot patterns observed experimentally, thus highlighting the cooling effect. Trelles goes on to suggest that the anode spot patterns represent multiple possible solutions, which can lead to steady state.

Insight into pattern formation on anodes can also be gleaned from cathode attachment studies aimed at elucidating similar self-organization phenomena. Almeida, Benilov and Faria have shown computationally that patterns on the surface of the cathode can be described using bifurcation analysis [29,30]. Here, owing to the fact that the discharge possesses axial symmetry, a continuum of possible solutions at a given discharge current exists. Perturbations can lead to branching or bifurcation which in turn leads to spatial mode changes and self-organization. By applying such analysis to a simple, self-consistent glow discharge model that also includes drift diffusion, Almeida et al observed multiple steady-state solutions corresponding to 2D and 3D patterns. 2D patterns were observed even when diffusion losses were turned off in the model. These patterns were discovered by locating the points of bifurcation which branch off from the expected fundamental mode where the attachment is uniform. Perturbing the solution around the bifurcation point in the radial direction allows for the 2D mode to be located. The range in current or voltage over which these states exist was then further elucidated by varying the current or voltage. Such an approach featuring a glow discharge model with local approximation may be applicable to the prediction of patterns on the surface of liquid anodes though local charge transport processes at the interface and through the liquid add additional complexity. Plasma patterns appearing on the surface of solid anodes in arc discharges have been observed in computational models and appear to agree at least qualitatively with that observed in experiment.

Some of these patterns are similar to those observed on liquid anodes. Computational modeling of 1 atm pressure discharges with liquid anodes on the other hand has proven elusive. Some success in at least qualitatively understanding pattern formation in DBD discharges has been realized by applying an equivalent circuit model in which coupling between filaments is modeled using a resistor. The system of equations transformed into a set reaction diffusion equations—the solution of which yields patterns [31, 32].

Lately, self-organization of anode spots DC low pressure glows has been successfully qualitatively modeled. This work utilized a drift diffusion model with local field approximation coupled and Poisson's equation [33]. In that work it was acknowledged that to address patterns quantitatively, the model must incorporate plasma chemistry, non-locality of electron energy, gas heating, collisions and neutral flows. More recently, a reaction diffusion model has been put forth that has been able to successfully predict the onset of pattern formation on liquid anode [34]. In this work, Rumbach et al treats local electron impacts resulting in ionization as an autocatalytic reaction which produces more electrons. Recombination and attachment are treated as inhibitors. The model assumes the patterns form in a thin sheath layer just above the liquid water. Two dimensional profiles predicted by this model are similar to experimental observations as shown in Fig 2.4. For both cases above [33, 34], a long cylindrical DC glow discharge tube was assumed to achieve the adequate boundary conditions. While the model does not treat nonlinear feedback associated with ionization, the electric field and gas heating, it represents a very important first step towards understanding the occurrence and form of self-organization patterns on the liquid anode.

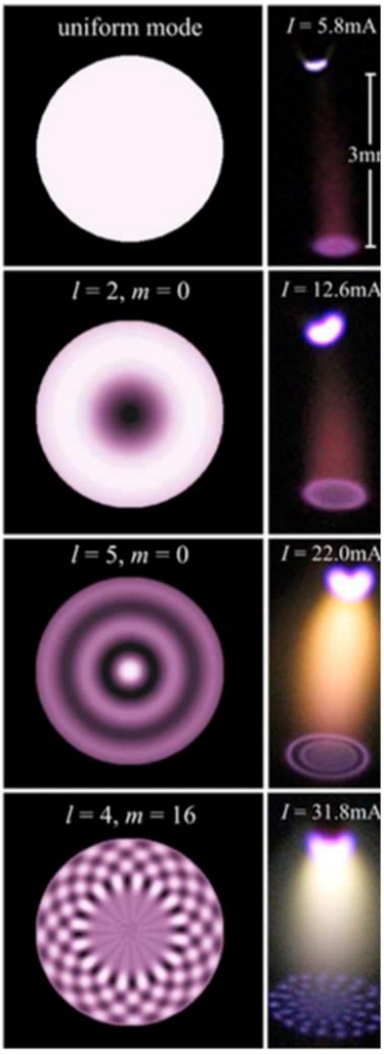

Figure 2.4: Comparison with model predicted modes (left) and experimentally observed pattern [30].

2.2.3 Experimental Insight

Experimental insight however has lagged theory. While there is some framework for the theoretical basis for spot formation, it is in general difficult to measure the experimental parameters that would facilitate either model validation or suggest additional model development [35]. Experiments carried out to date however have elucidated key variables governing spot formation. For example, Verreycken and colleagues [14] showed that for atmospheric pressure glows on liquid anodes, spot number increases in input current and tends to decrease with liquid

conductivity, suggesting that larger contact area and presumably accompanying spatial complexity is required to support the discharge current. As can be seen in Fig 2.5, they also

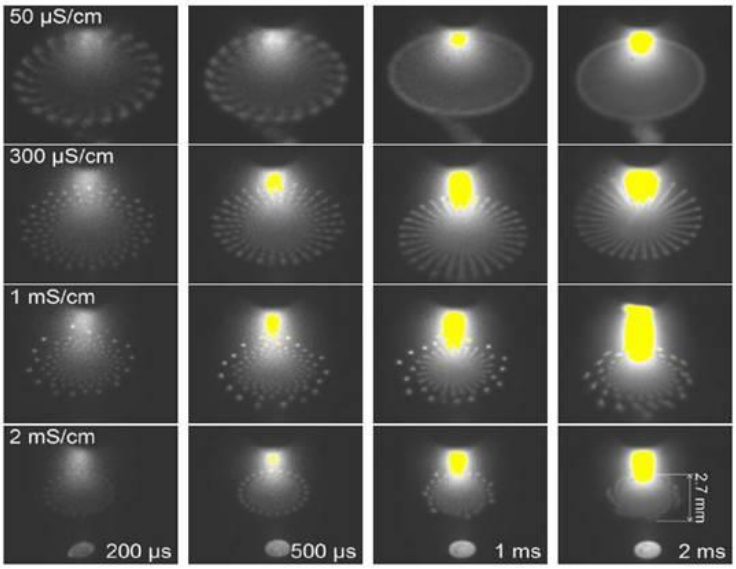

Figure 2.5: Variation in pattern complexity and size with conductivity and time [14].

confirmed with high-speed imaging that the spot patterns observed are not a consequence of a single fast moving attachment. Pattern rotation was attributed to negative ions. Wilson also attributed the rotation of a ring shaped attachment on a liquid anode to negative ion production [36]. In this work, rotation was found to occur in air but not in pure nitrogen, hydrogen or helium environments. This study did not find a correlation between cathode material and pattern behavior, suggesting that the effect is largely local, independent of cathode electrode processes. Bruggeman and colleagues [2] used high speed imaging to generate spatial maps of the discharge attachment with a liquid anode and found its structure was similar to that of a typical glow discharge. Gas temperature of the column was estimated from emission measurements to be ~ 3000 K. The temperature near the anode surface was considerably lower. This cooling is due to the liquid water acting as a heat sink. This temperature drop was suggested as the mechanism for stabilizing the discharge via cooling in addition to acting as a resistive layer to current flow. This

observation is consistent with Trelles's simulations, which purported of the importance of cooling of the anode region of a free burning arc [28]. It should be also pointed out that the group observed an increase in OH emission near the anode. This was attributed to higher water vapor concentration there [2]. Miao [37] investigated a conical attachment on a liquid anode. This work reported on the fluid dynamical effects driven at the anode surface by the anode attachment such as ripples. This work suggested the key role of surface charging, which may stabilize the discharge at low water conductivities. At higher conductivities, it was found that the discharge tended to be unstable.

Shirai and colleagues [4, 11-13] have extensively studied anode patterns on both liquid and solid electrodes. They identified a threshold current that was required for a given inter-electrode spacing to observe pattern formation. Furthermore, they observed that at low helium flows, the pattern was unstable while at high flows, the gas flow 'presses on' the surface disrupting pattern formation. Liquid anode temperature dependence was also observed. Here they found that anode spot patterns became more complex when the liquid temperature was actively raised. This effect was attributed in part to the influence of water vapor. They observed a polarity dependence in their essentially point to plane geometry. When the cathode was configured as the liquid electrode, cathode spot patterns did not appear. The group also identified the role of steam evolution from the surface and pattern formation. Finally, it was observed that patterns tended to favor formation in presence of electronegative gases (see Fig. 2.6).

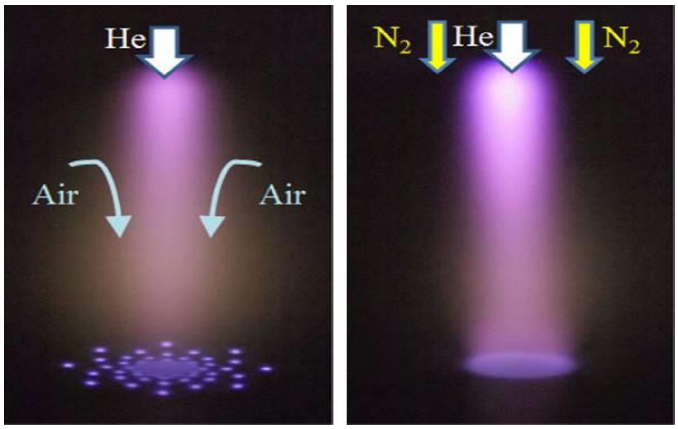

Figure 2.6: The effect of electronegative gas on pattern formation [13].

It was found that in contrast to operating in ambient air, when a curtain of nitrogen was used to minimize air diffusion into the discharge, the pattern was absent. Additionally, they found that the ratio of injected oxygen to air could be used to control the patterns observed. The role of negative ions in pattern formation is suggested in this work [11,13]. In general, it is well established that the presence of negative ions in discharges can lead to a type of ionization instability, which may play a role in the formation of the patterned anode spots. In fact, the role of negative ions has been alluded to in the formation of self-organized plasmoids in low pressure plasmas as well. Attachment instability can occur when the relative negative ion concentration is high. In this case, the attachment rate can increase with electron temperature due to an increase in the effective reduced electric field E/N, where N is the uncharged neutral gas density. This allows for an increase in average electron energy an increasing higher ionization rate leading a runaway condition. The recombination instability is also possible. In the presence of an increasing electric field, ionization of recombining ions can lead to an increase in heavy, charged molecules. Coupled with attachment associated with recombination electron mobility is reduced thereby leading to a reduction in the local ionization rate and thus a perturbation to the local electron density [38]. Such a process may play a role in the formation of anode attachments since

significant evaporation takes place at the surface of attachment in liquid anodes, leading to the introduction of attaching species via, for example, plasma driven disassociation of water. Negative oxygen ions can interact with oxygen to generate O_2 molecules for example: $O^- + O \rightarrow O_2 + e$.

Zhang et al investigated pattern formation with a pin to plane (liquid anode) configuration [39]. They observed a pronounced anode dark space when using acid electrolytes that contained fluorine or chlorine. Here it is conjectured that gas phase F or Cl derived from the solution, attaches electrons locally above the anode, giving rise to a prominent dark space, again highlighting the role of negative ions. Interestingly atomic hydrogen lines were not observed in the emission spectra. This was attributed to the production of H_2 gas by energetic electrons: $2H^+ + 2e^- \rightarrow H_2$ (g). Hydrogen emission however has been observed near the surface in other studies albeit at reduced intensities. The observed weak emission may be attributed to the large amount of water vapor present near the surface [2].

In liquid anodes, the water plays a key role in stabilizing the discharge. Zheng et al also investigated the formation of patterns on the surface of a liquid electrode by exciting a pin to plane (liquid) geometry with AC voltage up to 14 kHz rather than DC [40]. Here again, air was the working gas. In this work, patterns were observed only when the liquid electrolyte was at anode potential, consistent will all DC tests. This indicates the importance of an electron collecting liquid. Interestingly, in this work, the sodium from the electrolyte was not observed in the gas phase nor was OH radicals. The authors attributed the absence of these species near the surface to reduced localized vaporization in this discharge. Note that the patterns only appeared for a short time on a half cycle, so the localized power deposition is greatly reduced for similar currents and voltages in comparison to the DC case. Additionally, it was observed that at high

currents, the patterned attachment becomes diffuse. The diffuse attachment can be expected at increased current. As the size of the filaments increase, the relative inter-filament spacing decreases. When this occurs, lateral inhibition is overcome via diffusion and intricate structures will blur, melding into a single diffuse attachment [35].

2.3 Applications

Atmospheric pressure plasmas hold desirable conditions such as the high electron densities (more than 10^{12} cm^{-3}) and relatively low gas temperature (less than 2000 K), which demonstrate considerable interest for a wide range of applications: air pollution control, bio-decontamination, plasma-assisted combustion, material processing, surface treatment, and electromagnetic wave shielding. These properties can only be achieved in non-equilibrium plasmas where the kinetic temperature of the free electrons, T_e is larger than the temperature of the heavy species – gas temperature, T_g. As one of the source type from APG in non-thermal plasmas, the advantage of DC glow discharges is that it can generate relatively large volumes of decent homogeneous plasmas especially when the noble gases are participated.

2.3.1 Solid Surfaces

In particular to 1 atm DC glow, study SOPs in this class of discharge have a wide array of technological applications with correspondence to the types of the using electrodes. For example, the materials processing is the major application that can be applied to the SOPs study using solid electrodes. Such processing includes surface texturing, surface etching, and deposition. Realization of such discharges could essentially revolutionize materials processing by eliminating the need for expensive vacuum systems and associated energy costs for operation, which are typically required for materials processing. Higher fluxes to the surface are also possible at elevated pressure. Unlike DBD and streamer discharges, the attachment of the DC

glow under controlled conditions can be uniform as well as non-thermal — two key requirements for the aforementioned materials processing-type applications. In this regard, the 1 atm DC glow can serve as a basis for non-thermal materials processing.

In this dissertation, nanostructures were generated on the solid anode surfaces using 1 atm DC glow (chapter 8). Such unexpected observation also offers potential material applications in industries ranging from electronics to medicine [41-43]. Compare it to the nanostructures generated in conventional method using high ion beam in vacuum system, the 1 atm DC glow method holds the advantage of simple operation by avoiding the high costs associated with vacuum equipment. However, the disadvantage of plasma operated in high pressure often leads to instabilities and gas heating, conditions that are unsuitable for material applications. Nevertheless, under the self-organization condition, the plasma behaves as micro discharge when they self-organized on the metal surface. This characterization helped realize the sustainment of stable, and thus enable low-cost material application. The DC glow offers the prospect of low cost, atmosphere pressure nanostructuring. The nanostructuring is controllable via the adjustment of exposure time and discharge current. By translating the anode surface under the plasma column, one can raster scan nanostructures, thus affording an option to treat large scale surfaces.

2.3.2 Liquids

In addition to materials processing, because current continuity is mediated by ion activity and electron solvation in the electrolytic solution, the DC glow with liquid electrode can also be used to drive in-solution chemical reactions and thus supports environmental and medical quality applications. The self-organization of such plasmas on liquid media such as cancerous tumors is currently being investigated as a treatment method. Owing to subtle dielectric differences

between cancer cells and normal cells, selective self-organization can be exploited as a tool to eradicate diseased cells [44, 45]. Here it is the small variations in the external properties of the cells (cancer and normal cells) that lead to the self-organization. This so-called adaptive plasma pioneered by Keidar et al is a novel approach to treatment.

Plasmas in contact with water generate reactive oxygen and nitrogen species such as OH radicals, ozone, hydrogen peroxide, nitrites and nitrates, which can be used to decompose organic contaminants in solution via a process known as advanced oxidation [46]. In advanced oxidation, these reactive species attack and subsequently reduce organic contaminants in solution to carbon dioxide, water, and inorganic salts via a process known as mineralization [47- 49]. This nonselective process can be utilized in the treatment of waste water whose conductivity is sufficient to support a discharge [50, 51]. What is novel about such discharges in this context is that the Faradaic yield for reactive species can be nearly an order of magnitude higher than that corresponding to Faraday's electrochemical law—which states that the mass of species generated is proportional to the quantity of electricity passing through the electrolytic cell [52, 53]. Such discharges have also been suggested as a means to modify the surface of immersed substrates such as polymeric films. For example, Zheng et al modified the wettability of polyimide film samples immersed in an electrolyte exposed to a liquid cathode [54].

2.4 References

[1]. D. Staack, B. Farouk, A. Gutsol, and A. Fridman, Plasma Sources Sci. Technol. 14, 700 (2005).

[2]. P. Bruggeman J. Phys. D: Appl. Phys. 41 215201 (2008).

[3]. J. P. Trelles Plasma Sources Sci. Technol. 27 093001 (2018).

[4]. N. Shirai, S. Uchida, F. Tochikubo and S. Ishii 2011 IEEE Trans. Plasma Science 39 2652 (2011).

[5]. S. Kanazawa, M. Kogoma, T. Moriwaki, S. Okazaki, 8th Int. Symposium on Plasma Chemistry (ISPC-8), Tokyo, Japan, vol. 3, p. 1839 (1987).

[6]. S. Kanazawa, M. Kogoma, T. Moriwaki, S. Okazaki, J. Phys. D, vol. 21, p. 838 (1988).

[7]. B. Lacour, C. Vannier, J. Appl. Phys., vol. 38, p. 5244 (1987).

[8]. Y. Honda, F. Tochikubo, T.Watanabe, 25th Int. Conf. on Phenomena in Ionized Gases (ICPIG-25), vol. 4, p. 37, Nagoya, Japan, (2001).

[9]. B. Scheiner, E.V. Barnat, S.D. Baalrud, M.M. Hopkins and B.T. Yee Phys. Plasma 24 113520 (2017).

[10]. C. H. Thomas and O. S. Duffendck Phys. Rev. 35 73 (1930).

[11]. N. Shirai, S. Ibuka, and S. Ishii, Appl. Phys. Express, Vol. 2, no. 3 pp. 036001, Mar. (2009).

[12]. N. Shirai, S. Uchida, F. Tochikubo and S. Ishii, IEEE Trans. Plasma Sci. Vol. 39, no. 11, pp. 2652-2653, Nov. (2011).

[13]. N. Shirai, S. Uchida and F. Tochikubo, Plasma Sources Sci. Technol., Vol. 23, no. 5, pp. 1-10, Oct. (2014).

[14]. T. Verreycken, P. Bruggeman and C. Leys, J. Applied Physics, Vol. 105, no.8, pp. 083312-083312-4 (2009).

[15]. J. P. Trelles, J. Phys. D: Appl. Phys. 49 393002 (2016).

[16]. F. Tochikubo, N. Shirai and S. Uchida, J. Phys.: Conf. Ser. 565 012010 (2014).

[17]. Q. Chen, J. Li and Y. Li, J. Phys. D: Appl. Phys. 38 424005 (2015).

[18]. C. Richmonds, M. Witzke, B. Bartling, S. W. Lee, J. Wainright, C. C. Liu, and R. M. Sankaran, J. Am. Chem. Soc. 133 17582 (2011).

[19]. P. Rumbach, D. M. Bartels, R. M. Sankaran and D. B. Go, Nat. Commun. 6 7248 (2015).

[20]. Ch. Radehaus, T. Dirksmeyer, H. Willebrand and H.-G. Purwins, Phys. Lett. A, Vol. 125, no. 2, pp. 92-94, Nov. (1987).

[21]. Y. A. Astrov and H.-G. Purwins, Phys. Lett. A, Vol. 283, no. 5, pp. 349-354 (2001).

[22]. R. S. Islamov, Phys. Rev. E, Vol. 64, no. 4, PP. 046405, Oct. (2001).

[23]. M. Sanduloviciu, E. Lozneanu, and S. Popescu, Chaos, Solitons and Fractals, Vol. 17, no. 2, pp. 183-188 (2003).

[24]. M. S. Benilov, Phys. Rev. E, Vol. 77, no. 3, pp. 036408, Mar. (2008).

[25]. K. G. Muller, Phys. Rev. A, Vol. 37, no. 12, pp. 4836-4845, June (1988).

[26]. Yu. P. Raizer and M. S. Mokrov, Phys. Plasmas, Vol. 20, no. 10, pp. 101604, Oct. (2013).

[27]. A. A. Berezin, Chem. Phys. Lett., Vol. 123, no. 1,2, pp. 62-64, Jan. (1986).

[28]. J. P. Trelles, Plasma Sources Sci. Technol., Vol. 22, no. 2, pp. 025017, Apr. (2013).

[29]. P. G. C. Almedia, M. S. Benilov, M. D. Cunha and M. J. Faria, J. Phys. D: Appl. Phys. 42 194010 (2009).

[30]. P. G. C. Almedia, M. S. Benilov, and M. J. Faria, Plasma Sources Sci. Technol. 19 025019 (2010).

[31]. H. G. Purwins et al, Adv. Phys. 59 485 (2010).

[32]. T. Callegari, B. Bernecker and J. P. Boeuf, Plasma Sources Sci. Technol. 23 054003 (2014).

[33]. M. S. Bieniek, P. G. C. Almeida, and M. S. Benilov, Plasma Sources Sci. Technol., Vol. 27, no. 5, pp. 05LT03 (7pp), May. (2018).

[34]. P. Rumbach, A. E. Lindsay, and D. B. Go, Plasma Sources Sci. Technol. 28 105014 (2019).

[35]. P. J. Bruggeman, M. J. Kushner, B. R. Locke et al., Plasma Sources Sci. Technol., Vol. 25, no. 5, pp. 053002 (2016).

[36]. A. Wilson, D. Staack, T. Farouk, A. Gutsol, A. Fridman and B. Farouk, Plasma Sources Sci. Technol., Vol. 17, no. 4, pp. 045001 (2008).

[37]. S. Y. Miao, C. S. Ren, D. Z. Wang, Y. T. Zhang, , B. Qi, and Y. N. Wang, IEEE Trans. Plasma Sci., Vol. 36, no. 1, pp. 126-130, Feb. (2008).

[38]. J. A. Johnson and R. Ramaiah, Phys. Rev. A 36 774 (1987).

[39]. S. Zhang and T. Dufour, 2018 Phys. Plasmas 25 073502 (2018).

[40]. P. Zheng et al, Plasma Sources Sci. Technol. 24 015010 (2015).

[41]. J. R. Davis, ASM Handbook, Volume 5A: Thermal Spray Technology. In: Robert C, editor. Materials Park, OH, USA: ASM International, (2013).

[42]. J. Han, L. Wang L, R. Guo. Macromol. Rapid Commun. 32, 729–735 (2011).

[43]. C. I. Ossai and N. Raghavan, Nanotechnol Rev 7(2) 209-231 (2018).

[44]. M. Keidar, Phys. Plasmas 25 083504 (2018).

[45]. Z. Chen, S. Zhang, B. I. I. Levchenko, and M. Keidar, Sci. Rep. 7 12163 (2017).

[46]. J. Foster, Phys. Plasmas 24, 055501 (2017).

[47]. R. Munter, Proc. Estonia Acad. Sci. Chem. 50 59 (2001).

[48]. W. H. Glaze, K.W. Kang and D. H. Chapin, Ozone: Sci. Eng. 9 335 (1987).

[49]. X. Wang, M. Zhou and X. Jin Electrochim. Acta 83 501 (2012).

[50]. J. Gao et al, Water Res. 37 267 (2003).

[51]. Q. Lu, J. Yu and J. Gao, J. Hazard. Mater. B136 526 (2006).

[52]. S. K. Sengupta, R. Singh and A.K. Srivastava, J. Electrochem. Soc. 145 2209 (1998).

[53]. A. R. Denaro and A. Hickling, J. Electrochem. Soc. 105 265 (1958).

[54]. P. Zheng et al, Appl. Surf. Sci. 259 494 (2012).

CHAPTER III

Theoretical Background and Experiments

This chapter covers the theoretical background of the plasma physics that supported this self-organization study (Sec 3.1), a brief overview of possible mechanisms giving rise self-organization (Sec 3.2), and the general experimental methods that were used in this thesis work (Sec 3.3).

3.1 Self-organization Related Plasma Physics

In this section, the underlying plasma science of the DC glow is discussed. These processes lay the groundwork for understanding the occurrence of self-organization.

3.1.1 Theory of DC glow Discharge

3.1.1.1 IV Characteristics

Consider the general current-voltage characteristic of a DC electric discharge illustrated in Fig 3.1a. Three regimes are apparent: the dark discharge, the glow discharge, and the arc discharge. As explained in the last chapter, the 1 atm DC glow studied in this work is most similar to the glow discharge regime owing to similarities of discharge structure and IV response.

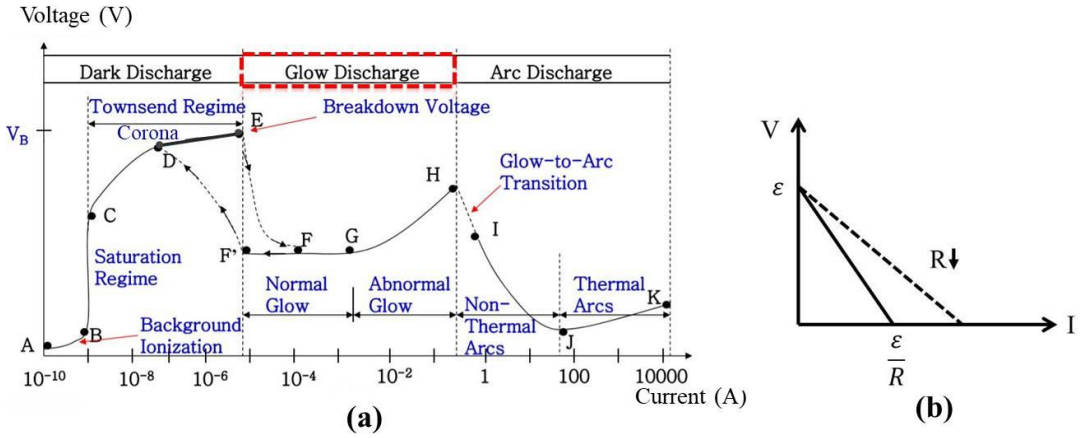

Figure 3.1 Typical current voltage characteristics of DC electric discharge are shown in (a) with its load line in (b).

The electric plasma discharge circuit includes an external ohmic resistance R to limit the current, the load line shown in Fig 3.1b is the result of Ohm's law:

$$\varepsilon = V + RI, \tag{3.1}$$

where ε is the electromotive force, V is the voltage across the plasma discharge gap, and I is the total discharge current in the circuit. If the external ohmic resistance is high and the current in the circuit is low (about10^{-10}–10^{-5} A), electron and ion densities are negligible and perturbation of the external electric field in plasma can be neglected. Such a discharge is known as the dark Townsend discharge. The voltage necessary to sustain this discharge does not depend on current and coincides with the breakdown voltage V_B shown at point E in Fig 3.1a. An increase of the ε or a decrease of the external resistance R leads to a growth of the current and plasma density, which results in the significant restructuring of the electric field. This leads to a reduction of voltage with current and to a transition from dark to glow discharge occurs. This very low current glow discharge is called the sub glow discharge (EF). Further ε increase or R reduction leads to the lower voltage plateau FG on Fig 3.1a, corresponding to the normal glow discharge

existing over a large range of currents in mA. The current density on the cathode is fixed for normal glow discharges. An increase of the total discharge current is provided by growth of the cathode spot through which the current flows. When the current is so high that no more free surface is left on the cathode, further current growth requires a voltage increase to provide higher values of current density. Such a regime is called the abnormal glow discharge and it corresponds to the growing interval GH in the figure.

In addition, further increases of current and voltage in the abnormal glow regime leads to higher power and transitioning to an arc discharge. The glow to arc transition usually takes place at currents around 1 A. Since the current range associated with this self-organization study was between 0 to 145 mA, it also shows that the 1 atm DC glow was in the range between behavior of normal and abnormal glow. However, the main characteristics of the discharge such as the breakdown voltage, the voltage current characteristic and the structure of the discharge are also dependent on the geometry of the electrodes, the gas used, the pressure and the electrode material.

3.1.1.2 Breakdown Process

The breakdown process is explained by the Townsend mechanism. It starts with an electron avalanche which is multiplication of some primary electrons in cascade ionization. It can be described by considering the simplest breakdown in a plane gap d by DC voltage V in a corresponding electric field $E = V/d$ (Fig.3.2). The initial current i_0 is a result of the

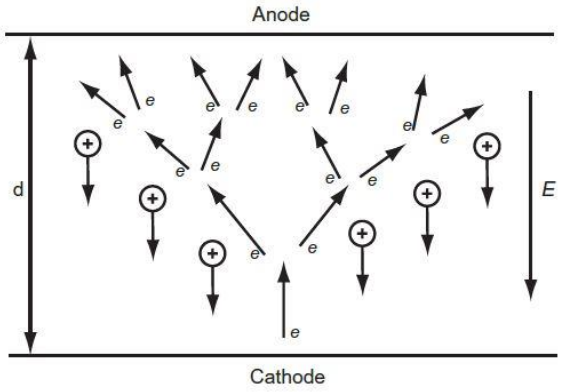

Figure 3.2: Townsend breakdown process in the gap between electrodes. [1]

primary electrons near the cathode being very low. The primary electrons drift to the anode, ionizing the gas and generating avalanches. The ionization in avalanches is explained by Townsend ionization coefficient α. This coefficient gives the electron production per unit length along the electric field. Simply the coefficient depends on the ionization rate coefficient k_i (E / n_0) where n_0 is the gas density, and can be expressed as

$$\alpha = \frac{v_i}{v_d} = \frac{1}{\mu_e}\frac{k_i}{E/n_0}, \tag{3.2}$$

where v_i and v_d are the ionization frequency and electron drift frequency respectively, and μ_e is the electron mobility. Each primary electron generated near a cathode produces $\exp(\alpha d) - 1$ positive ions moving back to the cathode. Then these ions lead to the extraction of $\gamma[\exp(\alpha d) - 1]$ electrons from the cathode due to secondary electron emission characterized by the Townsend coefficient γ. In the emission process, secondary emission coefficient γ describes the probability of electron emission of ion impact plays important role. This coefficient depends on the gas, electric field and cathode material. As a result the total electron current at the cathode can be given below:

$$i_{cathode} = i_0 + \gamma i_{cathode}[\exp(\alpha d) - 1]. \tag{3.3}$$

Since the ion current is negligible in the breakdown, the total current in the external circuit is equal to the electronic current at the anode, which can be found as $I = i_{cathode} \exp(\alpha d)$. Therefore leads to the Townsend formula:

$$I = \frac{i_0 \exp(\alpha d)}{1-\gamma[\exp(\alpha d)-1]}. \tag{3.4}$$

When the electric field and Townsend coefficient α grows sufficiently high, the denominator in Equation 3.4 vanishes and non-self-sustained discharge transitions to self-sustained current, where the breakdown occurs. In the other words, this provides the self-sustaining breakdown condition, or often called Townsend breakdown mechanism:

$$\gamma[exp(\alpha d) - 1] = 1, \alpha d = ln(\frac{1}{\gamma} + 1). \tag{3.5}$$

One can express the ionization coefficient as a function of pressure (neutral density) using the semi-empirical expression:

$$\frac{\alpha}{P} = C_1 \exp(-\frac{C_2}{E/P}), \tag{3.6}$$

where C_1 and C_2 are coefficients dependent on the electric field to pressure ratio *E/P*. Combining (3.5) and (3.6) yields an expression for the break down voltage—the famous Paschen's law:

$$V_B = \frac{C_2 Pd}{\ln(C_1 Pd)-\ln[\ln(\frac{1}{\gamma}+1)]}. \tag{3.7}$$

Breakdown of larger gaps is less sensitive to the secondary emission and cathode material, which explains the *E/P* reduction with *Pd.* This reduction of the break down electric field in electronegative gases is limited by the electron attachment processes which are characterized by Townsend coefficient (β mode):

$$\beta = \frac{v_a}{v_d} = \frac{1}{v_d} k_a(E/n_0) n_0 = \frac{1}{\mu_e} \frac{k_a(E/n_0)}{E/n_0}. \tag{3.8}$$

Here $k_a(E/n_0)$ and v_a are the attachment rate coefficient and frequency with respect to an electron. In this situation, the electron losses are in attachment per unit length:

$$\frac{dn_e}{dx} = (\alpha - \beta)n_e, \qquad n_e(x) = n_{e0}\exp[(\alpha - \beta)x]. \tag{3.9}$$

The Townsend coefficients, both α and β, are an expoenetial function of the reduced electric field. However, since β is not as strong as α in most cases, the ionization rate will greatly exceed the attachment in higher electric fields so that β can be neglected in short gaps. On the other hand, the Townsend breakdown electric fields in electronegative gases become almost constant and limited by the attachment processes such as in the larger gaps (centimeter sizes) and higher pressure. An example of breakdown electric fields in 1 atm for electronegative and non-electronegative gases (tested on self-organization) is listed in Table 3.1.

Table 3.1. Required electric field for Townsend breakdown of centimeter sized gaps in various gases at 1 atm.

Gas	***E/P*, kV/cm**	**Gas**	***E/P*, kV/cm**
Air	32	He	10
O_2	30	Ar	2.7
N_2	35		

3.1.1.3 DC Glow Discharge Structures

A classical DC glow discharge is usually demonstrated in low pressure (about 1 Torr) using a cylindrical tube with features consisting of glow regions, dark spaces, and a positive column in sequence (Fig. 3.3a). Such discharge can be defined as the self-sustained continuous DC discharge with cold a

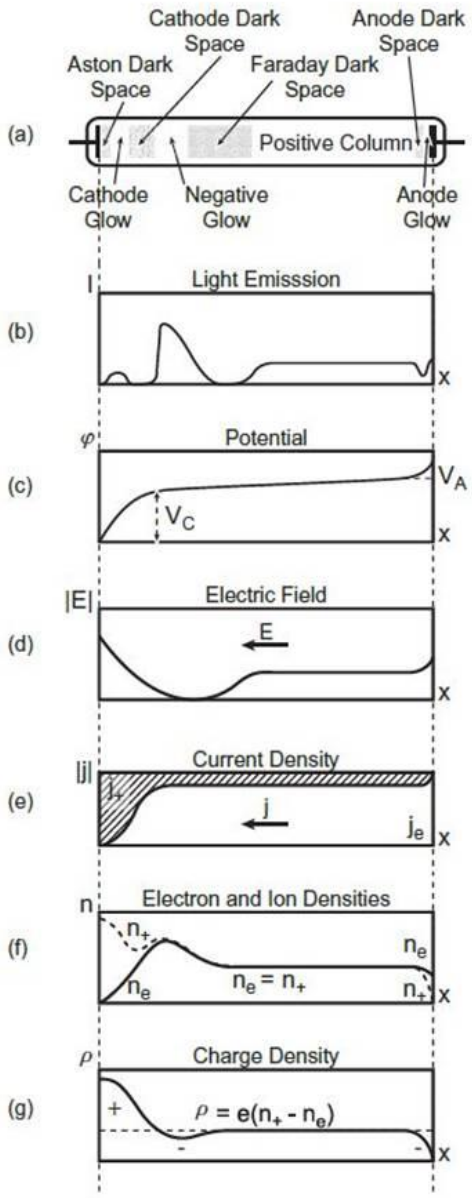

Figure 3.3: DC glow discharge in low pressure with (a) structures and (b – g) the physical parameters distributed in the glow [1].

cathode, which emits electrons as a result of secondary emission mostly introduced by positive ions. A distinctive feature of a glow discharge is the cathode layer with positive space charge, strong electric field, and potential drop of about 100 – 500 V [1]. The thickness of the cathode layer is inversely proportional to gas density. When the distance between the electrodes is large enough, quasi-neutral plasma with low electric field, the so called positive column, is formed

between the cathode layer and anode. The positive column is separated from the anode by an anode layer, where characterized by a negative space charge, slightly elevated electric field, and some potential drop.

The detailed glow patterns can be interpreted based on the distribution of the discharge parameters shown in Fig 3.3b-g. The Aston dark space is due to electrons being ejected from the cathode with insufficient energy for the excitation of the atoms. The electrons obtain enough energy from the electric field for electronic excitation then provide the cathode glow. Further acceleration of electrons in the cathode dark space leads mostly to ionization. This explains the low level of radiation and increase of electron density in the cathode dark space. The bright layer, negative glow is usually generated from the intensification of radiation that is given by the results of the high electron density at the end of the cathode dark space with a decrease of the electric field, electron energy, and ionization rate. Farther from the cathode, electron energy decreases, resulting in a transition from the negative glow to the Faraday dark space. Here plasma density decreases and the electric field grows up, establishing the positive column. The average electron energy in a positive column is about 1–2 eV, which provides light emission. The positive column can be extended so it is somewhat long and connecting the electrodes. The anode repels ions and pulls out electrons from the positive column, which creates the negative space charge and leads to an increase of the electric field in the anode layer. A reduction of the electron density explains the anode dark space, whereas the electric field increase explains the anode glow.

3.1.1.4 Positive Column

If the pressure in the tube is increased all the negative zones (the cathode dark space, negative glow, and Faraday dark space) compress toward the cathode and the positive column

expands to fill the space. The positive column can be long, homogeneous, and can release most of the discharge power. For example, at atmospheric pressure, a self-organized discharge with a fully expanded positive column in the DC glow from the cathode can be seen in Fig. 3.4. Unlike the low pressure DC glow discharge in the tube, here the anode dark space is much larger. It might indicate that the anode fall might be significant in playing a role in the overall dynamics.

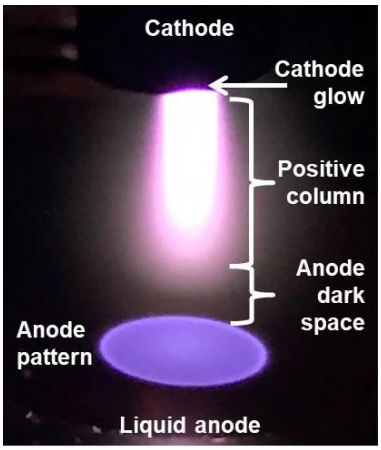

Figure 3.4: Typical structure of the 1 atm DC glow generated in PSTL[4] with self-organized solid disk show as the anode pattern (assume it is the anode layer with measured diameter of 4.3 mm) using liquid anode.

Non-equilibrium behavior of the discharge (Te >> T) is controlled by heat balance as

$$\omega = jE = n_0 c_p (T - T_0) V_T, \tag{3.10}$$

where ω is the power per unit volume, c_p is the specific heat, T and T_0 are the positive column and room temperatures, and V_T is the cooling frequency for cylindrical discharge tube of radius r and length d_0:

$$V_T = \frac{8}{r^2}\frac{\lambda}{n_0 c_p} + \frac{2u}{d_0}. \tag{3.11}$$

Here, the λ is the coefficient of thermal conductivity and u is the gas velocity. The first term in (3.11) is related to thermal conductivity; the second one describes convective heat removal, If

[4] The Plasma Science and Technology Laboratory (PSTL) is located in the department of Nuclear Engineering and Radiological Sciences at University of Michigan-Ann Arbor.

heat removal is dependent on thermal conduction, the discharge power causing a doubling of temperature ($T - T_0 = T_0$) that gives (3.10) to

$$\omega = jE = \frac{8\lambda T_0}{r^2}. \tag{3.12}$$

For most of gases, since the λ does not depend on pressure will approaches to a constant value approximately of 3×10^{-4} $Wcm^{-1}K$ near 1 atm, the specific discharge power in (3.12) also does not depend on pressure and can be estimated as 0.7 W/cm^3 for $r = 1\ cm$. Higher powers result in higher gas temperatures and glow discharge contraction. However, for the helium plasma there is an exception, its thermal conductivity is around of 15×10^{-4} $Wcm^{-1}K$ at 1 atm, the specific discharge power under Fig 3.4 conditions therefore can be estimated as 76 W/cm^3 by taking the *r* value as the radius of the positive column, which was measured as 2.14 mm. This value is 100 times larger using helium than any others. The measurements done here assumed a perfect cylindrical geometry for the positive column observed in Fig 3.4 by equalizing the diameter of the anode pattern to the sum of the visible positive column diameter and its sheath thickness.

Back to the derivation, the typical current density in the positive column with the heat removal controlled by thermal conductivity is inversely proportional to pressure:

$$jE = \frac{8\lambda T_0}{r^2}\ \frac{1}{(E/P)}\ \frac{1}{P}. \tag{3.13}$$

The corresponding electron density n_e in the positive column can be calculated from Ohm's law with form of $j = \sigma E$, yields

$$n_e = \frac{\omega}{E^2}\frac{mv_{en}}{e^2} = \frac{\omega}{(E/P)^2}\ \frac{mk_{en}}{e^2T_0}\ \frac{1}{P}. \tag{3.14}$$

Here v_{en} and k_{en} are the frequency and rate coefficient of electron – neutral collisions. Numerically, n_e (cm^{-3}) is approximately equal to 3× 10^{11} /p Torr in a positive column with conductive heat removal. In the case of Fig 3.4, by considering *E/P* value (10 kV/cm) from the Table 3.1, this heat removal electron density is estimated only at 38.57 cm^{-3}. This value is way lower when compared to the electron densities we spatially estimated in the plasma column (with a magnitude of 10^{14} cm^{-3} shown in chapter 5). Although this might not be a good example for the estimation, it gives an insight that the convective heat plays a very important role in helium plasma liquid coupled DC glow, perhaps as well as the self-organization pattern formation on the liquid anode.

3.1.2 Plasma Chemistry

As stated above, a DC plasma discharge is produced by the convection of electrons, which travel from the cathode to the anode region. Ionizing collisions between these electrons and molecules or atoms produces the electron-ion pairs that comprise the plasma. Here we summarized the main electron collisions that are taking place in the atmospheric pressure DC glow in the Table 3.2. The fundamental plasma chemistry that supported above calculations in the non-equilibrium glow discharge is qualitatively highlighted.

The balance of charged particles in the positive column follows the general rules, such that by a balance between generation and loss of charged particles. The generation of electrons and positive ions is mostly due to volume ionization with required electron temperature of about 1 eV to sustain a steady state. The mechanisms of charged particles losses can be related to the volume processes of recombination or attachment, and also provided by the diffusion of charged particles to the walls with further surface recombination but not at 1 atm pressure.

Table 3.2. Electron collision in electric field. Note that * indicates the metastable state.

Type	Electronic reaction	Atomic reaction	Photon reaction
Excitation and de-excitation	$e + A_2 \leftrightarrow A_2^* + e$		$hv + A_2 \leftrightarrow A_2^*$
Dissociation	$e + A_2 \rightarrow 2A + e$	$M^* + A_2 \rightarrow 2A + M$ Penning dissociation	
Ionization	$e + A_2 \rightarrow A_2^+ + 2e$	$M^* + A_2 \rightarrow A_2^+ + M + e$ Penning ionization	$hv + A_2 \rightarrow A_2^+ + e$ Photo ionization
At achment	$e + A_2 \rightarrow A_2^-$		
Recombination	$e + A_2^+ \rightarrow A_2$ $2e + A_2^+ \rightarrow A_2 + e$	$A^- + B^+ \rightarrow AB$	$e + A_2^+ \rightarrow A_2 + hv$ Radiative recombination

When the ionization degree in plasma is relatively high and diffusion can be considered ambipolar, the frequency of charge losses due to diffusion to the walls can be expressed as

$$v_D = \frac{D_a}{\Lambda_D^2}, \tag{3.15}$$

where D_a is the ambipolar diffusion coefficient and Λ_D is the characteristic diffusion length. Non-equilibrium discharges are controlled by volume process at condition when

$$k_i(T_e)n_0 \gg \frac{D_a}{\Lambda_D^2}. \tag{3.16}$$

Here, $k_i(T_e)n_0$ is the ionization rate coefficient. Because of ambipolar diffusion coefficient is inversely proportional to the pressure and gas density is proportional to the pressure, this condition actually restricts pressures.

At high pressures, the diffusion is relatively slow and the balance of charge particles is due to volume processes:

$$\frac{dn_e}{dt} = k_i n_e n_0 - k_a n_e n_0 + k_d n_0 n_- - k_r^{ei} n_e n_+ , \quad (3.17)$$

$$\frac{dn_+}{dt} = k_i n_e n_0 - k_r^{ei} n_e n_+ - k_r^{ii} n_+ n_- , \quad (3.18)$$

$$\frac{dn_-}{dt} = k_a n_e n_0 - k_d n_0 n_- - k_r^{ii} n_+ n_- . \quad (3.19)$$

In this set of equations, *n* represents concentration of the particles such as positive (+), negative (-) ions; rate coefficients k_i, k_a, k_d, k^{ei}_r , k^{ii}_r are related to the processes of ionization by electron impact, dissociative or other electron attachment, electron detachment from negative ions, and electron–ion and ion–ion recombination.

3.2 Mechanisms of Self-organization Formation

The occurrence of pattern formation and self-organization has been associated with the concepts of non-equilibrium, dissipative structures, instability, symmetry breaking, and bifurcation [2-5]. All those have shown that the self-organization processes are driven by forces within the system. A general criteria for a system to be self-organized can be shown in one of the following such as (1) a spatially ordered pattern that is significantly different from a random pattern; (2) a temporally ordered structure; (3) a system with negative entropy change ($dS < 0$); (4) a nonlinear dissipative system with limit-cycle behavior (which by definition produces quasi-periodic temporal oscillations); (5) a nonlinear dissipative system with resonances; and (6) a nonlinear dissipative system that is driven by an external force and counter-acted by a positive feedback force, triggered by an instability or turbulence[6].

Although the clear mechanisms of self-organization particularly in plasma physics is not understood, it is believed that they arise from space charge accumulation near the electrode

surfaces, while the specific geometric structure of a pattern depends on complex feedback mechanisms. In the case of non-thermal plasmas, driving forces include chemical, fluid dynamic, electrostatic, and thermal. Some theories applicable to the DC glow SOP are reviewed.

3.2.1 Reaction Diffusion

Reaction-diffusion models are the most widely adopted and effective model to explain the self-regulated pattern formation in a variety of systems [7-13]. The governing equation that applied to the model has an initial form of

$$\partial_t \boldsymbol{Y} = D\nabla^2 \boldsymbol{Y} + S(\boldsymbol{Y}), \tag{3.20}$$

where $D\nabla^2 Y$ indicates the diffusion term with a diffusion tensor D, and the $S(Y)$ is the reaction term. Here $\boldsymbol{Y}$ is a compound column vector. When steady state is reached with the left hand side will equal zero, the global equilibrium between production and diffusion in which $S(\boldsymbol{Y}) = -D\nabla^2 \boldsymbol{Y}$ can lead to pattern formation such as the dissipative structures. The simplest form of this model displaying pattern formation is given by a two component system of $\boldsymbol{Y}$ without cross diffusion:

$$\partial_t u = D_u \nabla^2 u + S_u(u, v), \tag{3.21}$$

$$\partial_t v = D_v \nabla^2 v + S_v(u, v), \tag{3.22}$$

where u and v are complementary characteristics of the system such as the concentration of the species, D_u and D_v are the diffusion coefficient constants. Solutions to this system of equations include wavefronts, clustering, spatiotemporal chaos, and composite patterns. A key aspect of such systems is that the diffusion rates of the reacting species are different and some form of feedback is present in the system to amplify the pattern development.

A key consideration when applying the reaction diffusion model to plasma systems is the identification of the activator and inhibitor (or autocatalyst as in the case of a Gray-Scott system)

along with the feedback source. For example, current has often been identified as the activator of the pattern with voltage serving as the inhibitor [14]. Consider for example of a discharge between two electrodes at atmospheric pressure. Here a single filament may form at a given applied voltage. With increasing voltage, current increases but eventually exceeds the magnitude for which can be collected practically at the surface. This is particularly the case for a resistive surface. In this case multiple filaments are required to support the current. In this manner, the attachment becomes more complex and perhaps seeds the self-organization.

3.2.2 Predator Prey[5]

A predator-prey formulation can be used to describe at least why more filaments are necessary. This formulation is nonlinear and can lead to complex a solution for the spatial distribution of the attachment. For a simplified insight into the physical processes leading to the need for more complex collection on the surface area, considering a single filament attached to an electrode with finite surface resistance. Such an approach has been used to formulate reaction diffusion for DC filaments on semiconducting surfaces [15]. In the present formulation, the current can be modeled as the 'prey' and the boundary layer resistivity can serve as the 'predator.' It must be kept in mind that the resistivity discussed here is local — the attachment is highly localized and thus the current transport is also local and can be expected to be subject to localized saturation; that is, the current in principle should be limited by the local diffusion of ions to and through the double layer to the attachment point to complete the circuit (in the case of a liquid electrode). Indeed, the nature of the liquid double layer below the attachment has the effect of shielding these local processes from the surrounding fluid is the same manner as the

[5] The text and discussion in this subsection have been previously published by J.E. Foster, Y.E. Kovach, J. Lai, and M. C. Garcia, "Self-organization in 1 atm DC glows with liquid anodes: current understanding and potential applications" Plasma Sources Sci. Technol. 29 034004 2020.

Debye sheath shields electrodes from the rest of the plasma in the gas phase. The conductivity in this localized region and the double layer properties below the attachment depends on local field strength and ion formation processes associated with the plasma as depicted in Fig.3.5. Here ions travel through

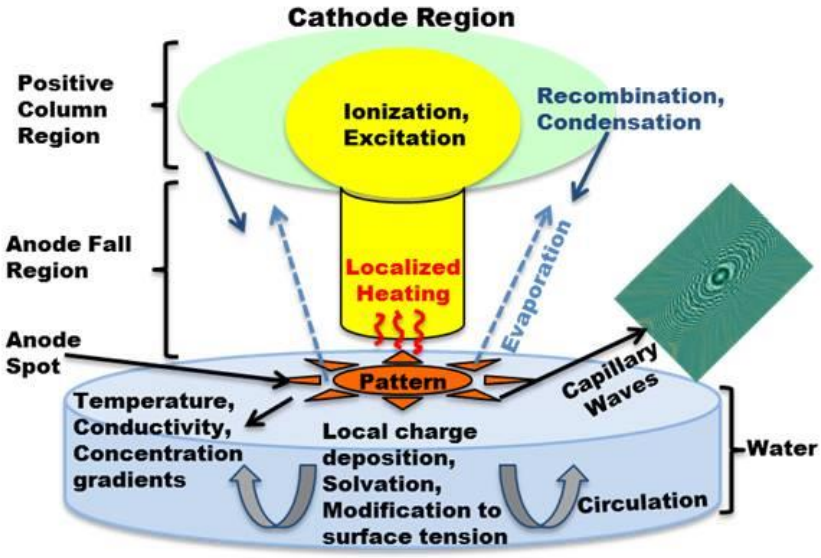

Figure 3.5: Physical process prevailing at the interface influencing local resistivity and charge transport.

the liquid to the attachment point to neutralize incoming electron charge. The relevant system of equations describing the predator–prey relationship between current *I* and resistivity ρ can thusly be written:

$$\frac{dI}{dt} = aI - bI\rho \,, \tag{3.23}$$

$$\frac{d\rho}{dt} = -c\rho + dI\rho \,. \tag{3.24}$$

Here, the time variation in the current I would increase exponentially without a limit if the surface can handle the transport. The second term represents the limiting factor of local resistivity, which in this case scales as the power deposited in the local attachment volume. *a, b* are constants. The second of the coupled equations represents the resistivity variation. It tends to

decay with increasing resistivity as its increase ultimately limits the amount of current collected (a type of feedback) and thus the amount of ion production both in gas phase and in local interface region. Reductions in resistivity reduce depletion as well. Resistivity on the other hand increases with more power locally deposited into the area near the attachment. This system of equations gives at least qualitative insight into why more area or filaments are needed. It is also a system of nonlinear equations that can give rise to spatial and spatial temporal solutions. A single filament will ultimately always be limited by the local resistivity derived from a lack of additional charge carriers for example. Simply put, the plasma can supply more current than the electrolyte can support.

The nonlinear discharge column response relative to the linear conductivity response of the bulk can lead to instability. The plasma interaction with the liquid can enhance conductivity locally but continuity and ultimately the discharge current that is possible is determined by diffusion from the bulk. Current therefore can only increase if there are more attachment points-more filaments or increasing discharge complexity to sustain the current. Similar depletion processes are also observed in batteries when operating at higher currents. In such a case, near electrodes (in an electrolyte solution) ions are removed or generated giving rise to temporal and spatial variations in conductivity [16]. Motion of the attachment at the interface is another mechanism that can manage such depletion as the local conductivity with a liquid electrode can actually change. In this case the attachment can simply rotate or displace to pristine solution where more carriers are abundant, thereby leaving the region of temporarily localized depletion—or inhibition zones. The translation time of such oscillatory can be expected to be on the time scale of depleted region recovery which should be of order the characteristic diffusion time of the solution. It should also be pointed out that the plasma attachment is not point-like but

rather extended and thus the attachment shape (regions of charge injection) can be expected to change spatially during such predator–prey oscillations.

3.2.3 Transport System

Reaction diffusion models can also be applied to the metal anodes, particularly by casting the *Y* term vector from equation (3.20) with multi fluids and the Maxwell models as

$$Y = [n_i\ n_e\ \varphi], \tag{3.25}$$

where n_i and n_e denote the number of density of ions and electrons, and φ is the electric potential. As for applying it to the DC glow discharge, the simplest set of equation *S* containing the basic physics necessary for the pattern formation are the continuity equations for conservation of electrons and a single ion species, the transport equations, written in the drift-diffusion approximation and coupled to the Poisson's equation:

$$\frac{\partial n_i}{\partial t} + \nabla \cdot \Gamma_i = n_e \alpha \mu_e E - \beta n_e n_i \quad \text{and} \quad \Gamma_i = -D_i \nabla n_i - n_i \mu_i \nabla \varphi\ , \tag{3.26}$$

$$\frac{\partial n_e}{\partial t} + \nabla \cdot \Gamma_e = n_e \alpha \mu_e E - \beta n_e n_i \quad \text{and} \quad \Gamma_e = -D_e \nabla n_e + n_e \mu_e \nabla \varphi\ , \tag{3.27}$$

$$\varepsilon_0 \nabla^2 \varphi = -e(n_i - n_e) \quad \text{and} \quad J = e\ (\Gamma_i - \Gamma_e). \tag{3.28}$$

In this equation set, as for the new variables with electron and ion denote as *e* and *i*, Γ represent the densities of transport fluxes, μ is the motilities. Here α is Townsend's ionization coefficient, β is the coefficient of dissociative recombination. $E = |\nabla \varphi|$ is electric field strength that associated with the electrostatic potential φ. In (3.28), J is the current density, where *e* is the electronic charge, and ε_0 is the permittivity of free space.

The solutions that come out from this system displayed as annular and planetary spots to ring, or stationary anode spots in DC glow discharge [17-20]. The key "to" applying this transport system to form patterns is similar to the bifurcation process. That is, by continuously

varying the control parameters, instabilities can arise that ultimately transition to well define structures. This process is different from chaos with its features exhibited as random behavior in nonlinear systems. In attempt to apply this formulism to DC glows, the bifurcation parameters are either current or electric field, or both. In such studies, anode spot pattern arise from the distribution difference of current density and electric field along the anode surface due to transport of charged species (Fig 3.6).

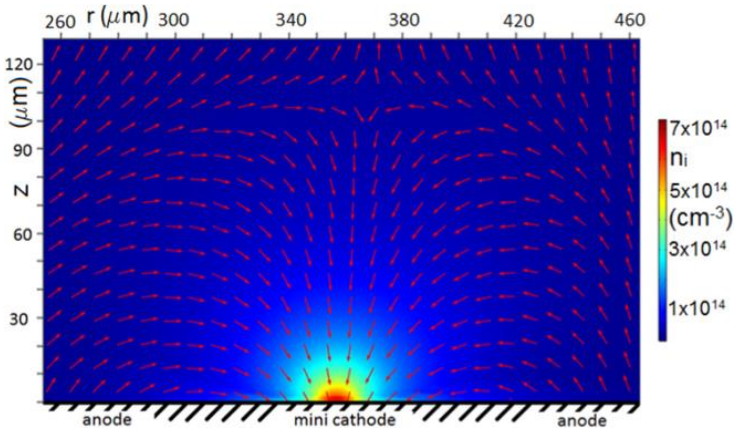

Figure 3.6: Distribution of the number of ions in the plane of symmetry passing through the center of the anode spot that resulted in transport system with the current density show in arrows [17].

However, the self-organization mechanisms studied in this method are limited to resolving the pattern morphology with complexity. It is limited in that it requires a wide array of assumptions regarding boundary conditions and sometimes not necessarily tied to the actual geometry of the model.

Reaction diffusion models may provide insight into pattern formation. In order to clearly understand the mechanisms of plasma self-organization, the species equation must be expanded to include solvation of species and investigate which generation or loss rates are the driving terms. For example, solvation of species may dominate species density over diffusion and local reactions. Experiments aimed at providing specific evidence of pattern formation where the aforementioned processes can be at least tracked would greatly improve our understanding of the

applicability of the reaction diffusion formalism to the observed self-organization. Another design parameter is the structure of the plasma discharge column, i.e. how many contact spots are created at the liquid electrode surface? This would be another term or boundary condition in a spatially resolved species equation and thus an important experiment. A model that takes into account these physical processes is necessary to truly understand the formation mechanisms of such complex phenomena on the liquid anode and metal anode surfaces.

3.3 Experimental Methods

The main experimental setup utilized in this work was a gas fed pin to plane discharge geometry which has been investigated in the past in the context of understanding SOPs [21-24]. The main plasma glow was generated by flowing 200 SCCM helium gas through the brass rod cathode to either the metal plates or liquid surfaces using DC power. In order to operate the plasma discharge precisely and to observe the self-organization successfully, the basic apparatus was built in house. As part of the research effort, here we summarize some of the main assemblies that have been applied and well supported for the experimental investigations during the dissertation study.

3.3.1 Prototype Design and Assemblies

Most of the design work was done in SolidWorks (2012 and 2016 version). Some of the components were built using the 3D printing technology (uPrinter by dimension, CatalystEX version 4.0.1, ABS-P40) and CNC EDM machines[6]. The initial design and prototypes are depicted in Fig. 3.7. The setups in the figure show a completed assembly but it was composed of

[6] The CNC EDM machine works are done in the LSA Scientific Machine Shop at University of Michigan and the Dellamar Manufacturing Company in Belleville Michigan.

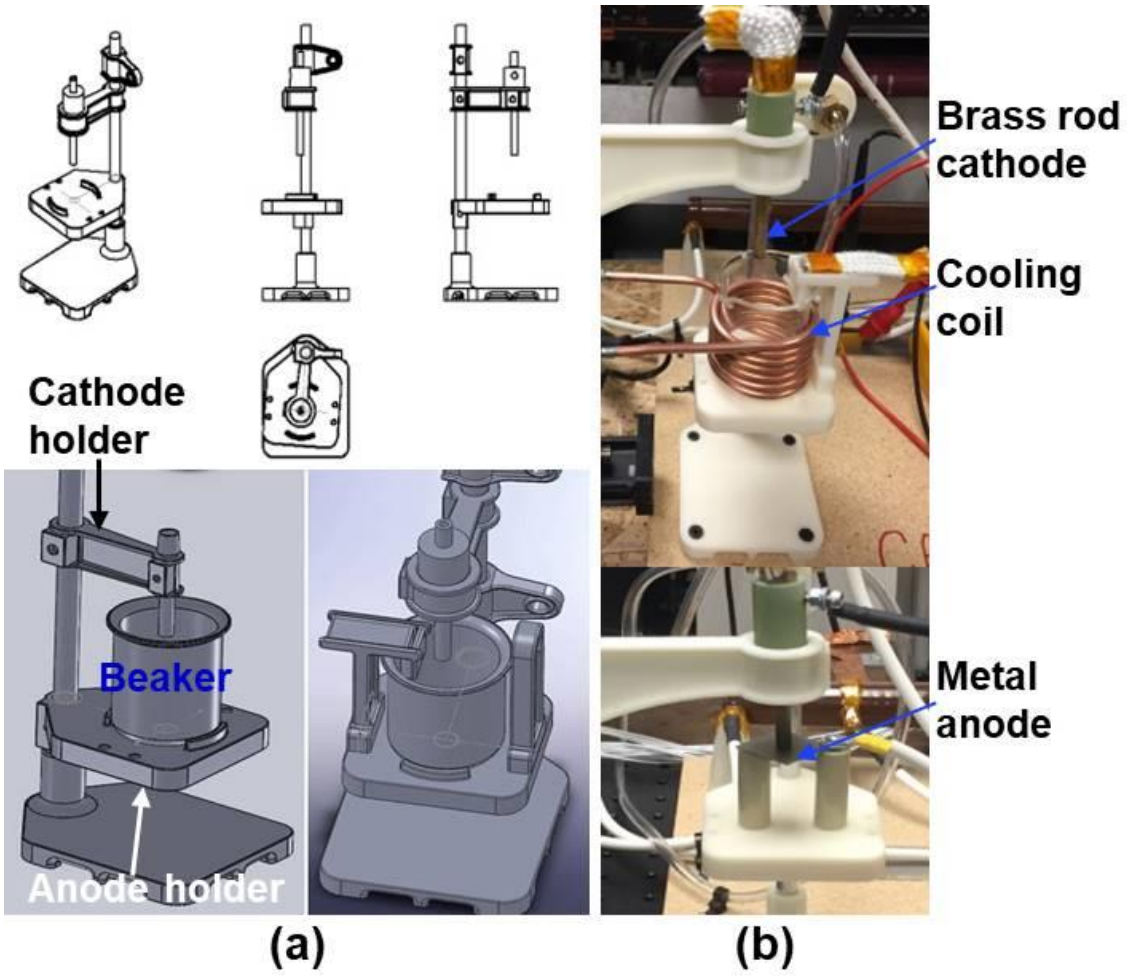

Figure 3.7: The initial setup design at each steps are shown in (a). Lab photographs of 3D printed setup are shown in (b) where the top setup was for liquid anode and bottom setup was for metal anodes.

individual small components. A beaker with 50 ml capacity was used in the study at the initial investigation stage. Plasma self-organization was first observed using NaCl solution at PSTL using a copper cooling coil. This initial cooling setup can be seen in the Fig 3.7b. However, self-organization was also observed later on without such cooling coils.

The cathode design is shown in Fig. 3.8a. It was made using the CNC machine by constructing a 3.5 mm hole and 500 μm hole through the

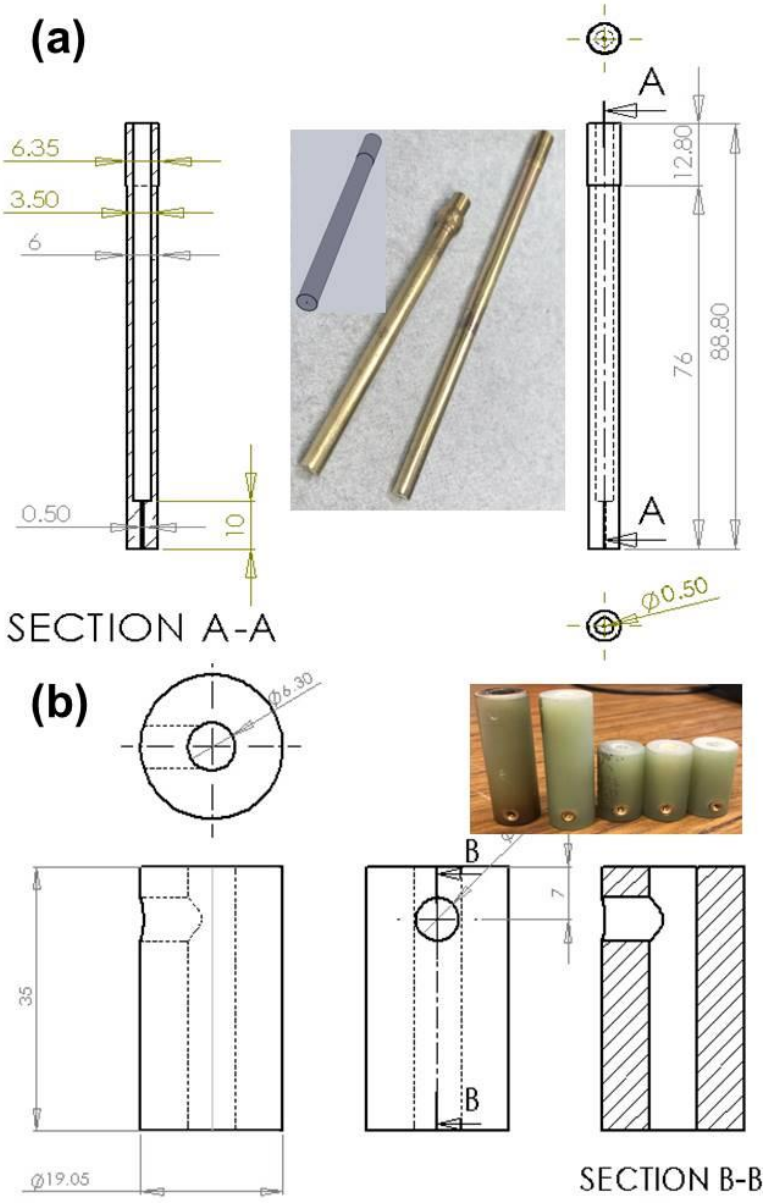

Figure 3.8: The machine schematics for (a) the brass rod cathode and (b) the cathode insulator. The scale units on the schematics are presented in mm. The parts demonstrated in this picture were machined in LSA Scientific Machine Shop at University of Michigan.

center of the brass rod with outer diameter of 6 mm. This provided a hollow cathode configuration for the brass rod cathode. More cathodes with the same design but different inner-hole diameters were machined. The results of applying them into the pattern study will be discussed in chapter 4. In the Fig 3.8b, an insulator was designed using phenolic rod (G10 RF4)

to cover the cathode so that it protects the 3D printed setup assembly. This material was chosen for is excellent temperature and insulation (electrical and thermal) characteristics.

For self-organization pattern studies using metal anodes in the 1 atm DC glow, a gas injection system was designed for testing the secondary gas effects on the patterns. Such a design with its 3D printed assembly can be seen in Fig 3.9. This circular design allows 4 gas injection

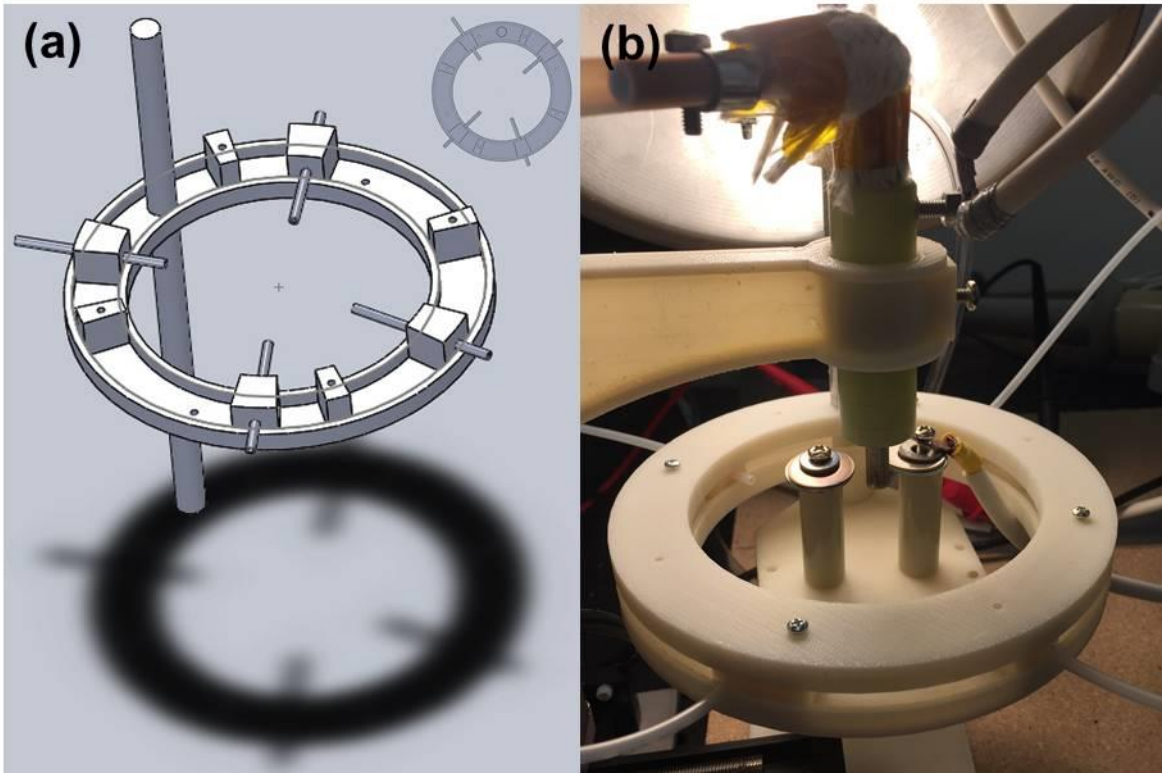

Figure 3.9: Secondary gas injection system with its (a) top and open cap view and (b) 3D printed assembly in the lab setup.

ports (1/8 inches gas tubes) to conveniently adjust their injection directions in 360 degree. Such specialized study results with operating details are discussed in next chapter.

A designed water cooling system in Fig 3.10 was employed in most of investigations. As shown in Fig 3.10d, the copper cooling box was made using CNC EDM machines. The purpose of designing and using it was to aim the study of anode cooling effects on the pattern formation. During each tests, the anode surfaces were cooled by the copper box with internal water flow

rate of 5 lpm from the chiller. The water temperature was usually set to 20 ℃ constant for all of the cases unless otherwise specified. The investigation of cooling effects particularly using this box and metal anodes was discussed in the chapter 4 as well.

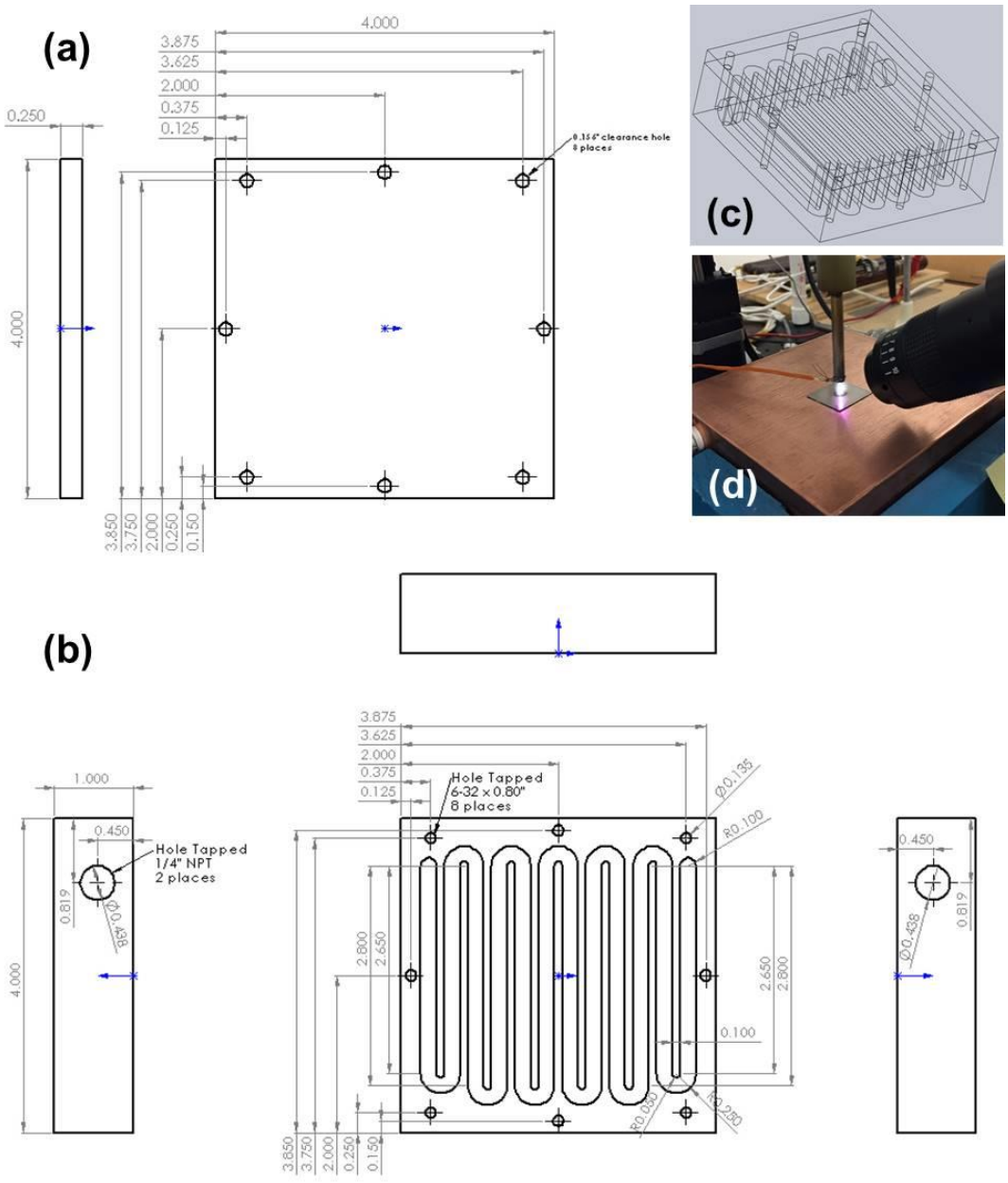

Figure 3.10: Cooling system is designed in (a) top view, (b) bottom view, (c) a 3D transparent view after putting the top and bottom together with a gasket, and (d) a photograph of using machined copper cooling box during the plasma discharge operation. The scale unit show on the schematics is inches. The parts demonstrated here were machined by the Dellamar Manufacturing Company in Belleville Michigan.

3.3.2 Software Design for Gap Control

The gap between the cathode and anode surfaces was carefully set using an automated motion control system. Gap length is one of the most important parameters determining the voltage magnitude for breakdown and the regime of occurrence of self-organization on the surface [1, 4]. Therefore, for this dissertation study, LabVIEW (version of 2014) code was written to control a VXM Stepping Motion Controllers (VELMEX, INC.) providing a precise control of gap lengths.

This code was created using two supporting sub views: the front panel in control and the block diagrams for the machine assessments and communications. For example, the snapshot of the front panel from the Virtual Instrument (VI) file is shown in Fig. 3.11. It consist three building

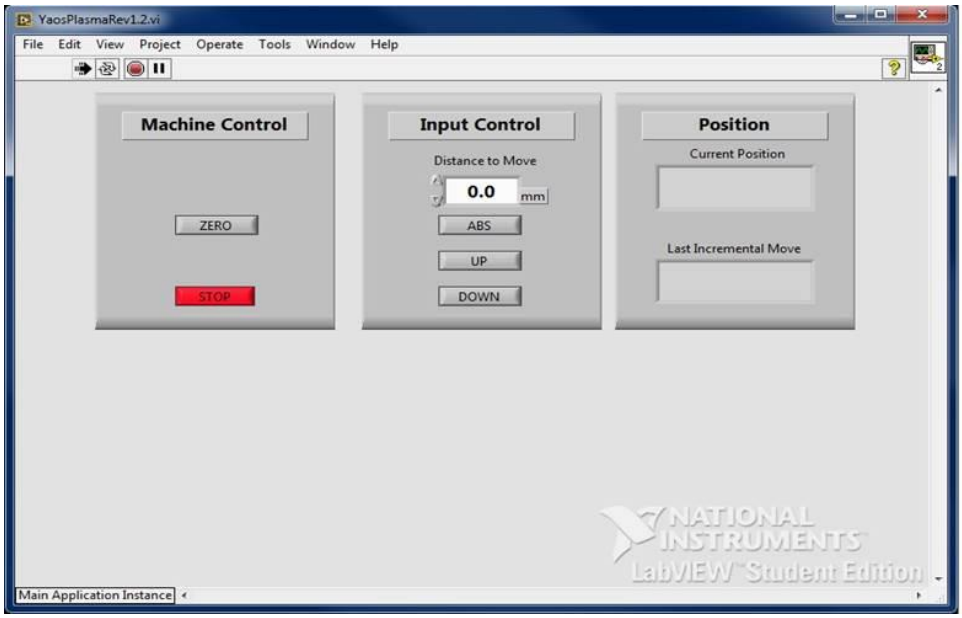

Figure 3.11: Example of the front panel from the LabVIEW code for controlling the gap length during the operation.

panels that support different operating functions. First one, machine control is designed to initialize the cathode position and stop the cathode movements. The desired moving adjustments can be entered in the second sub panel called input control. The absolute movement action button moves the cathode from its current position to the desired gap length refer to the anode surface which is at the zero position. The up and down buttons are used for the 0.5 mm increment or decrement that was related to their last movement respectively. Once the value has been entered, three different functions are accessible. The last sub panel indicates the current the cathode position from the anode surface and the information from the previous action. The block diagram from the VI file is given in Appendix B.

3.3.3 General Operation and Diagnostics

In addition, the standard operation, materials, electric and diagnostic apparatus applied in this research are described. During the operation, the helium gas (laboratory research grade 5.0, 99.999% purity) was controlled using a Alicat Scientific Mass Flow Controller. The standard liquid anode was a NaCl solution with conductivity of 12 $mScm^{-1}$ ± 0. 02. The solution pH is range between 6.5 and 7.2. The volumes of the liquid solution tested are 50 ml, 125 ml, and 200 ml. The physical and chemical properties such as pH and conductivity of the liquids are measured using the digital meter with various sensors (Thermo Scientific Orion). The return ground electrode composition that was used in these studies evolved over time — starting with copper and ending with silicon. The silicon electrode was found to be less susceptible to dissolution. Metal anodes applied to the research included tungsten (W), stainless steel (SS 304), and copper plates with their dimension being consistent at 25.4 mm × 25.4 mm × 0.5 mm.

The discharge was generated in either constant voltage mode (CVM) or constant current mode (CCM) depending on the plasma behavior in the gap. Particularly early on, the discharges

were operated in CVM. A DC high voltage power supply (GLASSMAN HIGH VOLTAGE, INC.) with a voltage Range of 0 to 3 kV and corresponding current range of 3 to 400 mA was employed in the entire power system. In this series electrical circuit, two sets of resistors are used: a ballast resistance in clusters and a 100 Ω single resistor. The ballast resistor was used to prevent the discharge from constricting into an arc. Its resistance was reduced from 25 kΩ initially to 15.75 kΩ for subsequent tests in response to the observation of the pattern formation. A high voltage probe (Tektronix P6015A) was employed in the initial examinations too. The discharge current was determined from the voltage drop across the 100 Ω resistor by using a multimeter (FLUKE 115). As a range of investigations were carried out in this work, the precise experimental setup with schematic is provided in the respective chapters.

Pattern observations were recorded using charge-coupled device (CCD) cameras such as Nikon D40 and High speed imaging systems (REDLAKE MotionPro HS-4, PHOTRON FASTCAM Mini UX100, PHANTOM v2640, and FASTCAM SA-Z)[7]. The lenses coupled with these cameras include an Edmund VZM (30 mm maximum), and Nikon lenses (focus length of 139.7 mm) with series number of a 211828 (55 mm), a 2840317 (50 mm with 12 mm extension tube), and a 2854307 (50 mm with 20 mm extension tube). The software for the video imaging and digital image data analysis are Photron PFV3, PFV4, and Phantom PCC 3.4. Pattern images captured using CCD cameras were usually at 30 frames per seconds (fps). All of the pattern observations on metal surfaces were at 50 fps for both CCD and high speed cameras. The details of direct plasma diagnostics such as using optical emission spectroscopy methods are described in chapter 5 and 6. Plasma column and liquid surface thermo gradients were measured using the

[7] PHANTOM v2640 and FASTCAM SA-Z were the high speed image cameras that provided by the High Speed Imaging Team in Subatomic Physics division P-25 at Los Alamos National Laboratory.

Thermography camera (FLIR SC655) and the Mutilogger Thermometer (OMEGA HH506RA) with K type thermocouples with epoxy coated tip (OMEGA 5TC-PVC) respectively.

A PSTL optical microscope (Leica, LAS EZ) was used early on to inspect the state of the electrodes. All of the resulting nanostructures observed either on the surface of metal electrodes or particles formed in the liquid electrolyte solutions were investigated in the University of Michigan's facility - Michigan Center for Material Characterization (MC^2). The main techniques applied to the this dissertation study include Scanning Electron Microscopy (SEM), Focused Ion Beam (FIB), Transmission Electron Microscopy (TEM), Dispersive energy X-Ray Spectroscopy (EDX) and Selected area electron Diffraction (SAED). The instruments from the MC^2 that successfully supported such investigations are named TESCAN MIRA3, Thermo Fisher Nova 200, Thermo Fisher Helio 650, and JEOL 3011 HREM.

3.4 References

[1]. A. Fridman, Plasma chemistry, Introduction to theoretical and applied Plasma Chemistry, Cambridge University Press, New york, 2008.

[2]. G. Nicolis and I. Prigogine, Self-organisation in nonequilibrium systems: Towards a dynamics of complexity, in Bifurcation Analysis, M. Hazewinkel, R. Jurkovich, and J. H. P. Paelinck, Eds., 1st ed. Dordrecht, The Netherlands: D. Reidel Publishing Company, pp. 3–12. (1985)

[3]. M. C. Cross and P. C. Hohenberg, Rev. Mod. Phys. **65** 851 (1993).

[4]. I. Procaccia and J. Ross, Science **198** 716 (1971).

[5]. J. P. Trelles, J. Phys. D: Appl. Phys. 49 393002 (2016).

[6]. M. J. Aschwanden et al., Space Sci. Rev., vol. 214, no. 2, p. 55, Mar. (2018).

[7]. A. J. Koch and H. Meinhardt, Rev. Mod. Phys.**66** 1481–507 (1994).

[8]. M. Rietkerk and J. van de Koppel, Trends Ecol. Evol. **23** 169–75 (2008).

[9]. V. Petrov, Q. Ouyang and H. L. Swinney Nature **388** 655–7 (1997).

[10]. R. B. Hoyle, Pattern Formation — an Introduction to Methods, Cambridge: Cambridge University Press, (2006).

[11]. T. Callegari, B. Bernecker and J. P. Boeuf, Plasma Sources Sci. Technol. **23** 054003 (2014).

[12]. E. Ammelt, Y. A. Astrov and H. G. Purwins, Phys. Rev. E **58** 7109–17 (1998).

[13]. C. Radehaus, H. Willebrand, R. Dohmen, F. J. Niedernostheide, G. Benge and H. G. Purwins, Phys. Rev. A **45** 2546–57 (1992).

[14]. C. Radehaus, T. Dirksmeyer, H. Willebrand and H. G. Purwins, Phys. Lett. A 125 92 (1987).

[15]. F. J. Niedernostheide, M. Ardes, M. Guil and H.G. Purwins, Phys. Rev. B 49 49 (1994).

[16]. J. W. Palko et al, J. Power Sources 397 252 (2018).

[17]. M. S. Bieniek, P. G. C. Almeida, and M. S. Benilov, Plasma Sources Sci. Technol., vol. 27, no. 5, Art. no. 05LT03. May (2018)

[18]. M. S. Bieniek, P. G. C. Almeida and M.S. Benilov, J. Phys. D: Appl. Phys. **49** 105201 (2016).

[19]. R. Sh. Islamov and E. N. Gulamov, IEEE Trans. Plasma Sci. **26** 7 (1998).

[20]. P. Rumbach, A. E. Lindsay and D. B. Go, Plasma Sources Sci. Technol. 28 105014 (2019).

[21]. N. Shirai, S. Ibuka, and S. Ishii, Appl. Phys. Express, Vol. 2, no. 3 pp. 036001, Mar. (2009).

[22]. T. Verreycken, P. Bruggeman and C. Leys, J. Applied Physics, Vol. 105, no.8, pp. 083312-083312-4 (2009).

[23]. N. Shirai, S. Uchida, F. Tochikubo and S. Ishii, IEEE Trans. Plasma Sci. Vol. 39, no. 11, pp. 2652-2653, Nov. (2011).

CHAPTER IV

Prior Investigation

The origin of SOPs particularly on the anode surface is not well understood. Early on, this thesis work investigated the occurrence of SOPs on both solid and liquid anodes surfaces. This chapter documents findings from this investigation.

4.1 Pattern Observation on Metal and Liquid Anodes

Self-organization patterns were observed in pin to plane discharge configuration with helium gas flow operated in ambient air. The discharge attachment patterns varied considerably On the liquid anodes, the pattern morphology appeared discrete dots, ring, or spokes. For example, Fig.1 (a) displays a photograph of an intricate surface self-organization pattern on the

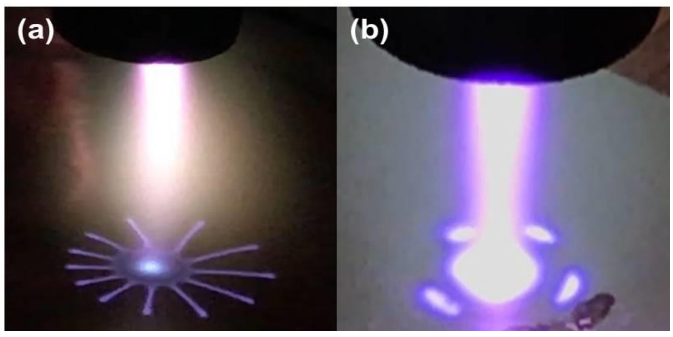

Figure 4.1: Photograph of typical self-organization patterns observed on (a) liquid anode and (b) metal anode in PSTL.

surface of liquid water. As can be seen in the figure, the pattern has the general appearance of spokes with lobes at the ends. The self-organization also appears on metal electrodes as shown in Fig 1(b). Luminous dot-like discharge with rotating motion about some local axis is the common type of pattern observed to form on the metal anodes [1]. The size and numbers of these patterns

vary with plasma discharge operating condition. Ring structures were observed from the metal anodes as well. However, spoke patterns were not observed to occur on solid metal electrodes.

4.2 Typical Controlling Factors

Self-organization of anode spots into distinct patterns that are either static or in motion has been observed for some time dating back to the 1930s [1]. Here we extend the study of the self-organization anode patterns to understand the control variables through by comparing pattern response on liquid and metal anodes.

4.2.1 Current

As reported [2-4], patterns are highly sensitive to discharge current. The pattern size, structures, and numbers (spokes, lobes, and dots) are usually increased with the increase in discharge current. These observations are consistent with measurements made in this work involving both liquid anode patterns (Fig. 4.2) and metal anode patterns (Fig. 4.3). The threshold for self-organization to appear is typically around 30 mA, also consistent with results in this work [5].

In the beginning of our work, two types of pattern structures were initially observed on the liquid anode surface. As can be seen in Fig. 4.2a, the size and number of the self-organized

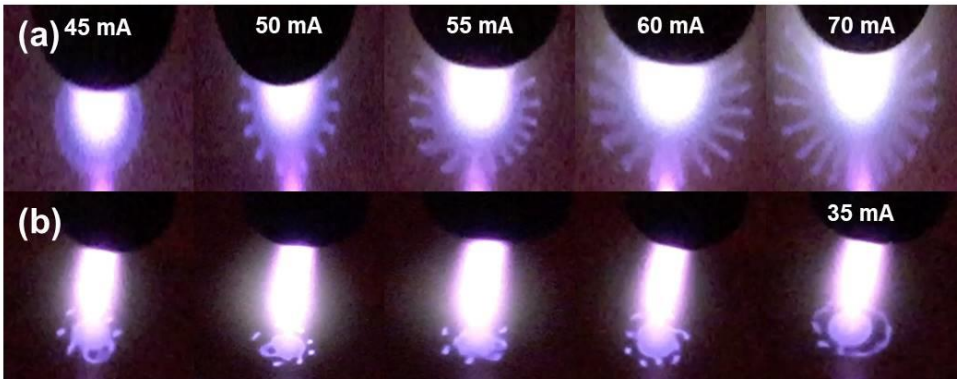

Figure 4.2 Self-organization pattern structures observed on the surface of NaCl solution are shown as (a) spokes and (b) rotating dots at fixed 35 mA with fixed gap length of 6 mm between the electrodes.

spokes increase with discharge current. Without current change, the dots were not changed but the rotation were maintained continuously (Fig. 4.2b).

On the metal surfaces, such as the copper anode as shown in Fig. 4.3, the plasma self-organization takes the form of a large primary central attachment around which individual dots

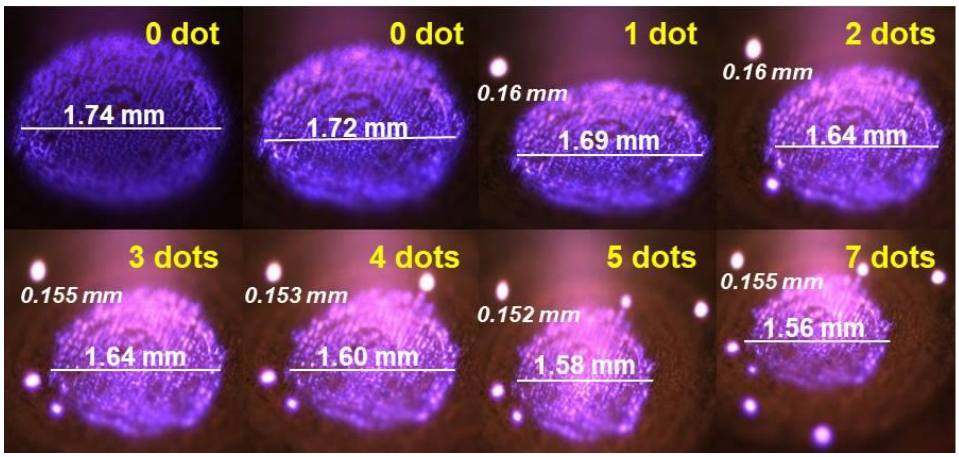

Figure 4.3: Self-organized dots evolution on the copper anode surfaces with fixed electrode gap distance at 7 mm.

discharges form. It was observed that the number of daughter dot-like attachments increase s with increasing discharge current while the size of central attachment decreases. If one considers the attachment surface area of the discharge to take the form of 2D footprints as inferred from the images, one can track how collection surface area changes with discharge current. It was found that as the current increased from 25 to 140 mA , estimate average current density increases markedly from 1×10^{4} Am^{-2} to 7×10^{4} Am^{-2} . Under these conditions, the total collection surface area did not change appreciably, decreasing only slightly from 2.38 mm^2 to 2.03 mm^2. Apparently, plasma production in the plasmoids structures increases with discharge current to support the requested current without the need for increased attachment surface area. It should be pointed out that anode cooling was applied to this particular study in order to avoid surface melting due to the relatively low melting temperature (1085 ℃) of copper compared to the

estimated gas temperature in the positive column of the discharge, which could be as high as up to 2000 ℃ [6].

4.2.2 Gap Length

Discharge morphology was also sensitive to the inter-electrode gap between the anode and cathode. It has been reported that patterns are more observable with larger electrode gap using liquid anodes [2]. A minimum of gap is required to form the self-organization but the exact gap distance depends on the solution properties such as the conductivity [4]. The reported minimum gap using liquid anode is in the range of 5 to 9 mm [1,3,4]. However, from this thesis study, with the same conductivity of the liquid, the self-organization was observed around 3 mm. The sensitivity of discharge shape to inter-electrode gap at a fixed discharge current of 45 mA with initial liquid conductivity was 12 $mScm^{-1}$ is illustrated in Fig. 4.4. It should be pointed out

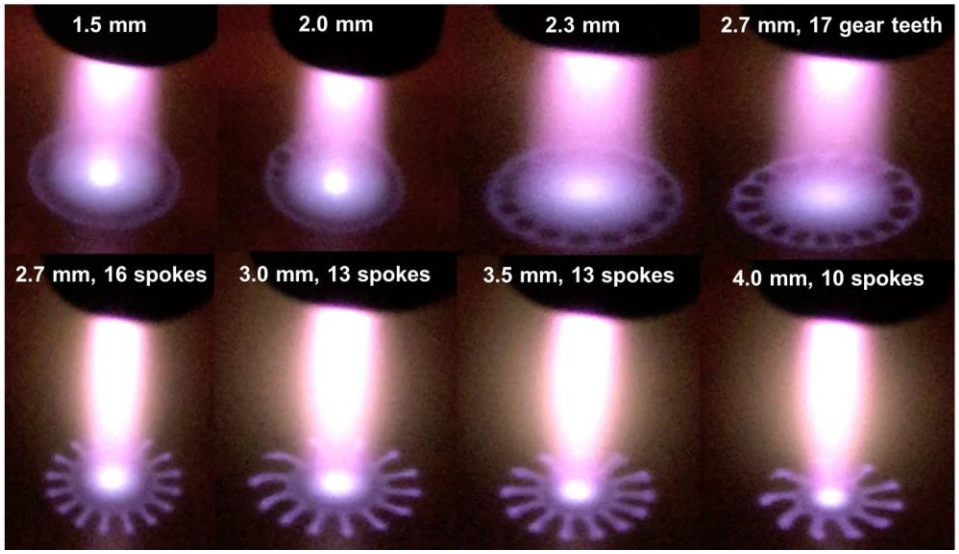

Figure 4.4: The evolution of self-organized anode pattern in spokes due to the gap control (1.5 to 4 mm) at constant current of 45 mA using NaCl solution.

that the corresponding voltages were increased markedly in order to sustain 45 mA current flow with increased gaps. As can be seen from the figure, the self-organized gear-like shape appeared when the gap length was around of 2 mm. Although the ring structures can be observed in a low

current such as 20 mA, it was not counted for self-organization patterns in the beginning of Shirai's study [5]. Here, the self-organized spokes were observed at gap length as low as 2.7 mm. It also can be seen that 2.7 mm is the distance for the pattern transited from the gears in the closed ring structure to open spokes. These patterns rotated on the liquid surface. The curved lobes observed from the spokes at 3 mm and 4 mm indicates such rotation.

In addition, the electrode gap sensitivity was assessed for metal anodes as well. Here, both copper and stainless steel plates anodes were investigated as a function of inter-electrode gap as illustrated in Fig. 4.5 (a) and (b) respectively. It was found that the minimum

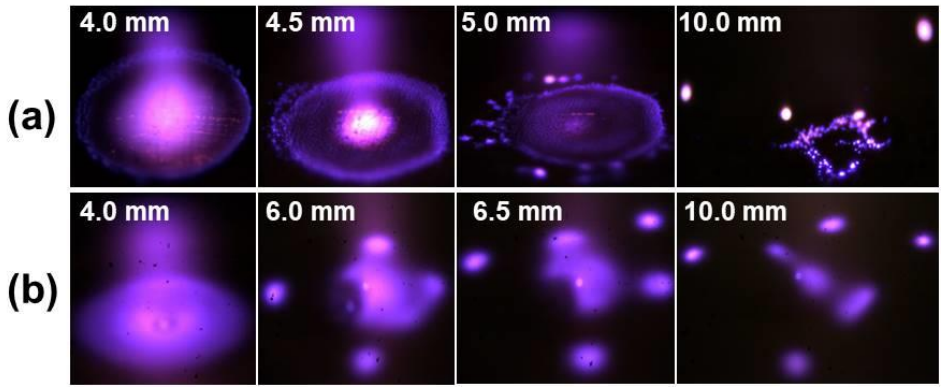

Figure 4.5: The gap control tested for the self-organization pattern on (a) copper anode with fixed current of 32.5 mA and (b) SS 304 anode surfaces with current of 55 mA .

gap required for the self-organization to form on the copper surface at 32.5 mA was 5 mm, and 6 mm for the stainless steel anode with discharge current of 55 mA. Such minimum gaps are still smaller than the minimum gap of 9 mm for self-organized dots that reported using metal anodes [6]. It is not known why the threshold current is much higher for steel. It is worth pointing out that copper has a considerably higher thermal and electrical conductivity than steel. It is known that anode vapor can enhance the local conductivity of the anode plasma and lead to constriction. Spots are some form of constricted plasma. Owing to its lower melting point (~1000 C), perhaps copper presents spots earlier because of this constriction process in contrast to steel (~1500 C

MP) which requires higher temperatures to locally vaporize. Detailed spectroscopic measurements on very small length scales are required to investigate this potential mechanism. Such an investigation is left to future work [7].

4.2.3 Conductivity

Self-organization has been shown to be very sensitive to electrical liquid conductivity in 1 atm DC glow with liquid anode. These studies show that by increasing the electric conductivity, the diameter of anode spots reduce with the disappearance of the individual spots [1], and the pattern structures tend to be more uniform [2, 4, 8]. In this thesis work, the effect of varying solution conductivity on pattern shape was investigated using NaCl solutions. Here, it was found that patterns did not change appreciably for conductivities ranging from 0.5 mS/cm to 48 mS/cm. Lower conductivity in the μS/cm range appear to be more favorable for pattern formation [2, 4], higher conductivities (> 60 mS/cm) tends to short the patterns out into spots [8]. In this work, patterns were investigated in this lower conductivity range. In order to further elucidate the conductivity effect, an experimental study was embarked aimed at understanding the effect of conductivity on pattern shape for a range of different electrolytes. Results from this study are presented in Chapter 6.

It should be pointed out that patterns were also observed with deionized water. The water used had a starting conductivity of 8 μm/cm. As can be seen in Fig. 4.6 there is no pattern, but after 10 minutes of operation, a pattern clearly emerges. What is known in these experiments is that the solution conductivity changes as a function of time owing to plasma induced species solvating in solution and electrolytic processes taking place at the immersed electrode. This observation of pattern evolution with time has also been observed but not reported with DI water

[3]. Here, the ending conductivity for this experiment after the termination of the experiment was non uniform for the bulk water, in range of few hundreds of µS/cm to mS/cm.

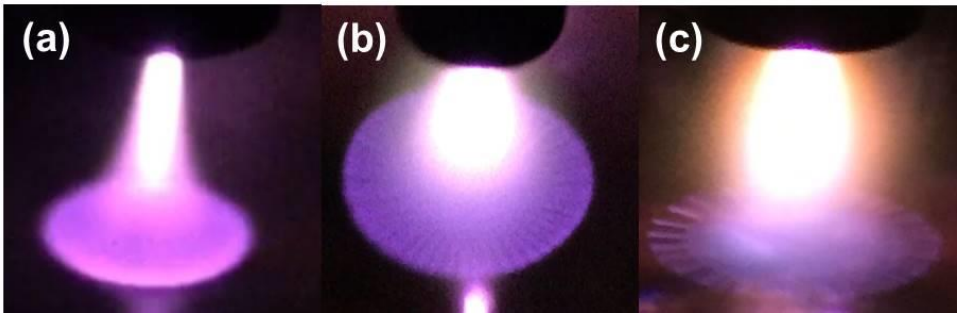

Figure 4.6: Plasma attachments on the liquid anode using DI water at (a) t = 0 minute, (b) t = 10 minutes , and (c) t = 20 minutes.

4.2.4 Gas Effects

The effect of helium flow rate and the introduction of gas mixtures (N_2 or O_2) have been shown to influence pattern complexity, though the mechanism is still not well understood [2, 3]. For example, when the helium flow increases to 400 SCCM from 200 SCCM, the pattern structure degrades. These studies also show that a shielding gas of nitrogen completely eliminates the pattern while in an all helium environment the pattern reappears with the introduction of oxygen. Such studies suggest the possible role of negative ions in pattern formation [5].

Similar sensitivity studies were also carried out in this work but using different feeding gas such as argon and nitrogen instead of helium. By flowing either Ar or N_2 at 200 SCCM to the NaCl solution in the ambient air, no pattern was observed, neither Ar nor N_2. When the flow rate was reduced from 200 SCCM to 50 SCCM for Ar and from 200 SCCM to 30 SCCM for N_2, patterns were observable for both cases. Two types of pattern were observed as shown in Fig. 4.7. In the figure, the current reduction occurred in the Ar plasma discharges along with time due to a vaporization of the liquid.

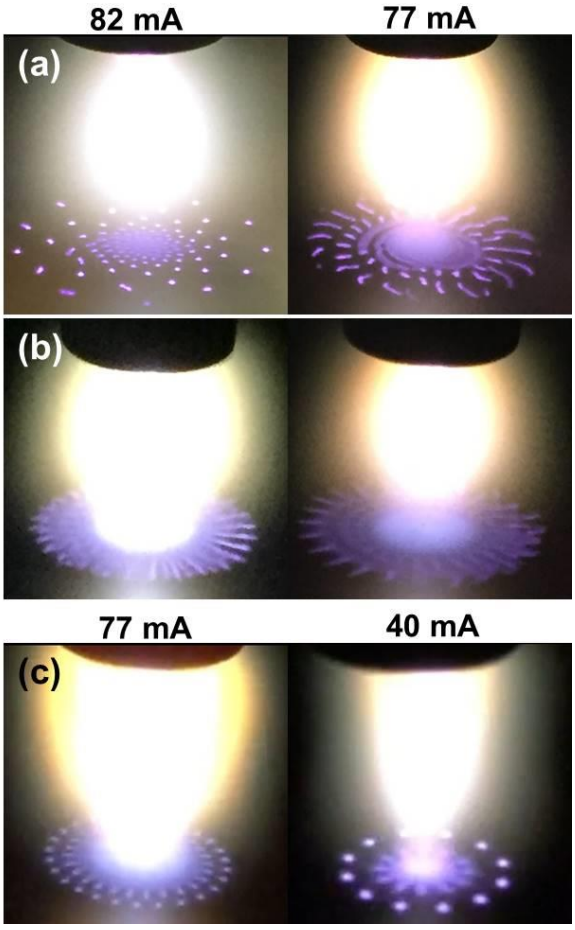

Figure 4.7: Pattern observed using different gases on the NaCl solution with conductivity of 12 $mScm^{-1}$ at gap length of 8 mm. (a) 50 SCCM of Ar, (b) 30 SCCM of Ar, and (c) 30 SCCM of N_2.

Note in Fig. 4.7 (a), when the pattern initially observed at 50 SCCM of Ar flow, appeared as discrete dots. After about 10 minute's plasma exposure, it varied to discrete short lobes. Such pattern transition is also observed at a Ar flow rate of 30 SCCM. The orange clouds around of Ar plasma column at 77 mA are likely evidenced the vaporization, which caused a change of the anode conditions. It also can be acting as electronegative gases that capture the free electrons and form negative ions in the discharge, thus leads to the pattern variation at the liquid surface. The vaporization process was taking place in the N_2 plasma discharge as well but did not cause any significant variation on the pattern morphology. Unlike the stable helium plasma glow operated on NaCl solution, neither Ar nor N_2 plasma were stable in spite of continuous glow between the

electrodes. Such unstable behavior is demonstrated from the observation when the plasma column tends to arc intermittently and the sound of boiling oil generated at the center of the local interface where the plasma touched liquid. In addition, it was tested that the discharge couldn't break down using DI water as liquid anode by feeding either Ar or N_2 gas sources.

In summary, less or more complex pattern structures were observed using either argon or nitrogen instead helium gas source. The threshold flow rate for pattern to be observable was tested to be 50 SCCM for argon plasma and 30 SCCM for nitrogen plasma. It suggests that pattern formation is not dependent on the type of the feeding gas, but the gas types affects the pattern morphologies.

4.2.4.1 Secondary Gas Injection to the Metal Anode

In order to assess the role of different gas species on discharge self-organization on metal anodes, a secondary gas injection system was designed and fabricated. In these experiments, the plasma was generated by feeding 200 SCCM of helium gas through cathode. The gas injection setup with inset containing an image of the plasma discharge is shown in Figure 4.8 a. In this test, the local gases such as Ar and N_2 with flow rate of 5 standard cubic feet per hour (or 2360 SCCM) were directed at the tungsten anode plate. The distance from each injection point to the center of the plasma discharge was approximately 1.8 cm. The pattern variations due to the introduction of these secondary gases are shown in Fig. 4.8 b. As can be seen from the figure, adding the Ar gas to the non-self-organized plasma attachment favors the pattern formation in dots. It may be that the presence of argon is locally increasing the ionization rate and subsequent constriction which is necessary for the formation of the sharp, highly localized discharges. The absence of this effect with nitrogen may be due to myriad of inelastic loss pathways accompanying this molecule such as vibrational structure and disassociation.

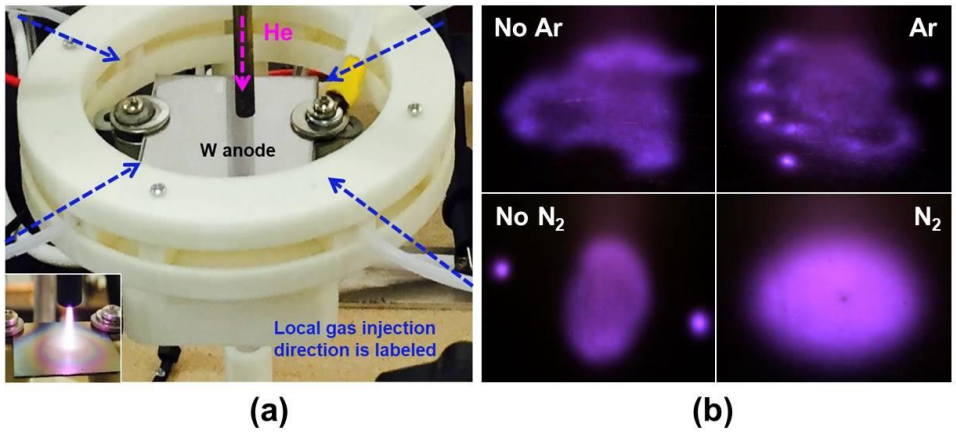

Figure 4.8: A 3D printed secondary gas injection system with a plasma discharge photograph at lower left corner is shown in (a) and the comparison between the plasma attachment with and without local gas injection is shown in (b). The discharge was operated at fixed electrode separation of 8 mm. In the case of Ar gas injection: current increased from 38.25 mA to 43.67 mA at constant 1.5 kV. For N_2 injection: current increased from 59.46 mA to 60.31 mA at constant 1.9 kV.

It is interesting to note that by stopping the local gas injection (either Ar or N_2) (without changing any other condition), the plasma attachment reverted to its initial attachment morphology: No self-organization without Ar and a two dot discharge appeared at the same location without N_2. It should be noted that the plasma attachment surface area and discharge current both increased with the introduction of the secondary flow, suggesting that the current density of the attachments tends to stay constant.

Interestingly, self-organized patterns in the form of discrete dots were observed on the metal anodes without any feeding gas such as the stainless steel example is shown in Fig. 4.9. Here, the number of dots generated increased linearly with discharge current. However, the discharge was not very stable to constriction and subsequent arcing.

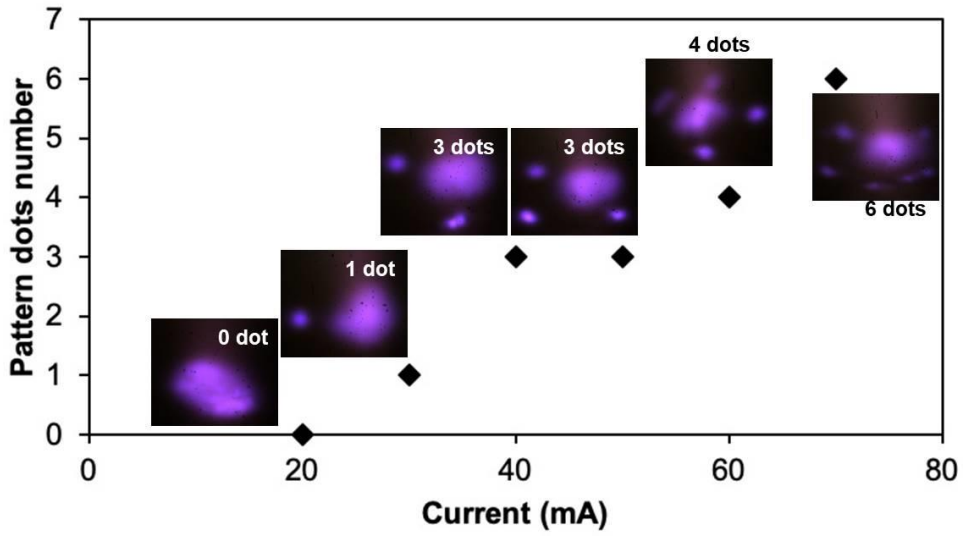

Figure 4.9: Self-organized dots observed on the stainless steel anode without helium gas flow in the ambient air.

Like the dot-like patterns that formed under the helium plasma discharge, these self-organized dots also rotated around a central attachment (the main plasma attachment). This observation suggests that at least on metal electrodes, pattern formation is not an effect peculiar to a specific gas type. Rather the primary role of the helium gas is likely discharge stability against the ionization instability and a source of stored energy in the form of metastable. Since pattern formed without gas flowing through the cathode, it also suggests that self-organization maybe independent of cathode flow.

4.3 Electrodes Condition

Electrode surface conditions and composition can also affect discharge properties. For example, work function, thermal conductivity, surface roughness, porosity, and surface resistivity all can affect formation processes of the anode spot. Here, the sensitivity of electrode surface properties and overall temperature was investigated.

4.3.1 The Effect of Anode Surface

Here, through the use of coatings, the surface of a stainless steel, silicon or tungsten anode plate was modified. Discharge morphology at similar operating conditions is shown in Fig. 4.10.

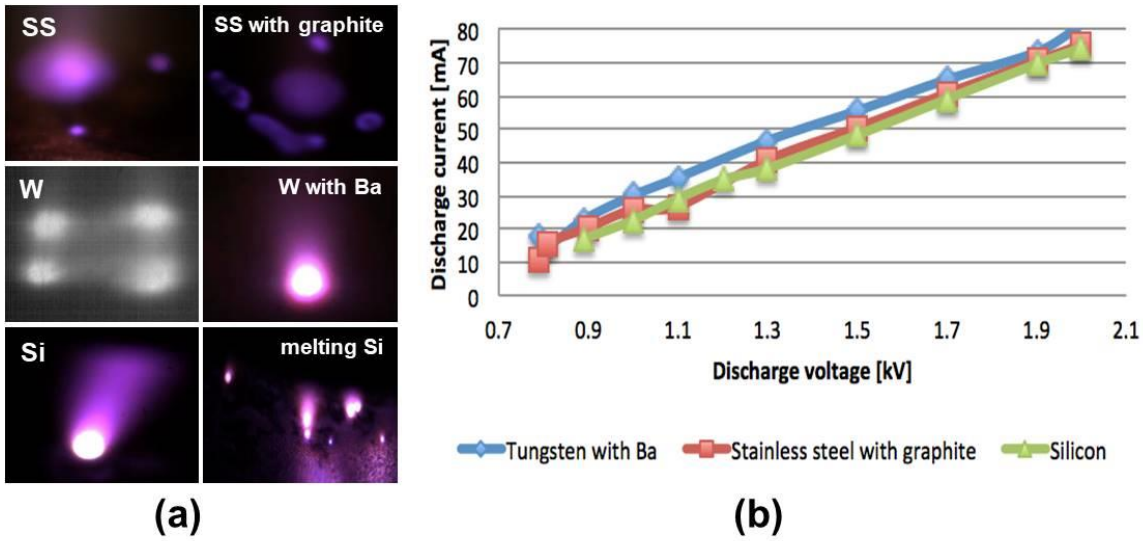

Figure 4.10: Anode material tested at 10 mm with (a) the surface coating and (b) discharge current with total voltage.

These tests were operated in constant voltage mode. It was observed that larger, more complex patterns resulted with graphite coating on stainless steel. Graphite has a considerably higher thermal conductivity than steel and it is more chemically resistant. Barium coatings reduce overall work function of the material and thus reduce the energy released into the material when electrons enter the metal. The barium coating on the tungsten surface tended to quench the pattern and overall stabilize the main plasma. It was found that silicon dioxide substrates could support the discharge. Here, multiple attachments appeared as dots on the silicon wafer surface. The localized attachments tended to melt the surface. The recorded current voltage characteristics of each surface type and coating arrangement is given in Fig. 4.10 (b). There is

no appreciable difference here in that in all cases, the current increased linearly with applied voltage.

This survey of surface effects suggests that indeed patterns are sensitive to material type and surface conditions. For example tungsten and stainless steel manifested markedly different pattern topologies. But when graphite was added to steel, the pattern was more varied akin to tungsten in some respects. Now tungsten's electrical conductivity is an order of magnitude higher than stainless. And graphite is lower than stainless, so the additional of graphite does not increase electrical conductivity. Rather graphite coating increases the thermal conductivity at the surface of the steel. This limited data set suggests that it is surface thermal conductivity that might be a key determiner of pattern morphology. The transport of thermal energy away from the attachment reduces localized evaporation, which is known in arc discharges to give rise to constriction and discharge intensification. This would tend to favor single attachments. For surfaces with higher thermal conductivity, it is plausible that these would require more attachments –more "dots" to support the requested discharge current as vaporization enhancements are reduced. A more detailed surface sensitivity survey is left for future work.

4.3.2 Cooling Effects on Metal Anode

Cooling the anode had a profound effect on discharge morphology. Here, the anodes were attached to a water cooled plate as discussed in Chapter 3. The general experimental setup is shown in Fig. 4.11 (a), which was operated in constant voltage mode. The chiller temperature was set to be 20 ℃. A comparison between the pattern with and without anode cooling system can be seen from the examples given in Fig 4.11 (b) and (c) corresponding to the tungsten and stainless steel respectively. For both anode metal surfaces, the patterns are more observable with higher intensity but smaller sizes. It requires less total voltage to sustain the same current when

the cooling is on while other conditions were being fixed. Here, for the operation condition provided in the figure, the total voltages applied to the system are 2 kV without cooling and 1.7 kV with cooling on tungsten anode. For stainless steel anode, total 2.1 kV applied without

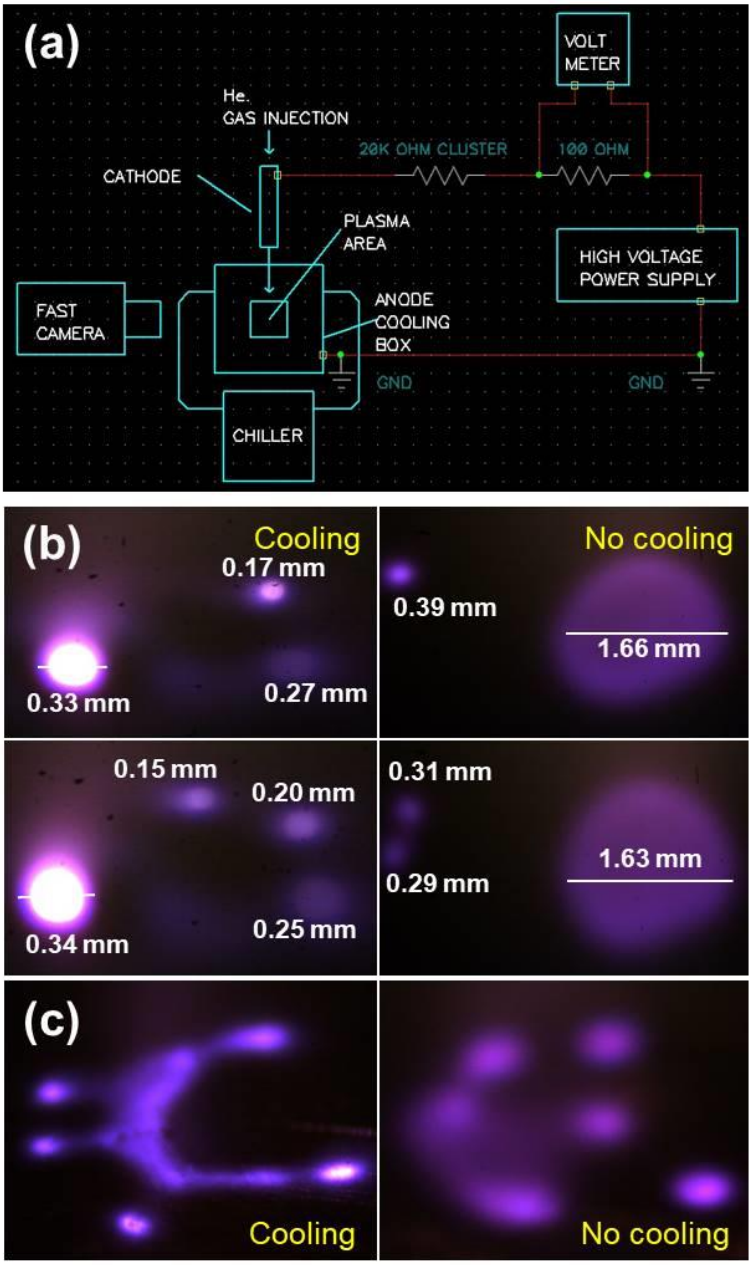

Figure 4.11: Anode metal cooling effects on self-organized plasma patterns is studied. (a) Experimental schematic that is not to the real scales. The pattern variation due to the cooling is observed on (b) tungsten anode at 53 mA with10 mm electrode gap, and (c) stainless steel anode at 58 mA with 8 mm electrode gap.

cooling and 1.6 kV when the cooling was used. In the case of the tungsten anode, with anode cooling, current density increased and less total power densities are required for the dots to form. This finding suggests cooling on anode metal surfaces stabilizes the dots pattern and favors the pattern formation. With the cooling system, less discharge voltage and smaller gap length are required to support pattern formation. Interestingly, these findings are consistent with the thermal conductivity insight gained from the coating studies. Here again localized heating is minimized, this time not via a graphite coating but with a cooled substrate. This would tend to increase the rate at which power deposited into the substrate is removed by a factor proportional to the difference between the local surface temperature and the bulk cooling plate at 20 C. Such removal means average surface attachment temperature can be expected to be lower along with reduced vaporization. These conditions favor more complex patterns or more "dots" to support the discharge current.

4.3.3 Cathode Orifice

The discharge sensitivity to cathode orifice diameter was also explored. It was thought that this parameter might affect discharge order at the anode surface. Indeed, an examination of the anode after plasma exposure revealed interesting heat patterns. The structures suggested that the main attachment is actually hollow. This can be seen from sub figures (a) to (f) in the Fig. 4.12 with silicon being the exception. In the case of silicon, the surface actually melted as can be seen in Fig 4.12 (e).

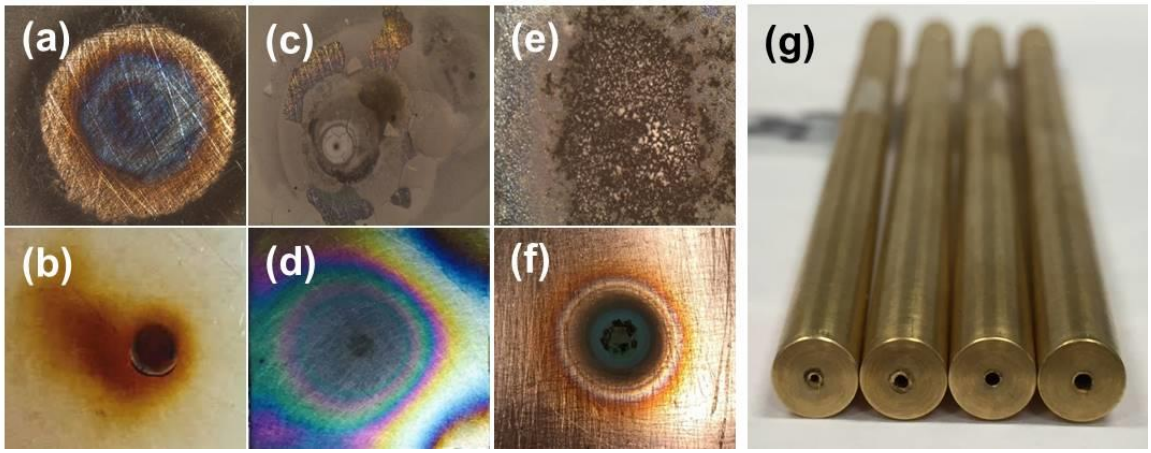

Figure 4.12: Hollow shaped heat patterns observed after the plasma exposure on (a) stainless steel with graphite coated surface, (b) stainless steel, (c)barium coated tungsten surface, (d)tungsten , and (f) copper surface. The melted silicon wafer surface is shown in (e). (g) is the photograph that shows the bottom view of the machined cathodes with diameters of 0.5 mm, 0.9 mm, 0.75 mm, and 1 mm (left to right). The cathodes demonstrated here were machined by the Dellamar Manufacturing Company in Belleville Michigan.

Recall from Sec. 4.2.4.1, the discharge "dots" were observed without any feeding gas suggesting that self-organization formation maybe independent of the cathode gas flow. This motivated the study to determine if in fact cathode geometry plays a role if any on discharge morphology and IV characteristics. Here three different cathode orifice diameters were investigated: 0.5 mm, 0.75 mm, and 1mm. The machined cathodes can be seen in the Fig 4.12 (g). The tests are done in constant current mode (current control) with NaCl anode solution (12 $mScm^{-1}$) with IV

characteristics shown in Fig. 4.13 (a). It is found that the 1 mm diameter

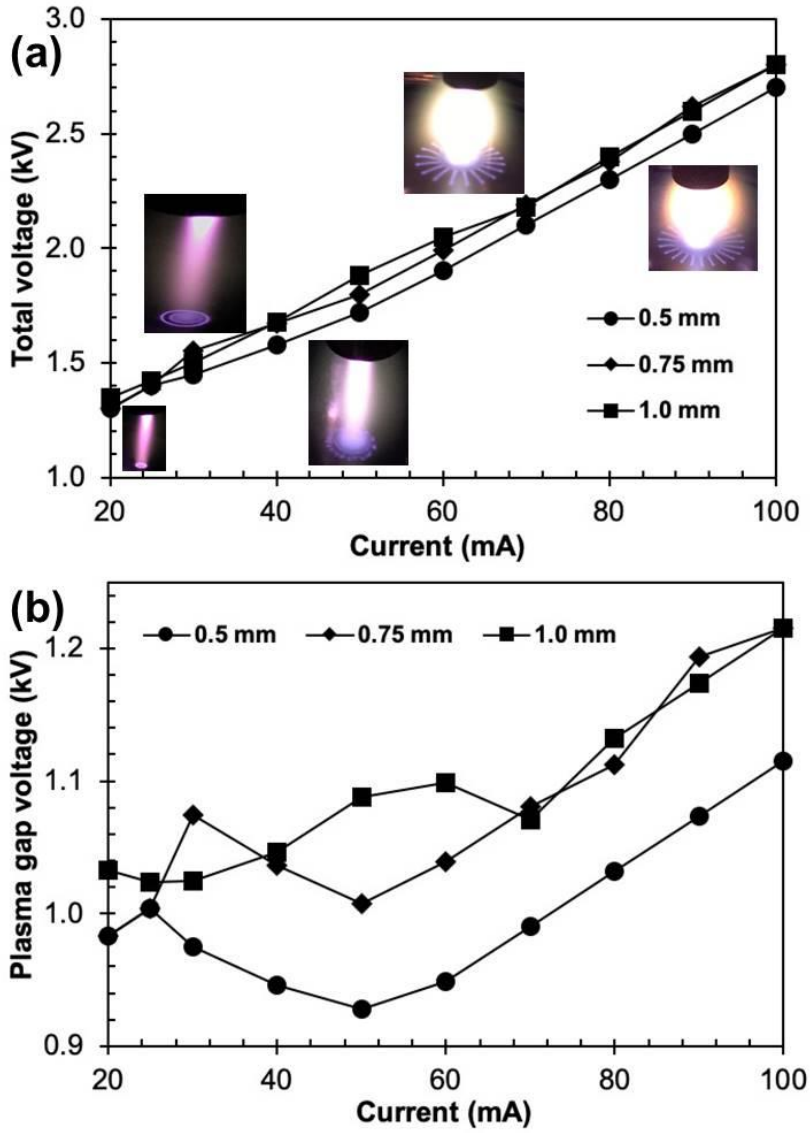

Figure 4.13: The voltage current characteristics with pattern formed at different current regions when three different cathode diameters were applied to generate the glow discharge. A helium gas (200 SCCM) was flowed to the NaCl anode solution with the electrode spacing of 8 mm to generate the 1 atm DC glow.

cathode requires a higher input voltage to sustain the same current level compare to other two cathodes. This behavior is especially noticeable in the current region from 40 to 60 mA, where the self-organization pattern are depicted as the rotating dots or short lobes after the ring structure formation and before the stable spokes appear. This observation matches with the results in chapter 6 with this region being defined as the pattern transition region. It was found

that the response of the pattern formation at some current regions is delayed approximately 10 mA corresponding to the cathode inner hole diameters. For example, in the case of cathode one (0.5 mm), at 25 mA, the ring structures is observable with transition to patterns at 50 mA, and stable spokes observed at 60 mA. When cathode two (0.75 mm) was tested, the ring structure appeared at 30 mA with the rotating dots as the transition pattern at 50 mA, but the spokes stabilized at 70 mA. The last cathode (1 mm) resulted ring structure at 40 mA with the short lobe transition pattern at 60 mA and stable spokes observation at 70 mA. Besides such delays of the pattern transition in response to the current region, the overall pattern morphology in this study wasn't affected by changing the cathode inner-hole diameters.

However, the plasma discharges tended to be more unstable with increasing cathode orifice size. This can be observed from the voltage current characteristics of the plasma in the gap that is plotted in Fig 4.13 (b). The V-I curve recorded using cathode one (0.5 mm) shows a typical IV feature of normal glow. Such normal glow can also be seen through the V-I data provided by cathode two (0.75 mm) but it is difficult to identify from the last cathode (1 mm). Here, the Reynolds numbers for the flow are estimated to be 1234 using cathode one (0.5 mm), 1851 using the second cathode (0.75 mm), and 2468 for the last one. Since the Reynolds number is near 2500 in the case of 1 mm cathode, the plasma likely present in the transition from laminar to turbulent flow for this case. Therefore, this unstable behavior in the plasma discharge could be due to the instability that induced by the plasma turbulence. Another note is the turning points that can be found from each case in the figure. 50 mA is found for first two cathodes and approximately 70 mA for the last cathode with a largest inner-hole diameter. These turning points actually reflect the current region for the pattern transition. Such unique phenomena is also observed and studied in chapter 6 with multiple electrolytes investigations. Despite the

plasma discharge instability and current response to the pattern transition are affected by varying the inner-hole diameter of the cathodes, this study confirms that the self-organization formation itself is independent of the cathode configuration.

4.5 Conclusion

In this chapter, self-organization pattern related basic controlling parameters for both liquid and anode surfaces are studied and documented using 1 atm DC glow. This survey extends insight into pattern formation beyond that which is currently in the open literature. For example, discharge sensitivity to electrode type or coatings, secondary gas injection, anode cooling and cathode geometry has all been explored here.

In summary, two types of typical major self-organization patterns (dots and spokes) have been observed on liquid anodes and metal anodes. We update here that the minimum electrode gap space for the pattern formation is found to be 3 mm for liquid anodes and 5 mm for the metal anodes. With the gap control, pattern numbers can be affected. Increasing the gap will reduce the pattern number on liquid but increase the number of dots on the metal surfaces.

Both argon and nitrogen gases can also be used as gases for pattern formation. For liquid anodes, self-organizations were observed from argon plasma and nitrogen plasma with their gas flow rate of 50 SCCM and 30 SCCM respectively. On the metal anodes, argon favors the pattern formation while nitrogen diminishes the pattern dots. The Characteristic of the plasma pattern structures can be affected by the types of gas source. However, to generate plasma self-organization, the gas type is not indispensable. In fact, it didn't required any feeding gas to form a self-organization dots on the metal surfaces after a successful break down achieved in the ambient air.

Pattern formation appears to depend on thermal conditions at the anode for solid anodes. Particular to the metal surfaces, the desired thermal condition can be achieved by material coating and cooling. Unlike the gas injection that provides the constant current density, current increase and anode cooling enhances the current density of the plasma attachments as well as the total power density. The current region for the pattern transition is affected by the cathode sizes but the actual pattern formation is independent of the cathode configuration.

4.6 References

[1]. A. Wilson, D. Staack, T. Farouk, A. Gutsol, A. Fridman and B. Farouk*Plasma Sources Sci. Technol.*, Vol. 17, no. 4, pp. 045001, 2008.

[2]. T. Verreycken, P. Bruggeman and C. Leys, J. Applied Physics, 105, 083312 (2009).

[3]. N. Shirai, S. Uchida and F. Tochikubo, Plasma Sources Sci. Technol.23, 054010 (2014).

[4]. N. Shirai, S. Uchida, F. Tochikubo and S. Ishii 2011 IEEE Trans. Plasma Science 39 2652 (2011).

[5]. N. Shirai, S. Ibuka, and S. Ishii, *Appl. Phys. Express*, Vol. 2, no. 3 pp. 036001, Mar. (2009).

[6]. P. Bruggeman, J. Liu, J. Degroote, M.G. Kong, J. Vierendeels, and C. Leys, J. Phys. D: Appl. Phys. 41 215201 (2008).

[7]. G. Y. Zhao, M. Dassanayake, and K. Etemadi, *Plasma Chem Plasma Process* 10, 87–98 (1990).

[8]. S. Zhang and T. Dufour , Phys. Plasmas 25 073502 (2018).

CHAPTER V

Spatial Resolved Plasma Column Characteristics on Liquid Anode [8]

In this chapter, optical emission spectroscopy is used to study a 1 atm DC helium glow discharge with a liquid anode to obtain insight into the physical mechanisms underlying observed plasma self-organization at the liquid surface. Plasma column conditions such as gas temperature, electron density and species composition were determined by means of optical emissions spectroscopy techniques and correlated with the appearance and structure of anode patterns over a broad burning voltage range with fixed flow rate and liquid conductivity. The discharge column was stratified from a species standpoint with the attachment near the liquid surface containing more sodium and water emission, while near the cathode the predominant emission was from nitrogen and helium. The experiment suggested complex interplay between the transport of liquid phase species and the actual composition of the plasma, suggesting the importance of processes such as localized boiling and perhaps physical sputtering.

5.1 Introduction

In chapter 2, a survey of anode pattern formation in atmospheric pressure glow studies, competing processes such as diffusion and space charge in the presence of a resistive conducting electrode play important roles in discharge surface attachment behavior. A requirement of any self-organization process is that the system is driven far from thermal equilibrium and that in the

[8] The text and discussion in this chapter has been previously published by Y.E. Kovach, M. C. Garcia, and J.E. Foster, "Optical emission spectroscopy investigation of a 1 atm DC glow discharge with liquid anode and associated self-organization patterns" IEEE Trans. Plasma Sci. 47 3214 2019.

presence of random fluctuations in the presence of feedback, the organization process is amplified [1]. Such local negative entropy changes which give rise to organization are possible in open systems where there is nonlinear dissipation. The dissipated energy exits the system globally so that globally entropy does increase but reactants are constantly being replenished-in this case from the plasma. In general, such self-organization arising from reaction diffusion systems are derived in some manner from a balance between a local activator (for example current) and the inhibitor (diffusion and or voltage) [2, 3]. Key to understanding the self-organization process is the identification and subsequent quantification of these parameters. What adds to the complexity of the DC atmospheric glow with liquid anode is that during operation, the solution itself chemically changes leading to temporal and spatial variations in conductivity, pH and concentration. These in turn can lead spatially varying reaction diffusion systems, which in turn can seed plasma pattern formation as well.

From experimental data, it is clear that the spot formation is a local process with a strong dependence on gas composition and surface conductivity. In this work, we investigate the general structure of the atmospheric pressure glow spectroscopically. Here variation in species and discharge temperature along the plasma column is ascertained along with plasma density. The localized attachment at the liquid surface is the source of input water vapor. Such localized boiling is also a source of droplets which also contain ions in the electrolytic solution. The presence of this gas source influences ionization rates and energy transfer in the plasma column and is also a source of feedback; that is, the higher the current, the higher and the evaporation rate. This interchange may play a role in the formation of the self-organization patterns on the surface. In this work, we investigate the influence of water vapor and in-solution ions on discharge characteristics as a function of operating condition using optical emission spectroscopy

techniques as well and correlate these changes with observed changes in the self-organization pattern at the liquid surface.

5.2 Experiment

Fig. 5.1 shows a schematic of the discharge apparatus, which is of the point to plane geometry. This arrangement is in contrast with the Verreycken study [4] in that in this case, the discharge develops along a jet of flowing helium.

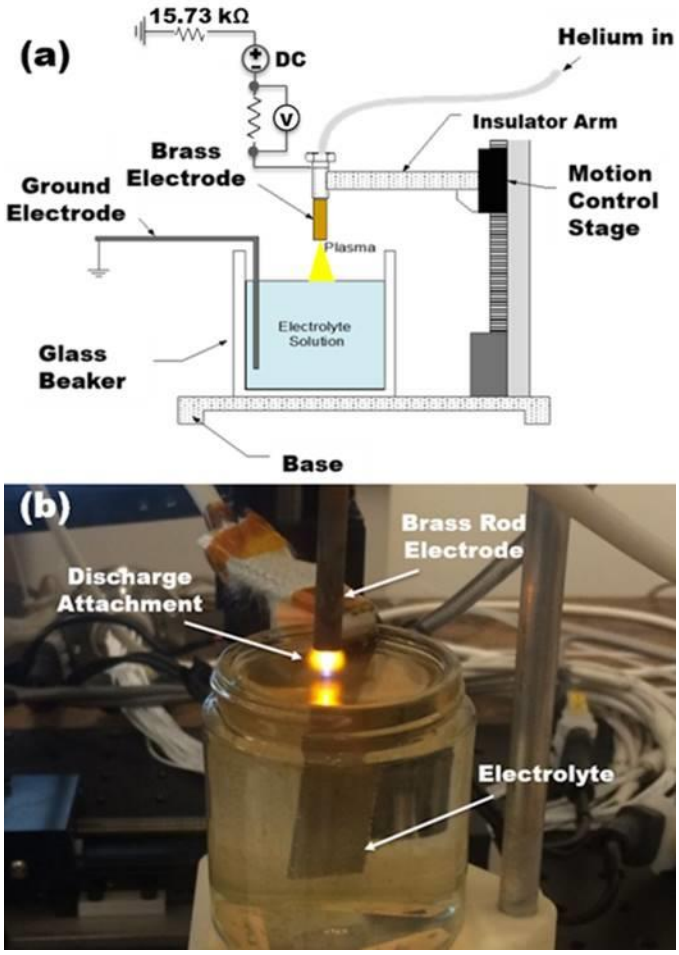

Figure 5.1: Experimental setup is shown in (a) sketch of the discharge configuration (not to scale) with a photo of (b) operation in 1 atm DC glow.

The liquid anode consisted of a NaCl solution with an initial concentration of 9 g/L and an initial electric conductivity of 12 $mS \cdot cm^{-1}$ at room temperature in contact with a grounded return electrode [5]. The inter-electrode spacing could be varied between 1 mm and 8 mm.

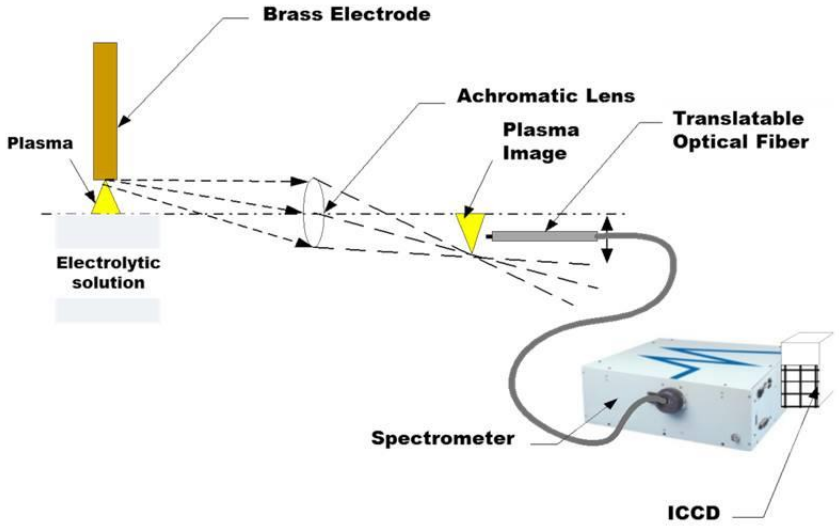

Figure 5.2: Schematic depiction of imaging approach for OES diagnostic.

Optical Emission Spectroscopy (OES) techniques were employed to diagnose plasma generated over the liquid. Fig. 5.2 schematically depicts the experimental setup used to acquire the OES measurements. Light emission from the plasma was analyzed by using a Czerny-Turner type spectrometer (Acton Series, SP-2300i) of 0.3 m focal length equipped with a 1800 grooves/mm holographic grating and a fast intensified CCD camera (PI-MAX3, Princeton Instruments) was used as a detector. The spectra were recorded with aspectral resolution (measured through the instrumental broadening) of 0.13 nm.

Line integrated emission spectra acquiried at different axial positions along the axis of the plasma column relative to the position of the cathode exit plane (z = 0, 3, 5 and 8 mm) were collected and focussed at 1:1 magnification onto an optical fiber using an achromatic lens. Position z = 8 mm corresponded to the discharge position at the liquid anode surface. For each

experimental condition, the spectrum was recorded three times. In order to deal with water evaporation and keep the distance constant, the beaker was refilled with water till a mark and refilled after every single measurement.

The spatially resolved emission spectra were used to determine the spatial variations in species, gas temperature, excitation temperature, and electron density along the discharge axis.

5.2.1 Patterns and VI Character

The discharge attachment at the surface of the anode varied with applied voltage. In this work, the discharge gap was fixed at 8 mm from end face of powered electrode to the surface of the water. Fig. 5.3 illustrates the variations in the discharge current with voltage applied across

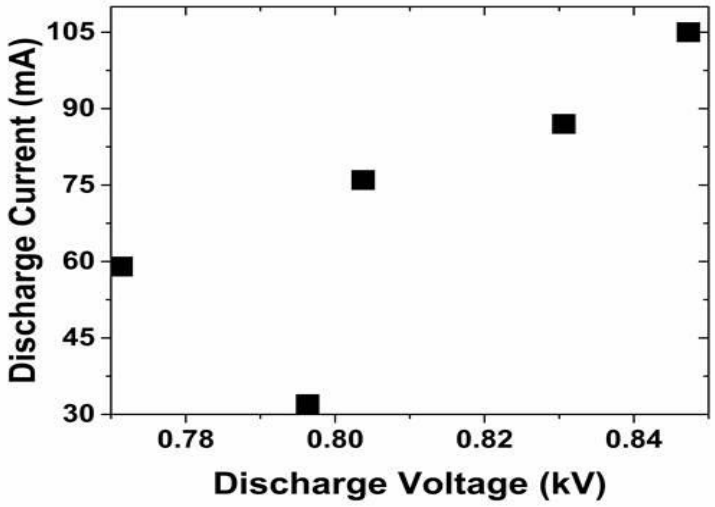

Figure 5.3: Discharge current variation with discharge voltage.

the gap. Discharge voltage and associated discharge current are summarized in Table 5.1, which includes the total voltage applied as well as the gap voltage, the total voltage minus the series resistance voltage drop.

Table 5.1. Voltage and current values in the plasma.

Total Voltage V(kV)	*Gap Discharge Voltage* (kV)	*I* (mA)
1.3	0.796	32
1.7	0.771	59
2.0	0.804	76
2.2	0.831	87
2.5	0.848	105

As can be seen in the figure, generally the discharge current increases with increasing applied voltage. Above an applied voltage of 1.3 kV, the discharge impedance drops. With increasing applied voltage, gap impedance decreases by nearly a factor of two. The appearance of a spoke-like attachment accompanies the initial drop in impedance, suggesting that the pattern is essentially a preferred, lower resistance pathway towards discharge maintenance, in contrast to the double ring attachment. Interestingly, over the range of total applied voltages, the gap voltage is relatively constant ~0.8 kV, which is behaviour typical of a normal glow. In a normal glow, the discharge is sustained by secondary electron emission. The case of the 1 atm glow with liquid anode, vaporization of water and metal ions derived from droplets associated with localized boiling at the attachment may be the secondary processes that play a role in sustaining the anode spots. Under these experimental conditions with the exception of the lowest burning voltage, self-organization patterns were observed on the surface of the water. Fig. 5.4 (a)-(e) show the spatial optical emission patterns observed for the different voltage (current) conditions listed in Table 5.1.

For total applied voltage of V = 1.3 kV (Fig. 5. 4(a)), a ring-like pattern was observed. Three apparent changes were observed to occur with increasing voltage. The attachment at the anode attachment structure differentiated into a well defined wagon wheel like pattern with increasing voltage with the spoke length and number increasing with increasing voltage. This

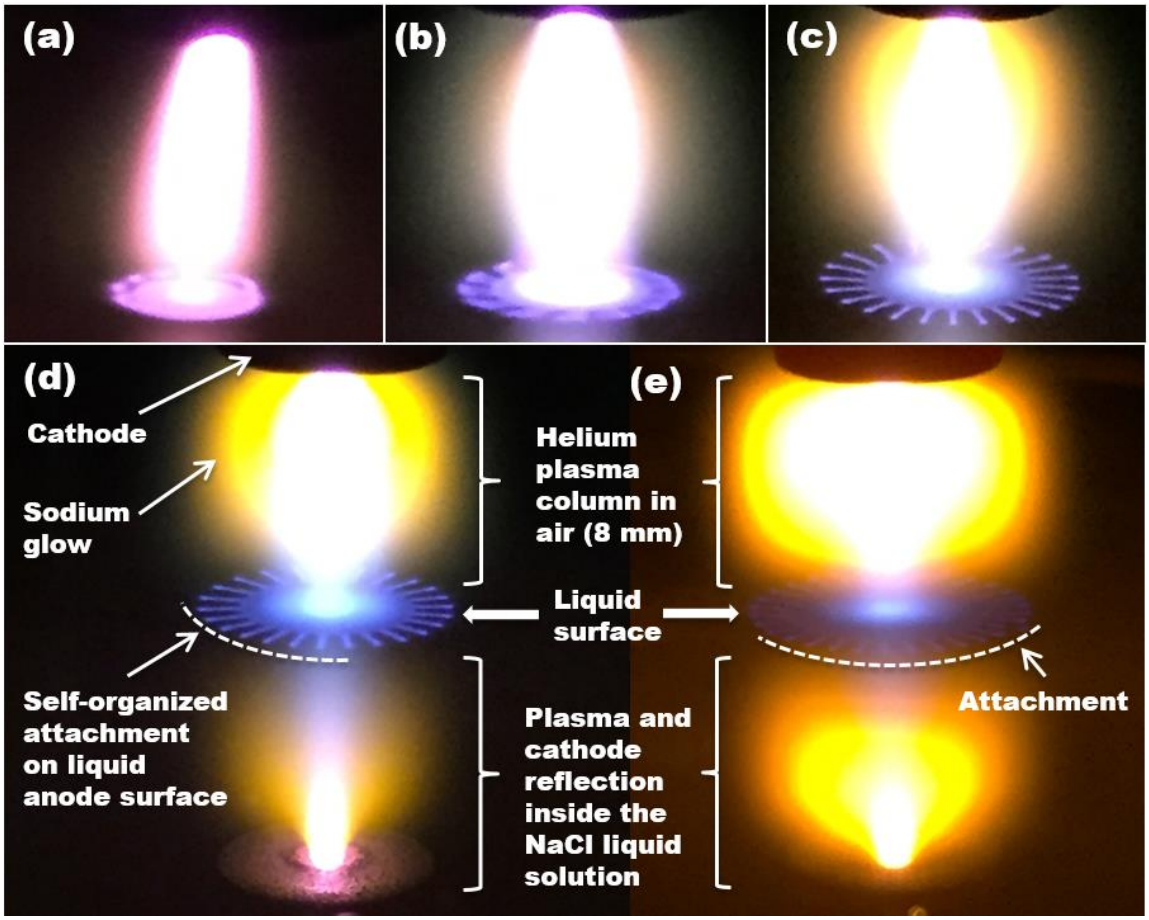

Figure 5.4: Variation in discharge column and attachment shape with increasing the total voltage: (a) V = 1.3 kV; (b) V = 1.7 kV; (c) V = 2.0 kV; (d) V = 2.2 kV and, (e) V = 2.5 kV.

observation is similar to Shirai et al [6] where the wagon wheel and gear like structures were observed at the higher currents corresponding to elevated voltages. Fig. 5.5 illustrates the

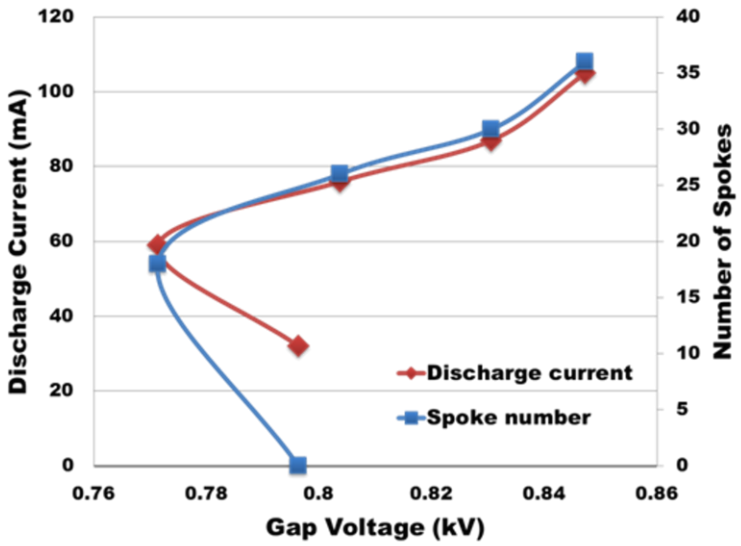

Figure 5.5: Discharge current and spoke number variation with gap discharge voltage.

variation in spoke number with gap voltage. As can be seen here, initially at breakdown and subsequent discharge formation, there are no spokes at all. Subsequent increase in the discharge current gives rise to the formation of spokes as well as an initial small decrease in discharge voltage. Apparently, spokes occur only above a threshold discharge current. Once the pattern has formed, the number of spokes tends to increase monotonically with increasing discharge current as can be seen in the figure. The anode attachment at the surface became bluer with increasing voltage as well, which could indicate a change in the local electric field reflecting changes in the nature of dissipation there (electron heating, increased collisionality). The shape of the discharge column was also observed to change with increasing voltage, changing from cylindrical to oblong to an oblate spheroid cloud. The color of the discharge attachment changed with increasing voltage as well, transitioning from purple pink to yellow, indicating the intrusion of sodium into the discharge. The mechanism for sodium transport is not well understood though localized boiling likely plays a key role. It is well known that fine droplets leave with the steam [7]. Indeed, in industrial applications, such droplets are problematic in that it leads to the

deposition of corrosive deposits such as salts in steam generation systems and boilers [7, 8]. The evaporation of these fine droplets in the gas state is a likely source of sodium in the gas phase. Indeed, Shirai and colleagues have observed presence of electrolyte species in the gas phase for a DC glow with liquid cathode. Droplet evolution may play some role in these observations as alluded to in that work as well [9]. Field-induced extraction is possible as well if the local field in the sheath is high enough. Also associated with high localized fields is Taylor cone formation which can produce jets of fine droplets injected into the gas phase [10]. As will be discussed later, the presence of this cloud is accompanied with a reduction of the plasma emission from positions z = 3 mm and z = 5 mm along the axis. As can be inferred from the reflection images, the sodium cloud appears to extend to the cathode region of the discharge. The anode spot patterns observed on the surface were not always static, rather in cases, the pattern rotated about its vertical axis of symmetry.

5.3 Results

5.3.1 Optical Emission Spectra

Figures 5.6(a)-(c) show typical optical spectra emitted from 300 to 800 nm at different axial positions: (a) exit plane of the cathode, (b) midpoint of the plasma column and, (c) and just above the liquid surface.

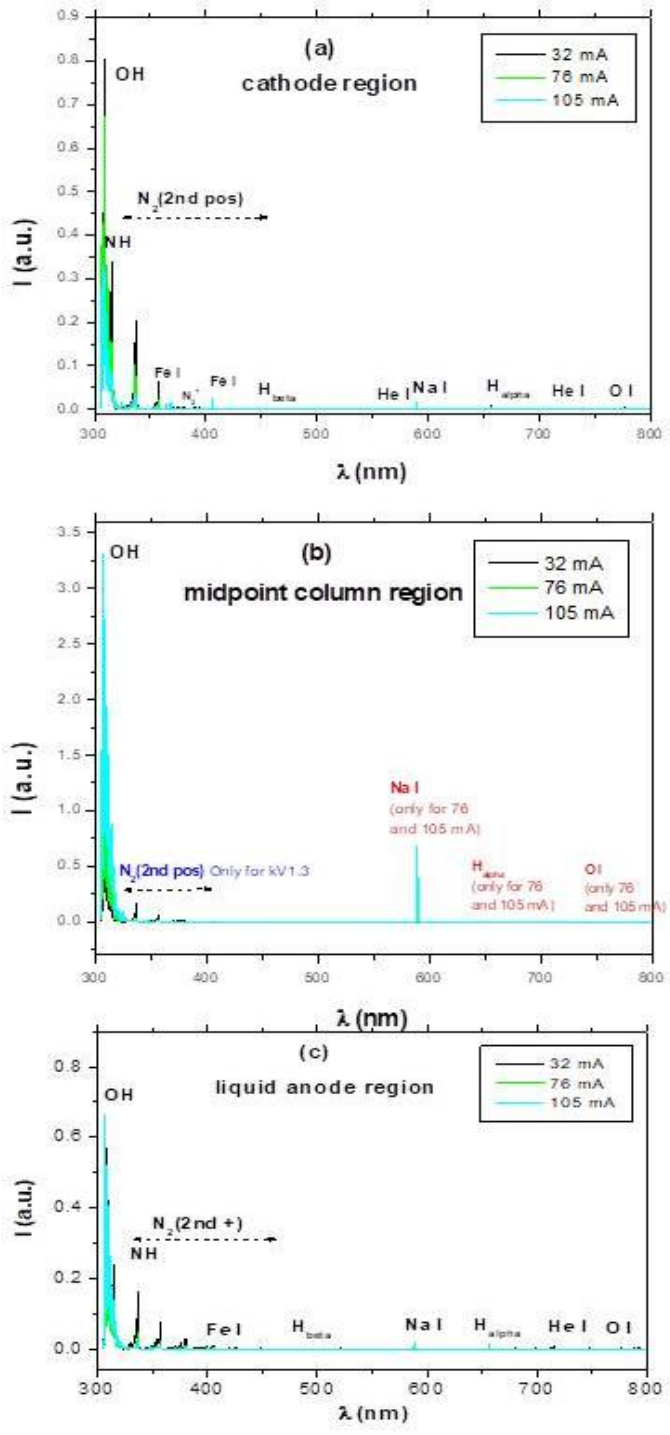

Figure 5.6: Emission spectra along plasma column: (a) Cathode region (z = 0 mm); (b) midpoint column region (z = 3 mm); (c) liquid anode region (z = 8 mm).

In all cases, the most prominent peaks correspond to the OH emission (3060 Å system). A strong emission was also detected for NH (3360Å) and N_2 (2^{nd} positive) systems, especially under lower voltage conditions (1.3 kV). For higher voltages the emission of N_2 (2^{nd} positive) notably reduced. Weak emissions of He I lines and atomic hydrogen Balmer series lines (H_α and H_β)are observed. Fe I lines (368.74 nm, 406.36 nm, with upper level energies of 4.2 and 4.6 eV respectively) were also identified in the spectra at 2.5 kV. The presence of iron is most likely due to evaporation of solvated iron ions in solution. The iron ion source in solution is presumably the immersed return electrode. The iron electrode supplies ions into the solution. That is , iron ions enter into solution via electrolytic processes at the immeresed electrode. These ions can be introduced into the gas phase via the evolution of droplets at the attachment point. Shirai and colleagues used an iron anode to serve as an iron ion source for the production of ferrous nanoparticles in solution [11]. Na I 589.0 and 589.6 nm lines, corresponding to resonant transitions from *3p* states of sodium atomic system (of very low excitation energy, 2.1 eV) towards the ground state, were also detected. The presence of sodium is also attributed to the evaporation of solvated sodium ions. These lines were most intense in the mid region rather than near the liquid surface where presumably the sodium concentration is highest. The contradiction is resolved if the electron temperature near the surface is simply too cool (owing the high evaporation rates there) to support a sufficiently high excitation rate. Direct measurements of temperature using a collisional radiative model would be required to fully understand electron dynamics at the surface, which is left to future work.

5.3.1.1 Vapor Cloud Optical Emission

Interestingly, the mid region of the plasma discharge is bulb shaped at elevated voltages and is yellow in color—owing to the presence of sodium. The shape of the cloud can be

explained if one assumes that the discharge attachment is highly localized. This assumption is consistent with the relatively small diameter of the self organized patterns < 1 mm, corresponding to current densities approaching 20 A/cm^2. The localized attachment gives rise to localized boiling and droplet entrainment with steam. Evaporation and droplet evolution in this case takes the form of a cosine distribution [12]. If the steam and droplet evolution rate is relatively high, then the evolved water tends to be focused with the shape of the plume following a modified cosine distribution scaling as $\sim(\cos\phi)^n$, where ϕ is the angle relative the surface normal. In such a case, the nature of the evaporated plume depends on the ratio of the heat source size to the equivalent mean free path of the evaporating particle, n [13]. The uncertainty in this work is the actual temperature of the water at the attachment which could range from 373 K to temperatures approaching the spectroscopically determined gas phase just above the liquid surface of ~1000 K. Over such a tempearature range, the local vapor pressure as determined by the Clasius-Clapeyron equation can vary by many orders of magniude greatly exceeding the local atmospheric pressure. Associated with such high local pressures is the neutral flux , which scales linearly with vapor pressure, leading to focused emission and an asymptotic value of approximately 3 for n. Interestingly, such focusing effects are effected by the naure of the attachement. Here self organization can actually seed the nature of the vapor plume.

Electron diffusion from the main column excites the water vapor and sodium vapor (produced from evaporating droplets), giving rise to the sodium cloud glow as observed in experiment. This situation is depicted schematically in Fig. 5.7. The excitation threshold of the sodium D lines is low ~ 2 eV. Hot electrons as they diffuse radially outward,

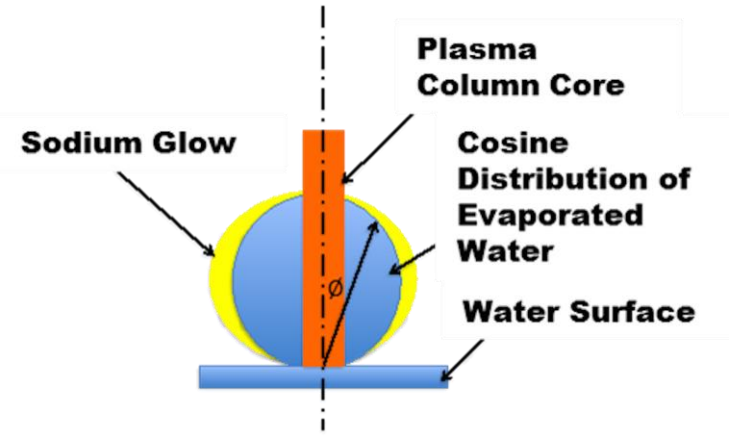

Figure 5.7: Possible mechanism for the bulb shaped sodium cloud.

loosing enegy along the way from the core to the terminal radius where they can still excite the sodium. The reduced nitrogen intensity at the higher voltage may also be a manifestation of electron cooling via collisions with water molecules, whose flux into the gas phase increases with input voltage. In summary, the observation of metal ions in the gas phase is notable in that it highlights a transport mechanism for solute atoms or molecules in solution driven by the plasma. Such transport acts also as a feedback mechanism, impacting overall plasma column impedance. The relative imporatance of water injection into the discharge can be estimated. The ratio of water vapor evaporation to helium flow rate yields the relative importance of the various gas to discharge maintenance. The evaporation flux from the located plasma attachment at the liquid surface is related to the local vapor pressure, p_v: $\Gamma = \frac{p_v}{\sqrt{3\pi mkT}}$, where m is the water molecule mass, k is Boltzmann's constant, and T is the temperature of the water at the attachment. The ratio of water molecules emitted from a square mm area to the number per unit time of injected helium molecules is approximately 10. Indeed, the discharge is indeed dominated by water vapor evaporation.

5.3.1.2 Excited Species in Plasma Column

Table 5.2 summarizes plasma excited species observed in the emission spectra (marked with "x") as a function of current. The NH radical was also detected suggesting plasma activated chemistry between ambient nitrogen and water vapor derived from the anode. This multistep process can lead to the formation of NH. It was only observed near the cathode suggesting that its production requires energetic electrons. The production of NH in similar plasmas has been studied. Here two mechanisms are possible. In one case, if the nitrogen is sufficiently energetic (~ 1 eV) then : $N+H_2 \rightarrow NH+ H$. Activation energy for such a reaction is high. While near the cathode, the plasma temperatures can reach several thousand Kelvin, it is unlikely that this mechanism dominates but perhaps contributes at a lower production rate. The following reaction is also plausible: $N^+ + H_2 \rightarrow NH + H^+$ [14].

Table 5.2. Spectroscopic features of species observed by OES in the plasma.

Species	λ (nm)	Transition	E_u (eV)	I (32 mA)	I (76 mA)	I (105 mA)	Region of the spectrum
OH	308.90	$A^2\Sigma^+ \rightarrow X^2\Pi$	4.0	x	x	x	UV
NH	336.01	$A^3\Pi \rightarrow X^3\Sigma^-$	3.4	x	x	Only next the cathode	
N_2	315.93	$C^3\Pi_u \rightarrow B^3\Pi_g$	11.1	x	x	Only next the cathode	
	337.13	$C^3\Pi_u \rightarrow B^3\Pi_g$	11.1	x	x		
	353.67	$C^3\Pi_u \rightarrow B^3\Pi_g$	11.1	x			
	357.69	$C^3\Pi_u \rightarrow B^3\Pi_g$	11.1	x	x		
	367.19	$C^3\Pi_u \rightarrow B^3\Pi_g$	11.1	x			
	371.05	$C^3\Pi_u \rightarrow B^3\Pi_g$	11.1	x			
	375.54	$C^3\Pi_u \rightarrow B^3\Pi_g$	11.1	x	x		
	380.49	$C^3\Pi_u \rightarrow B^3\Pi_g$	11.1	x	x	x	
	385.79	$C^3\Pi_u \rightarrow B^3\Pi_g$	11.1	x			

	389.46	$C^3\Pi_u \rightarrow B^3\Pi_g$	11.1	x			Violet
	394.30	$C^3\Pi_u \rightarrow B^3\Pi_g$	11.1	x	x	x	
	399.84	$C^3\Pi_u \rightarrow B^3\Pi_g$	11.1	x	x	x	
	405.94	$C^3\Pi_u \rightarrow B^3\Pi_g$	11.1	x	x		
	409.48	$C^3\Pi_u \rightarrow B^3\Pi_g$	11.1	x			
	414.18	$C^3\Pi_u \rightarrow B^3\Pi_g$	11.1	x			
	420.05	$C^3\Pi_u \rightarrow B^3\Pi_g$	11.1	x			
Fe I	368.74	$4p \rightarrow 4s$	4.2			x	
	406.36	$4p \rightarrow 4s$	4.6			x	
N_2^+	391.44	$B^2\Sigma_u^+ \rightarrow X^2\Sigma_g^+$	18.9	x	x	Only next the cathode	
N_2	426.97	$C^3\Pi_u \rightarrow B^3\Pi_g$	11.1	x	x	Only next the cathode	Indigo
	434.36	$C^3\Pi_u \rightarrow B^3\Pi_g$	11.1	x	x	Only next the cathode	
	441.67	$C^3\Pi_u \rightarrow B^3\Pi_g$	11.1	x			Blue
	449.02	$C^3\Pi_u \rightarrow B^3\Pi_g$	11.1	x			
	457.43	$C^3\Pi_u \rightarrow B^3\Pi_g$	11.1	x			
	481.47	$C^3\Pi_u \rightarrow B^3\Pi_g$	11.1	x			
H I (H_β)	486.13	$4d \rightarrow 2p$	12.7	x	x	x	
He I	501.56	$3p \rightarrow 2s$	23.1	x			Green
	587.56	$3d \rightarrow 2p$	23.1	x	x	Only next the cathode and liquid	Orange
Na I	589.00	$3p \rightarrow 3s$	2.1		x	x	
	589.60	$3p \rightarrow 3s$	2.1		x	x	
H I (H_α)	656.27	$3d \rightarrow 2p$	12.1	x	x	x	Red
He I	667.81	$3d \rightarrow 2p$	23.1	x	x	Only next the cathode and liquid	
O I	777.19	$3p \rightarrow 3s$	10.7	x	x	x	
	777.42	$3p \rightarrow 3s$	10.7	x	x	x	

	777.54	$3p \rightarrow 3s$	10.7	x	x	x	

Emission from the axis of the discharge at middle positions was greatly reduced at the high voltage, higher current conditions. The density of the vapor cloud is expected to go up with increasing voltage since the discharge current and thus power deposited into the liquid also increases. The cloud presumably consists of sodium, helium and water vapor. The origin of this reduced emission (at levels below the detection sensitivity of the optical system) could be ascribed to both, the very low electron temperature values in these cases (as shown later), and also to the quenching of excited states provoked by the presence of water vapor [15]. Alternatively, at elevated power, the vapor cloud may serve as a resistive barrier to electron transport. The supersaturated vapor region in the vicinity of the attachment would reduce electron mobility (E/N reduced), reduce electron temperature and increase locally electron losses by attachment. This obstructed flow could possibly contribute in part to the visible shape of the positive column. Electron density and flow would tend to be higher along the outter surface of the vapor cloud where the E/N is higher and collisionality reduced. This effect would also contribute to pattern formation as electron flow is no longer strictly axial.

Evidence supporting this vapor barrier mechanism comes from observed water evaportaion rates. In general, for the 200 ml jars used in this experiment, the water level was observed to drop at an average rate in the order of 0.15 mm/min due to evaporation. Evaporation occurs at the localized plasma attachment point as the bulk solution was under the boiling temperature. This 0.15 mm/min level drop corresponds to a water evaporation rate of about up to 1 SCCM of water vapor into the discharge, saturating the volume above the surface with water vapor including likely water clusters as well. It is this upward rising neutral gas that has the potenetial to cool the plama near the liquid surface thereby reducing excitation by electron

impact in that region. This vapor effect is a function of power and may indeed serve as ballasting for the discharge. At high powers, it is likely that ionization makeup for losses in the vapor layer must come from ionization processes driven by sheath effects at the liquid surface. Future work will involve absorption spectroscopy to elucicated the role of this water vapor "fountain" effect. Interestingly, helium emission was found near the surface of the liquid. These emission lines have their upper levels lying around 23 eV suggesting the presence of energetic electrons. The presence of energetic electrons in turn suggests the presence of an appreciable voltage drop at the liquid surface. Additionally, visually at the liquid surface, the discharge manifests itself as a localized plasma attachment distinct and essentially detached from the main plasma column. This surface plasma is presumably preduced by electron impact, implying the pressence of an electron accelerating sheath that serves as the energy source. This sheath therefore may be the source of energy for the self-organization patterns at the surface, which in turn supports the notion that the patterns are a type of anode spot similar in nature to low pressure variants.

5.3.2 Gas Temperature

The gas temperature (T_{gas}) was estimated from the rotational temperature deduced from the theoretical simulation of OH(A-X) spectra and their comparisons to the experimental ones. The spectra was simulated using LIFBASE software developed by Luque and Crosley [16], using an instrumental resolution of 0.13 nm. Fig. 5.8 shows the values of T_{gas} measured for the diferent discharges studied.

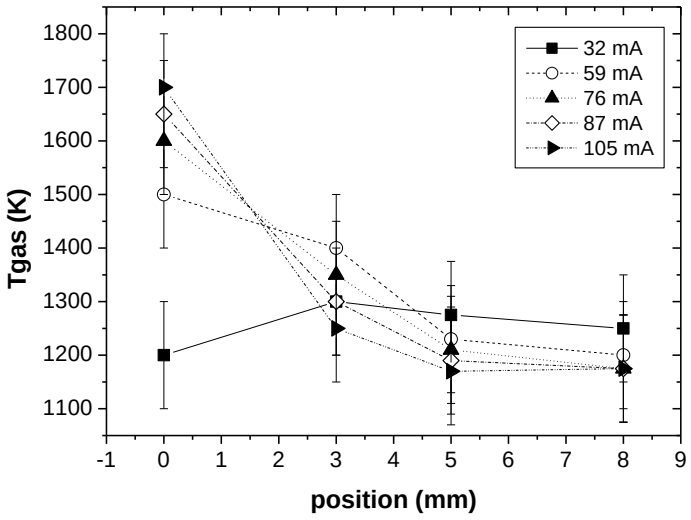

Figure 5.8: Axial evolution of the gas temperatures at different space of the plasma column.

Unlike the 32 mA case, in which the gas temperature is relatively constant along the axis of the discharge, for the rest of cases, the gas temperature decreased at positions closer to the liquid, suggesting modest cooling at the liquid surface. This is to say that evaporative cooling is more important to discharge at the higher currents. Indeed, the patterns may be comprised predominantly of water vapour plasma. Interestingly, there is a steep gas temperature drop off beyond the cathode. The temperature in the mid-discharge region and beyond is relatively constant. Here it is conjectured that evaporation of water into the discharge regulates the gas temperature. In many respects it acts to cool the discharge. The combination of this cooling effect and the forced convection owing to the injected helium flow likely plays a key role in stabilizing the discharge as well. Magnitude-wise, based on these measurements, the discharge is hot but non-thermal in nature with heavy species temperature of order a tenth of an electron volt with electron temperatures expected in the range of a few eV [10].

5.3.3 Electron Density

The electron density (n_e) of the discharge was determined from the Stark broadening of H_β (486.13 nm) atomic hydrogen Balmer series line. The profile shape of this line is very sensitive to the micro-elecric field induced by charged particles (electrons and ions) that surrounds the emitter atom (H). H_β line is commonly employed for determination of electron densities from 10^{20} m^{-3} and above [17]. Even though H_α has a higher intensity, this line is less suitable to measure n_e (especially for small electron densities cases, and optical systems with not very high spectral resolutions) due to its smaller due to its smaller full width at half maximum (FWHM), its higher sensitivity to self-absorption and its stronger dependence on kinetic equilibrium conditions in the plasma.

It was assumed that the profile of the emitted H_β line has a Voigt profile, a convolution of a Gaussian shape profile and a Lorentzian shape profile. The Gaussian line contribution is attributed to the *Doppler and instrumental* broadening and Lorentzian part is associated with *van der Waals* and *Stark* broadenings. The line full width at half maximum of this Voigt profile $\Delta\lambda_V$ is related to the Lorentzian and Gaussian contributions through the expression:

$$\Delta\lambda_V = \frac{\Delta\lambda_L}{2} + \sqrt{\left(\frac{\Delta\lambda_L}{2}\right)^2 + \Delta\lambda_G^2} \tag{5.1}$$

The *van der Waals* broadening contributing to the Lorentzian FWHM of the H_β line was calculated using the expression [18]:

$$\Delta\lambda_{vdw} = \frac{C}{T_{gas}^{0.7}}(nm) \tag{5.2}$$

The coefficient C in eq. (5.2)was calculated in first instance for helium as perturbing atom resulting in a value of 2.5, in a similar way to the coefficients obtained by Laux et al. [19] and by Bruggemann et al [20] for air and water vapor perturbing molecules (3.6 and 4.10, respectively).

In these plasmas with relatively low gas temperature, the van der Waals contribution has a non-negligible effect [21].

On the other hand, the Doppler broadening contributing to the Gaussian FWHM of the H_β line was calculated from

$$\Delta\lambda_{Doppler} = 3.48\times10^{-4}T_{gas}^{1/2}(nm) \tag{5.3}$$

H_β line profile detected was also affected by the instrumental function of the spectrometer and experienced an *Instrumental* broadening $\Delta\lambda_I$. The instrumental function of the spectrometer was measured from the profile line Ne I 632.8 nm emitted by a helium-neon laser. When using equal entrance slit width and CCD pixel width, this function has an approximately triangular shape, well fitted with a Gaussian function [17]. From the FWHM of this line a $\Delta\lambda_I$ = 0.13 nm was measured.

Thus, the Voigt FWHM was measured from the best Voigt profile fit, and taking into account the abovementioned considerations, the actual *Stark* broadening for line was determined. The electron density was derived from $\Delta\lambda_{Stark}$ using the following equation [17]

$$\Delta\lambda_{Stark} = 4.8\times\left(\frac{n_e}{10^{23}m^{-3}}\right)^{0.68116}(nm) \tag{5.4}$$

The H_β line could not be detected at positions z = 3 and 5 mm in many cases, thereby precluding calculation of the electron density at these positions. Table 3 gathers the Voigt FWHM measured for H_β line at z = 0 and z = 8 mm positions, $\Delta\lambda_V$. It also includes their corresponding lorentzian contributions $\Delta\lambda_L$ calculated from them using (1), and taking into account that the gaussian contribution is given by

$$\Delta\lambda_G^2 = \Delta\lambda_{Doppler}^2 + \Delta\lambda_I^2 \tag{5.5}$$

The van der Waals contribution was determined from (2) considering both, a 100% of helium and 100% vapor surrounding hydrogen atoms [18]. Finally, their corresponding Stark contributions were determined from the following expression

$$\Delta\lambda_L = \Delta\lambda_{vdw} + \Delta\lambda_{Stark} \tag{5.6}$$

It should be pointed out that the van der Waals contribution to the lorentzian FWHM depends on the type of gas surrounding the emitter atom (hydrogen). This dependence does affect the determination of the Stark contribution and, eventually, the electron density determination. Changes of $\Delta\lambda_{Stark}$ upon current increases are also presented in Table 5.3.

Table 5.3. Widths for H_β line at z = 0 and z = 8 mm positions.

z = 0 mm							
I (mA)	$\Delta\lambda_V$**(nm)**	T_{gas} **(K)**	$\Delta\lambda_L$**(nm)**	$\Delta\lambda_{VDW}$**(nm) (supp 100 % vapor surr H)**	$\Delta\lambda_{Stark}$**(nm) (supp 100 % vapor in VDW)**	$\Delta\lambda_{VDW}$**(nm) (supp 100 % He surr H)**	$\Delta\lambda_{Stark}$**(nm) (100 % He in VDW)**
32	0.1640 ± 0.0010	1200 ± 100	0.0601 ± 0.0010	0.0287 ± 0.0017	0.0310 ± 0.0020	0.0177 ± 0.0010	0.0424± 0.0014
59	0.1706 ± 0.0001	1500 ± 100	0.0705 ± 0.0006	0.0245 ± 0.0011	0.0460 ± 0.0013	0.0151 ± 0.0007	0.0553± 0.0010
76	0.1713 ± 0.0003	1600 ± 100	0.0715 ± 0.0006	0.0234 ± 0.0010	0.0481 ± 0.0012	0.0144 ± 0.0006	0.0570 ± 0.0009
87	0.1733 ± 0.0006	1650 ± 100	0.0746 ± 0.0007	0.0225 ± 0.0010	0.0517 ± 0.0012	0.0140 ± 0.0006	0.0604 ± 0.0009

105	0.1746 ± 0.0003	1700 ± 100	0.0766 ± 0.0006	0.0224 ± 0.0009	0.0541± 0.0011	0.0138 ± 0.0006	0.0627 ± 0.0008
z = 8 mm							
I (mA)	**$\Delta\lambda_V$(nm)**	**T_{gas} (K)**	**$\Delta\lambda_L$(nm)**	**$\Delta\lambda_{VDW}$(nm) (supp 100 % vapour surr H)**	**$\Delta\lambda_{Stark}$(nm) (supp 100 % vapour in VDW)**	**$\Delta\lambda_{VDW}$(nm) (supposing 100 % He surr H)**	**$\Delta\lambda_{Stark}$(nm) (100 % He in VDW)**
32	0.167 ± 0.007	1250 ± 100	0.065 ± 0.008	0.0278 ± 0.0016	0.037 ± 0.008	0.0172 ± 0.0010	0.048 ± 0.008
59	0.173 ± 0.005	1200 ± 100	0.076 ± 0.005	0.0287 ± 0.0017	0.047 ± 0.006	0.0177 ± 0.0010	0.058 ± 0.006
76	0.176 ± 0.007	1175 ± 100	0.079 ± 0.008	0.0291 ± 0.0017	0.050 ± 0.008	0.0180 ± 0.0011	0.061 ± 0.008
87	0.177 ± 0.003	1175 ± 100	0.081 ± 0.003	0.0291 ± 0.0017	0.052 ± 0.004	0.0180 ± 0.0011	0.063 ± 0.003
105	0.179 ± 0.003	1175 ± 100	0.083 ± 0.003	0.0291 ± 0.0017	0.054 ± 0.004	0.0180 ± 0.0011	0.065 ± 0.003

Fig. 5.9 shows the values of electron density measured for the discharges studied at axial positions z = 0 and 8 mm, corresponding to $\Delta\lambda_{Stark}$ values in Table 3, considering a 100 % of helium, vapour and air as perturbers, respectively, in calculations.

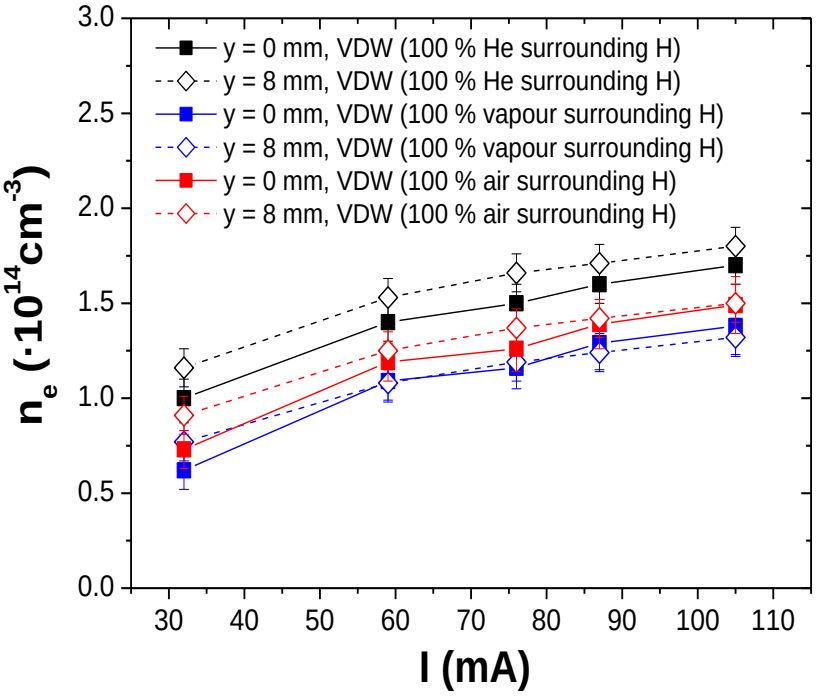

Figure 5.9: Electron density dependence on plasma current considering different perturbs surrounding H atom in the calculation of the van der Waals contribution.

In any case, the plasma density grows almost linearly with increasing current. Also, as can be seen in Fig. 5.9, regardless of the variation in the compositions used in the van der Waals calculations, the calculated electron densities appear to be quite similar at the cathode region and at the liquid surface. This is quite remarkable as one expects region above the liquid to be liquid density owing to evaporation and thus more collisional with greater attachment losses. The similarities may be attributed to the presence of significant voltage drops in these regions (cathode and anode fall voltage/anode spot), which would drive ionization. At the surface the high evaporation rate combined with the lower ionization potential of water (12.6 eV) may be enough to offset attachment and vibrational excitation losses thereby slightly exceeding production in the cathode region as observed here. Intuitively, one can surmise that significant ionization takes place at the surface as inferred from the bright, localized attachments at the

water surface as well as the presence of helium emission. Excited helium near the surface can also contribute to Penning ionization.

5.3.4 Excitation Temperature

The *excitation temperature* (T_{exc}) was estimated from the Boltzmann-plot representation [$log(I\lambda/Ag)$ versus E_p) obtained from H I lines measured (H_α and H_β). When the Saha ionization-recombination balance for the upper levels of H I system is established by electron collisions, the population of these levels conforms to a Saha-Boltzmann distribution with ionization and excitation temperatures equal to the electron temperature [22]. In the present case, it is not known whether or not this condition is fulfilled, so we only consider the excitation temperature obtained as a first estimation of electron temperature.

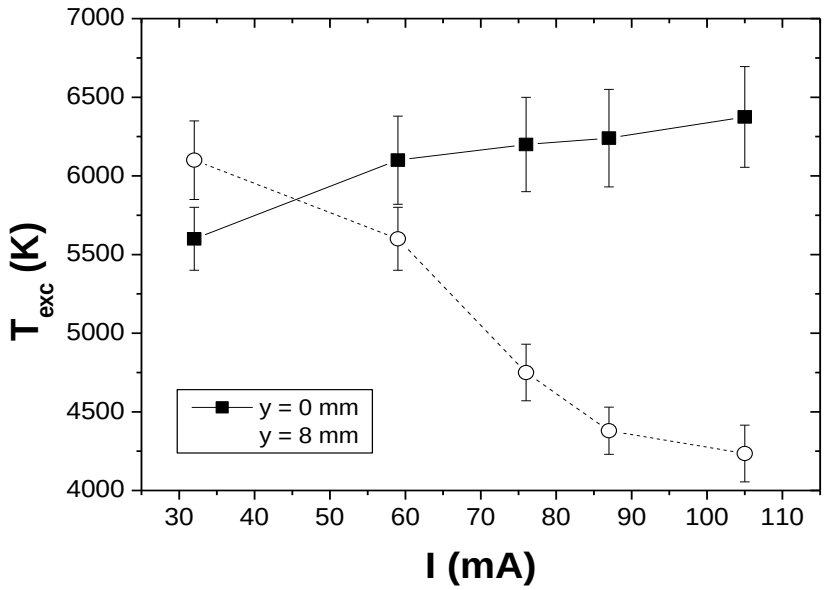

Figure 5.10: Excitation temperature in response to the current.

Figure 5.10 shows the values of T_{exc} measured for positions y = 0 mm and y = 8 mm, where H I lines could be detected under all experimental conditions. As can be seen in the figure, the excitation temperature drops significantly near the liquid surface. This is consistent with

cooling effects owing to evaporation, the rate of which increases with increasing discharge power. This observation is consistent with the reduction in gas temperature with increasing voltage as well. The vapour has an overall cooling effect on the plasma near the anode. The excitation temperature near the cathode experiences slow growth with increasing input voltage.

5.3.5 Species Emission

Here, a more detailed study of the emission of the different excited species in the plasma is presented. Fig. 5.11 and Fig. 5.12 (a) and (b) show variations of the intensity of different emissions lines observed in spectra, under the different experimental conditions studied (error bars were not deliberately included in Fig. 5.12 in order the different trends could be seen as clearly as possible).

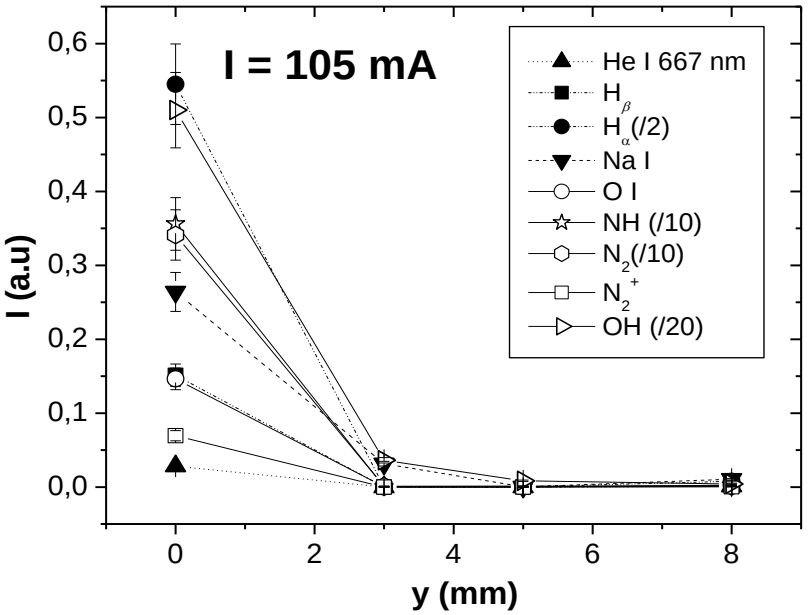

Figure 5.11: Spatial emission of different excited species in the plasma.

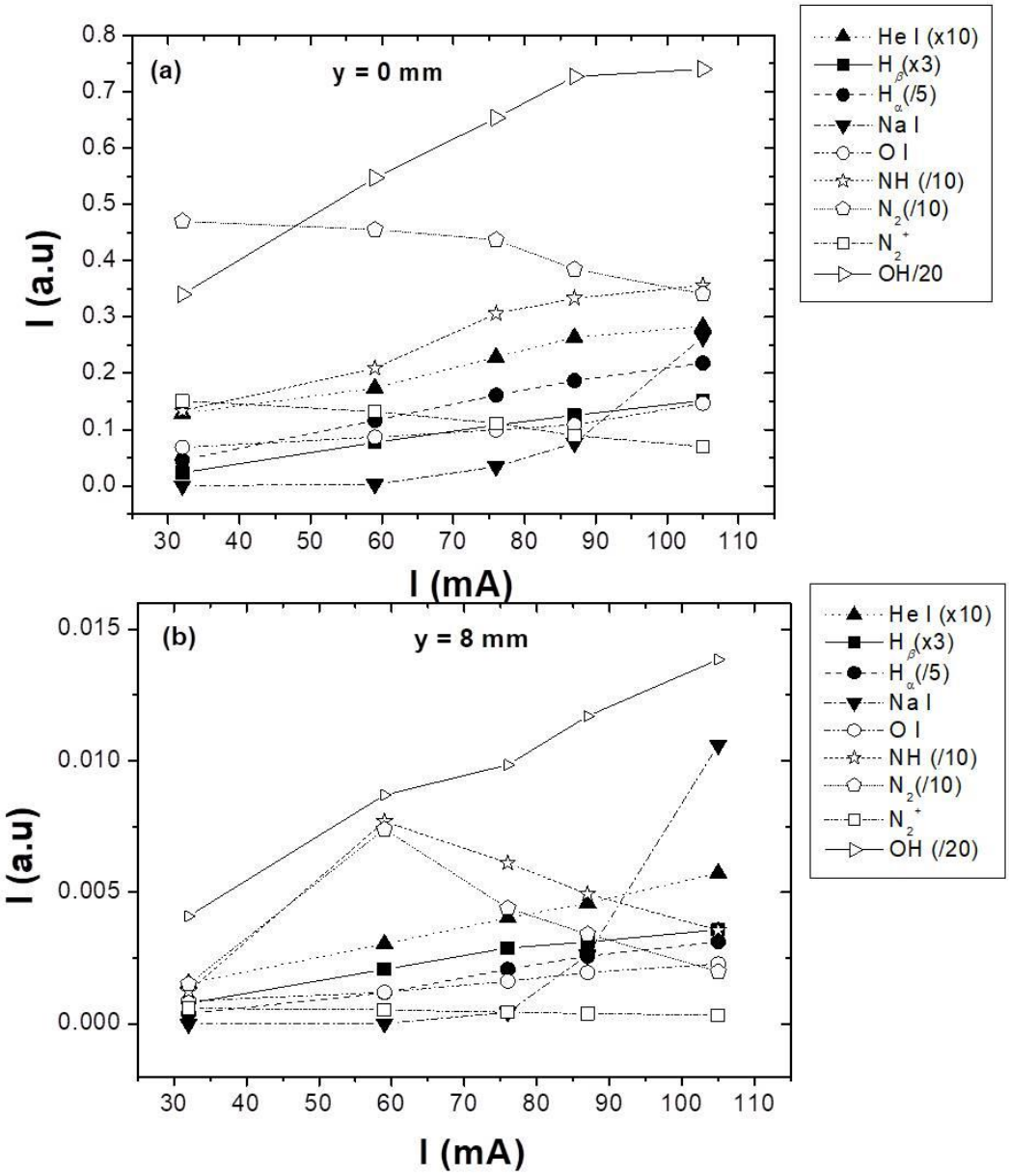

Figure 5.12: Emission of the different excited species in the plasma near (a) the cathode and (b) the anode.

Helium was the carrier gas of the discharge, so likely helium excited atoms (including helium metastable atoms) could be playing an important role in the kinetics of this plasma. Helium excited species *1s3d* were observed mainly at the cathode region. The high excitation energy of these species (≈ 23 eV) explains their weak emission. Figures 5.12(a) and (b) show the

increase of the intensity of He I line with the voltage (at positions y = 0 and y = 8 mm, respectively), in a similar trend as the electron density.

In the spectra excited hydrogen atoms and OH radicals were also detected, due to the presence of water vapor in the discharge.

The axial profiles of the emission of H_β and H_α hydrogen atomic lines (excitation energy 12.9 and 12.1 eV, respectively) were also plotted in Figs. 5.12 (a-b). Figures 12(a) and (b) show the increase of the intensity of hydrogen atomic lines emission with the discharge current, in a similar trend as electron density and helium lines intensity.

The emission of $OH(A^2\Sigma^+ \rightarrow X^2\Pi)$ rot-vibrational band was especially intense in the spectrum, which is partly due to the relatively low excitation energy of these states (≈ 4 eV). In Fig. 5.11 and 12(a) and (b) the intensity of the band head of $OH(A^2\Sigma^+ \rightarrow X^2\Pi)$ band head measured in arbitrary units under the different experimental conditions studied is also included. This intensity decreased with increasing distance from the cathode, and increased with the current following the same trend as the intensity of He I and H I lines. The saturation observed for the 2.5 kV total voltage condition at position y = 0 mm could be ascribed to some self-absorption effects, enhanced by high amount of OH species existing in this case. It is also possible that electron temperature cooling owing to vapour injection may also play a role in the reduced excitation rate of this transition.

As a consequence of the entrance of air into the plasma, excited species containing nitrogen were also present in the spectra recorded. This fact is typical in discharges created in direct contact with the air. In this way, emission of the first negative system of molecular ion $N_2^+(B^2\Sigma_u^+ \rightarrow X^2\Sigma_g^+)$ (band head at at 391.44 nm) was detected. Helium metastables (19.8 eV)

would have energy enough to create N_2^+(B) states (18.9 eV) from the following Penning type reactions like [23]

$$He^m + N_2(X^1\Sigma_g^+) \rightarrow He^0 + N_2^+(B^2\Sigma_u^+) + e^- \quad (5.7)$$

Dimer ions of nitrogen were mainly detected at the position nearest the cathode. The intensity of the band head of first negative system of the molecular ion N_2^+followed a different behaviour with voltage when compared to those of helium and hydrogen atoms and OH radicals. An inferred decrease in the amount of species N_2^+(B) was observed when voltage applied (and the discharge current) was raised, even though the amount of helium species increased. This fact should be probably due to the higher concentration of vapor water (and reduction of the fraction of air present) in the discharge, quenching activated helium species.

Nitrogen molecules were also detected. Excited helium neutrals have more than enough energy to excite any state of the N_2 second positive system (excitation energy ≈ 11. 1 eV). As in the case of N_2^+ emission, the intensity of the N_2 ($C^3\Pi_u \rightarrow B^3\Pi_g$) band head at 337.13 nm the change with the voltage did not follow the same trend as electron density.

As already mentioned, the presence of NH species was also identified from OES (see Figs. 12). This diatomic association molecule could be generated by

$$N + H_2O \rightarrow NH + OH \quad (5.8)$$

Dissociative recombination reactions are considered as a possible channel for molecular nitrogen ions destruction and *N* formation in plasmas open to the air generated at atmospheric pressure [24]

$$N_2^+ + e^- \rightarrow N + N \quad (5.9)$$

This reasoning could explain the reduction of the amount of species N_2^+ observed at y = 0 mm position when the current increased, taking place at the same time as the amount of species NH and OH increases.

The presence of excited oxygen atomic species in these discharges was also indicative of the inlet of air into them. Optical emission at 777.2 nm, corresponding to transitions from *3p* states (≈ 10.7eV) of O I system, was observed. These species were probably created by dissociative recombination of O_2^+species generated from Penning type reactions

$$He^m + O_2(X^3\Sigma_g^-) \rightarrow He^0 + O_2^+(b^4\Sigma_g^-) + e^- \tag{5.10}$$

The population of O I species also increased with voltage (see Fig. 7.12).

Finally, emission of Na I 589.59 nm line is shown in Fig. 7.12. In this case, an exponential increase of the emission with the voltage was observed consistently with increased evaporation rate with input power.

5.3.6 Electric field

Measurement of the electric field in the positive column has been performed using the optical spectroscopy technique proposed by Paris and colleagues [25]. This method is based on the measurement of the intensity ratio of two nitrogen spectral bands: the first negative system of N_2^+ (band head at 391.4 nm) and the second positive system of N_2 (band head at 394.3 nm). An estimation of E/N can be done using the following expression:

$$R_{391/394} = 46\exp[-89\left(\frac{E}{N}\right)^{-0.5}], \tag{5.11}$$

where E/N numerically equals the field strength expressed in units of 10^{-21} Vm^2. Finally, considering the gas temperature in Sec. 5.3.2, the E can be obtained. Fig. 5.13 shows the electric field in the positive column measured both near the cathode and near the water, in the discharges

shown in Fig. 5.4 (a-e). Line integrated emission spectra corresponding to these two axial positions were collected and focused onto an optical fiber using an achromatic lens (at 1:1 magnification). For each experimental condition, the spectrum was recorded three times. As shown in Fig. 18, the electric field near the liquid anode surface has a value around 37.0 kV/cm for the five cases studied. As can be seen here, at least for this work, the local electric field estimated is above the ionization threshold for a 1 Atm air discharge.

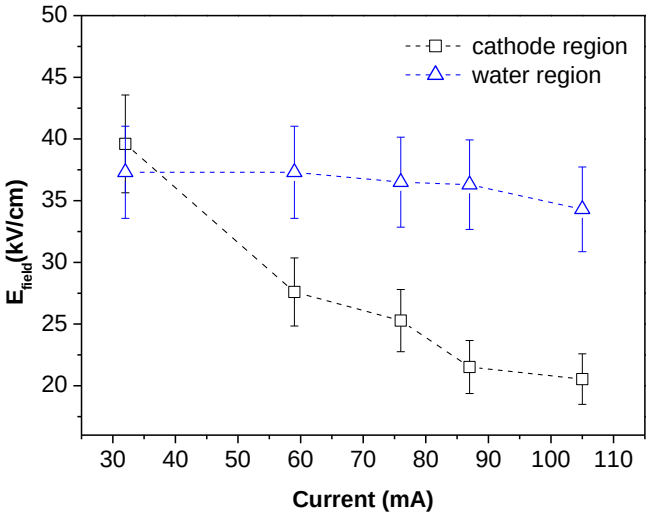

Figure 5.13: Electric field in the plasma column.

5.4 Conclusion

Optical emission spectroscopy was used to assess the plasma conditions of a DC 1 Atm glow discharge. In this work, was found that discharge species composition depends on spatial location. This work also highlights the importance of localized boiling. This data suggests that the introduction of the associated water vapor plays a role in cooling the plasma locally. Additionally droplet entrainment by steam is apparently a vehicle for the introduction of solute into the gas phase as well, such as metal ions including sodium and iron observed here.

Interesting chemistry was observed in the cathode region with the production of NH radicals. These radicals could potentially serve as precursors for the production of ammonia. The observed helium emission near the cathode and liquid anode suggests nontrivial anode and cathode fall voltages, which apparently serves to accelerate electrons to energies necessary to excite the helium. This observation may be the underlying reason for the relative similarities between the electron density near the cathode and that near the liquid anode. Finally, the overall shape of the sodium vapour cloud appears to be consistent with what one would expect of localized boiling. Here, the localized anode attachment is the heat source for evaporation with vapour leaving in the expected cosine distribution.

5.5 References

[1]. M.J. Aschwanden, F. Scholkmann, W. Béthune, W. Schmutz, V. Abramenko, M.C.M. Cheung, D. Müller, A. Benz, G. Chernov, A.G. Kritsuk, J.D. Scargle, A. Melatos, R.V. Wagoner, V. Trimble, and W.H. Green, Space Sci. Rev., Vol. 214, no. 2, pp. 1-75, Mar. (2018).

[2]. De Wit , "Spatial patterns and spatiotemporal dynamic in chemical Advances," in chemical physics, Vol. 109, I. Prigogine, Stuart A. Rice, Ed., Canada: John Wiley & Sons, Inc., pp. 435-513 (1999).

[3]. K. Showalter, and I. R. Epstein, Chaos, Vol. 25, no. 9, pp. 097613, Apr. (2015).

[4]. T. Verreycken, P. Bruggeman and C. Leys, J. Applied Physics, Vol. 105, no.8, pp. 083312-083312-4 (2009).

[5]. N. Shirai, S. Uchida, F. Tochikubo and S. Ishii, IEEE Trans. Plasma Sci. Vol. 39, no. 11, pp. 2652-2653, Nov. (2011).

[6]. N. Shirai, S. Uchida and F. Tochikubo, Jpn. J. Appl. Phys., Vol. 53, no. 4, pp. 046202 (2014).

[7]. R. K. Bagul, D. S. Pilkhwal, P. K. Vijayan, and J. B. Joshi, Sadhana, Vol. 38, no. 6 pp. 1173-1217 (2013).

[8]. R. F. Davis, Proc. Inst. Mech. Eng., Vol. 144, no. 1, pp. 198–216, June (1940).

[9]. N. Shirai, M. Nakazawa, S. Ibuka, and S. Ishii, Jpn. J. Appl. Phys., Vol. 48, no. 3, pp. 036002, Mar. (2009).

[10]. P. J. Bruggeman, M. J. Kushner, B. R. Locke et al., Plasma Sources Sci. Technol., Vol. 25, no. 5, pp. 053002 (2016).

[11]. N. Shirai, T. Yoshida, S. Uchida and F. Tochikubo, Jpn. J. Appl. Phys., Vol. 56, no. 7, pp. 1-7, July (2017).

[12]. M. Knudsen, Annalen der Physik, Vol. 48, pp. 1113-1121 (1915).

[13]. Powell, P. Minson, G. Trapaga, and U. Pal, METALL MATER TRANS A.,Vol. 32, no. 8, pp. 1959- 1966, Aug. (2001).

[14]. J. H. van Helden, P. J. van den Oever, W. M. M. Kessels, M. C. M. van de Sanden, D. C. Schram, and R. Engeln, J. Phys. Chem. A., Vol. 111, no. 45, pp. 11460-11472, Nov. (2007).

[15]. V. Bernatskiy, V. N. Ochkin and I. V. Kochetov, J. Phys. D: Appl. Phys. Vol. 49, no. 39, pp. 395204, Sept. (2016).

[16]. J. Luque and D. R. Crosley, "LIFBASE: Database and spectral simulation program," Version 1.9, SRI International Report MP-99 (009), (1999).

[17]. Yu Nikiforov, Ch. Leys, M. A. Gonzalez and J. L. Walsh, Plasma Sources Sci. Technol., Vol. 24, no. 3, pp. 1-18, May (2015).

[18]. Rodero, and M. C. Garcia, J. Quant. Spectrosc. Radiat. Transf., Vol. 198, pp. 93–103, Spet. (2017).

[19]. O. Laux, T. G. Spence, C. H. Kruger and R. N. Zare, Plasma Sources Sci. Technol., Vol. 12, no. 2, pp. 125–138, May (2003).

[20]. P. Bruggeman, D. Schram, M. A. Gonzalez, R. Rego, M. G. Kong and C. Leys, Plasma Sources Sci. Technol., Vol. 18, no. 2, pp. 025017-025017(13), May (2009).

[21]. Yubero, M. D. Calzada and M. C. Garcia, J. Phys. Soc. Jpn., Vol. 74, no. 8, pp. 2249–2254, Aug. (2005).

[22]. J. A. M. van der Mullen, Phys. Rep., Vol. 191, no. 2, pp. 109-220 (1990).

[23]. Q. S. Yu and H. K. Yasuda, Plasma Chem. Plasma P., Vol. 18, no. 4, pp. 461-485, Dec. (1998).

[24]. A. H. Timmermans, J. Jonkers, I. A. J. Thomas, A. Rodero, M. C. Quintero, A. Sola, A. Gamero and J. A. M. van der Mullen, Spectrochim. Acta B, Vol. 53, no. 11, pp. 1553-1566 (1998).

[25]. P. Paris, M. Aints, F. Valk, T. Plank ,A. Haljaste,K.V. Kozlov and H.E.Wagner, J. Phys. D: Appl. Phys. 38 3894–3899 (2005).

CHAPTER VI

Pattern Sensitivity to the Types of Electrolytes[9]

In this chapter, pattern sensitivity to electrolyte type was investigated using 13 different electrolytes. The study is based on the hypotheses that since patterns are sensitive to conductivity. Broadly speaking, conductivity is sensitive to electrolyte type, and then pattern morphology should vary with electrolyte type. The impact of electrolyte type on discharge morphology should also be affected by the introduction of ions form solution electrolyte that enters the gas phase via droplets. These ions directly affect discharge processes in the discharge column and thus may play a role in effecting the pattern plasma shape.

Therefore, self-organization pattern formation and behavior were studied as a function of discharge current, solution ionic strength, and their chemical property evaluation. The response of the patterns to variation in these parameters was measured using an imaging camera and optical emission spectroscopy (OES). Observed pattern characteristic length scales for the electrolytes tested ranged from 2 mm to 13 mm and typically increased with current over the investigated range of 20 mA to 80 mA. Complex self-organized pattern structures not reported to date were also observed. The factors associated with pattern formation and associated complexity are discussed and summarized.

[9] The results discussed here and portion of the text in this chapter have been submitted to the journal of plasma sources Science and Technology in the article reference of PSST – 103974.

6.1 Introduction

While a lot of progress has been made in terms of identifying key control parameters, a thorough understanding of the plasma liquid interface and the related complexity of plasma induced liquid chemistry will likely be necessary to fully appreciate the appearance and formation mechanism of self-organized patterns. Here the study is subject to the experimental investigation on the sensitivity of pattern formation to variations in electrolyte chemistry. In this work, we extend previous investigations by probing the effect of pattern variation on electrolytic solution type and ionic strength. The observation of complex self-organization patterns on the liquid anode surface is reported as a function of discharge current. A transition region is also observed at a characteristic discharge current, below which, not patterns were observed to form. The variation in emission spectra with different electrolytes is also discussed altogether. The goal of this work is to further elucidate experimentally the control variables that lead to self-organization on the anode surface of liquid electrodes.

6.2 Description of the Experiment

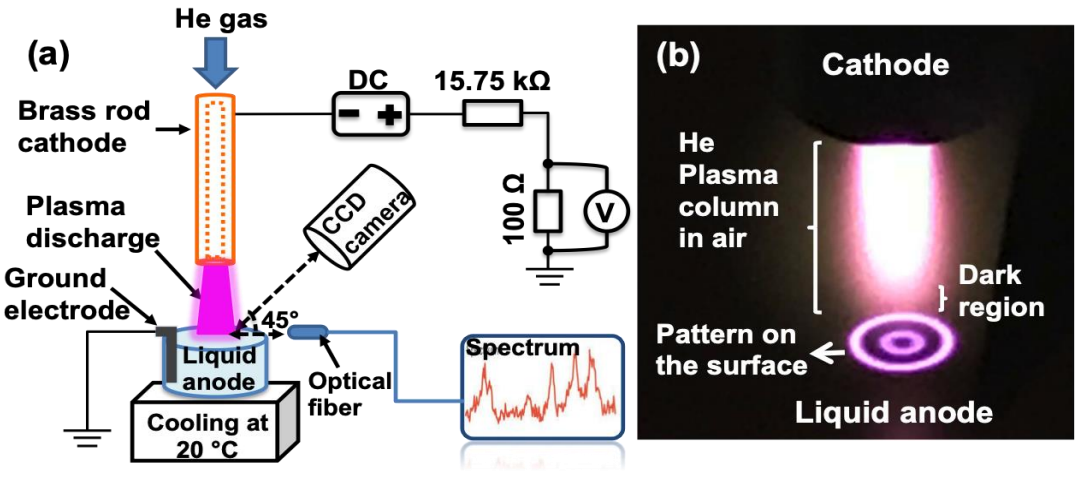

Figure 6.1: Experimental setup is shown in (a) schematic configuration (not to scale) and (b) actual plasma glowing discharge with a double ring shaped pattern structure on the liquid anode surface that captured by using a CCD camera.

A schematic of the atmospheric pressure DC glow discharge apparatus is shown in Fig. 6.1(a). Here, the anode was 1% electrolytic solution similar to that used by Shirai [1]. In this study, a range of electrolytes was investigated. A silicon wafer placed at the bottom of the beaker containing the electrolyte served as the returning ground electrode. Liquid anode solution beaker with volume capacity of 125 ml was affixed to a water-cooled heat exchanger whose surface temperature was set at approximately 20℃. Thirteen different salt solutions were investigated, which included a range of cation charge states (Na^+, K^+, Mg^{2+}, Cu^{2+}, Zn^{2+}, Fe^{2+} and Fe^{3+}) and two types of anion states(SO_4^{2-} and Cl^-). These aqueous solutions were prepared by dissolving the salts into DI water. Most of the salts were anhydrous compounds except there were three salts containing water molecules with their hydrated form, which stated as $MgSO_4 \cdot 7H_2O$, $CuSO_4 \cdot 5H_2O$, and $CuCl_2 \cdot 2H_2O$.

Besides the standard control condition that stated in chapter 3 (200 SCCM helium, CCM, 0 to 3kV, and 100Ω resistor in the series circuits), the inter-electrode gap was set at 8 mm. A 15.75kΩ ballast resistor was used to prevent the discharge from constricting into an arc for a current limitation concern. Images of the plasma column with self-organized anode pattern on the liquid surfaces were captured by using a CCD camera that was positioned approximately 45-degree angle with respect to the liquid surface. A double ring shaped self-organized pattern image is given as an example that is shown in Fig. 6.1(b). The thicknesses of the inner and outer ring were similar at approximately 0.25 mm inner and outer ring diameters of around 1 mm and 2.6 mm respectively. In the figure, the dark space region, typical of glow discharge, can be observed just above the anode liquid phase. This discharge is similar to the one in Fig. 3.4 but with different pattern structures. An optical fiber coupled to an Ocean Optics Spectrometer (OOIBase32) was set approximately 1.5 mm above the electrolyte surface to study emission near the liquid anode surface. In all the cases, the experiments took place in ambient air at 1 atm. The total plasma exposure time at each discharge operating condition was 20 minutes. Solution conductivity,

nitrate (NO_3^-) and nitrite (NO_2^-) concentrations, and pH were measured before and after the plasma exposure.

6.3 Plasma Discharge Characteristics

The discharge characteristic of the various electrolytes investigated in this work exhibited similar overall dependences with varying current with some subtle differences in cases. Fig. 6.2

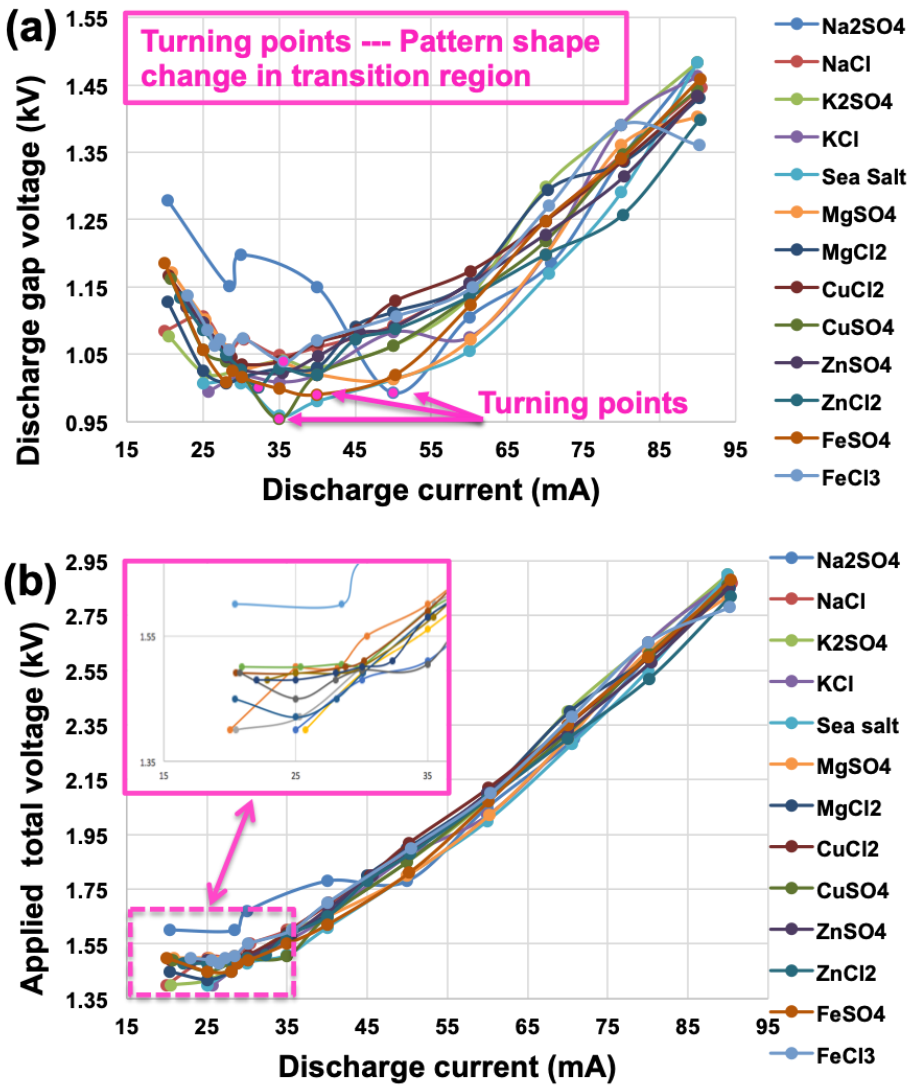

Figure 6.2: Voltage current characteristics for different electrolytes are shown in (a) plasma glow discharge in gap that between the electrodes and (b) total power applied into the operation system

2(a) shows the discharge potential variation as function of discharge current, which represents

the potential drop from the plasma glowing column with an 8mm inter electrode gap. The discharge potential was estimated as the potential difference between the total applied voltage and the voltage drop across the series ballast resistances. For each electrolytic solution, a turning point was observed, centered around 40 mA, with the exception of sodium sulfate, whose turning point occurred closer to 50 mA. When the current is below 40 mA, the discharge exhibited so called negative resistance where the voltage decreased with increasing current. Beyond the turning point, the discharge behaved ohmically. This turning point suggests a mode change common with all electrolytic solutions investigated here. As will be discussed in the next section, the turning points were found to be related to self-organization pattern onset.

In Fig 6.2(b), the variation of the total applied voltage with discharge current is shown in linear behavior with the exception of points below 40 mA, which the total applied voltage is relatively flat. In general, with increasing current the discharge voltage can be expected to increase linearly, matching the drop across the ballast resistor, but because it is below 40 mA, the discharge gap exhibits negative resistance, this effect at the lower currents dominants the behavior of the total voltage. Consequently, as can be seen from the plots in dashed box, the voltage is sufficient enough to maintain a self-sustaining discharge. This feature indicates a typical phenomenon in the breakdown process of dc glow discharge. In breakdown the entire region between the cathode and the anode participates in the process, which requires a much higher voltage and therefore leads to hysteresis in the voltage-current characteristics [2]. In this study, the pattern complexity with the current instability is also observed in below 40 mA current regions that are shown in section 6.5.

6.4 Pattern Formation and Electrolytes type

6.4.1 Pattern Evolution with Discharge Current

As we have demonstrated in chapter 2, in many studies to date, discharge current has been identified as an important parameter affecting the self-organized anode pattern formation on the surface of the liquid solution [3, 4]. Typically, salt water or tap water is used as the electrolyte in these discharges. In this recent effort, the effect of discharge current on pattern formation with thirteen different liquid electrolytic solutions was investigated. Figure 6.3 depicts that the pattern formation as discharge current is varied from 20 mA up to 80 mA for both SO_4^{2-} and Cl^- negative ion based solutions. The pattern size variation with discharge current observed under this range was measured to vary between 2 mm and 13 mm by collecting the largest diameter of each structure. Although the pattern structures are not totally identical at 40 mA, the estimated pattern diameters (include core attachment with either dots or spokes around) are ranged between 4 mm to 6 mm. The patterns associated with the $FeCl_3$ solution differed in morphology from the other 12 solutions investigated. At lower currents the pattern was not symmetrical and tended to vary with time. Additionally, the plasma discharge column is bent when the current is less than 40 mA. This observation is also discussed in the Sec. 6.5.2. At higher currents, the attachment formed a disk; in fact, this solution is associated with the largest pattern structure. Presumably this solution required the largest contact area at a given discharge current in order to sustain the discharge. Its dissolution in water does produce more chlorine ions than the other electrolytes and thus one can expect a higher negative ion concentration in the gas phase owing to escaping chlorine. The electron attachment by chlorine increases the electron loss rate. All patterns tended to rotate. It was observed that the pattern rotation was relatively stationary at 60 mA, thus reflects the higher mobile stability of the pattern in this current region.

As shown in the Fig. 6.3(a), a single ring attachment is observed at 20 mA for all solutions in SO_4^{2-}electrolyte group. As the discharge current is increased to 28 mA, a rotating double ring attachment appears on the surface. This observation with the current range matches Shirai's results [1]. At discharge currently slightly above this value, the attachments present time varying spatial patterns. Patterns observed above this unstable regime, e.g. 40 mA, consisted of dot-like structures with the exception of Na_2SO_4 solution, which yielded spokes. Note that this differentiation of the attachment to more complex shapes tends to occur at the value of the local minimum discussed in Fig. 6.2. Crossing this current region, pattern shapes tend to evolve into shapes with increasing complexity. This variation demonstrates a transition process for the attachments. At 60 mA, stable rotating spokes were observed on the surface of all solutions. With increasing current above 60 mA, the spokes tended to elongate. These spoke structures were also observed to be less stable at the higher currents. For instance, some honeycomb cell shaped structures can be observed at 80 mA for almost all of the 12 solutions except $FeCl_3$ solution. Here such structures are visible from both K_2SO_4 and KCl solutions.

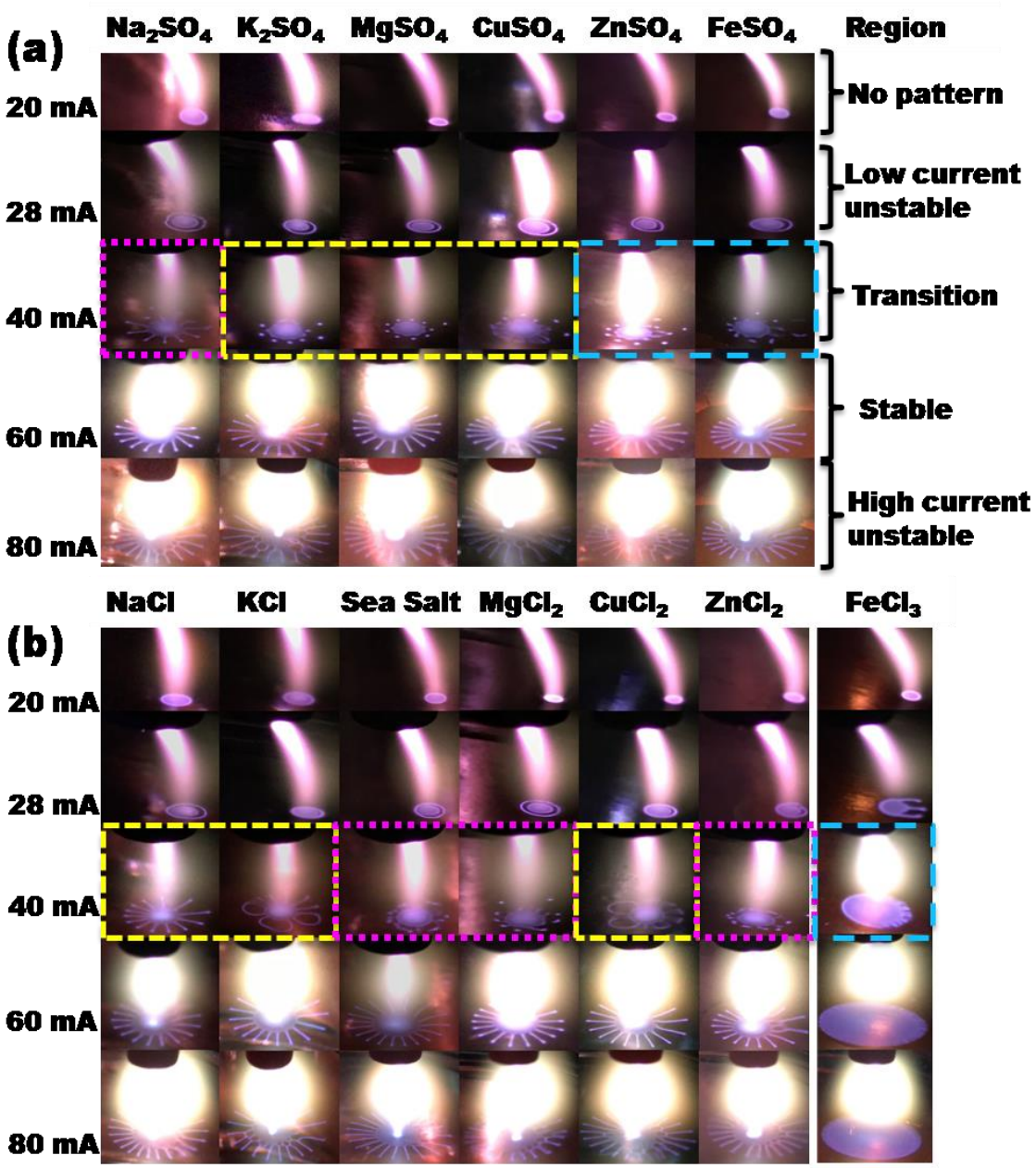

Figure 6.3: Pattern structure variations between 20 to 80 mA are demonstrated in two negative ions based solution groups: (a) SO_4^{2-} group and (b) Cl^- group. The dashed lines used in the figure are to categorize the similar pattern behavior that reflected from their similar ionic strength in section 6.4.2.

With the exception of the Fe^{3+} ion chloride salt, the pattern evolution of the Cl^- electrolyte group as shown in figure 6.3(b), exhibited similar behavior as in SO_4^{2-} group as function of current with the same positive metal ions (Na^+, K^+, Mg^{2+}, Cu^{2+}, Zn^{2+}). On the other hand, at 40 mA, in the Cl^- group, a spoke attachment rather than localized dots attachments were observed.

This observation suggests a possible dependence of solution anion mobility which will affect the rate of negative charge flow from the interface. Here the Cl^- mobility is 1.0382 $m^2s^{-1}V^{-1}$, almost twice that of SO_4^{2-} at 0.544 $m^2s^{-1}V^{-1}$ [5-7]. Of the ionic solutions investigated, the patterns observed with the ferric chloride solution deviated the most. Beyond 20 mA, the attachment was disk-like with protrusions that were motion. The number of short protrusions as can be seen in the figure increased with current. Interestingly, the protrusion locations were not radially symmetric; rather they favored one side of the disk. At higher currents (>60mA), the pattern took the form of an enlarged rotating disk. It should also be pointed out that the plasma column did not appear to make physical contact with the liquid surface; rather a pronounced dark space was observed as we have shown in Fig. 3.4. This dark space or anode fall region may play some role in determining attachment shape. In addition, as the only solution that includes"+ 3" charge metal ions, the unique patterns observed with $FeCl_3$ suggests that the charge of the cations may also affect the structure formation of self-organization patterns by effecting local chemical properties such as conductivity and complex formation.

6.4.2 Ionic Strength Effects

The apparent difference between the iron chloride solution and the other salt solutions investigated suggests ion species dependence. The ionic strength is a measure of the charged ionic species concentration in a solution that also affects local equilibria as related to electrolyte disassociation. The ionic strength I of a solution is a function of the concentration of all ions present in a solution:

$$I = \frac{1}{2}\sum_i Z_i^2 C_i \tag{6.1}$$

where Z_i and C_i represent as the charge and the molar concentration of ion i respectively. The sum is taken over all ions in each solution. The Debye-Huckel electric field screening length

scale varies inversely with the square root of the ionic strength. Thus, the relative importance of electric field driven effects such as local ion local transport in the double layer region and near field, depends on ionic strength. Theoretically, it is therefore of interest to compare pattern formation behavior as a function of the ionic strength. By applying equation (6.1), the ionic strength of each aqueous solution with their corresponding molar concentration was calculated in Table 6.1 and Table 6.2. First table includes all the results from SO_4^{2-}group with highest molar concentration of Na_2SO_4 solution. Recall from Fig. 6.3, at higher discharge currents, the plasma attachments tended to form spokes. However, of the solutions investigated in this group, Na_2SO_4 developed spokes at much lower currents than that which was observed in the other solutions.

Electrolytes	Molar Concentration (M/L)	Ionic Strength (M)
Na_2SO_4	0.0615	0.184
K_2SO_4	0.0501	0.150
$MgSO_4$-$7H_2O$	0.0354	0.142
$CuSO_4$-$5H_2O$	0.0350	0.140
$ZnSO_4$	0.0541	0.216
$FeSO_4$	0.0575	0.230

Table 6.1. Ionic strength of the solutions in the SO_4^{2-} group.

Electrolytes	Molar Concentration (M/L)	Ionic Strength (M)
NaCl	0.1494	0.149
KCl	0.1171	0.117
Sea salt	0.2781	0.278
$MgCl_2$	0.0917	0.275
$CuSO_2$-$2H_2O$	0.0512	0.154

$ZnCl_2$	0.0641	0.192
$FeCl_3$	0.0538	0.323

Table 6.2. Ionic strength of the solutions in the Cl^- group.

It is interesting to look at the pattern behaviors referring to their ionic strength in the 40 mA transition region. For example, a similar evolution in pattern morphology was observed in the K_2SO_4, $CuSO_4$and $MgSO_4$ solutions, whose ionic strengths were close. So do $ZnSO_4$and $FeSO_4$ solutions, which formed more a like pattern structures with their ionic strength in the same scale. Likewise, for the solutions with similar ionic strength in Table 6.2 show the same trend appears, such as NaCl, KCl, and $CuCl_2$ solutions resulted in spoke liked structures with and without some curvature at the edge of the patterns. Dot structures were displayed on the sea salt, $MgCl_2$, and $ZnCl_2$ solutions. Of all the solutions, the $FeCl_3$ mixture has highest ionic strength due to the larger charge of Fe^{3+} induced largest stoichiometric coefficient of 6. Its pattern at 40 mA exhibited as a unique pattern and subsequent pattern evolution in comparison of that was observed in the other solutions.

In more detail, these pattern variations associated with their solution ionic strengths at this transition current region is summarized as shown in Table 6.3. As for the solutions in both groups (SO_4^{2-} or Cl^-), their resulting pattern structures have been matched with different ranges of ionic strength by increment of 0.05 moles (M). It was found that their pattern appearances are different at the lowest ionic strength range which is from 0.1 to 0.15 M. However each group observed a spoke structure from a participated solution in the ionic strength range of 0.15 to 0.20 M. Between 0.2 and 0.3 M, more active dots have been captured in both groups but with data vacancies. Although this observation might not be sufficient to support the ionic strength effects on the self-organization pattern formation, it is interesting that the pattern shapes can be grouped

Table 6.3. Summary of observed pattern structures at 40 mA transition region with their corresponding solution ionic strength. The dashed lines represent the data vacancies in this investigation.

I (M)	**SO_4^{2-}**		**Cl^-**	
Range	**Pattern**	***Solution***	**Pattern**	***Solution***
0.10 - 0.15	dots	$CuSO_4$	spokes	KCl
		$MgSO_4$		$NaCl$
		K_2SO_4		$CuCl_2$
0.15 - 0.20	spokes	Na_2SO_4	spokes	$ZnCl_2$
0.20 - 0.25	dots	$ZnSO_4$	---	---
		$FeSO_4$		
0.25 - 0.30	---	---	dots	$MgCl_2$
				sea salt
0.30 - 0.35	---	---	disk	$FeCl_3$

based on ionic strength. This observation is also highlighted in Fig 6.3 using the dashed line boxes as group dividers. Dissimilarly, with the higher molar concentration and ionic strength in Cl^- group, the observed patterns on the surface of these solutions tended to be more active in motion and more complex in morphology than the patterns in SO_4^{2-} group at same transition region of 40 mA. This can be simultaneously considered with the higher mobility of Cl^- ion,

which stated previously in section 6.4.1 that might explain the role played in the complexity of pattern formation and stability at the interface.

In the case of ferric chloride aqueous solution, a dark orange colored precipitate layer was observed to form on the surface. Presumably the precipitate was formed from the reduction driven by solvated electrons at the plasma liquid interface. The precipitate is presumptively Iron (III) hydroxide $Fe(OH)_3$. This solid can result from equations: $e + H_2O \rightarrow H + OH$ and $Fe^{3+} + 3OH^- \rightarrow Fe(OH)_3$. The precipitate tended to form a thin layer everywhere but at the attachment point — which appeared to form in a "hole" on this thin layer. The presence of the layer likely impacts the spatial development of the pattern, giving rise to a disk shaped pattern — here the pattern forms for the most part on the surface of the precipitate. This behavior illustrates the relationship between liquid phase chemistry driven by the plasmas which serves in this case as the initiator and the self-organization which is the result of feedback to the discharge. The relatively uniform disk-like attachment rather than spokes is likely a consequence of the presence precipitate layer which homogenizes attachment conditions. The exact composition and mechanism for this particular case is discussed in chapter 7.

Overall, however, the general evolution of these patterns with increasing discharge current was still similar to that observed in the both groups. Here, one thing needs to point out is that this work was initially controlled with the same mass concentration of each electrolytes so that the operation condition can be matched to some of the previous self-organization pattern researching works [1]. In order to further investigate the pattern effects due to the ionic strength, it would be prudent to control the molar mass. At equal molar concentrations, one can directly compare the impacts of activity variations which yield insight into the effective concentration of the solution. This consideration will be taken in our future approaches.

6.5 Observation of Pattern Complexity

6.5.1 Behavior at 30 mA

In contrast to the pattern formation at each current interval in Fig. 6.3, more complex pattern structures were observed at currents below 40 mA hereafter designated the low current regime. Figure 6.4 illustrates observed patterns with different electrolyte solutes in DI water in this unstable region. For the purposes of this work, unstable is defined as inconsistence in pattern evolution with small changes to the discharge current. This is in contrast to pattern formation at higher currents where the patterns evolve deterministically and repeatedly with increasing discharge current. Typically, the discharge current can be controlled reliably within 5 mA. As

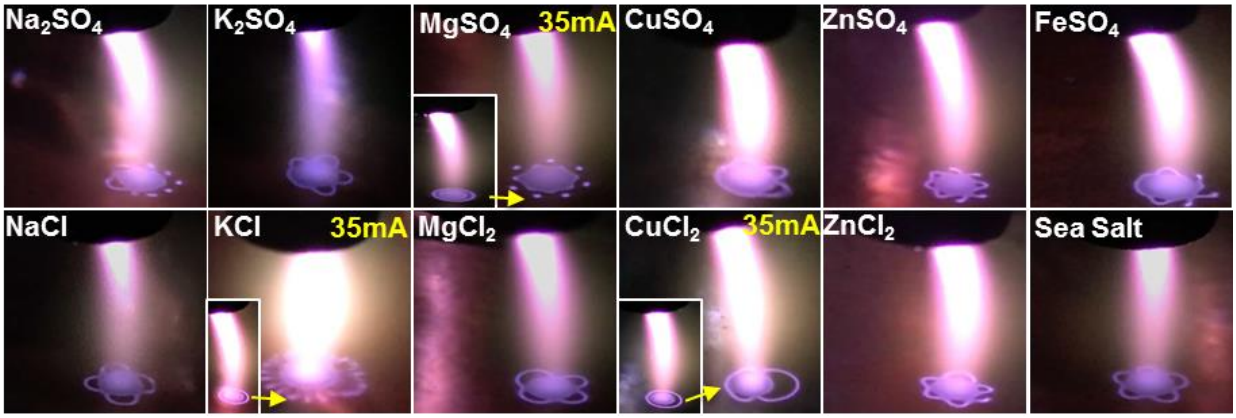

Figure 6.4: Pattern observation at 30 mA of each solution.

can be seen, at 30 mA, Na_2SO_4 solution, the anode surface attachment consisted of a series of dots, some of which were in motion symmetrically surrounding a central disk or central circular core. A clearly visible flower-shaped structure with round edge was observed on the surface of NaCl, K_2SO_4, $MgCl_2$, and sea salt aqueous solutions; a star-like pattern structure with an open leg appeared on the surface of $ZnCl_2$ solution; and star like structure with multiple legs was observed on the surface of $ZnSO_4$ and $FeSO_4$ solutions. On $CuSO_4$ solution, the pattern took the

form of multiple lobes. KCl, $MgSO_4$, and $CuCl_2$ solution attachments took the form of a pure, double ring structure. It is interesting to note that after slight adjustment of the discharge current up to 35 mA, the double ring structure was observed to transition into a completely different complex pattern. It is not well understood why these complex and less stable patterns form at the low current regime. Such complex shapes are apparently necessary to sustain the discharge at these reduced currents.

6.5.2 Unusual Pattern Structures

Three unusual patterns were observed at low discharge current. These patterns to the authors' knowledge have not been reported in atmospheric DC glow studies with helium plasma. As shown in Fig. 6.5(a), six pointed star shaped structure with a solid circular plasma attachment in the center was observed on the $CuSO_4$ electrolyte at 39 mA. The measured lengths between each vertex of the star are likely uniform with a value of 3 mm, which results two overlapped equilateral triangles. The circular shaped center core of the star holds a diameter of 2.3 mm. It was found that this pattern only exists in the low current regime (below 40 mA). The early stage of the evolution of this shape can be seen in figure 6.4 at a lower current of 30 mA. This shape is unstable in that small changes in the discharge current lead to a transition into anode surface consisting of ordered dot-like attachments (reduction in current) or spokes (increase in current). The star pattern varies in time as well rotating as well as transforming cyclically from a star with 6 points to one with 7 points. Such behavior suggests an instability that leads to bifurcation. Locally, solution chemistry changes due to plasma driven redox processes in addition to modifications to local pH and electrical conductivity. As this is a low current mode, the attachment morphology may be more sensitive to local changes in charge transport. For the

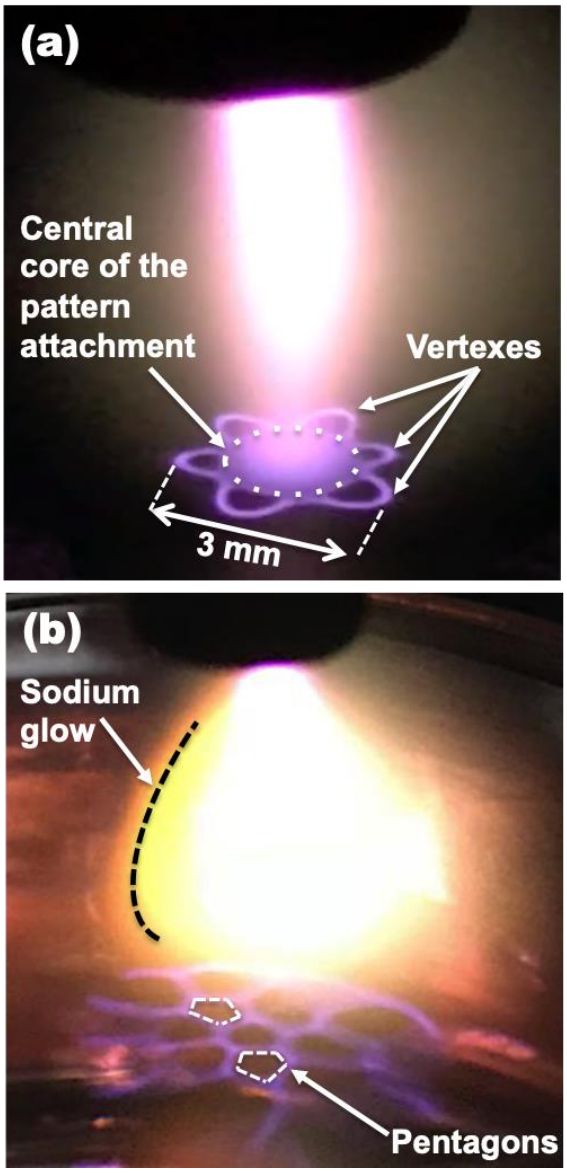

Figure 6.5: Star shaped and Honeycomb shaped unusual pattern structures observed on the surface of (a) $CuSO_4$ anode solution and (b) sea salt anode solution respectively.

discharge to be maintained critical gas phase ionization processes must occur in the presence of liquid water derived loss processes such as the emission of water vapor and attachment. If gas phase processes are marginal, then local processes at the surface including anode fall voltage and collection surface area can be expected to change. Interestingly, one possibility is the prospect of morphology changing to minimize the generation of loss mechanisms derived by the attachment

at the solution surface such as reduced local current density and anode fall voltage. In turn this could be realized through a shape change that will lead to the complex pattern formation.

Figure 6.5 (b) illustrates another unusual pattern. In this case, the plasma attachment has a honeycomb-like morphology with pentagon shaped cells. The reason why the plasma does not spread to fill the cells is not clear. Such a shape does allow for the spreading of the discharge attachment over a large surface area while maintaining a modest current density. It is also possible that chemically driven surface processes may be occurring such as the formation of a precipitation layer. In this case, the discharge is present along cracks or fissures in the thin film. Indeed, the morphology is similar to patterns observed in desiccated thin films [9]. The likely precipitate in this case would be sodium hydroxide related to the interaction of sodium with OH with surface desiccation driven by localized plasma heating leading to polygonal cracking. The honeycomb structure observed at this low current condition is similar to that observed at 80 mA in Fig. 6.3 but here is more structurally complete. The typical length of a side of the pentagon cells is about 1 mm. This unique attachment was observed 25 mA. This pattern is actually observed only when the current is reduced from some higher value, indicating a type of hysteresis. Here, the current was reduced from 100 mA down to 25 mA to realize the pattern. Normally spot complexity follows increases in current, proceeding from a single attachment, ultimately to spokes. Unlike the plasma column to other cases, the plasma glowing discharge presents as a glowing ball with yellow light emission around of its edge. In Shari's paper, when the liquid cathode discharge was applied, yellow light emission is observed. It was considered to originate from sodium atoms vaporizing from the electrolyte surface [1]. The same idea is applied here and also in our previous chapter: by analysis the helium plasma spectrum in near water surface region, the yellow glowing emission represents the glowing sodium species in the

vapor from the anode liquid. According to the study on plasma liquid interaction, the glowing sodium cloud was observed on the sea salt solution when the spoke pattern was formed as well [8]. A prominent dark space is also observed just above the anode surface with the $FeCl_3$ electrolyte in high current region (Fig. 6.3b). Here the presence of the attaching gas chlorine derived from the solution was suggested as a mechanism—which drives the depletion of electrons locally [9].

Another interesting pattern observed is shown in Fig. 6.6 with ferric chloride electrolyte. As can be seen in the figure, the shape evolves asymmetrically with increasing current. As with

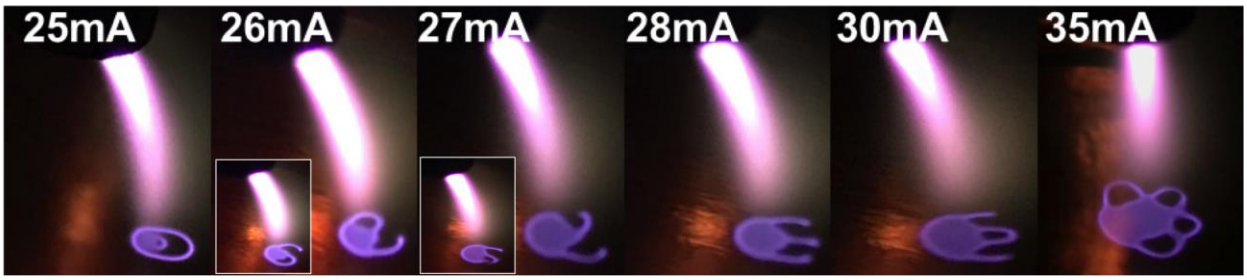

Figure 6.6: Pac man ghost shaped pattern evolution is observed with increasing current on ferric chloride electrolyte.

the previously described complex patterns, these pattern structures are only observed in the low current region (<40mA). The pattern evolves from a double ring to a disk with protrusions. The number of protrusions increases with increasing current. These protrusions eventually evolve into a distorted flower like pattern with the “legs” connecting to form closed contours, forming the petals. The observed patterns were not steady—rather they tended to exhibit rotation, particularly manifested in the “leg”-like protrusions.

Presumably the pattern is necessary for the maintenance of the discharge at these lower currents. Losses due to inelastic collisions with water vapor and attachment must be balanced with ionization processes. The losses on the other hand are a function of not just the actual

current magnitude and associated anode fall voltage, but also the collection surface area. It is very much a possibility that the change in the pattern at the surface is a feedback mechanism that allows the discharge to be maintained. That is, the pattern that evolves in current could be a mechanism by with losses introduced into the plasma column is reduced. By spreading the discharge currently over such sinuous rills, the amount of water and thus chlorine evolutions into the gas phase is minimized. This is a direct consequence of the fact that for a fixed current and voltage, once can have reduced current density if you increase the area –the complexity of the area. Just increasing the footprint is not enough as the surface is active. Rather one can also control the spatial location where the vapor is derived. The probability of the vapor reaching the core of the plasma column is minimized with complex shapes in contrast to say a disk. So the complex shape might be considered as a feedback mechanism–a solution to supporting the discharge at such reduced currents. The same would hold for any current—that pattern that forms minimizes losses derived from plasma liquid interactions. This phenomenological possibility is based on the realization that in the center of the discharge, the attachment is largest. If we assume current collected scales with surface area then, in the center, the evaporation rate will be highest because it is the electrons that deposit the thermal energy to the surface. This deposited energy is associated with the random thermal energy associated with temperature and the energy gained as the electron falls through the anode sheath. Evolution of vapor acts as a ballast that cools as well as restricts flow. Electrons that diffuse radially from centerline can be expected to have both lower temperature (from cooling collisions) and lower density (they must escape) attachment processes. So the current density incident on the surface off centerline is just

$$\vec{j} = \sigma \cdot \vec{E} \,, \tag{6.2}$$

where the conductivity is reduced on centerline but off axis its behavior is more complex. Here the conductivity σ is

$$\sigma = \frac{ne^2}{mv_m} \ , \tag{6.3}$$

in simple form. Here *e* and *m* are elementary charge and mass constants. Note locally it's the ratio of the density *n* to the collision frequency v_m that determines the magnitude of the conductivity. Off axis, density is reduced but the collision frequency can be expected to be significantly reduced off axis as well. In this respect, the local electrical conductivity can actually be higher off axis and thus collection can be favored in this case off axis. The complex patterns may then simply be related to discharge self-optimization where the current collects along the path of least resistance. Tendrils protrusions offer low resistance paths to collection and thus may actually be favored. Such processes are likely even more exaggerated at near threshold discharge conditions such as at low current. This possible basis for self-organization is testable if one is able to spatially map out the attachment rate and local electron density.

The importance of water vapor of the influence of water vapor on inelastic energy losses, transport and attachment in relation to pattern formation is suggested also in the shape of the plasma column. As can be seen in Fig. 6.7, the discharge column at lower currents bends away

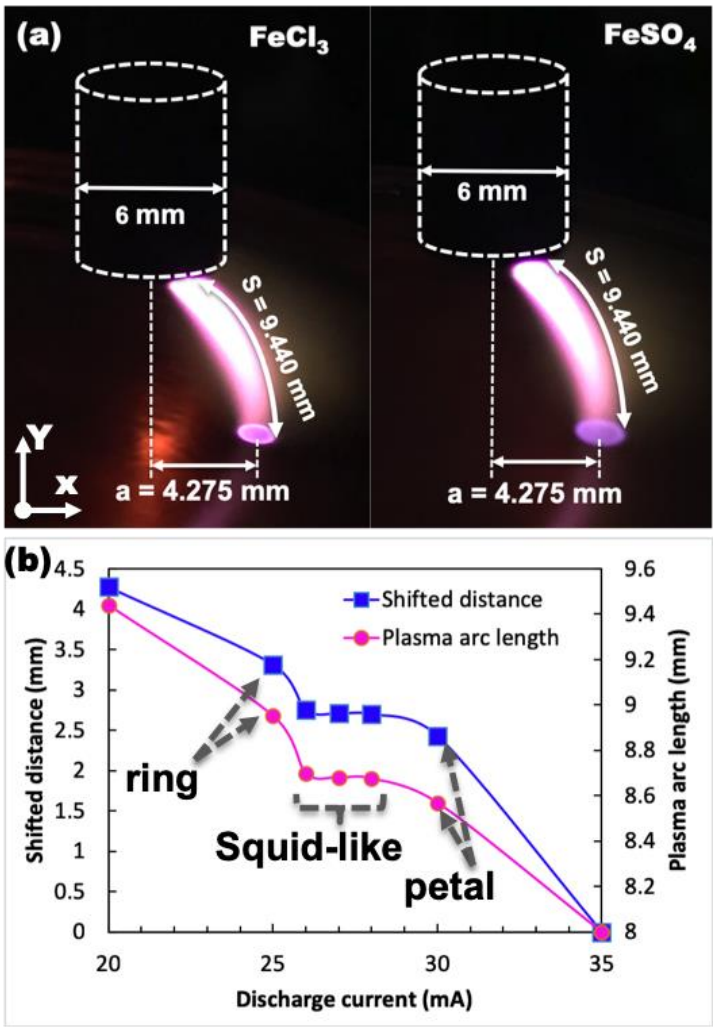

Figure 6.7: Estimation due to the plasma curvature observation is illustrated in (a) plasma measuring configuration with consistency for $FeCl_3$ and $FeSO_4$ anode solution at 20 mA, (b) the reduction of shifted distance (left axis) from the plasma attachment to centerline and arc length (right axis) of the curved plasma column along with the current increments in low current region for $FeCl_3$ solution, which refers to figure 6.6.

from the axis as can be seen by the increases in radial distance "a" at the attachment point on the surface of the liquid. The hot gas derived from the cathode flows axially to the surface and is not expected to change appreciable since the flow rate is fixed. So this hot gas impinges on the surface giving rise to localized evaporation — virtually a water vapor fountain. The arcing of the discharge column away from centerline can be thought of a more or less a macroscopic response to increased collisionality and losses on axis. Again, the ratio of plasma density to collisionality

determines the local conductivity. The arc may be a manifestation of charge taking the least resistance path to the anode — in a manner similar to what was suggested for the patterns. Along this path, the water vapor density is reduced and radially scattered electrons traverse this simpler path. For all the solution cases, in the low current regime, it was observed that corresponding plasma columns exhibited curvature sensitivity to current adjustments. This can be seen from figure 6.6 with visible variation, the curvature of the plasma column reduces while the current increases. The column achieves the zero-curvature at 35 mA, that is, the plasma column is nearly vertical (parallel with anode surface normal). For all of the solutions at 20 mA, the pattern attachment shifted to around 4 mm. As a typical example, Fig. 6.7 (a) illustrated the consistent measurements from $FeCl_3$ and $FeSO_4$ solution at 20 mA. The arc length can also be estimated. If one assumes the curved plasma column is geometrically parabolic with its known vertex of (0, 8 mm) located at centerline, its function then can be written as

$$f(x) = 8 - \frac{8}{a^2}x^2, \tag{6.4}$$

where *a* indicates the shifted distance of plasma attachment. Thus, the arc length of the curved plasma column, *s*, can be estimated in Cartesian by the expression of

$$s = \int_0^a \sqrt{1 + \left(\frac{d}{dx}(f(x))^2\right.}\, dx, \tag{6.5}$$

which gave a result of 9.440 mm for both cases. By applying the same method, the plasma attachment shifted distances and arc length of the curved plasma column from 20 to 35 mA for the $FeCl_3$ solution can be calculated as shown in Fig. 6.7(b). The attachment is curved rather than linear shaped owing to bouncy and convection effects.

All in all, at similar operating conditions, the pattern formation on different electrolytes displayed varying degrees of complexity with more complex shapes appearing in the unstable lower current regime. This observation is somewhat consistent with previous studies in the same

current range condition even though the electrolytes were different. For example, in Verreycken's study [10], complex patterns such as a three-blade boomerang, rosette-like structures, and concentric circles were observed in low current range between 9 and 30 mA with fixed inter-electrode distance at 5 mm. According to the observations from Shirai [1], a complex pattern was observed by feeding an external O_2 gas at 30 mA with fixed gap length at 7 mm. Also, the pattern became more varied with a random shape changing movement if an O_2 sheath flow is used suggesting the possible role of negative ions.

6.6 Evolution of Solution Chemistry

The interaction of plasma with liquid water activates the solution changing its chemical properties in a variety of ways such as altering the pH and electrical conductivity. The change in species concentrations as well as nanoparticle formation can all occur in solution. In this work, conductivity, pH, nitrate and nitrite ion concentration changes were monitored. These changes are displayed in Fig. 6.8. All measurements were taken at room temperature. The initial conductivities and pH of each electrolyte was spatially uniform in each test jar, which was measured before the plasma exposure. After 20 minutes of plasma exposure (discharge current from 20 to 90 mA, voltage at range of 0 to 3 kV for total and 0 to 1.5 kV for the plasma gap), the chemical properties of solution became stratified; that is, chemical properties were spatially non-uniform in the axial direction in the test beaker due to the direct plasma-liquid interaction on the surface of liquid. While it is known that circulation takes place induced by the plasma attachment, at least in this case, the induced circulation effects apparently do not extend to the bottom half of the solution. And as such, the chemical property measurements after each experiment were taken from two space regions: top half (half beaker region from the liquid

surface) and bottom half (from half region down to the bottom of the beaker). Figure 6.8 (a) indicates that the average electrical conductivity near the surface of liquids increased by 25%

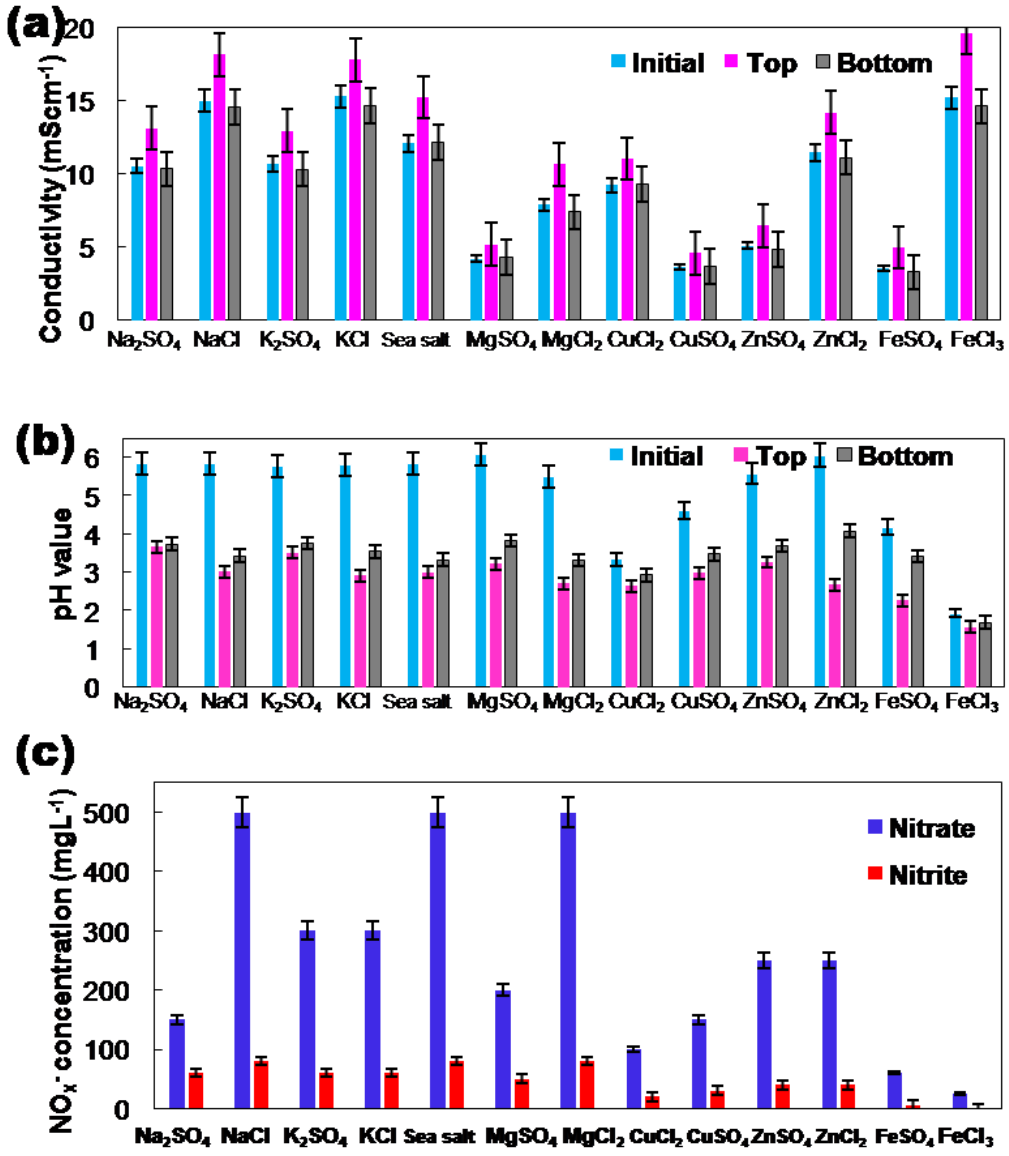

Figure 6.8: Chemical property comparisons of each solution are shown in (a) Conductivity, (b) pH, (c) Nitrate NO_3^- and Nitrite NO_2^- ions concentration after the plasma exposure. The initial results indicate the measurements from the original solution before the plasma exposure. Top and bottom results are the values measured after the plasma exposure at regions of top and bottom solution. The error bar is estimated using the standard error from three tests.

after total 20 minutes plasma-liquid exposure. On the other hand, the conductivities in the bottom half either remained unchanged or slightly decreased. According to Bruggeman's [11], the

conductivity of the liquid cathode was also increased significantly with 20 minutes plasma exposure. The increase in conductivity in the topmost portion is likely due to both the introduction and production of ions in this region via plasma driven chemistry (e.g. electron solvation, ionization, direct negative ion injection, disassociation, dissociative attachment, etc.). It is interesting to note that the solutions $FeCl_3$ and $CuSO_4$ with both the highest and lowest conductivities respectively were associated with the most complex patterns. Recall from the section 6.4.2, these two electrolytes listed as highest and lowest value on both molar concentration and ionic strength as well.

The influences of electrolyte solution pH on patterns have been studied in an atmospheric pressure AC glow discharge [12]. It was shown in that work that the pattern sizes were influenced increasingly when the liquid changes from lower pH acid to neutral. PH controls disassociation kinetics of ions and thus can directly affect current flow. Spatial variations in this kinetics may therefore play a role in the evolution of pattern shape in order to maintain a fixed current. In this work, as can be seen in Figure 8b, the pH varied spatially. The region of solution closest to the plasma contact boundary (41% reduction in average) had a significantly lower pH relative to the bottom half (average of 31% reduction). This finding suggesting that the inducted reactivity is local and dominated by diffusion at least in the far field-as there is a great deal of evidence to suggest that transform in the near field is driven by plasma driven convection and circulation processes — such as Marangoni flow. Acidification of liquid (water) via plasma exposure has been well studied for atmospheric pressure plasmas [11, 12-16]. In this work, the general conclusion is that over time the pH of the solution changes, essentially dropping—mostly likely due to the introduction NO_x (x stands for 2 and 3) species into the water. Patterns however were present at the baseline pH and did not vary is shape appreciably with time and

thus pH variation. That said, at least the plasma induced pH does not play a major role in shape evolution. The primary reason why this result may differ from those studies with a set pH in that the overall solution conductivity is not fully transformed owing to stratification. In this case, the reservoir of unchanged solution is significant and thus transport effects locally can be compensated at the return electrode by relatively pristine solution.

At elevated gas phase discharge conditions, NO_x species are produced. These species are up taken into solution and become solvated [17]. Nitrate (NO_3^-) and Nitrite (NO_2^-) concentration in solution were measured, as shown in figure 6.8 (c). These ions drive solution acidification which can be shown in reactions:

$$HNO_2 \leftrightarrow H^+ + NO_2^-, \tag{6.6}$$

$$3HNO_2 \leftrightarrow H_3O^+ + NO_3^- + 2NO. \tag{6.7}$$

The concentration of these species before plasma treatment was below the detection limit. After helium plasma exposure, it is noted that NaCl, sea salt, and $MgCl_2$ aqueous solution have largest NO_x^- uptake, suggesting electrolyte dependence. It should be pointed out that increased NO_x uptake has been observed in the presence of chlorite ions. In general, NO is not very soluble in water. The oxidation of NO via chlorite ions leads the formation of NO_2 and eventually NO_3 which are highly soluble in water. This leads to increased uptake of NO_x species from the gas phase. Reactions at the gas liquid interface include:

$$ClO_2 + NO \rightarrow NO_2 + ClO, \tag{6.8}$$

$$ClO_2 + NO_2^- \rightarrow NO_3^- + ClO. \tag{6.9}$$

This mechanism has been investigated as a means to remove the greenhouse gas NO_x products from exhaust flues [18]. Chlorite ions can form through plasma interacting with liquid water leading to the direct reaction of O with Cl^- ion derived from the salts [19]. It is this

mechanism that may be at play in the increased NOx concentrations in the chloride based salts. The concentration of nitrate for all species was higher than nitrite suggesting the oxidative power of the solution [20].This observed difference matches with the experimental results from Lukes and coworkers [21]: higher NO_3^- production than NO_2^- only happens under acidic conditions; otherwise, the nitrite production will higher than nitrate. The simulation result reported by Bruggeman and coworkers were also confirmed that the long-lived stable species NO_3^- had 100 magnitudes higher concentration than short-lived NO_2^- species in aqueous solution [22]. In addition, from the figure, it is also seen that alkali (earth) positive ions (Na^+, K^+, and Mg^{2+}) tend to have larger nitrate concentrations than those solutions with transition metal (Cu, Zn, and Fe) ions. This particular result agreed with some of the studies which have been proven that such transition metals can act as scavengers for the reduction of nitrate and nitrite [23-25]. Specially, for instance, zinc powder is often used as a nitrate reagent to reduce nitrate into nitrite [26].

6.7 Pattern Association with Species Emission

6.7.1 Spectra in Behavior of Current

The UV-optical emission spectra between 200 and 800 nm were recorded in a discharge current range of 25 to 80 mA for all of the aqueous solutions. All of the spectra were taken 1.5 mm above the liquid interface. At each fixed current, spectra had the same overall characteristics for all of 13 electrolytes. As a typical example, Fig. 6.9 shows emission spectra recorded under different discharge current conditions for KCl and K_2SO_4 solutions. The emission in the gas phase for the K_2SO_4 solution was significantly more intense than that observed with the KCl solution. This difference may be due to the different in discharge power (figure 6.2) and the presence of Cl negative ions in the gas phase for the KCl solution. The emission spectra are

dominated by the second positive system of nitrogen (N_2 (C-B)), OH (A-X) band at 309 nm, and NO (A-X) band below 273 nm [11, 27].

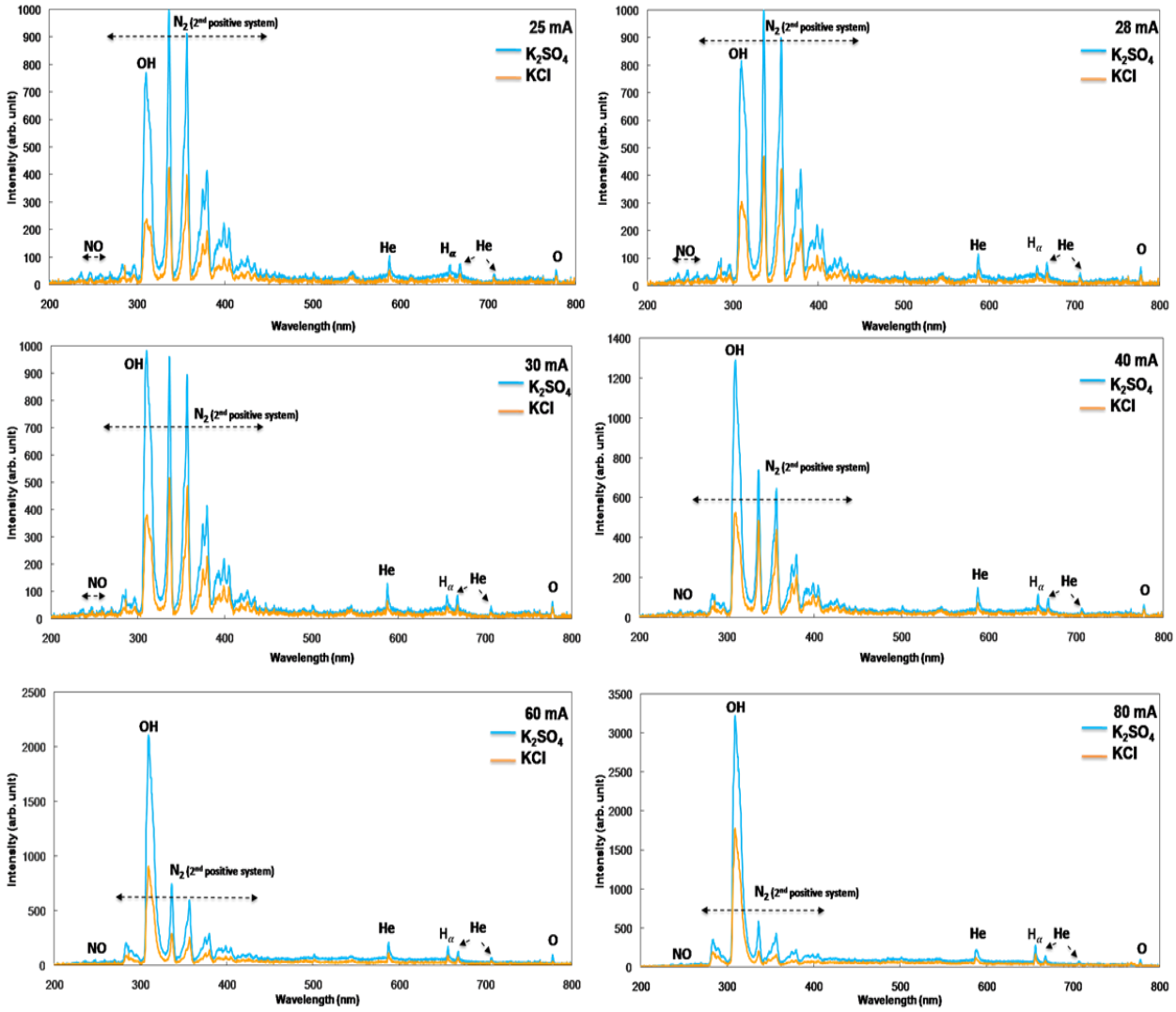

Figure 6.9: Optical emission spectrum from anode K2SO4 and KCl solution at different discharge current.

The OH emission is typically observed with intense emission at 309 nm [11, 27]. Above 500 nm, excited atomic helium at 587.5 nm, 668.5nm, and 706.5nm, atomic hydrogen (α) line at 656 nm and Oxygen triplet at 777 nm are also observed [28, 29]. According to Tian and Kushner's [16], O_2^+ species is a dominant positive ion in the gas gap just above the water due to its low ionization potential. Dissociative recombination reactions $O_2^+ + e^- \rightarrow O + O$ could be responsible

for O formation. It's worth noting that OH associated with water transport into the gas phase dominates emission at higher discharge currents.

As can be seen from the spectra, with increasing discharge current — from 30 to 80 mA, nitrogen emission tended to decrease while the OH emission increased in intensity. A transition from a nitrogen dominated discharge to one dominated by water vapor is suggested. This transition actually reflects the pattern structure change from a single dot attachment (without pattern stage) to a spoke-liked structure (stable pattern stage). A water vapor dominated discharge seems to favor pattern formation — suggesting the role of evaporation and associated water vapor driven gas phase processes. Here the OH is derived from the reaction: $e + H_2O \rightarrow H^- + OH$. A detailed spatial analysis of the plasma column was investigated in the last chapter.

6.7.2 Species Emission

Figure 6.10 further illustrates this point by plotting the OH and N_2 intensity distribution and their intensity ratio. Particularly, this N_2 emission is obtained by the highest intensity band of the second positive system of nitrogen, which is the (0-0) transition at 336 nm. The species production from the $CuSO_4$ and $FeCl_3$ solution that demonstrates the uniqueness in pattern formation and solution chemistry are also considered here. Except for K_2SO_4 case, under 30 mA, the emission of N_2 band increases with current as the power delivered to the plasma rises. From 30 mA, although the plasma becomes more energetic, the emission of N_2 band decreases with current. This is because the amount of vapor in the discharge rises while the proportion of N_2 decreases. The emission of the OH band has an increasing trend with current. Until 30 mA, this increase is most likely related with an increasing power in the plasma. From that point, evaporation seems to become important leading factor to more OH species in the discharge

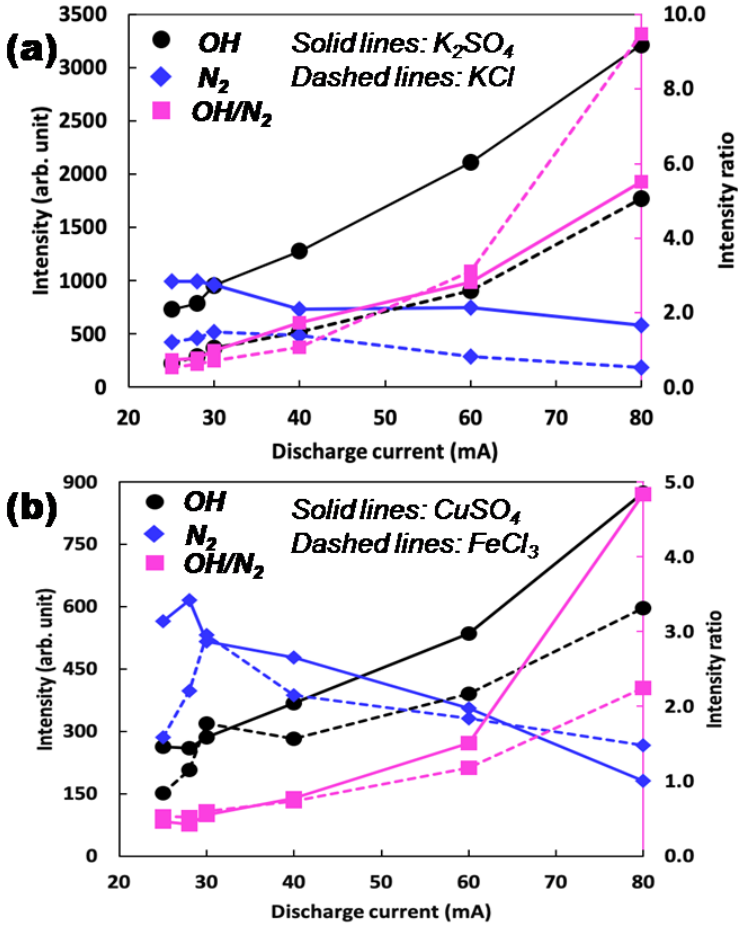

Figure 6.10: The intensity distribution (left axis) and intensity ratio (right axis) of OH (309 nm) and N_2 (336 nm) is shown as a function of discharge current from (a) K_2SO_4 and KCl anodes, (b) $CuSO_4$ and $FeCl_3$ anodes. In this figure, the solid lines represent data for the solution in SO_4^{2-} group, dashed lines for Cl^- based solutions.

favoring OH band emission. In this way, air (and so nitrogen) in the discharge is progressively replaced by water vapor, which also can be demonstrated from the intensity ratios between OH and N_2. This observation is consistent with their difference in excitation energy as well, since the excitation of N_2(C) has an energy threshold of 11.5 eV, and the required energy of OH (A) excitation is about 4 eV.

In addition, the examination of other species such as NO (A-X) band with highest line at 247 nm, O I line at 777 nm , excited atomic helium line at 587.5 nm, and hydrogen Balmer in

alpha line were also carried out from the above four solutions. As shown in figure 11, although the K_2SO_4 solution results the most intense emission, the helium and hydrogen excitation are

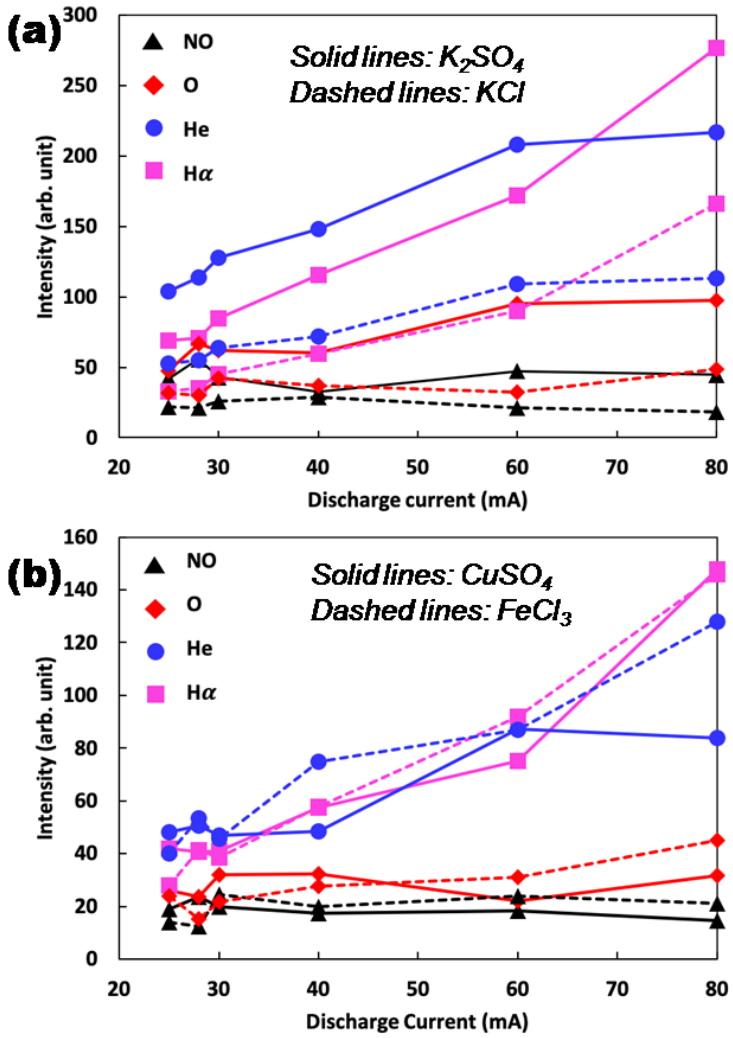

Figure 6.11: The intensity distribution of excited species such as NO (247 nm) , O I (777 nm), NO (247 nm) He (587.5 nm), and H_α (656 nm) in response to the increasing discharge current from (a) K_2SO_4 and KCl anodes, (b) $CuSO_4$ and $FeCl_3$ anode solutions.

both increased with current for all of the solutions. This is most likely due to the power increasing in the discharge with the current. When the current passed 60 mA and went to the high current region, the hydrogen excitation dominated. These excited species seem to be controlling the excitation of oxygen and NO especially when the current passed 30 mA and plasma becomes more energetic. Less than 30 mA, these species excitation shows either an

inverse or more perturbed behavior in Fig. 6.11 (b) other than it in Fig. 6.11 (a). This observation is somewhat interesting in reflection of the unusual complex pattern formation that existed in the same unstable low current region.

6.8 Conclusion

In this work, the influence of electrolyte type on pattern evolution with increasing discharge current was experimentally investigated. Different current regions are defined in response to the pattern variation. The sizes of the pattern structures and their morphologies were observed to be consistent at each region. It was found that the IV characteristic had a distorted U shape where the appearance of the pattern coincides with the local minimum in voltage. At low currents around this local minimum, complex, unstable patterns were observed. The chemical properties of electrolytes have been measured and evaluated to the pattern behavior. Based on the observations here, the pattern evolution did not depend appreciably on ionic strength. Other key observations include:

(1). Ferric chloride solution displayed the most unusual complex pattern evolution. Because plasma induced precipitation occurred concurrently with pattern formation, it is possible that the precipitate layer may have played a role ultimately in determining the morphology of the pattern. In this regard, the interplay between plasma induced chemistry and its associated complexities as related to pattern formation are highlighted.

(2). from the optical emission spectroscopy, it was observed that the pattern formation undergoes a transition with increasing discharge current from nitrogen dominated emission to OH dominated emission. This observation suggests that local evaporation processes may play a key role in self-organization.

(3). at the low unstable current region, small current perturbation can lead to the pattern complexity. The morphology of these complex patterns observed variously that might depend on the type of the electrolytes. The perturbation demonstrated by the excited species from different solutions under this region suggests that the pattern complexity could also be driven by the plasma liquid chemistry.

6.9 References

[1]. N. Shirai, S. Uchida, and F. Tochikubo, Plasma Sources Sci. Technol., 23, 054010, (2014).

[2]. M. A. Lieberman, and A. J. Lichtenberg. Principles of Plasma Discharge and Materials Processing. 2nd ed., Hoboken, New Jersey, John Wiley & Sons, Inc., pp. 535-39 (2005).

[3]. N. Shirai, S. Ibuka, and S. Ishii, Applied Physics Express, 2, 036001 (2009).

[4]. P. Bruggeman, et al, J.Phys. D.: Appl. Phys., 41, 215201 (2008).

[5]. P. H. Barry, and J. W. Lynch, J. Membrane Biol. 121: 101-117 (1991).

[6]. J. A. Dean, Lange's Handbook of Chemistry, 15th Edition, McGraw-Hill, New York, (1999).

[7]. P. Vanysek, Ionic conductivity and diffusion at infinite dilution. In: CRC Handbook of Chemistry and Physics (83rd Edn; ed. D.R. Lide), CRC Press, Boca Raton, (2002)

[8]. J. E. Foster, Phys. Plasmas 24, 055501 (2017).

[9]. X. Ma, J. Lowensohn, and J. C. Burton, Phys. Rev. E., 99, 012802 (2019).

[10]. T. Verreycken, P. Bruggeman, and C. Leys, J. Applied Physics, 105, 083312 (2009).

[11]. P. Bruggeman, E. Ribel, A. Maslani, J. Degroote, A. Malesevic, R. Rego, J. Virerebdeels, and C. Leys, Plasma Sources Sci. Technol.,17,025012 (2008).

[12]. P. Zheng, X. Wang, J. Wang, B. Yu, H. Liu, B. Zhang and R. Yang, Plasma Sources Sci. Technol. 24 015010 (2015).

[13]. D. Moussa, F. Abdelmalek, B. Benstaali, A. Addou, E. Hnatiuc, J. I. Brisset, EPJ Appl. Phys. 19, 189 (2005).

[14]. S. Ikawa, K. Kitano, and S. Hamaguchi, Plasma Process. Polym. 7, 33 (2010)

[15]. K. Oehmigen, M. Hahnel, R. Brandenburg, Ch. Wilke, K. D. Weltmann, and Th. von Woedtke, Plasma Process. Polym., 7, 250 (2010).

[16]. W. Tian, and M. Kushner, J. Phys. D: Appl. Phys. 47, 165201 (2014).

[17]. K. Takahashi, K. Satoh, H. Itoh, H. Kawaguchi, I. Timoshkin, M. Given, and S. MacGregor, Japanese Journal of Applied Physics 55, 07LF01, (2016).

[18]. A. Pourmohammadbagher, et al, Ind. Eng. Chem. Res., 0, 14, 9278 (2011).

[19]. V. Jirasek, and P. Lukes, PSST, 38, 035015 (2019).

[20]. J. Chauvin, F. Judee, M. Yousfi, P. Vicendo, and N. Merbahi, Scientific Reports 7, 4562, (2017).

[21]. P. Lukes, E. Dolezalova, I. Sisrova, and M. Clupek, Plasma Sources Sci. Technol. 23, 015019 (2014).

[22]. C. A. J. Van Gils, S. Hofmann, B. Boekema, R. Brandenburg, and P. J. Bruggeman, Phys. D: Appl. Phys. 46, 175203 (2013).

[23]. S. E. Bae, K. L. Stewart, and A. A. Gewirth, J. AM. CHEM. SOC. 129 33 (2007).

[24]. M. J. Alowitz, and M. M. Scherer, Environmental Science & Technology 36, 3, (2002).

[25]. N. Chebotareva, and T. Nyokong, Journal of Applied Electrochemistry 27, 975-981 (1997).

[26]. S. A. Mir, Asian J. Chem., 19, 5703-5710 (2007).

[27]. R. W. B. Pearse, and A. G. Gaydon, The Identification of Molecular Spectra. 2ed., New York, John Wiley & Sons Inc. (1950).

[28]. NIST Atomic Spectra Database, (2017).

[29]. Q. Xiong, A. Y. Nikiforov, M. A.Gonzalez, C. Leys, and X. P. Lu, Plasma Sources Sci. Technol. 22, 015011, (2013).

CHAPTER VII

Development from Liquid: Particle Emission

This chapter reports the unexpected observation of droplet emission from a $FeCl_3$ solution during the self-organization pattern study. While such emission may be indeed being present in other salts, it was most pronounced (observable) in this electrolyte. Here the trajectories of the particles are discussed along with possible mechanisms for emission. The composition of the particles within the droplets is also examined.

7.1 Introduction

The emission of droplets from DC glows with liquid electrodes has been reported by Shirai and colleagues [1]. In this case, the liquid served as the cathode. In that work, the observation of Taylor cones at the surface is believed to be the origin of the particles. On the other hand, with a liquid anode, the conventional wisdom based on indirect measurements suggests that the field at the anode surface is weak. Based on these observations, one would conclude that the field conditions are not amenable to deformation of the surface. This however is an apparent contradiction as the anode pattern is indeed an anode spot supported by localized ionization and thus the field near the surface has to at least the ionization potential over the characteristic length scale of the plasma — in this case approximately 1 mm which suggests at least 250 V/cm if once considers helium. As attachment is present as well the local field is likely

considerably higher than this. It is known that particles form in some salt solutions in DC glows with liquid electrodes. Such particles are nanoscale and thus can greatly distort the electric field and thus give rise to the formation of Taylor cones in the case of a liquid anode as well. Particle emission from these plasmas with liquid anode has not been reported to date. On the other hand, emission from liquid cathode has been observed and has been attributed to Taylor cone formation. The instability at the Taylor cone tip leads to charged droplet formations which are subsequently accelerated. The emission mechanisms reported herein the case of a liquid anode is likely also a Taylor cone process. The observation is significant for two reasons 1) the emission gives insight into the electric field present at the surface that supports the anode spot formation at the surface and 2) the emission droplets apparently contain nanoparticles. In this respect, the mere observation provides a great deal of insight into the maintenance of plasma attachment at the anode and perhaps self-organization itself.

In the last chapter, it was found that the pattern structures are affected by the chemical composition and associated chemical properties of the electrolyte salts such as ionic strength and activity. In the course of assessing self-organization behavior sensitivity to electrolyte type, particle emission was observed. So far this emission has been observed in clearly only with the $FeCl_3$ electrolyte. Because the particle or droplet emission occurred during self-organization, a possible relationship may exist. Again, this relationship would be consistent since both localized anode spot formation and Taylor cone emission require locally high electric fields at the surface.

In this chapter, we report on the observation of particle emission during a plasma liquid interaction under atmospheric pressure. To the author's knowledge, such particle emission from a liquid anode surface under atmospheric DC glow plasma conditions has not been previously reported. The investigation carried out here focuses on characterizing particle emission process

and the identification of the emitting particles. This study addresses a number of questions: 1) where is the location of the particle ejection relative to the self-organization pattern? 2) What is the emission velocity of the particles? 3) Why do the particles emit light? 4) What is the composition of the particles emitted? By understanding the emission phenomena, the particles themselves can be used as probes for understanding the bulk plasma column as well [2].

7.2 Experiments

The general experimental setup is shown schematically in Fig 7.1 (a). Here, the

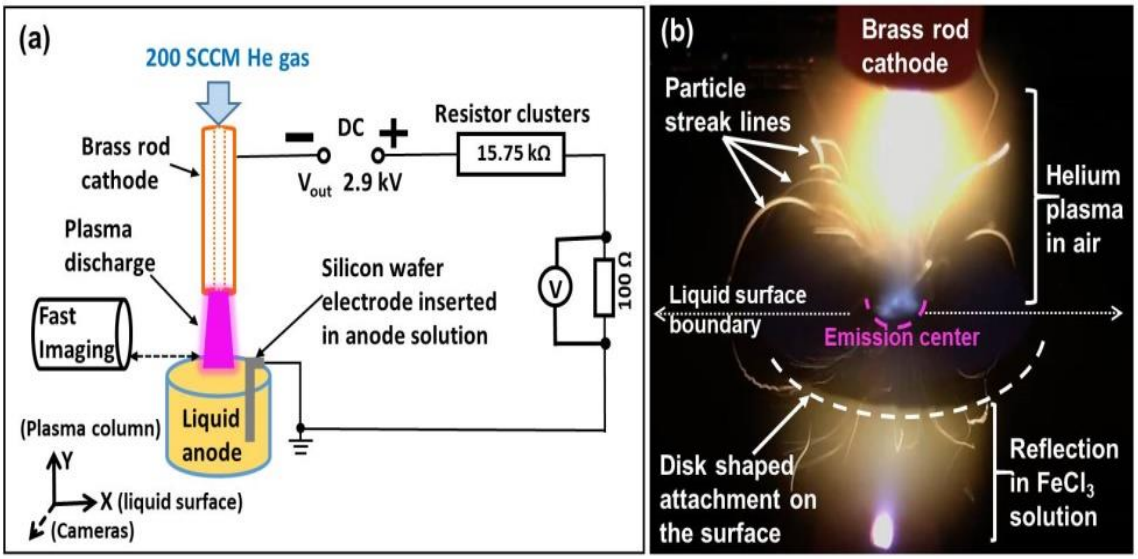

Figure 7.1: Schematic of experimental apparatus in (a) and a snapshot photograph of particle emission in (b) during discharge operation. Note that this sketch is not to scale.

additional experimental conditions are explained . Further details regarding the apparatus may be found in Chapter 3. A 125 mL $FeCl_3$ solution with initial conductivity of 15 mS/cm served as an anode. The physical silicon return electrode was immersed in this solution to facilitate the coupling to the power supply. During the experiments, the gap spacing between the cathode and anode was fixed to 8 mm. A 15.75 kΩ and a 100 Ω resistor were connected in series for the purpose of ballasting to prevent the glow to arc transition and expedite current measurement

respectively. A single high speed imaging camera (Photron Mini UX, or Phantom) was oriented perpendicular to the plasma-liquid (Y-X) plane in order to capture the particle emission events. Due to the difficulty of particle tracking in response to their size and emitting speeds, two cameras with different resolutions were tested separately for the purpose of capturing the particles at different emitting speeds. This also allows one to obtain the emission speed range of these emitting particles. Here, one camera with maximum speed of 2000 fps, was more favorable for tracking the particles with slower emitting speed. The second camera had an acquisition speed of 27k fps. At 100 mA discharge current (1.1 kV discharge voltage calculated using equation 3.1), visible, luminous particle emission from the liquid anode in the vicinity of the self-organized pattern was observed as shown in Fig. 7.1 (b) that acquired at 30 fps. As can be seen in this figure, at this frame rate, the emitted particles appear as glowing streaks.

7.3 Particle Trajectory

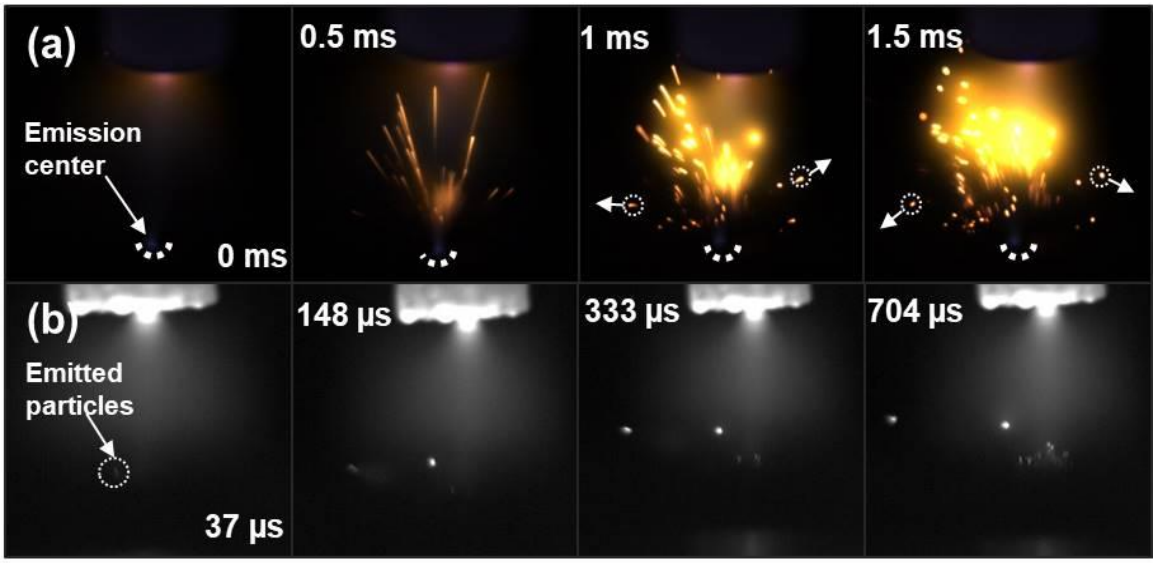

Figure 7.2: Time resolved particle emission using two high-speed imaging cameras at different exposure rates of (a) 2000 fps and (b) 27000 fps.

Through repeated experiments, it was observed that such emission events occur continuously and randomly. In order to confirm the origin of these emitted particles and resolve their emission speed, two high speed imaging cameras were used to map the particle trajectories in plasma liquid planes. Fig. 7.2 illustrates typical particle emission with different frame rates. As can be seen in Fig. 7.2 (a), at the exposure rate of 2000 fps, the particles emitted from the emission center located on the liquid anode with their appearance as luminous streaks at 0.5 ms due to their energetic launching. Note that some of the streak shows that the particle nearly crosses the 8 mm in 0.5 ms, suggesting that the vertical component of the initial velocity of these emitting particles can be as fast as 16 ms^{-1}. After 1 ms, some downward directed particles are apparent at 1.5 ms. Interaction of particles with background plasma column is observable at later times can be seen from the additional excitation apparent as particles reach the core of the discharge as inferred from the over exposed glow. By increasing the frame rate even faster particles could be observed. When imaged at 27k fps as depicted in Fig. 7.2 (b), the particles quickly leave the field of view in 37 μs.

By tracking a single particle that emitted from the plasma-liquid plane from each single emission process, 2D particle trajectories of each tracked particles were mapped out spatial - temporally as shown in Fig. 7.3 (a) and (b) for both exposure cases. Although their trajectories are consisting with overall tendency, there is an incoherent movement that existed during the launching at lower exposure rate of 2k fps. This difference might be due to the tracking speed resolution of the camera in response to the size of the particles. It also can be seen from the figure that the displacement of the particles emitted in plasma-liquid plane in function form of $y = f(x, t)$, where y and x are directed parallel with the plasma column and liquid surface direction at time t respectively.

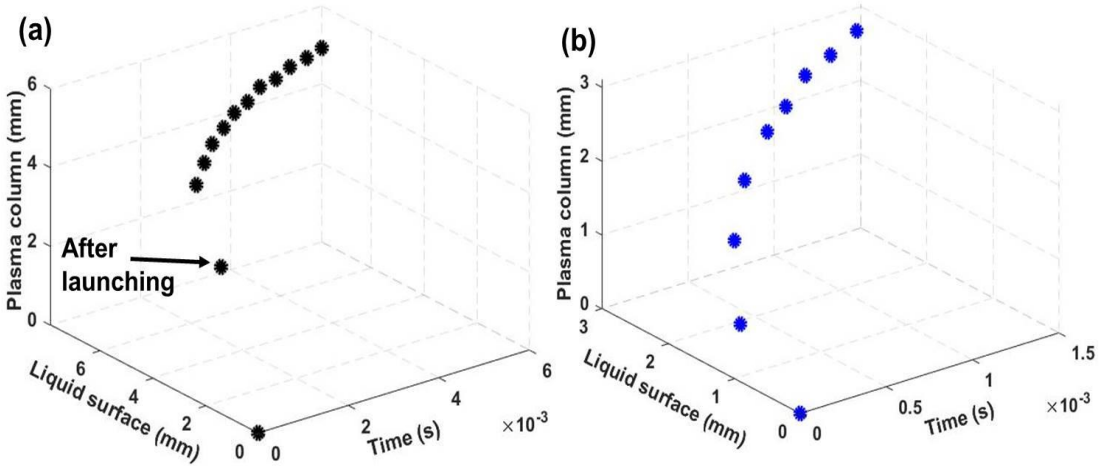

Figure 7.3: Experimentally recorded particle trajectories with their displacement curve fitting from a typical particle emission that recorded at (a) 2000 fps and (b) 27000 fps with their estimated velocities. Note that this measurement was done in plasma-liquid plane (Y-X) only.

It should be noted here that we obtain information only in one plane. Motion within an orthogonal plane is not tracked owing to the limitation of the tracking setup. In this respect, the estimates given here represent a lower limit of the particles velocity. $\mathbf{V_0}$ (V_{0x} V_{0y}) Based on this reasoning, one can estimate this lower limit, the initial injection velocity was estimated to be 7.9 ms^{-1} and 33.2 ms^{-1} with their corresponding incident angle of 55.4 degree and 35.7 degree at 2k fps and 27k fps respectively. Estimated particle's flying velocity $\mathbf{V}$ (V_x, V_y) during the entire visible tracking time can be seen in Fig. 7.4. Both cases show that the emitting speed of the

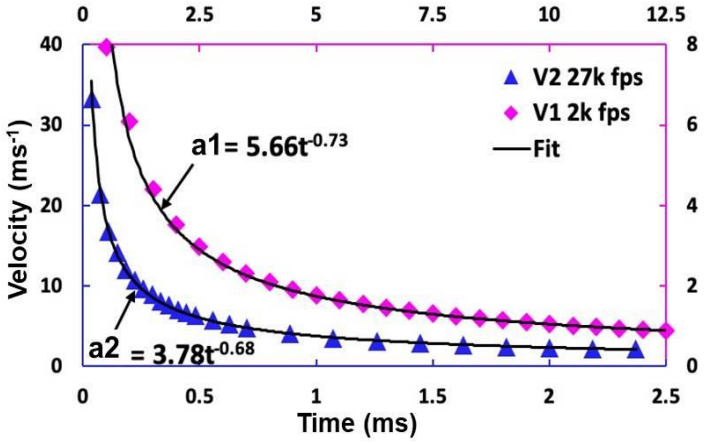

Figure 7.4: Velocity decaying curve indicates the negative acceleration of the particles.

particle decays with time increment. The fit function represented that the experimental slowing down process of each particle is well followed a power law during their emitting trajectory. That proves that particles were slowing down with their acceleration reduction. Approximately 4 times faster emission is observed at 27k fps than the emission observed at 2k fps suggests that the particle sizes might play a role during its flight.

7.4 Particle Collection

In order to collect and study emitted particles, a normal impact system is designed for the particle collection as can be schematically seen in Fig. 7.5 (a). In this setup, a silicon wafer

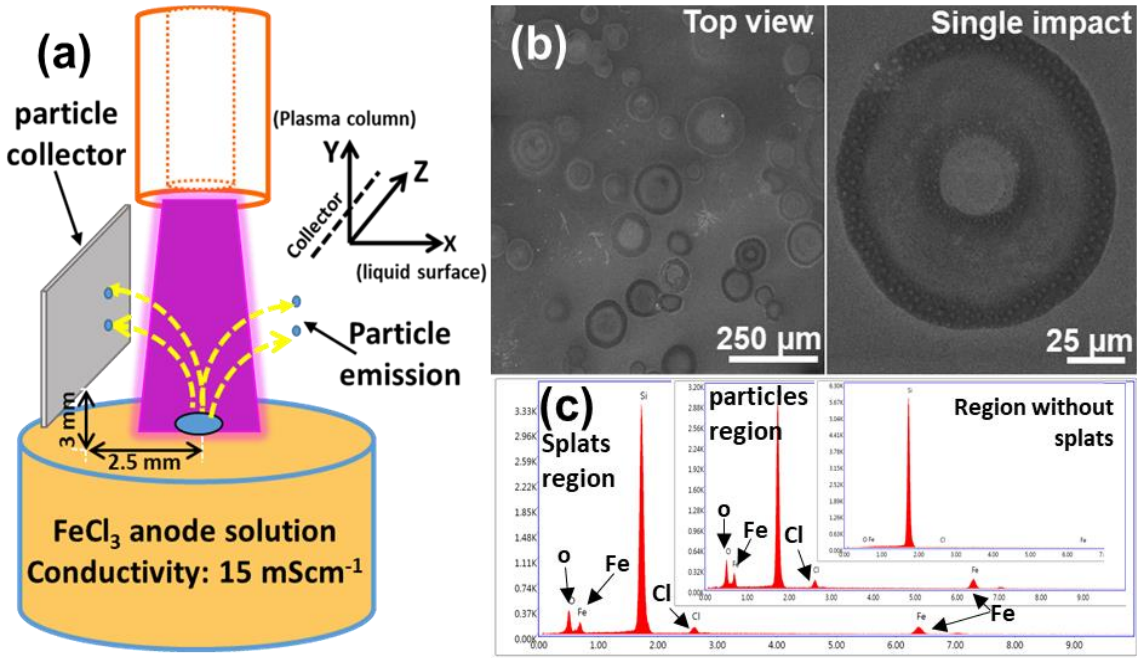

Figure 7.5: Schematic of particle collection design is shown in (a), SEM images of the resulting splats after the collection in (b), and (c) the composition spectrum detected using EDX from various regions.

served as a witness plate to intercept the particles. Collected particles appeared as splats on the collector. Splat [3-6] formation is commonly observed in plasma sprayer studies where a molten metal particle impact to a solid plate. In the case of this experiment, emitted particles were luminous. It is hypothesized that the glow is due to rapid oxidation of the emitted particles in the plasma column which presumably leads to melting. If this is the case, then the emitted particles

are molten iron based droplets, and thus splats should result upon impact with the collection plate. Previous studies have shown that the shape of the splats formed after impact depends on conditions such as droplet speed, size, and angle [7-9]. To ensure the particles emitted from the plasma-liquid plane are normal impacted (impact angle of 90 degree) to the collector surface, the silicon wafer was oriented normal to the emission plane at a distance of 2.5 mm away from the plasma column and 3 mm above the liquid surface. This fixed placement setting secured impact speed by collecting the right particles (normal impact and aligned in emission plane) at the time after they horizontally traveled exact for 2.5 mm (x) from the emission center. This time is the impact time (t_{impact}) when the particle impacts he collector. Knowing this impact time, the distance travelled on plasma column direction (y) can be found. With both components($V_x = \frac{x}{t_{impact}}, V_y = \frac{y}{t_{impact}}$), the magnitude of the impact velocity is obtained, which was found to be 7.5 ms^{-1} at 2k fps and 2.85 ms^{-1} at 27k fps for those tracked two particles.

The collected the particles were examined using a scanning electron microscopy (SEM) with the resulting splats shown in Fig 7.4 (b). As can be seen in the figure, the morphology of the splats show as a result due to the droplet normal impacted to a solid surface, which suggests that these emitted particles were indeed liquid before impact. The size of collected splats is ranged between 40 μm and 200 μm. It was observed that there were a number of individual solid particles uniformly distributed at the boundary edge region of a single impacted splat as can be seen in the figure, which further provides an insight that the emitting particles were molten. The sizes of these solid particles ranged between 1 μm to 2.5 μm.

Energy dispersive X-ray spectroscopy (EDX) was applied to examine the particle compositions. As depicted in figure 4(c), it is consistent that Fe (22%), O (18%), and less portion of Cl (nearly 3%) were detected from both the splats and solid particle regions. Note that the

detected background Si was not under the consideration here. At the region without any resulting spats, no anode solution based elements were found. Indeed, it confirms that the particles emitted were from the $FeCl_3$ solution. Three scenarios are possible to explain the molten particles. 1) The particles originate in a molten state due to the formation and heating at the self-organization plasma at the interface. 2) Particles are emitted trapped in a liquid droplet which evaporates as is moves through the positive column, ultimately becoming molten through heat exchange with the hot plasma column - approximately up to 2000 K as inferred from optical emission of plasma [8], or 3) they are emitted as pristine metal particles and are oxidized exothermically in flight. The nonsteady flight of the imaged particles suggests that they emerge as particles trapped in droplets. Indeed, very high speed imaging did in fact reveal the presence of droplets originating from the surface.

In theory, the energy of emitted particles before the impact is the total energy of the kinetic (KE_1) and surface energy (SE_1). After the impact, when the spreading splats radius reached to its maximum, there is no more kinetic energy ($KE_2 = 0$). Instead, the work done in deforming the droplets against viscosity exists (W). Therefore, the total energy after impact would be considered as the sum of the surface energy and the energy lost to viscous dissipation. Following this energy conservation:

$$KE_1 + SE_1 = SE_2 + W. \tag{7.1}$$

Several analytical models have been developed in order to predict the maximum diameter of the splats [11-13]. Here assuming the molten particles had spherical geometry before the impact, applying an analytical model developed by Pasandideh-Fard et al, the actual initial diameter of the molten droplet d can be solved from the Equation below [3]:

$$\frac{D}{d} = \frac{1}{2}\left(\frac{Vd}{v}\right)^{1/4}, \tag{7.2}$$

where D is collected splat diameter size resulted from the impact, V is the magnitude of the impact velocity of the particles, and v is the kinematic viscosity of the melting droplets at 6.0×10^{-6} m^2s^{-1}. This value is estimated using the viscosity of iron at melting temperature of 1538 °C [14]. As a result, the estimated particle size distributed in range of 31.85 µm to 115.4 µm and 38.65 µm to 140 µm for two tracked particles by applying the impact speed of 7.5 ms^{-1} and 2.85 ms^{-1} respectively. The result shows that the initial droplet sizes are more dependent on the impact speeds other than its initial emitting speeds.

The origin of the particles that form the splats is another outstanding question. During the course of discharge operation, nanoparticles form in the liquid phase. It is hypothesized that these emitted particles are the origin of the splats. To test this hypothesis, particles from the solution were collected and analyzed. Fig. 7.6 depicts the nanosized iron oxide particles that

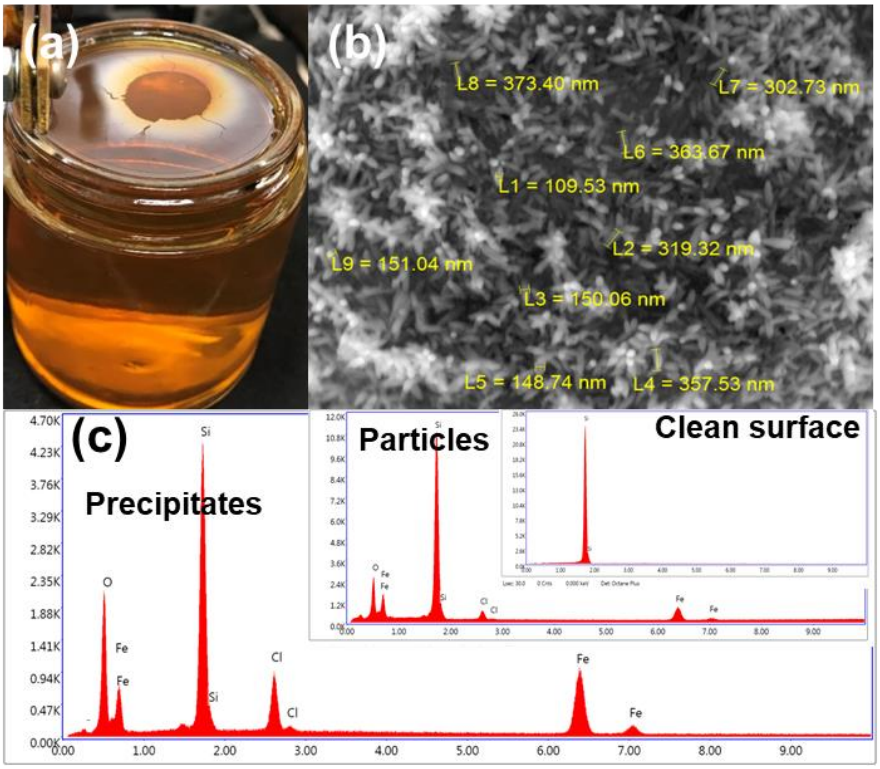

Figure 7.6: Evidence of iron oxide based nanoprecipitates are demonstrated in (a) photograph of the floating solid on the top of the solution surface after plasma exposure, (b) SEM image of nano-scale particles from the precipitates in (a), and (c) detected composition spectrum at different targets using EDX.

form in solution. The particles here have the morphology of rice grains. In Fig. 7.6 (b), it is interesting to note that each individual grains self-assembles as nanomicelles. Without counting the background Si which was from the collector itself, the main composition distributed as 37.4% of Fe, 38% of O, and 6.5% of Cl from precipitates region. The grains include 26.4% of Fe, 25% of O, and 3.6% of Cl. Besides the background Si signal, no main elements were observed from the clean surface of the collector. The compositions identified here are consistent to the composition of emitted particles in Fig 7.5.

In addition, different material based collectors such as stainless steel plates and microscope slides were applied into the inspection in order to eliminate the possibility of Si elements in the particle, as well as eliminating the possible emissions could due to the thermite reaction between the silicon and iron oxide. As predicted, the tested results indicate that there was no Si signal from the collected splat regions under EDX examination in all of the cases.

The mechanism of particle emission is not well understood. According to above observations, what role does plasma liquid interaction at local interface play in the emission of the particles? Presumably the particles are generated via electrolytic processes in the volume of the liquid. It is possible that the localized plasma induced chemistry at the interface during the self-organization process plays a role in not only particle formation but also their subsequent ejection into the gas phase.

Just for testing, based on the composition of the particle and the estimated size of the particle, we can estimate the actual force associated with emission. This crude estimate assumes particles are emitted from surface and does not take into account the possibility that the particles originate in droplets. In this respect, the estimate is a lower bound. This estimate is more

accurate for smaller sized droplets if one assumes the some mean particle sized. Using the force law without considering drag force as

$$F = ma = (\rho V)\frac{dv}{dt}, \tag{7.3}$$

where V is the lower bound volume for the emitted droplet at 1.692×10^{-14} m^3. Assume there is no mass loss in this simplified estimation, we have a mass of a droplet originated from the $FeCl_3$ solution for 1.75×10^{-11} kg, where the density is 4% weight of the solution as 1.033 kg/L (assumed uniform solution). The initial acceleration can be extracted from Fig. 7.4, which is positive at first time step change, 15800 m/s^2. Finally, the initial emission force is roughly estimated to be 0.2765 μN.

7.5 Thermal Gradients

A thermal effect such as localized heating and evaporation is one potential mechanism driving the emission of particles that may be formed in the liquids. This thermal effect may contribute synergistically with the electric field to destabilize the interface. Two sets of thermal measurements have been taken under different diagnostics in this study.

7.5.1 Infrared Imaging

In infrared camera was used to image the discharge area to assess local temperatures. Images took before and after the plasma ignition are shown in Fig. 7.7. As can be seen in Fig. 7.7a, the bulk solution is at room temperature about 20℃. A dark area observed immediately below the cathode but on the surface of the liquid indicated the cooling effect of the helium gas before plasma formation.

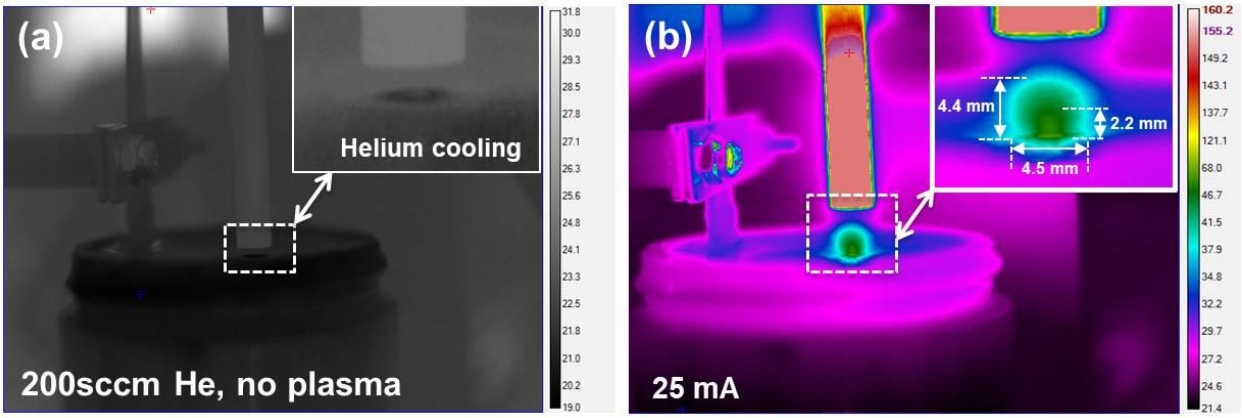

Figure 7.7: Images taken by an infrared camera. (a) Before plasma breakdown and (b) plasma discharge at 25 mA. The temperature unit is in ℃.

Fig. 7.7 (b) depicts a 25 mA plasma discharge under IR view. Here, the cathode is the hottest object in the figure. Interestingly, in the plasma column, the anode glow appeared as a sphere that is located on the liquid anode surface. The temperature of the sphere is not uniform by distributing the lower temperature (around 40℃ or 313.15 K) on its surface and holding its highest temperature (50 – 60℃ or 323.15 – 333.15 K) in the center. Note that this interpretation is qualitative as the nonthermal plasma emission can lead to nonphysical interpretation at the IR sensor. The hemispherical region is likely water vapor derived from localized heating of the liquid by the anode spot.

7.5.2 Thermocouple

Also of interest is the temperature of the liquid immediately below the anode spot. This was measuring using a miniature thermocouple. A setup design with 3D motion control is shown in Fig. 7.9 (a). The thermocouple couple was placed 2 mm directly underneath the plasma attachments. The constructed measuring process during the discharge operation is photographed in Fig. 7.9 (b). Here, the pattern formed as self-organized dots on the liquid surface during the measurement. Total 21 minutes plasma exposure applied. As the results shown in Fig. 7.10, the local temperatures increased with time.

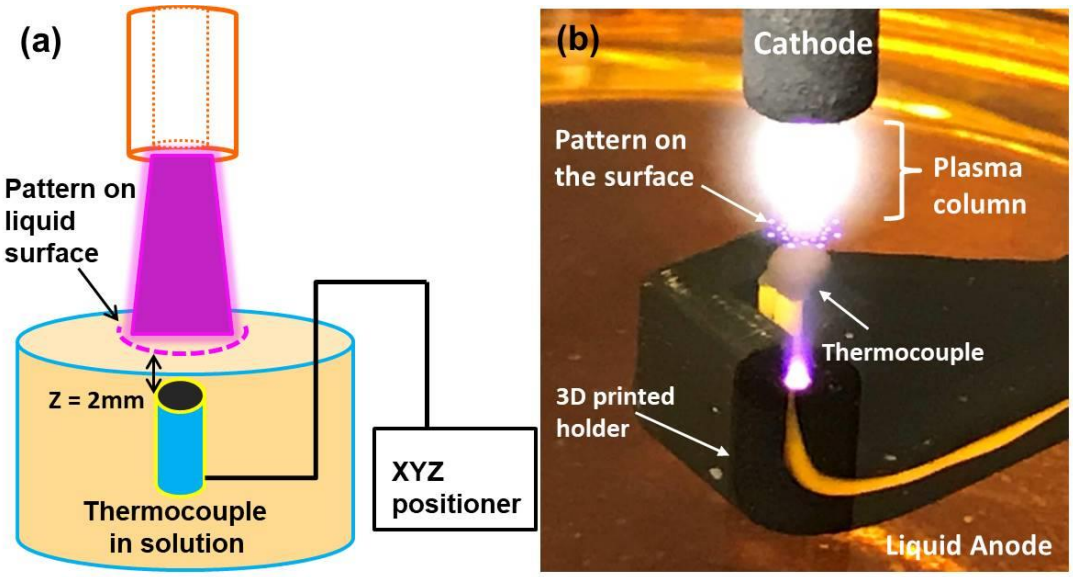

Figure 7.8: Thermocouple was used to measuring the liquid temperature underneath the SOP. (a) A design sketch. (b) A photograph was captured during the measuring and operation with self-organization appeared above the thermocouple.

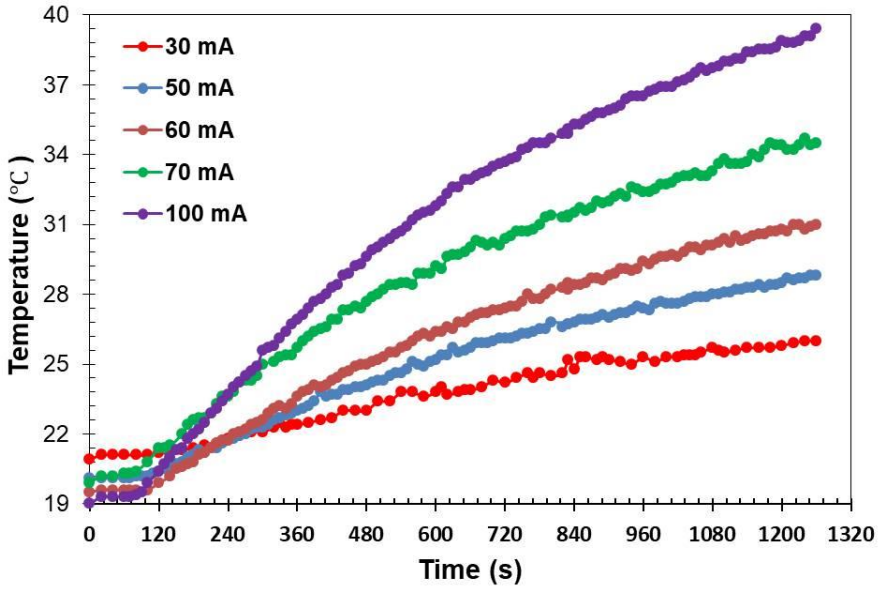

Figure 7.9: A local temperature profile using $FeCl_3$ anode solution with gap of 8 mm.

The measured temperature was higher at the higher currents. From the plot, at early times (2 minutes), the temperature was relatively constant, suggesting time constant – formation of

vapor later at contact point may insulate the water below surface owing to reduced thermal conductivity (steam is factor of 1/30 water).

A noticed thermal fluctuation started after about 10 minutes plasma exposure, and it takes about 10 to 20 seconds for the temperature to stabilize. This observation further suggested a local cooling might be under processing. Indeed, this can be seen from the thermal transformation with a puzzling variation that demonstrated in Fig. 7.11 (a). Here, thermal transformation indicates the anode liquid temperature rise after the plasma is turned off, which shows there is a cooling process during the plasma injection. In this plot, the post plasma exposure measurements (liquid temperature) were taken within 30 seconds after the plasma turned off. At each current, the total time for plasma to expose on the anode liquid is 20 minutes. As can be seen in the figure, the temperature increased rapidly but with almost equal increment at each tested current between both measurements. At time around 20.5 minutes (after 20 minutes plasma exposure, plasma turned off for 0.5 minutes), the anode liquid temperature reached to its peak value that show as the post plasma exposure temperature on the plot. It was observed that the temperature reduces rapidly after 30 seconds. With the same current intervals, the IV curve in Fig 7.11 (b) shows the total power increasing but the discharge power is likely remaining constant.

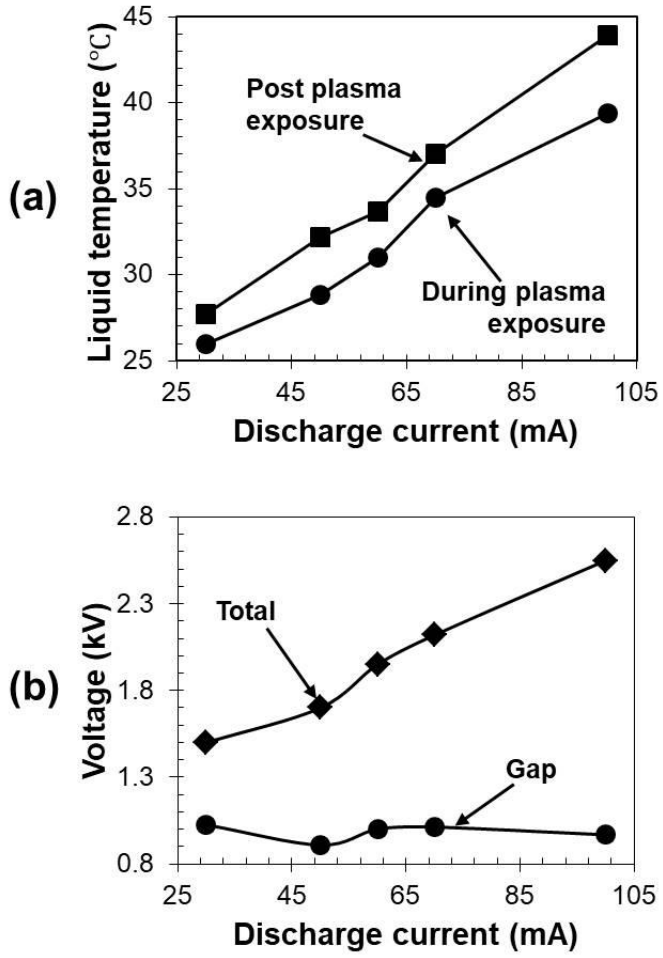

Figure 7.10: A thermal transformation is shown in (a) with the IV curve of total and plasma discharges are shown in (b). Here the plasma exposure time was 20 minutes.

7.6 Droplet Observation

As mentioned previously, early experiments indicated luminous streaks. The witness plates suggested nanoparticle emission. However, more advanced imaging revealed the presence of actual droplets, suggesting that the nanoparticles are emitted into the gas phase as droplets and thus the Taylor cone mechanism may be the origin of the emission or that the originate as molten species (Fig. 7.12). Here we hypothesized that the repulsion of the positive ions at the anode

surface and pull of the electric field on the positive ions overcome the surface tension of the liquid and make it expand into the Taylor cone, the tip of which, being the least stable point, elongates into a liquid filament. This filament breaks up into individual charged droplets.

Figure 7.12 is a snap shot of an observed droplet traveled from anode to cathode. During its travelling, it actually impacted the cathode and then returned to the plasma column. The fact that the droplet did not instantly evaporate upon contact with the cathode suggests either Leidenfrost effect insulation or the droplet is actually molten metal. Upon impact the droplet was also observed to oscillate (presumably volume conserving shape oscillations).

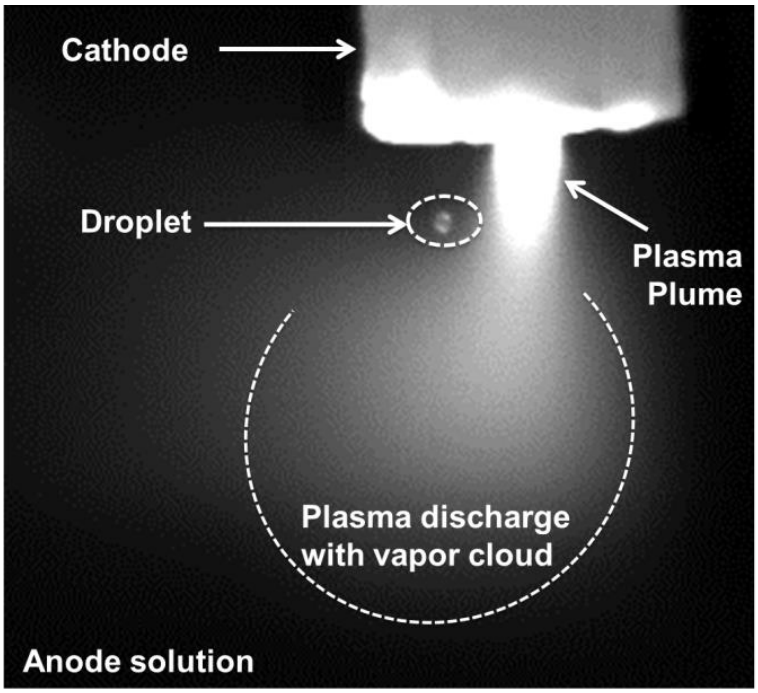

Figure 7.11: A single droplet traveled from the anode to cathode during the plasma glow. This image was captured at exposure of 10k fps.

In average, it was determined that the droplet had slightly different ascent and descent speeds as 593 mms^{-1} and 506 mms^{-1} respectively. The time difference between the descending and ascending path of the droplet is about 2.3 ms. The changes in speed could be due to charging

effects or velocity uncertainty due to out of plane motion. The size of the droplet is measured approximately 0.35 mm in average diameter with spherical volume of 0.0225 mm^3.

Assume the droplet has the same density of the uniform solution, which was stated in Sec. 7.4 as 1.033×10^{-6} $kgmm^{-3}$. The kinetic energy of the droplet can be estimated using

$$KE = \frac{1}{2} mv^2 = \frac{1}{2} \rho V v^2 , \tag{7.4}$$

where v is either the ascent or descent speed of the droplet during its travelling. Here the estimated kinetic energy of the droplet is 4.09 nano joules for the ascent and 2.97 nano joules for the descent. Neglecting the error during the estimation, the kinetic energy difference shows that approximately 1 nano joule energy has been transferred or lost after the droplet touched the cathode. This might be referred to the energy that required evaporating this volume of the droplet. Additionally, the charge state of the droplet is unclear at this point. If the charge on the droplet is defined, the electric filed could be estimated, which requires future effort.

7.7 Conclusion

For the first time, luminous particle emission has been observed from $FeCl_3$ anode solution under self-organization condition in atmospheric pressure helium plasma. The recorded emission process suggests that the particle emission originated from the center of the plasma attachment at the plasma liquid interface. The experimental investigation for tracking the emitting particles was limited to the plasma-liquid plane. 2-D spatial-temporal trajectories were mapped out with the corresponding velocity profile has been estimated. These emitted particles were experimentally collected as resulting spats with their characteristics including the morphologies, sizes and compositions have been analyzed. It was found that the emitted particles appear to be molten as droplets with their initial diameter ranged between 31.85 μm to 140 μm. The emitted particle composition has been identified as iron oxide with their initial emitting

speeds between 7.9 ms^{-1} and 33.2 ms^{-1}. These energetic emission processes suggest that the luminous light along the particle trajectory are likely the result from the rapid oxidation of melting iron particles. The initial emission force was estimated in micro newton scale. The droplet traveled between the electrodes with kinetic energy in nano Joule. Overall, this effort thus provides insight not only into the physics of particle emission, but also potentially into the underlying processes driving the self-organization formation itself.

7.8 References

[1]. N. Shirai, R. Sekine, S. Uchida, and F. Tochikubo, Jpn. J. Appl. Phys. 53 026001 (2016).

[2]. Z. Wang, J. Xu, Y.E. Kovach, B.T. Wolfe, E. Thomas Jr, H. Guo, J.E. Foster, and H-W Shen, Phys. Plasmas 27, 033703 (2020).

[3]. J. Mostaghimi, M. Passandideh-Fard, and S. Chandra, Plasma Chem. Plasma P, 22, 1 (2002).

[4]. K. Shinoda, and H. Murakami, Journal of Thermal Spray Technology, 602, 19 3 March (2010).

[5]. K. Shinoda, T. Koseki, and T. Yoshida, Influence of Impact Parameters of Zirconia Droplets on Splat Formation and Morphology in Plasma Spraying, J. Appl. Phys., 100(7), Art. No. 074903 (2006).

[6]. Y.Z. Zheng, Q. Li, Z.H. Zheng, J.F. Zhu, and P.L. Cao, Applied Surface Science, 317 526-533 (2014).

[7]. J. Liu, H. Vu, S.S. Yoon, R. Jepsen, and G. Augilar, Atomization and Sprays 20,4, 297-310, (2010).

[8]. M. Rein, Fluid Dyn. Res., 12 61 (1993).

[9]. S. Ueda, H. Shi, X. Jiang, H. Shibata, and A.W. Cramb, Metallurgical and Materials Transactions B, 34B 503 (2003).

[10]. Y. E. Kovach, M. C. Garcia, and J. E. Foster, IEEE Trans. Plasma Science, 47, 7 (2019).

[11]. M. Pasandideh-Fard, Y. M. Qiao, S. Chandra, and J. Mostaghini, Phys. Fluids 8, 650 (1996).

[12]. C. Ukiwe and D. Y. Kwok, Langmuir 21, 666 (2005).

[13]. D.C. Vadillo, A. Soucemarianadin, C. Delattre, and D.C.D. Roux, Phys. Fluids 21, 122002 (2009).

[14]. D.S. Viswanath, T.K. Ghosh, D.H.L. Prasad, N.V.K. Dutt, and K.Y. Rani (2007).Viscosity of Liquids: Theory, Estimation, Experiment, and Data. Springer. Pg 278 ISBN 978-1-4020-5 481-5 (2007).

CHAPTER VIII

Self-organized Plasma Induced Nanostructures[10]

In this chapter, the formation of nanostructures such as "fuzz", holes, and flakes were observed on tungsten and stainless steel anodes in a 1 atm glow discharge with helium as the feed gas. The structures exhibited morphology similar to the tungsten fuzz growth observed in experiments that simulate wall conditions in fusion reactors, suggesting similar physics may be present in both scenarios. The anode surface temperature ranged between 1000 and 1300 K with an ion fluence rate of order of 10^{24} $s^{-1}m^{-2}$. In this work, SEM and TEM were used to characterize the evolution of nanostructure formation as a function of time. Observed nanostructures were found to vary with the morphology of the discharge plasma attachment. The composition of the structures was found to be predominantly the native metal by using EDS. This work gives some insight into the formation of nanostructures at atmospheric pressure which has not only applications for material processing but also provides potentially another avenue to study fuzz formation processes relevant to fusion plasma-wall interactions.

8.1 Introduction

As part of an ongoing effort to have a better understanding on the physical origin of the self-organization and accompanying pattern motion, the sensitivity of the discharge attachment response to surface composition of the anode electrode was investigated. Here the study aims

[10] The text and discussion in this chapter has been previously published by Y.E. Kovach, Feifei Zhang, Fei Gao, and John E. Foster, "Study of plasma induced nanostructure formation and surface morphology changes on tungsten and stainless steel at atmospheric pressure", Journal of Vacuum Science & Technology A 37, 011301 (2019).

was to determine the effect of metal anode thermal conductivity and work function on discharge character. Significant surface nanotexturing was observed after plasma exposure; that is, in the general vicinity of the plasma attachment, organized, nanoscale-sized structures were observed. While a number of different metals were investigated, stainless steel and tungsten electrodes are the two metals that are highlighted here largely because they both exhibited the most pronounced nanotexturing. Tungsten has an order of magnitude higher thermal conductivity than steel but they both share similar work functions. The melting point for tungsten is roughly twice that of stainless steel. Presented here are observations of nanostructure on an anode electrode in an atmospheric DC glow discharge. While such structures are of interest for a variety of applications ranging from anti-icing, anti-fouling, optical detectors to catalysis, the formation of nanostructures on plasma facing surfaces in tokamak is actually a problem. It has been shown that various nanoscale structures can grow on plasma facing surfaces when the helium ion flux exceeds 10^{22} $s^{-1}m^{-2}$ at surface temperatures of order 1000 K and at helium ion energies of at least 60 eV. The problem with appearance of such fiberous structures, dubbed tungsten fuzz, is that it could potentially flake and by doing so serve as a high Z dust thereby polluting the fusion plasma. Bremsstrahlung radiation amplification owing to the introduction of tungsten in the plasma would make it difficult to achieve ignition. Additionally, it has been shown that the nanostructure could greatly affect hydrogen retention and the thermo-optical properties of the surface in question [1].

The actual formation mechanism of the tungsten fuzz is still not well understood. Computational models suggest that implanted helium produces bubbles in the bulk material. These bubbles coalesce over time forming larger ones and then eventually penetrate the surface forming pinholes and ultimately over time fibrous nanoscale structure [2]. Key to all models

however is the importance of substrate temperature and minimum ion energy. Research findings suggest helium penetration at energies as low as 10 eV [3]. It is interesting to note that the nanotextured tungsten observed in this present work is morphologically quite similar to that produced in the fusion simulator experiments over similar exposure times (approximately 1-10 hours) [4, 5]. This observation is somewhat remarkable, which suggests that despite the significant differences in exposure conditions, the physical processes at play may be similar eventually leading to the same type of nanostructuring.

8.2 Experiment

A schematic of the atmospheric pressure DC glow is shown in Figure 8.1a.

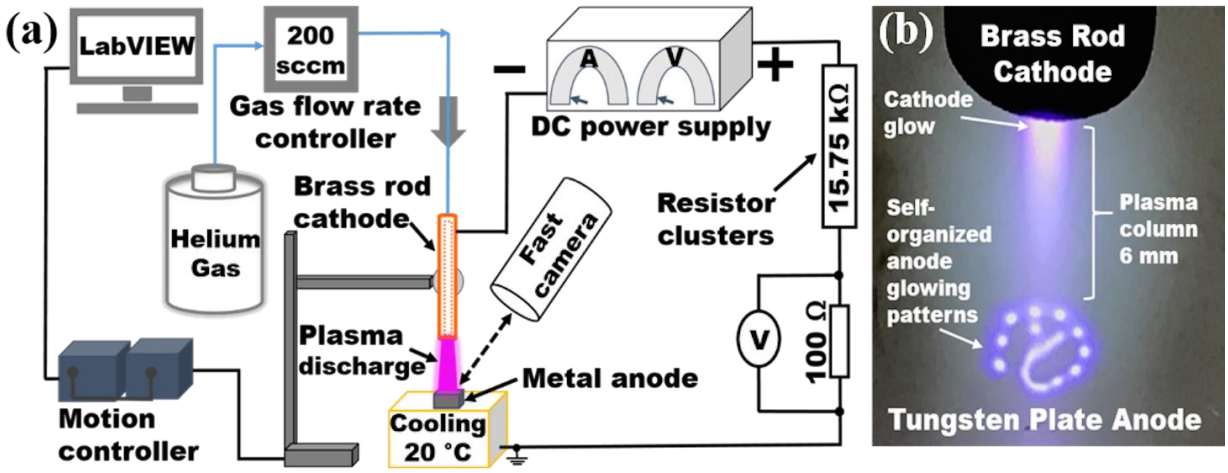

Figure 8.1: The electrical circuit used to generate plasma discharge on a metal anode surface is shown in (a) along with a picture of an actual atmospheric glow discharge shown in (b).

Standard operation condition applied here. In all the cases, the experiments took place in ambient air at atmospheric pressure. In one test case, the discharge was operated without helium gas flow for elucidating some of the mechanisms of the observed surface nanostructuring. The inter-electrode gap used during the nanostructuring experiments was tested up to 12 mm base on each specific experimental purpose. The Reynolds numbers, calculated for a fixed flow of 200 SCCM

of helium for the discharge gap lengths from 1 mm to 12 mm respectively, ranged between 143 and 1715. This result indicates the flow type is laminar since the Reynolds numbers are less than 2000 [6,7]. The temperature of the anode surface was assessed using an optical pyrometer (MIKRON, M90-V), which yielded a color or brightness temperature. In the work reported here, the brightness temperature was converted to the true temperature by correcting for the emissivity, as the electrodes are not true black body emitters. In this effort, both polished and unpolished stainless steel (304) and tungsten (99.95%, metals basis) target plates were used as anodes. The exposure times for tungsten electrodes ranged between 2 minutes and 30 minutes.

8.2.1 Basic Glow

For all practical purposes, the structure of the atmospheric pressure DC glow discharge has all the characteristics of a glow discharge such as discharge current-voltage characteristics and discharge spatial structure [8]. These similarities were found in this work as well. For instance, visually the discharge has a distinct cathode and anode glow region as well as a defined positive column, as can be seen in figure 8.1 (b). The current is limited by both power supply and a resistor that limits maximum current to 0.3 A. This limitation prevents the discharge from constricting into an arc and therefore allows it to behave as a nonthermal glow. Even so, the gas temperature in these discharges of this type is typically high of order ~1800 K but not as high as the electron temperature which has been estimated from laser Thompson scattering experiments to be a few electron volts, thereby making the T_e approximatly10 times T_{gas}, thus nonthermal. According to Nikiforov [9], at low ionization, high pressure plasmas, the electron density of an atmospheric glow discharge or plasma jet is in the range of 10^{13} cm^{-3} to 10^{15} $cm^{-3.}$ In this work, the plasma density as inferred from Stark Broadening measurements through H_β line detection suggests densities of order 10^{14} cm^{-3}.

Typical discharge behavior is resistive (roughly 16 Ohms) with the discharge current increasing linearly with increasing discharge voltage for a given inter-electrode gap. At fixed voltage, the discharge current tends to decrease monotonically with increasing gap. This

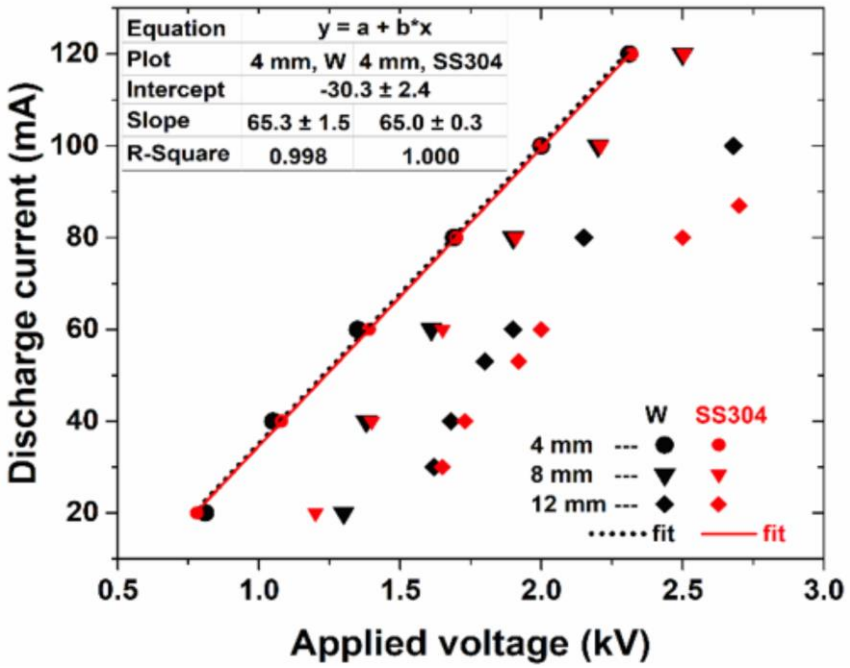

Figure 8.2: The current-voltage discharge characteristic of a tungsten (W) and stainless steel (SS304) electrode acquired at several interelectrode gaps.

behavior is expected as energy and power losses associated with both scattering and attachment increase with discharge volume. Furthermore, the mean electric field and thus ionization rate in the positive column also decreases with increasing gap length. Such behavior is shown in Fig 8.2 for helium plasma discharge in air with both tungsten and stainless steel anodes. In addition, for each case in this work, the plasma breakdown took place at a1mm inter-electrode gap distance. For both stainless steel and tungsten anodes with helium flow, the breakdown voltages were found to be 600 V and 800 V respectively. A1.3 kV breakdown voltage was recorded for an airglow without any helium flow.

8.3 Initial Observations

8.3.1 Tungsten

After operating the discharge over a range of discharge currents (~104 mA at voltage ~2.3 kV), noticeable texturing was visually observable in the region of the plasma attachment. Figure 8.3 depicts a typical pattern that forms on the surface of tungsten if the discharge current is sufficiently high. Initially, it was suggested that this might be due to localized melting at the

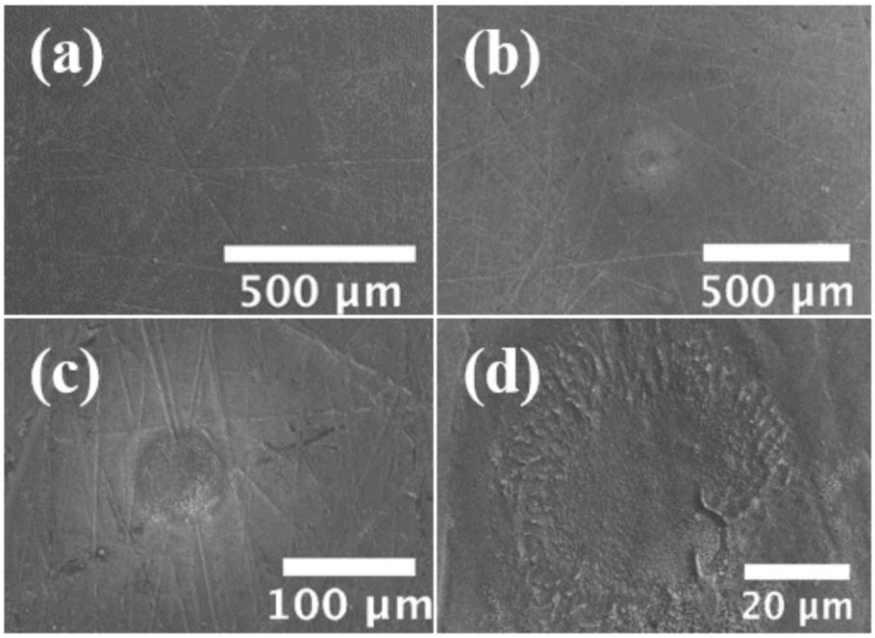

Figure 8.3: SEM images of tungsten sample surface were captured (a) before the plasma exposure and (b-d) after plasma exposure. Surface texture is apparent with increasing magnification.

anode surface. If the degree of material evaporation could be determined from images, in principle, it should be possible to estimate the energy deposited into the anode locally. This energy could then be used to estimate the magnitude of the local anode fall voltage, a parameter that is difficult to assess at atmospheric pressure using electrostatic probes owing to the small sheath thickness and the high collision frequency with background neutrals. The surfaces were analyzed using SEM to understand the nature of the possible melting. Surprisingly, the surface

was not so much as melted but rather textured on a nanoscale. Surface nanostructuring was observed on both tungsten and stainless steel substrates with helium flow after exposure to the DC glow discharge. The tungsten substrate was treated for approximately 23 minutes with an inter-electrode gap of 6 mm at a discharge current of 73.5 mA and an average discharge voltage of 1.75kV. After exposure, the samples were analyzed via electron microcopy.

Fig 8.3 shows the effective "footprint" of the plasma attachment on the tungsten anode after plasma exposure along with surface morphology before plasma exposure. The texturing is noticeable at increasing magnification. Note that the center of the footprint is actually hollow which suggest that the discharge itself is hollow resulting in a ring shaped attachment at the anode. Such hollow features have been observed in DC glows as well as in helium plasma jets

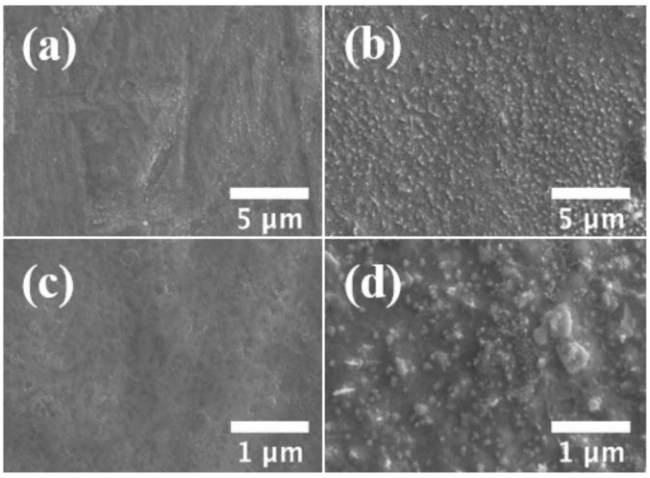

Figure 8.4: The morphology of a tungsten sample is compared between (a, c) untreated surfaces and (b, d) plasma treated surfaces.

although the formation mechanism is not completely understood [10, 11]. The current density is therefore significantly higher than the apparent circular footprint outline. As mentioned, the anode plasma attachment is localized. Figure 4 compares observed texturing outside the region

that without plasma exposure to a region inside the plasma attachment ring. Discrete, granular-

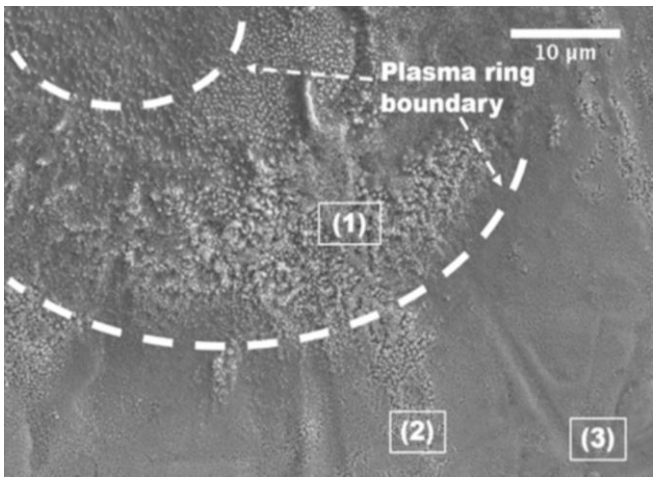

Figure 8.5: A diverse range of textural structures were observed in 3 distinct regions.. Region (1) indicates the location in plasma ring. Region (2) is located at the edge of the plasma ring. Region (3) shows the outside region of the plasma ring.

like structures are clearly apparent on the surface of the plasma treated area.

Further, most of the features shown have submicron characteristic dimensions. As depicted in Fig 8.5, the region of plasma attachment featured in general three types of nanostructuring. Inside the ring region (region 1), the texturing is fiberous. Nano "fuzz" formation was observed just outside the ring attachment area (region 2). Somewhat further away from the mid region of the ring (region 3), nanoholes were observed. In detail, the fibrous zone of region 1 displayed rich texturing of two distinct forms: needle-like fibers and fiberous

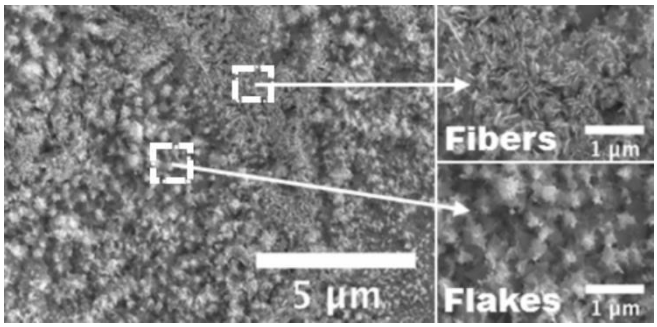

Figure 8.6: Nanofibers and flakes were observed in region (1) of figure 8.5.

protrusions, which had somewhat of a flake like appearance. These features have length scales ranging from 20 nm to 200 nm, which are displayed in Fig. 8.6. Just outside the attachment

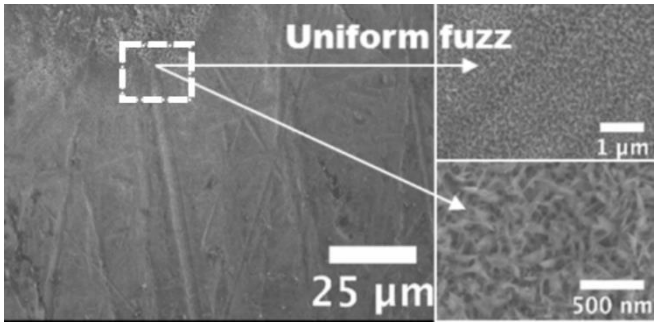

Figure 8.7: Tungsten fuzz was observed in region (2) of figure 8.5.

ring region, tungsten fuzz was observable. This nanostructuring is clearly seen in the Fig. 8.7. As shown here, the structuring is uniform and extensive. Under the highest magnification, the structures are quite regular and seemingly interwoven. Nanoholes were observed outside the

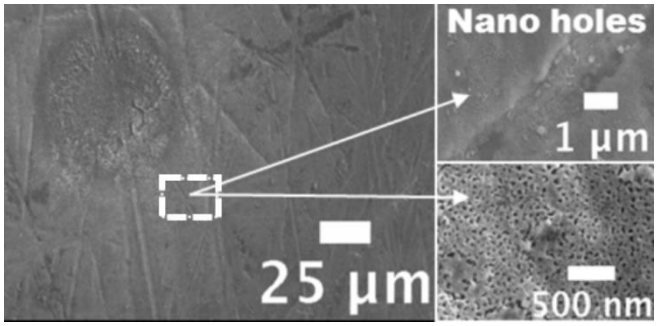

Figure 8.8: Nanoholes were observed in region (3) of figure 8.5. Note the relative position of the nanoholes with respect to the location of the discharge attachment footprint.

"footprint" of the plasma discharge as shown in Fig 8.8. Presumably, this area is cooler and subjected to reduced ion flux. The observed holes are reminiscent of ruptured helium bubbles at the surface of substrates exposed to energetic helium flux [3]. In those studies, it is observed that the nanoholes can form when the ion energy is low (<20 eV) if the surface is sufficiently hot. Nishijima and colleagues suggest nanohole formation can occur at energies as low as 6 eV, the threshold for surface barrier potential energy for helium injection into the tungsten between

atoms in the lattice [12]. This hole region, which located outside the region of the main attachment, is clearly surface textured indicating non-zero plasma bombardment albeit at presumably a reduced flux.

In order to assess the composition of the surface structures, energy dispersive x-ray spectroscopy (EDS) was used (Fig. C.1). It was found that these surface features were predominantly tungsten and to a lesser extent, some oxygen was observed. It is interesting to note that in regions just outside the plasma footprint, EDS indicated the presence of copper as well. Presumably, this copper originated from the brass cathode and migrated via diffusion to the surface. The fact that it appears in regions outside the plasma footprint suggests that net deposition takes place here. Its absence in the ring footprint area suggests that those regions experience ion bombard at a rate that either matches or exceeds the copper deposition rate. This suggests that incident helium energies may exceed the sputter threshold for copper, which is approximately 25 eV [13].

8.3.2 Stainless Steel

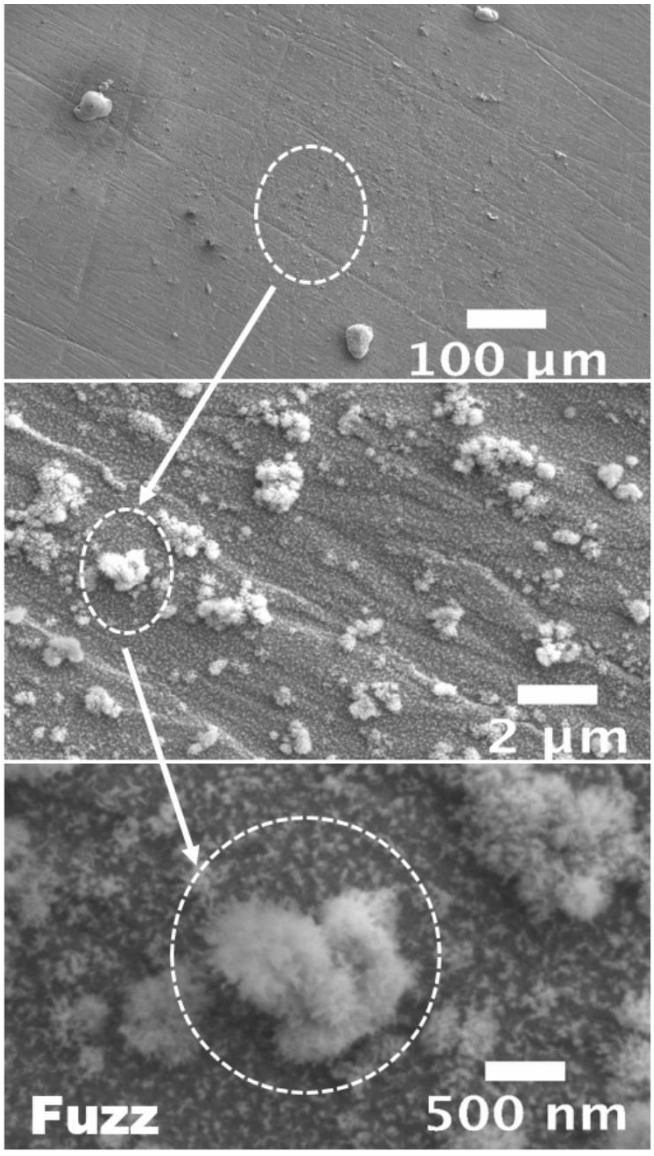

Figure 8.9: Nanofuzz was observed on the stainless steel surface after helium plasma exposure.

Similar to the tungsten, nanostructuring was also observed on stainless steel anode plates as well. The substrate was exposed to helium plasma for 68 minutes in total during the study of self-organization patterns. Voltages ranged between 0 and 2.74 kV with currents up to 142 mA. In the region of the plasma footprint, nanofuzz structures were observed. Fig. 8.9 illustrates the fuzz structure with nanometer-sized features. EDS revealed these structures composed

predominantly of iron and nickel with oxygen (see Fig. C.2). However, there was no clear circular plasma footprint on the stainless steel surface after the helium plasma exposure. Since the total exposure time was long, this absence is likely due to plasma modification of the surface along with time (plasma driven resurfacing), which naturally sets an upper limit for exposure time. For comparison purposes, the discharge was also operated without helium gas flow. As stated earlier, the breakdown voltage for this operating condition was high, 1.3 kV (roughly twice of that with helium flow). The substrate was exposed to the air plasma for roughly 34 minutes at an average current of 62 mA. The discharge burned in regular room air. Under these conditions, nanostructures were not observed. For completeness, SEM images of this surface are shown in Figure 8.10. As can be seen in the figure, the footprint of the discharge is apparent.

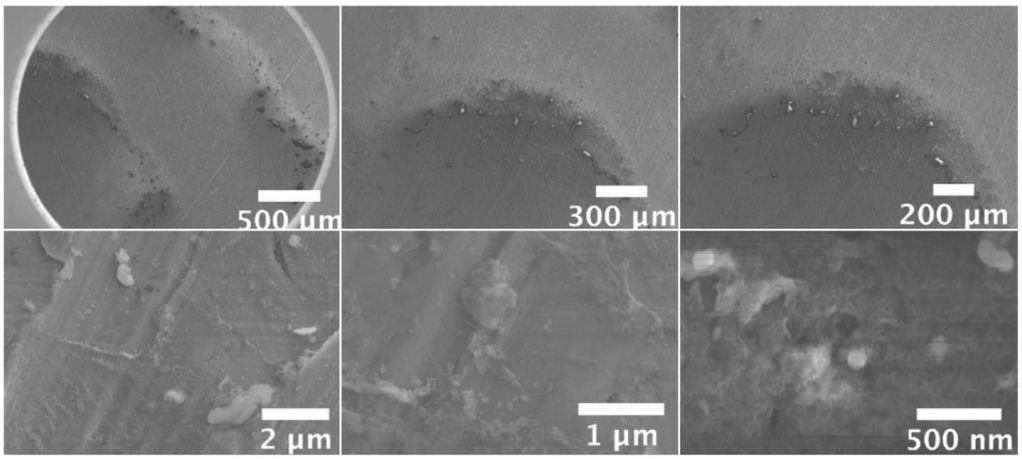

Figure 8.10: Nanostructures were not found on the stainless steel anode surface after air plasma exposure.

However, there were no observable nanoscale structures. EDS analysis indicated the presence of iron oxide in the regions of the plasma footprint and the surrounding halo region (see Fig. C.3). This data suggests at least over this range of operating conditions, nanostructuring does not occur suggesting the importance of helium.

8.4 Time Resolved Nanostructures

As discussed previously, various nanoscale structures were observed on both tungsten and stainless steel anodes when exposed to helium plasma under atmospheric pressure condition. These structures were observed over a range of discharge operating conditions and exposure times. Of particular interest is the development and evolution of these features with time under carefully controlled discharge conditions. In this manner, one can correlate their occurrence under specific operating conditions and yield insight into the formation mechanism. In order to achieve this, a controlled set of experiments was performed to understand the structure development. First, in order to minimize the possibility of nanostructure seeding via surface roughness [14], tungsten samples were mirror polished. The polished surfaces were then exposed to the helium plasma for set time intervals and then examined. After each treatment interval, the electrode was displaced to allow the discharge to attach at an untreated location on the 2.54 cm by 2.54 cm substrate accumulating approximately 7 treatment sites on a given substrate. Note attachments were approximately 2.5 mm in diameter. After treatment, the various locations were examined using SEM. This method removed any bias regarding polishing quality since each attachment was generated on a surface with the same surface treatment. This sample was also water cooled as described previously. For these time resolved measurements, the applied voltage was fixed at 1.8kV with a constant discharge current of 53mA with a fixed inter-electrode spacing length of 12 mm. The plasma exposure time for a given treatment site ranged from 2 min to 30 minutes. In this manner, the time evolution of the nanostructures was determined.

8.4.1 Macroscopic View

Figure 8.11 illustrates the observed macroscopic surface changes on the tungsten substrate as a function of time. On average after two minutes of plasma exposure, the hollow-shaped plasma footprint with a textured (light in color) central region is apparent. Subsequent exposure of duration up to 20 minutes, the circular footprint pattern is less apparent. After 30 minutes of plasma exposure, the circular footprint gives way to lighter colored spots on the surface. This transition is related into the time evolution of the discharge itself, which over time

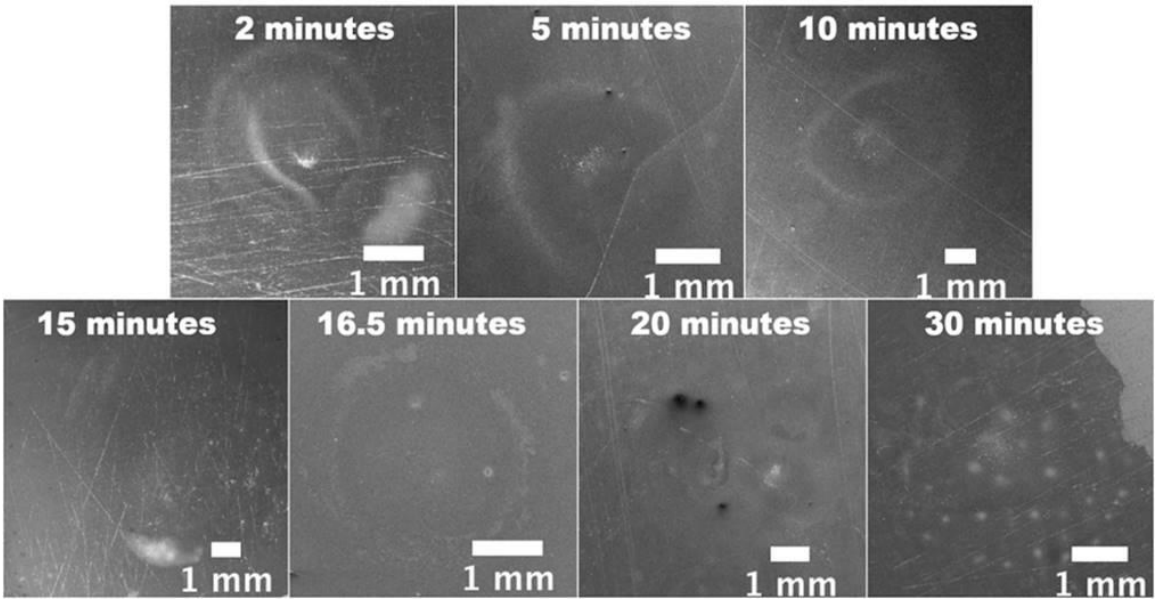

Figure 8.11: SEM images of the time evolution of the plasma attachment as inferred by surface texture changes were captured on a tungsten anode surfaces after helium plasma irradiation.

self organizes into a discrete ensemble of plasma attachments, essentially glowing dots. SEM analysis of the spotted regions (to be shown in figure 8.13) revealed uniform distribution of fuzz similar to that shown in Fig. 8.7.

8.4.2 Surface Condition in the Center

In depth, analysis of the spotted regions is presented in Figure 8.12. While a range of

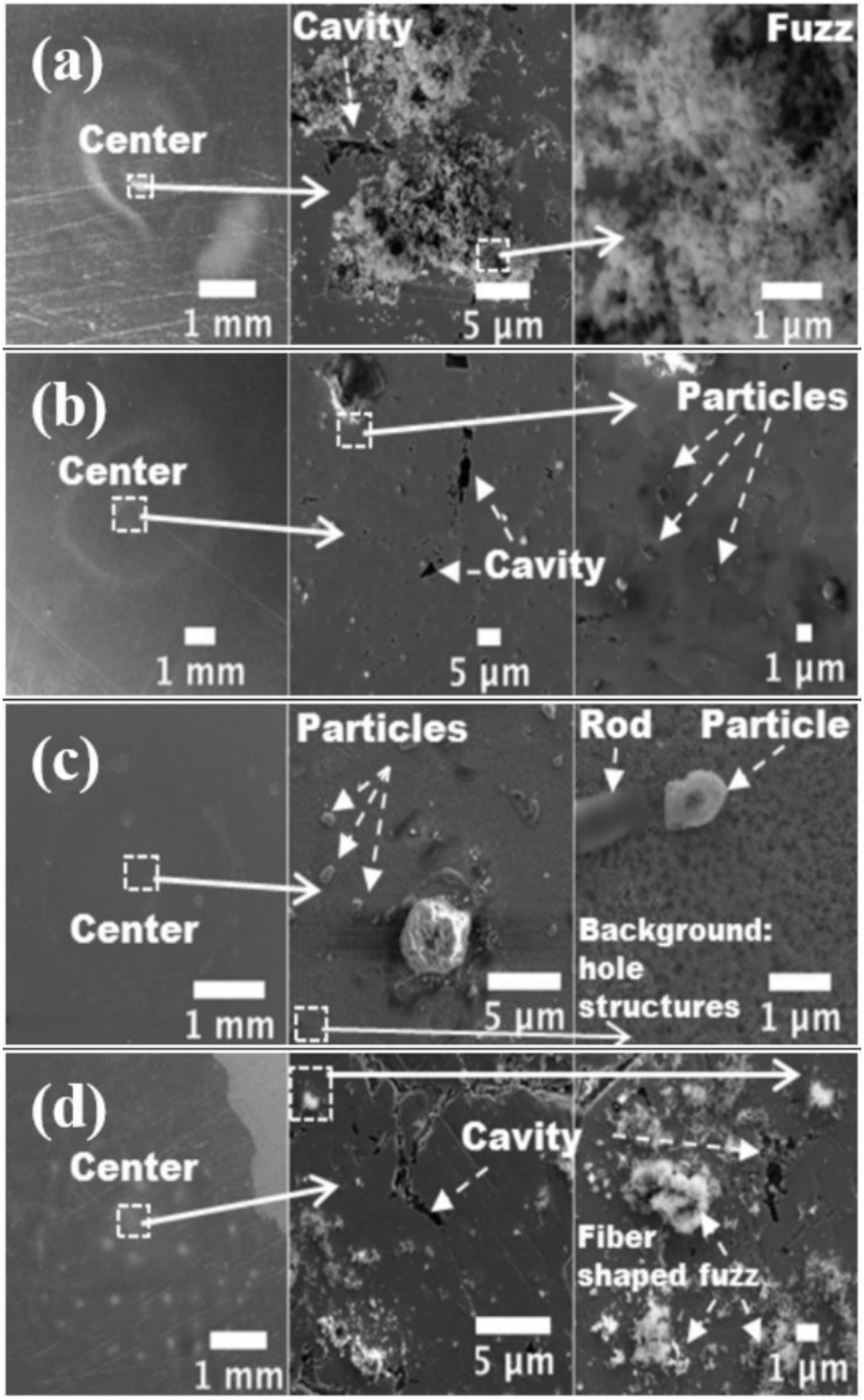

Figure 8.12: Fuzz and cavity structures were found in center of discolored spotted regions at (a) 2 minutes, (b) 10 minutes, (c) 16.5 minutes, and (d) 30 minutes. Dashed box regions denote areas of additional SEM analysis.

structures and surface changes were observed via SEM analysis, as one can see in its sub figures, apparent fuzz growth is apparent in many of the images. Figure 8.12 focuses on structures located at the middle of the attachment. As can be seen after 2 minutes of exposure, sub-micron sized fuzz is apparent. Cavities are also present after 2 minutes of exposure. After 10 minutes of exposure, surface near center contains what are perceived to be particles and cavities, some of which with dimensions less than a micrometer. After 16.5 minutes, the surface is heavily textured with submicron-sized holes. Particles appear to be present on the surface as well. However, no fuzz structures were observed in the center region at this time point. After a full 30 minutes of exposure, fibrous fuzz is apparent in the center region along with cavities. Fuzz and holes are nanoscale in size. What is interesting about these features is the insight that the yield regarding the evolution of the discharge. Over time, the discharge apparently evolves from a double ring like attachment to multiple dot attachments. The key question is whether the texturing observed on the surface is a consequence of discharge evolution or whether the texturing generated via plasma exposure affects the attachment pattern. In other words, this latter question concerns whether or not plasmas self-organization into the dot patterns is a consequence of surface changes. Furthermore, if the pattern changes are a type of feedback in response to the surface morphology, it may be possible to seed self-organization by a priori texturing the surface to test this possibility. This question is left to future work. It should be pointed out that EDS confirms that the observed fuzz and cavity are tungsten in composition. In the damage studies on tungsten due to helium plasma irradiation, micro-cracks or cavities appear similarly on tungsten surface under fusion condition due to the bombardment of helium ions [15-17].

8.4.3 Nanostructure Evolution

Structures similar to those observed in simulated plasma-facing tungsten samples were also observed outside the center of the discharge attachment. Figure 8.13 illustrates these structures with how the overall surface evolves as a function of time outside the central attachment region. After 2 minutes of exposure, crack like cavities and holes were observed. These features were observed both between the double ring attachment "footprint" and on the ring impression as well. Fuzz growths were also observed. At 10 minutes exposure, in addition to the cavities and fuzz, nanoholes and rod structures were observed. The formation of the rod structures on the surface is somewhat puzzling. Measured width of rods observed ranged between 20 to 80 nm. Rod-like structure has been observed in tungsten sputter deposition experiments. Here the so called Beta-phase W (100) nanorods has been observed. These simple cubic structures tend to have faceted, pyramidal a shape at the ends [18]. While some of these morphological features are apparent on the observed rods, it's not clear if the same mechanism is at play as strictly speaking tungsten vapor is not likely under these conditions [19].

Tungstate nanorods have been fabricated and studied for semiconductor applications. One synthesis method involves exposing the hot tungsten to an oxygen environment. Cracks in the natural tungsten oxide layer serve as reservoirs of tungsten. It has been shown that cracks expose (110) orientation planes most readily absorb oxygen. In this case, those cracks exposing (110) crystalline prominences were the location sites for nanorod growth, essentially along the crystalline plane. In that work, a tungsten wire was heated to around 800℃ in the presence of oxygen [19]. These conditions are similar to that prevailing in this experiment. The morphology of the nanorods observed in this work is very similar to that observed by Tokunga. In this regard, this suggests that the role of the plasma in this case is simply thermal — a source of

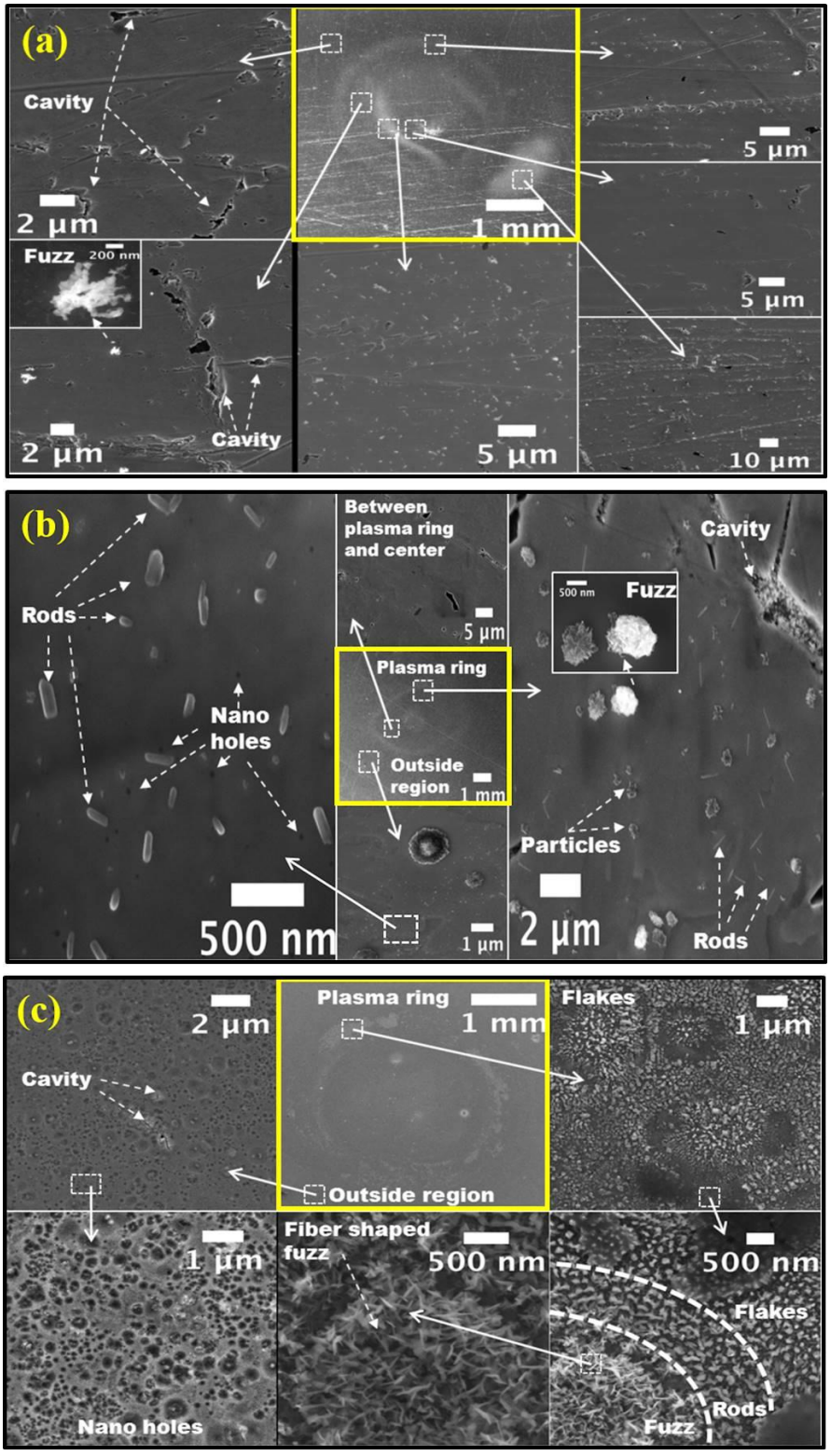

Figure 8.13: Nanostructure observations from locations around plasma attachment are shown after (a) 2 minutes, (b) 10 minutes, (c) 16.5 minutes and (d) 30 minutes plasma exposures. Note that the original plasma footprint images are highlighted with a box on each panel. Dashed box regions denote areas of additional SEM analysis.

localized heat deposition to give rise to crack formation in the natural oxide layer. Nanohole diameters are measured to have a diameter between few nanometers to 20 nm. Interestingly, the cavities at 10 minutes exposure also appear to be nanotextured. This can be seen in panel (b) of Figure 8.13. The nanostructuring of microcavities has been also observed on the surface to tungsten plates exposed to fusion-like plasma. In this case, it was reported that nanoglobules structures were observed inside pinholes and microcracks [14].

Heavily textured, intricately nanostructure surface features were observed beyond the central region after 16 minutes of exposure, as can be seen in panel (c). Significant nanohole coverage is observed in regions outside the main plasma attachment "footprint," in presumably the cooler, lower plasma density region of the attachment. There the morphology at closer inspection appears almost web like, nanoflake and fiber shaped structures were found at the edge of the plasma ring with rod-like structures appearing in between. EDS indicate that the fuzz is in composition of tungsten (see Fig. C.4). In particular, according to Kajita [3], such extended rod-like structure can only be seen when the fluence is rather low, it is difficult to distinguish it from flakes when the fluence is high. In the outside of plasma print region, nanoholes or bubbles are observed as shown in panel (c) as well. After 30 minutes of plasma treatment, the surface both on plasma dot footprints and beyond appears to be densely covered with nanofuzz patches as shown in panel (d). EDS measurements confirm that this fuzz is indeed tungsten (see Fig. C.5). Cavities are present as well. Surface particles also appear to be covered with cavities, nanoparticles and nanoholes as well. Surface particles range in size from ten nanometers to a few micrometers in diameter. Apparently, these particles also exist in the nanocavities. In particular, nanoholes (~80 nm diameter) and cracks with widths between 20 nm to 90 nm are

observed on the surface of the large growth depicted in the figure. The nanostructuring action apparently takes place on any material present on the surface.

In these time-solved tests on mirror-polished tungsten (which minimizes the likelihood of prior features seeding structure), the same nanostructured features (fuzz, flakes, fibers, holes, and particulates) observed in fusion simulators have been observed in this atmospheric pressure DC glow. These data suggest that similar processes are taking place and that nanostructuring are not germane to fusion type plasma.

8.5 Discussion

The nanostructuring observed on the tungsten and steel surfaces in atmospheric pressure is very similar to the tungsten fuzz structures observed in fusion plasma surface interaction studies. In fusion work, the formation of such structuring is believed to related with helium bubble formation [3, 4]. In many of these studies, the sample is biased negatively so as to attract ion flux to the heated target at the desired beam energy. Recent studies suggest that at least for helium ions on tungsten, the nanostructuring occurs in the 1000 – 2000 K range. Nanostructures appear at ion energies above 20 eV though nanoholes can apparently appear at energies below this. The typical helium flux required for nanostructuring on tungsten in this temperature range is ~ 10^{25} s^{-1} m^{-2} [3, 20]. While the target plasma exposure approach featuring the DC glow discharge differs from the plasma surface interaction studies in supporting fusion research, it is worthwhile to examine conditions prevailing in the glow to see if similar mechanisms are at play. Perhaps the biggest difference is the operating pressure, which is one atm for the DC glow — the presence of ambient air and high collisionality. The maximum temperature on tungsten at the location of the self-organized patterns without cooling was estimated to range between 1000 and 1300 K by using Wien's approximation. During the estimation, tungsten was considered as a

grey body, which has a spectral emissivity [21] less than that of a black body. As result, these surface temperatures are in reasonable agreement with operational temperatures where nanostructures and bubbles form [4, 22].

The ion fluence is more difficult to compare. If we assume that the 1 atm DC glow discharge has a negative anode fall voltage (plasma potential higher than anode), then we can expect ion flow to the surface at some energy acquired over the last mean free path [23]. This assumption is not unreasonable, as one would expect an accelerating potential present to give rise to the surface texturing and damage. In this case, the ion flux at the cathode matches the ion flux to the anode. The metered current is therefore a combination of ion and electron current. The electron current to the anode is just twice the ion current to first order if one neglects the secondary emission current. This neglect of the secondary electron current is justified since at the discharge voltages observed in this experiment as the secondary electron emission coefficient is much less than one. The actual electron current to the electrode is actually twice the metered current. Moreover, since the electron current "emitted" at the cathode is equal to the ion current, ion current is just half the total electron current incident on the anode. The metered current is simply the sum of the electron and ion current. The ion current can be easily calculated from density and plasma temperature data.

Density estimates in this type of discharge is $\sim 10^{14}$ cm^{-3}. If we assume an electron temperature of a few eV, then we can estimate the ion flux: $\sim 10^{24}$ $s^{-1}m^{-2}$ [24]. This value, though on the lower end, is consistent with fluxes associated with nanostructuring reported in the literature [13]. Densities at the anode surface could be considerably higher than this during self-organization as the estimate depends on both local density and temperature. The incident ion energy may be estimated as well. Because the halo region of the plasma footprint was absent of

deposited copper derived from the cathode rod, the incident ion energies must be at least great than the sputter threshold for this element. This means that the ions must be hitting the surface with energies at least higher than approximately 25 eV. Furthermore, this suggests that the anode is indeed below the local plasma potential by this much. This value is consistent with the reported literature as well in regards to lower limit for observed nanostructure formation. In summary, the prevailing conditions, based on these crude estimates, suggest that temperature, energy, and flux meet necessary lower limits for nanostructuring. The role of oxide formation is not addressed here. Although it most certainly plays some role in structure formation since the process in this case takes place in ambient, which explains in part the presence of the tungsten rods observed.

The tungsten nanostructure formation was investigated to a limited extent using TEM to look for the presence of helium bubbles, to determine the crystallinity, and to assess subsurface structure. Figure 8.14 shows TEM electron diffraction pattern from the tungsten filaments of

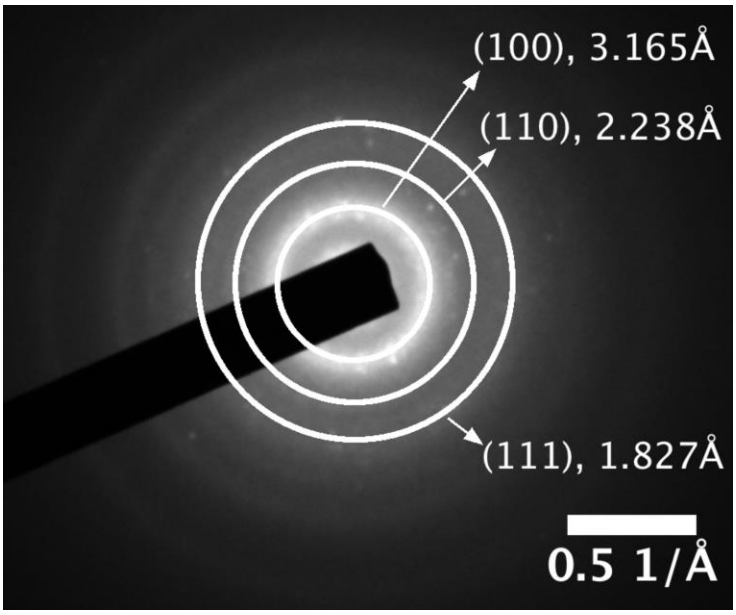

Figure 8.14: An electron diffraction pattern from a tungsten nanostructure feature was acquired using TEM.

helium plasma induced nanostructure. The discrete bright areas indicate crystalline structures on the surface. TEM images also revealed the presence of subsurface bubbles as well as can be seen in Fig 8.15. This tungsten TEM sample was prepared by using Focused Ion Beam (FIB) in bright field at beam high voltage of 300 kV. Here the bright regions constitute the voids. The characteristic dimension of the larger of these voids measured several hundred nanometers similar to that observed in literature [4, 13, 25]. The fact that the voids were present in the material suggests that nanostructuring processes taking place in the fusion simulator samples are similar to those observed in the helium atmospheric pressure glow.

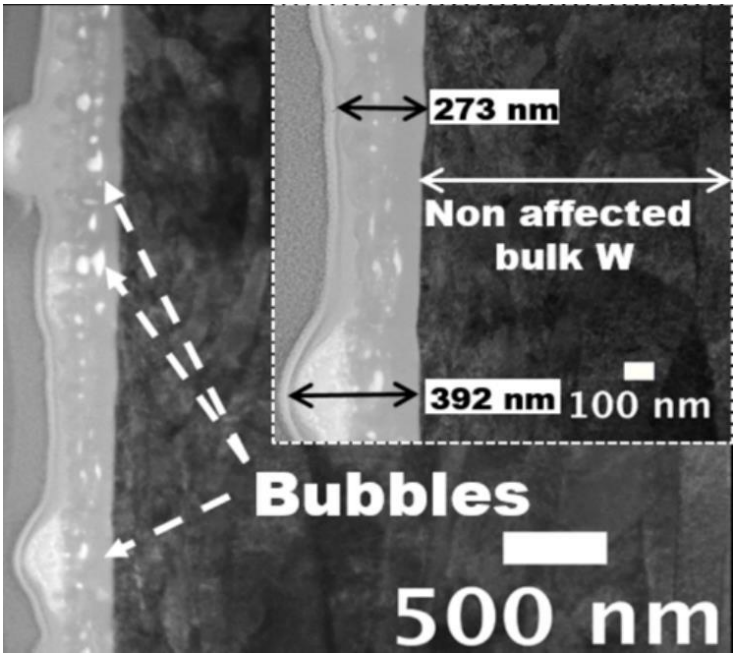

Figure 8.15: TEM image in bright field shows subsurface bubbles observed in tungsten sample with beam high voltage of 300 kV.

It is worth pointing out as discussed earlier that neither surface polishing nor controlled experimental parameters affected the appearance of nanostructures on samples. Also notable is that the anode patter actually evolved over time. Figure 8.16 illustrates the variation in the discharge pattern over time. The evolution of the observed nanostructuring over time is believed

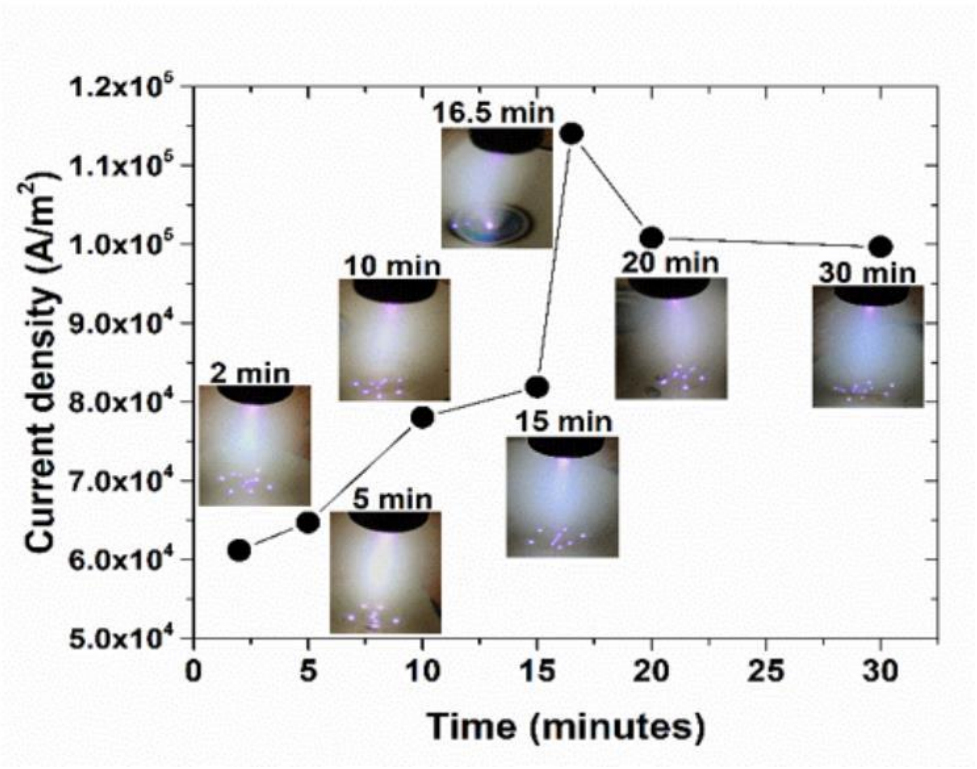

Figure 8.16: Discharge current density variations are displayed as a function of time.

directly related to the changing discharge and perhaps changes in surface morphology. As can be seen in the figure, the local current density tends to increase with exposure time. Here the average current density is determined from the average size of attachment spots, total number of spots, and the total discharge current. The fact that the discharge transitions from a ring like attachment to a self-organized array of dots may be related to thermal effects. Indeed, observation of spots on metal electrodes in arc discharges has been well documented and model. It has been asserted that cooling effects may drive an instability that leads to the self-organization. The time dependent non-equilibrium model Trelles used was able to show the formation of anode spots in a high current free burning arc discharge [26]. The self-organization observed in this case is similar to the anode patterns observed in atmospheric pressure glows. This model suggests that anode cooling plays a key role in self-organization. Model suggests

imbalance between heavy particle cooling at the anode, which lowers heavy particle temperature and electron collection at anode. To maintain equilibrium, electron temperature must increase to maintain plasma conductivity. No chemical or electrode effects were included in model yet it reproduced the spots thus highlighting the cooling effect.

Other studies suggest that the presence of a resistive layer located at the surface can lead to self-organization. The ohmic barrier would tend to regulate and thus stabilize the current flow and the resulting pattern. Raizer suggests that space charge can give rise to filamentation and thus the redistribution of the electric field at the surface, which can lead to self-organization [27]. Muller suggests that pattern formation is a consequence of a bistable layer in contact with a resistive zone at the anode surface [28]. What is clear is that over time, the surface in contact with the discharge heats up and in turn gives rise to increases in material resistivity. The increase in resistivity for tungsten is roughly quadratic with temperature [29]. Therefore, energetically, it would be more favorable for the ring attachment to spread out or break up into smaller current carrying attachments to minimize local resistivity and thus maintain current flow at a fixed voltage. Spreading out is not viable since at 1 Atm diffusion path lengths are so small that the footprint of the attachment is inherently small. Breaking up into discrete attachments is however viable. Breaking into smaller attachments also allows for attachment sites to loose heat laterally as well along the surface between spots. The fact that the spots tend to be in motion as well is consistent with this reasoning. The attachment spots are in motion to minimize local heating and thus local resistivity at the attachment point. As time wears on, the average plate temperature increases necessitating the need for more spots. In this regard, the self-organization and the resulting texturing may be the basis of a minimization principle.

Here, if the discharge is to be maintained at roughly constant power, self-organization into dots is therefore necessary. In this case, the self-organization behavior may be cast as a variational calculus problem. Phenomenologically, the configuration that minimizes the power expenditure is the "path" that is actually chosen. Assuming fixed voltage, the plasma therefore essentially evolves to such the integral $J = \int_{x_1}^{x_2} f\{y(x), y'(x)\}$ dx is an extremum, where in this case the minimum of this function is sought. Here the x parameter represents the surface area associated with the actual attachment, and the function y is electrical conductivity at the surface associated with plasma heating at x, while the compound function f is the current density. If these functional form of the functional and function y is determined, then the self-organization may be predictable. These same physical processes may prevail in DC glows with liquid anodes as well.

8.6 Conclusion

Surface nanostructuring generated by plasma exposure to a metal plate target serving as the anode of a DC helium-fed, 1 Atm glow has been characterized. These structures were present on the plasma-exposed surfaces of both tungsten and stainless steel. Time resolved images revealed surface evolution in which nanoholes, various shapes of tungsten fuzz, and nanoparticles were observed. Figure 8.17 summarizes qualitatively the structures observed relative to the location of the plasma footprint. Interestingly, the morphology depended on the relative spatial location to the discharge attachment footprint. Presumably, large gradients in plasma conditions and temperature exist in the general vicinity of the attachment. The discharge attachment tended to evolve over time, transitioning from a ring-like attachment to dots. With this evolution over time, the average current density was observed to increase.

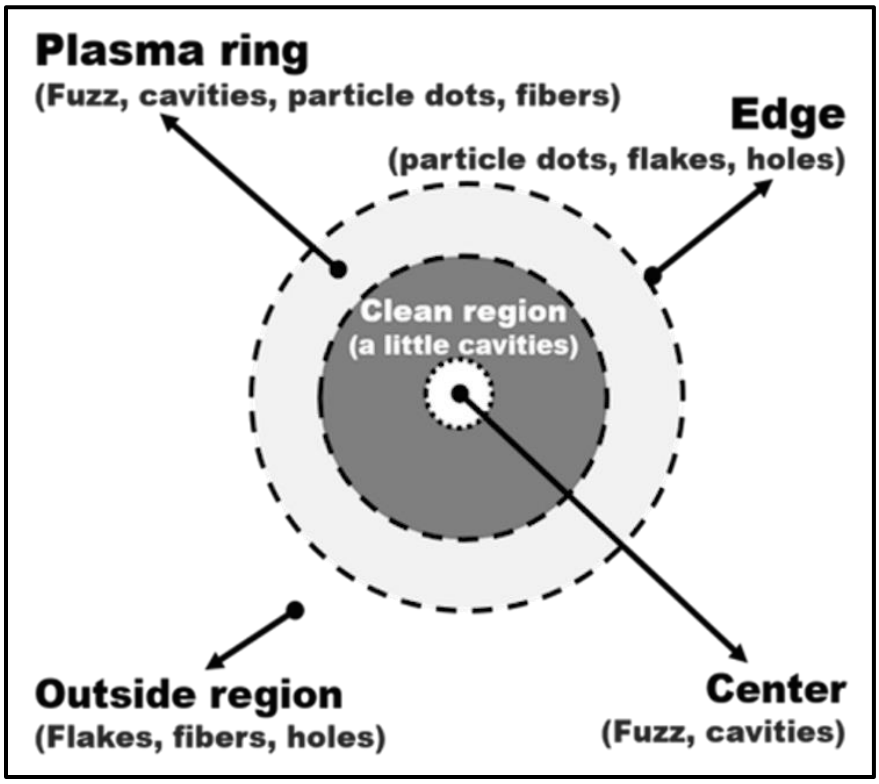

Figure 8.17: A diagram depicts the locations of various observed nanostructures on the circular ring shaped plasma footprint.

It is possible that the discharge attachment morphology was a consequence of surface morphological changes. Furthermore, nanorods were also observed and appear to be a consequence of localized thermal heat treatment. Helium bubbles similar to those observed in fusion target studies were observed in this work too. Overall, it was found that observed nanostructuring was similar in morphology and size to that observed on tungsten samples exposed to near-wall, fusion simulated helium plasmas at low pressure such as shown in Table 8.1. Remarkably, in both cases surface temperature and helium ion fluence were similar despite the pressure difference. These findings suggest similar mechanisms may be active in the surface evolution of substrates exposed to the 1 atm glow and those exposed to fusion-like plasma in the presence of helium.

Table 8.1. Similarities between atmospheric pressure glow and fusion experiment.

Experimental parameters	1 atm DC glow	Fusion condition
Surface temperature (K)	1000 to 1300	1000 to 2000 (typically ~1400)
He ion fluences (m^{-2})	10^{23} to 10^{24}	10^{24} to 10^{25}
Length scales (nm)	Fiber/Rod thickness: ~20 to 80	Tendril thickness: ~20 to 100
	Hole diameter: < 80	Bubble/pinhole diameter: < 100
	Fuzz layer depth: ~400 ± 120	Fuzz layer depth: ~600 ± 150
Ion incident energy (eV)	TBD	> 20

8.7 References

[1]. S. Kajita, W. Sakaguchi, N. Ohno, N. Yoshida, and T. Saeki, Nucl. Fusion 49, 095005 (2009).

[2]. S. I. Krasheninnikov, Phys. Scr. T145, 014040 (2011).

[3]. S. Sharafat, A. Takahashi, Q. Hu, and N. M. Ghoniem, J. Nucl. Mater. 386-388, 900-903 (2009).

[4]. M. J. Baldwin, T. C. Lynch, R. P. Doerner, and J. H. Yu, J. Nucl. Mater. 415, S104-7, (2011).

[5]. P. Fiflis, D. Curreli, and D. N. Ruzic, Nucl. Fusion 55, 033020 (2015).

[6]. F. M. White, Fluid Mechanics. 7th ed., (McGraw-Hill, 2009), Chap 6-7, Table A.4.

[7]. D. J. Jin, H. S. Uhm, and G. Cho, Phys. Plasmas 20, 083513 (2013).

[8]. D. Staack, B. Farouk, A. Gutsol, and A. Fridman, Plasma Sources Sci. Technol. 14, 700 (2005).

[9]. A.Y. Nikiforov, C. Leys, M. A. Gonzalez, and J. L. Walsh, Plasma Sources Sci. Technol. 24, 034001 (2013).

[10]. N. Shirai, S. Uchida, F. Tochikubo, and S. Ishii, IEEE Trans. Plasma Sci. 39, 11, 2652 (2011).

[11]. M. Y. Qian, C. Y. Yang, S. Q. Liu, Z.D. Wang, Y. Lv, D. Z. Wang, Chin. Phys. B 24, 12, 125202 (2015).

[12]. D. Nishijima, M. Y. Ye, N. Ohno, and S. Takamura, J. Nucl. Mater. 329-333, 1029-1033 (2004).

[13]. I. Tanyeli, L. Marot, D. Mathys, M. C. M. van de Sanden, and G. D. Temmerman, Nature Sci. Rep. 5, 9779 (2015).

[14]. Y. Li, Y. Yang, M. P. Short, Z. Ding, Z. Zeng, and J. Li, Nucl. Fusion 57, 016038 (2017).

[15]. N. J. Dutta, N. Buzarbaruah, and S. R. Mohanty, J. Nucl. Mater. 452, 51-56 (2014).

[16]. M. Bhuyan, S. R. Mohanty, C. V. S. Rao, P. A. Rayjada, and P. M. Raole, Applied Surface Sci. 264, 674-680 (2013).

[17]. V. Shirokova, T. Laas, A. Ainsaar, J. Priimets, U. Ugaste, E.V. Demina, V.N. Pimenov, S.A. Maslyaev, A.V. Dubrovsky, V.A. Gribkov, M. Scholz, and V. Mikli, J. Nucl. Mater. 435, 181-188 (2013).

[18]. K. L. Bjorklund, J. Lu, P. Heszler, and M. Borman, Thin Solid Films 416, 41-48 (2002).

[19]. T. Tokunaga, T. Kawamoto, K. Tanaka, N. Nakamura. Y. Hayashi, K. Sasaki, K. Kuroda, and T. Yamamoto, Nanoscale Res. Lett. 7, 85 (2012).

[20]. G.M. Wright, D. Brunner, M.J. Baldwin, R.P. Doerner, B. Labombard, B. Lipschultz, J.L. Terry, and D.G. Whyte, Nucl. Fusion 52, 4, 042003 (2012).

[21]. R. D. Larrabee, J. Opt. Soc. Am. 49, 619-625 (1959).

[22]. T. J. Petty, M. J. Baldwin, M. I. Hasan, R. P. Doerner, and J. W. Bradley, Nucl. Fusion 55, 093033 (2015).

[23]. B. N. Chapman, Glow Discharge Processes: Sputtering and Plasma Etching. (Wiley, New York, 1980), Vol.1, pp77-133.

[24]. D. Staack, "Characterization and Stabilization of Atmospheric pressure DC microplasmas and their Application to Thin Film Deposition," Ph.D. Thesis, Drexel University, Pennsylvania, United States (2008).

[25]. G. M. Wright, D. Brunner, M. J. Baldwin, K. Bystrov, R. P. Doerner, B. Labombard, B. Lipschultz, G. De Temmerman, J. L. Terry, D. G. Whyte, and K. B. Woller, J. Nucl. Mater. 438, S84-S89 (2013).

[26]. J. P. Trelles, Plasma Sources Sci. Technol. 22, 025017 (2013).

[27]. Y. P. Raizer, and M. S. Mokrov, Phys. Plasmas 20, 101604 (2013).

[28]. K. G. Muller, Phys. Rev. A 37, 4836 (1988).

[29]. D. Lide, CRC Handbook of Chemistry and Physics, 75 edition. (CRC Press, 1995).

CHAPTER IX

Concluding Remarks

9.1 Dissertation Summary

This dissertation aims to elucidate the origin of plasma self-organization observed at the anode of 1 atm DC glows. The investigation is largely experimental with the chief aim of understanding mechanisms associated with pattern formation. Such structural insight is a necessary step in understanding the process which ultimately should lead to the formulation of accurate models and ultimate technologies based on pattern control.

To carry out the aforementioned objectives, the response of patterns—occurrence and evolution to key control parameters was explored for the liquid anode. The work extends our understanding of the sensitivity of pattern formation to control parameters over a range beyond that which has been reported to date. For example this work explored pattern formation at gaps nearly half that reported to date. Additionally, pattern formation with gases other than helium was explored. Patterns were observed using Ar and N_2 gases as the feeding gas at gas flow rates of 50 SCCM and 30 SCCM, respectively — considerably lower than operation on helium. Pattern formation was also found to be independent of the cathode configuration (orifice size).

Optical emission spectroscopy was used to assess the plasma conditions in the DC glow with liquid anode by 1) understanding the full structure of the plasma column and 2) determining if there is a correlation between changes in properties in the column and the occurrence of the self-organization. In that work, it was found that discharge species emission depends on spatial

location such as shown the domination of OH near the water surface suggesting evaporation. The plasma parameters were also spatially estimated: the gas temperatures ranged from 1200 to 2000K, while the excitation temperature is between 5500 and 6250K; and the electron density was on the order of 10^{14} cm^{-3}. It was found that gas temperature along the column was fairly similar which is somewhat surprising as one would expect considerably cooler temperatures closer to the liquid surface. Additionally, a very strong correlation between the appearance of patterns and the significant presence of water vapor were in the positive column. Also, the appearance of salt ions in the gas phase suggests droplet emission into the gas phase where it is subsequently excited by the plasma.

Pattern sensitivity to electrolyte type was also investigated using 13 different electrolyte solutions. This study extends the insight regarding pattern variation from traditional macroscopic experimental parameters such as current and voltage to micro analysis: electrochemistry and perhaps helps understand the plasma chemistry driven in the sub-surface liquid phase. In this work, pattern evolution showed as a function of discharge current with their morphology complexity corresponds to the electrolytes types. The pattern sizes ranged between 2 to 13 mm corresponding to the current range of 20 to 80 mA. Previously unreported unusual pattern structures have been reported in terms of the evolution of solution chemistry and the current perturbations. Pattern formation undergoes a transition with increasing discharge current from nitrogen dominated emission to OH domination, which further confirms that local evaporation process play a key role in self-organization.

Beyond self-organization studies on liquid, for the first time, a luminous particle emission has been observed from $FeCl_3$ anode solution under self-organization condition. 2D spatial-temporal trajectories for two single particles were mapped out by limiting the particle tracking

process on the plasma-liquid plane only. It was found that the emitted particles appear to be molten as droplets with their initial diameter ranged between 31.85 μm to 140 μm. The emitted particle composition has been identified as iron oxide with their initial emitting speeds between 7.9 ms^{-1} and 33.2 ms^{-1}. These energetic emission processes suggest that the luminous light along the particle trajectory are likely the result from the rapid oxidation of melting iron. One potential mechanism for this process is the emission of droplets by anode electric field driven Taylor cone. The evaporation of the liquid water in flight leads to the exposure and subsequent rapid oxidation of the metal particles. These particles form in the liquid solution due to anodic processes at the immersed silicon anode. Although a future data analysis is needed in order to solve the mechanisms of the particle emission, it provides an insight into injection particle dynamics as well as the energetics associated with self-organization pattern formation (e.g. the local electric field).

Similarly, SOPs investigation using metal anodes focused on the pattern variation due to the basic parameter control of, local gas injection and the anode cooling effects. It was found that increasing the current or gap, or anode cooling favors the pattern formation. A minimum 5 mm gap was found to be required for the discharge to self-organize on the metal surfaces. Beside the constant current density that was provided due to the secondary gas effects, Pattern structures appeared consistently in dots with rotation on metal electrodes in contrast to the complex patterns observed on liquid surfaces. Dot size ranged between 0.1 to 0.3 mm in diameter. Investigation of anode surface conditions revealed the importance of local thermal conductivity — with more complex patterns favoring higher thermal conductivity surfaces.

Unexpectedly, nanostructures were found to form on the anode surface after plasma exposure on both tungsten and stainless steel surfaces. These structures exhibited morphology

similar to the tungsten fuzz growth observed in experiments that simulate wall conditions in fusion reactors, suggesting similar physics might be present in both scenarios. The anode surface temperature ranged between 1000 and 1300 K with an ion fluence rate in the order of 10^{24} $s^{-1}m^{-2}$. Observed nanostructures were found to vary with the morphology of the discharge plasma attachment. The composition of the structures was found to be predominantly the native metal. This work gives some insight into the formation of nanostructures at atmospheric pressure, which not only has applications for material processing, but also provides potentially another avenue to study fuzz formation processes relevant to fusion plasma-wall interactions.

The self-organization patterns observed in this work are summarized in Table 9.1. These pattern structures are repeatable. By controlling one of the conditions listed in the table, the pattern morphology can be achieved. The current region was defined in chapter 6.4.1. Here, again, the low current is less than 40 mA. The high current region indicates that the current is higher than 60 mA. The pattern transition region is around 40 mA. The complexity degree of the pattern structures are described in terms of simple and stable (SS), simple but unstable (SUS), complex but stable (CS), complex and unstable (CUS). Here the meaning of "simple" is more biased to the normal observation with simpler control condition, such as current or gap. When the pattern is complex, it shows that additional conditions such as solution chemistry are required to achieve a complex formation. In this work, all of the complex pattern structures were observed at 8 mm gap. The definition of "unstable" is explained in chapter 6.5.1 as well.

Table 9.1. Summary of pattern taxonomy.

Complexity Degree	**Morphology**	**Observation conditions**	**Image Location**
SS	Dots	Low current, Gas types, Metal or liquid anode, High gap	Chap. 4, 8
SS	Ring	Low current, Low or high gap	Chap. 5, 6
SS	Double ring	Low current, High gap	Chap. 6
SS	Gear teeth	Low current, Low or high gap	Chap. 4, 5
SUS	Ring dots and small gears	30 to 40 mA, Gas type	Chap. 4, 6
SS	Spokes	High current, Low or high gap	Chap. 4, 5, 6
CUS	Flower	30 mA, Electrolyte types	Chap. 6
CS	Star	35 to 39 mA, $CuSO_4$	Chap. 6
CS	Disk	High current, DI water, $FeCl_3$	Chap. 3, 4, 6
CUS	Pac man ghost	26 to 35 mA, $FeCl_3$	Chap. 6
CUS	Honeycomb (pentagon)	Reduced current at 25 mA, At least 80 mA	Chap. 6

This work extends our basic understanding of self-organization and the physics of the discharge with underlying mechanism for the formation of the plasma spots at the collection surface – liquid or solid. These outcomes will be of benefit to the low temperature plasma community by enriching the experimental insight into these enigmatic anode plasma patterns. The unexpected observations such as particle emission and nanostructure formation amplifies the magnitude of this plasma system in regards to the undiscovered country yet remaining to be explored and highlights the importance of this research in regards to technological applications that exploit or mitigate self-organization: materials processing, chemical synthesis, waste water treatment, and medicine.

While the experimental campaign has revealed much about self-organization processes, still remaining is a self-consistent phenomenological model that can explain the observed processes. This missing piece has remained elusive. The works presented here however stand as a basis for any model developed to simulate this system. Such a model would be expected to not only be multiphase but also include plasma as well as electrochemical processes in addition to fluid mechanics to truly resolve this system. This dissertation hopes to buoy future self-organization studies by providing the experimental boundaries from the standpoints of plasma physics, chemistry, and nano-synthesis.

9.2 Future Work

Future work is suggested from the experimental point of view. For the perspective future work, one important parameter that has not been satisfactorily measured in the DC atmospheric pressure glows is the local electric field, particularly its value at the collection surface—the planar electrode. A direct measurement of the electric field at the surface however is desired. At this point, we just don't know enough about the prevailing field conditions near the surface.

However, based on our prior work and the estimated field (37 kV/cm) using OES, For example, the mechanisms of particle emission from the center of the SOP on liquid surface, where the discharge attachment is directly located, we can hypothesize that high fields local to the metal or liquid anode surface are necessary to maintain the self-organized structures or even drive the SOP formation. This work will help solving the key question: What is the sign of the anode fall potential? Due to the measurements challenge, this work suggests it should be done using laser facilities that have higher resolutions. Additional, Taylor cone droplet emission may provide some insight into the electric field at the surface.

Another important diagnostic remaining in future work is particle imaging velocimetry (PIV). It is a diagnostic that is well suited to studying fluid phenomena driven by plasma-derived forces and energy deposition on liquid electrodes. We have observed induced circulation in the bulk solution on the plane of the discharge in DC glows. These processes are present only when the plasma attachment is present. With PIV, we can map the velocity flow field below the discharge attachment and in the plane of the discharge attachment to better understand the energy transfer. This can be done for conditions with and without self-organization. With the velocity flow field known we can infer the forces present. The measurement will also allow us to infer instabilities due to plasma contact with the liquid surface. Such instabilities may be the seeding that initiates the self-organization. The objective here is to see the formation in real time, which has never been done in any previous study.

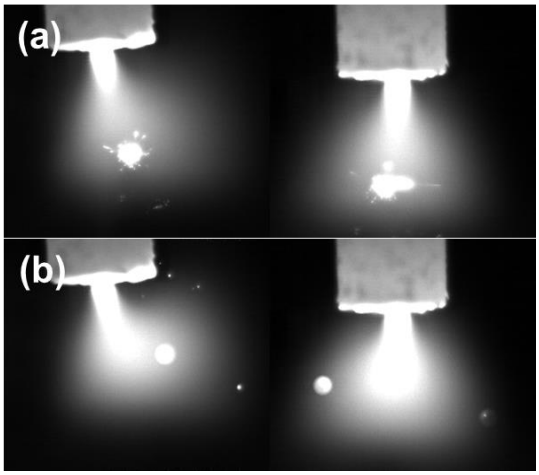

Figure 9.1: Events of (a) initial explosion and (b) vapor and particles after the explosion that captured from two synchronized cameras at same time frame. Left images are recorded from camera 1, and right images were from camera 2. These images captured at 27k fps.

Finally, more detailed analysis of particle trajectories into the gas phase is warranted. The complex behavior of these droplets (see high speed images in Figure 9) as observed at very high speed imaging suggests the droplets charge as they travel. Question abound: 1) what is the size distribution of the droplets 2) what is the charge on the droplets; does disruption play a role in droplet size 3)what is the residence time of the droplets, 4) what role does droplets play in mass transport into the gas phase and how does this impact discharge characteristics 5) are Taylor cones the true origin of the droplets and what role does self-organization have in regards to either occurrence as well as the formation of Taylor cones and 6) is droplet emission always present regardless of electrolytes? 7) Do all droplets contain nanoparticles? The presence of droplets in the gas phase makes for a very interesting system. Indeed, one can call it "*wet" dusty plasma*. Here the physical process of this complex plasma is much more dynamic in that the surfaces are active chemically and physically.

Besides the above three main approaches, there is still a lot of prospective work that can help improve this plasma self-organization study in 1 atm DC glow. Based on the summary of

the outcomes in this dissertation, we will address additional aspects that might probe in the future.

Do patterns appear at low pressure? In the case of a liquid anode, the low vapor pressure electrolytes maybe considered. Additionally, spatial mapping of OH concentration near the surface would provide insight into the role of water vapor on pattern formation.

From the droplets observation with the hypothesis of the Taylor cone effects, the question on the charge state of droplets is the key to solve the emission mechanism and local electric field. It is possible that the charge state of the droplets may be studied using biasing at the collector.

As for the broad parameter spaces we have investigated in this dissertation, another valuable future approach that is worth to try is to use machine learning to predict pattern onset by training.

Appendix A: Fundamental Background of Plasma

A.1 Definition

A plasma is a collection of free charged particles moving in random directions that is, on the average, electrically neutral. A useful definition is also stated as “plasma is a quasineutral gas of charged and neutral particles which exhibits collective behavior”.

A.2 Criteria

There are four conditions that an ionized gas must satisfy to be considered as plasma. First, the plasma is “quasineutral"; that is, neutral enough so that one can take

$$n_i \cong n_e \cong n \ , \tag{A.1}$$

where *n* is the plasma density, *i* and *e* are the notation for ions and electrons respectively. It is not so neutral that all the interesting electromagnetic forces vanish.

Second is that it needs to be dense enough that the Debye length λ_D is much smaller than the system dimension *L* (or the size of plasma):

$$\lambda_D << L \ , \tag{A.2}$$

here the Debye length is a measure of the shielding distance or thickness of the sheath, which is expressed as

$$\lambda_D = \left(\frac{KT_e}{4\pi ne^2}\right)^{1/2} \ , \tag{A.3}$$

where *K* is the Boltzmann’s constant 1.38×10^{-16} erg/*K*. T_e is the electron temperature. The density is n and e is the Elementary charge, 1.6022×10^{-19} C.

In addition to the second condition, “collective behavior” of plasma requires the number of particles in a “Debye sphere” much greater than one, that is

$$N_D >>> 1, \text{ and } N_D = n\frac{4}{3}\pi\,{\lambda_D}^3. \tag{A.4}$$

The last condition has to do with collisions. In order for the gas to behave like a plasma rather than a neutral gas, it is required that the plasma collision frequency is much larger than the collision frequency between the neutral atoms:

$$\omega_p \gg \gamma_{collision}. \tag{A.5}$$

The plasma frequency, in low temperature plasma, is the same as the electron plasma frequency:

$$\omega_p = \omega_e = \sqrt{\frac{e^2 n}{\varepsilon_0 m_e}}, \tag{A.6}$$

Where m_e is the electron mass, and ε_0 is the permittivity of free space.

A.3 Type

Plasma can be determined by its ionization degree and temperature into two categories: thermal plasma in quasi-equilibrium ($T_e = T_i = T_g$) and non-thermal plasmas in non-equilibrium ($T_e \gg T_i > T_g$). Here, the temperature parameters include, electron temperature T_e, ion temperature T_i, and gas temperature (heavy species) T_g.

Most of non-thermal plasmas are weakly ionized plasma, which has a low ionization degree. The plasma source we applied in this dissertation research is one of the weakly ionized non-thermal plasma. Usually these plasmas have the flowing features: (1) they are driven electrically; (2) charged particle collisions with neutral gas molecules are important; (3) there are boundaries at which surface losses are important; (4) ionization of neutrals sustains the plasma in the steady state; and (5) the electrons are not in thermal equilibrium with ions.

Appendix B: LabVIEW

This appendix demonstrates the block diagram that designed and supported the operation for the VXM Stepping Motion Controller. The front operational panel has descripted in chapter 3, Sec. 3.3.2. The block diagram here was also written using a LabVIEW (version of 2014) code.

Fig B.1 depicts the VI files of the block diagram. As can be seen from the figure, it was constructed as a series of sequences where the first one is completed before the next can continue. The first frame sets are the communication parameters used to communicate to the machine controller. The second frame sends the remote command to the controller getting it ready to receive position commands. The third frame is the main operating sequence. It controls all input from the front panel and continues to execute until the stop command is received from the front panel. It preforms the math functions necessary for moving the machine and converts the mm position entered into steps that the machine controller can understand. The last two sequences tell the machine controller to quit and close the port when the task is completed.

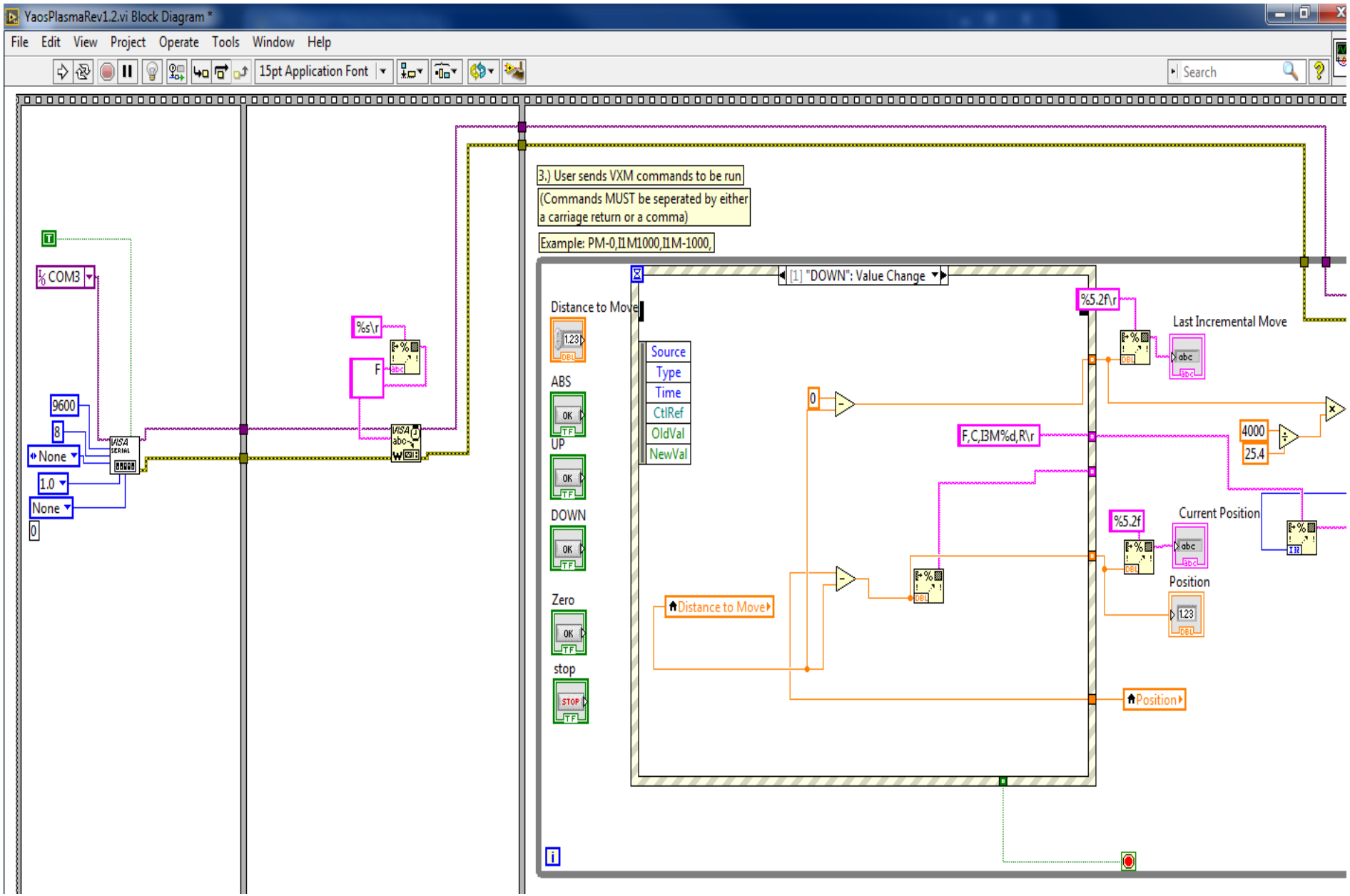
YaosPlasmaRev1.2.vi Block Diagram *
File Edit View Project Operate Tools Window Help
15pt Application Font
Search
COM3
9600
8
None
1.0
None
0
%s\r
F
3.) User sends VXM commands to be run
(Commands MUST be seperated by either a carriage return or a comma)
Example: PM-0,I1M1000,I1M-1000,
[1] "DOWN": Value Change
Distance to Move
Source
Type
Time
CtlRef
OldVal
NewVal
ABS
UP
DOWN
Zero
stop
STOP
0
F,C,I3M%d,R\r
%5.2f\r
Last Incremental Move
4000
25.4
%5.2f
Current Position
Position
Distance to Move
Position

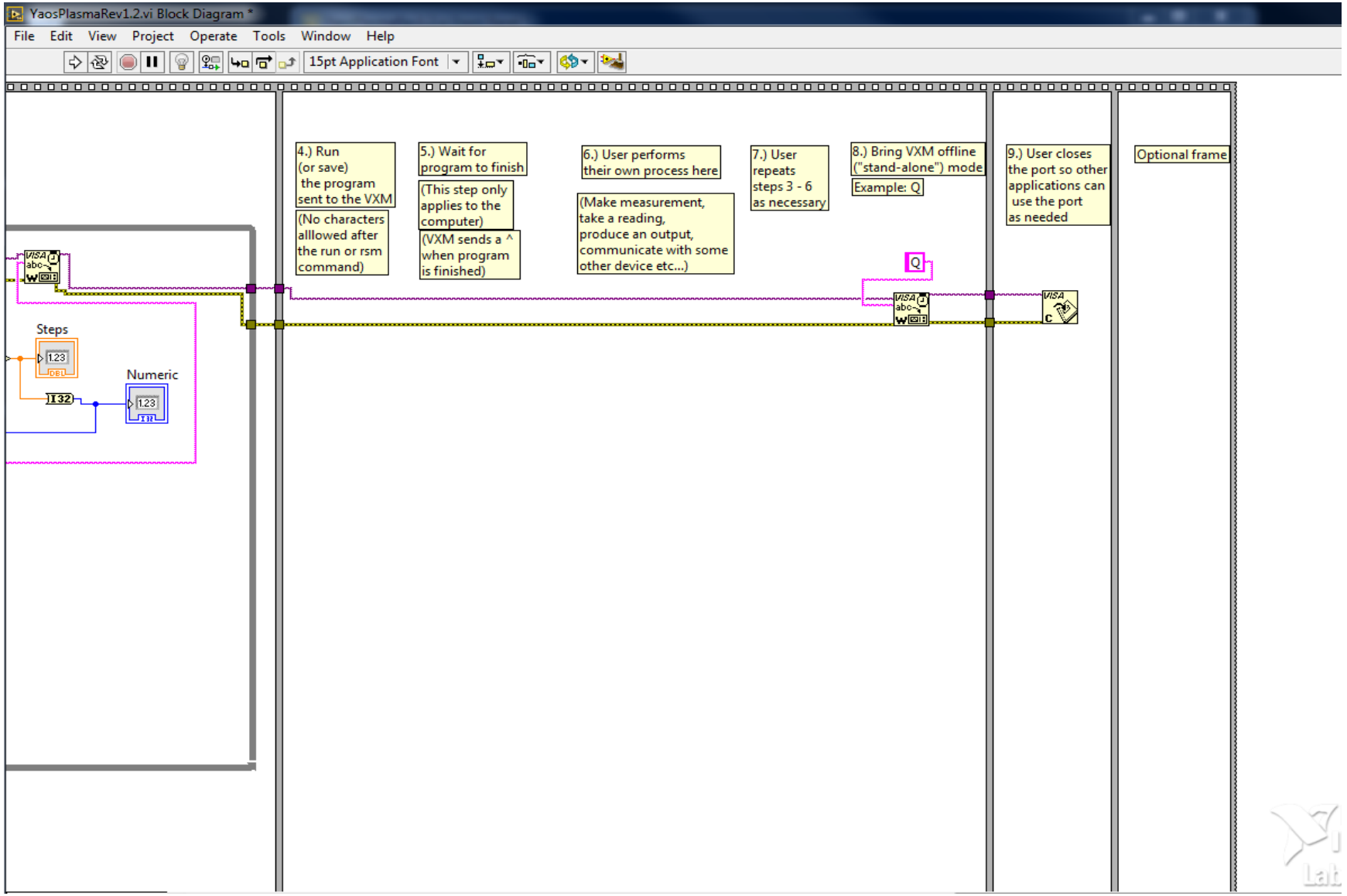

Figure B.1: Block diagram for controlling gap by operating the motion controller. Top figure is the left region; bottom figure is the right region.

Appendix C: EDX

This appendix provides additional evidences in order to support the experimental results in chapter 8. Figures C.1 to C.5 show the typical EDS with composition identification that associated with the nanostructures that were generated on metal anodes.

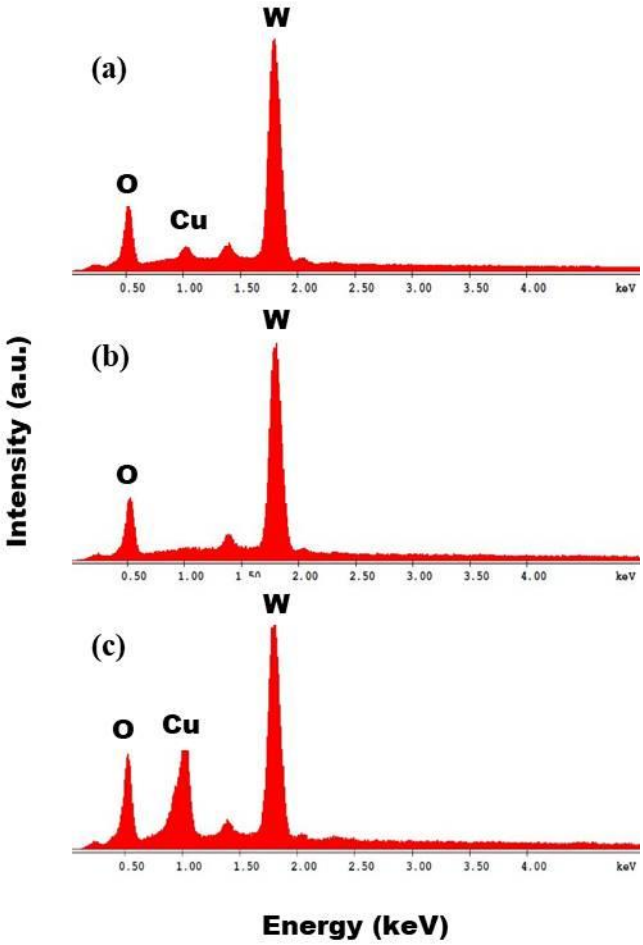

Figure C.1: EDS data were analyzed for initial observation of tungsten on (a) plasma footprint region, (b) fuzz region, and (c) plasma edge region.

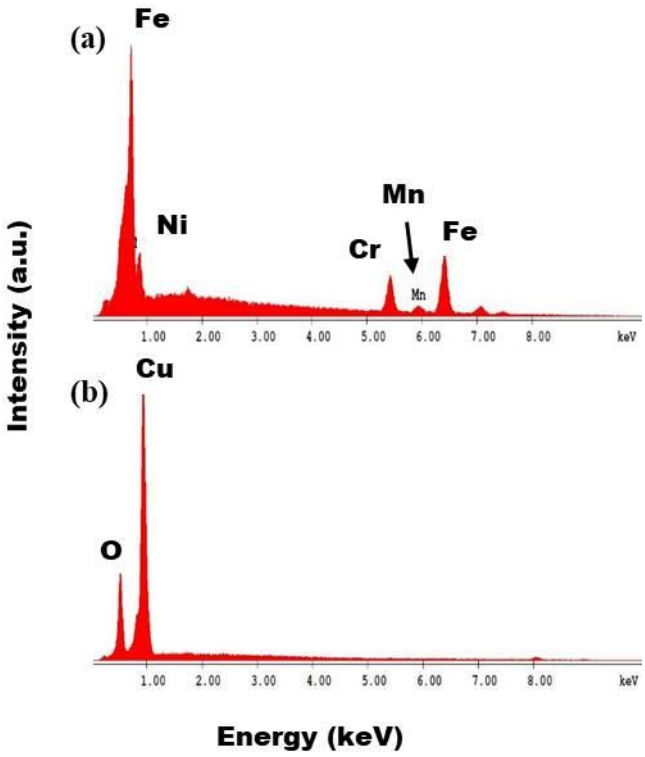

Figure C.2: EDS data were analyzed for stainless steel under helium plasma exposure at (a) plasma attachment region and (b) particle growth region.

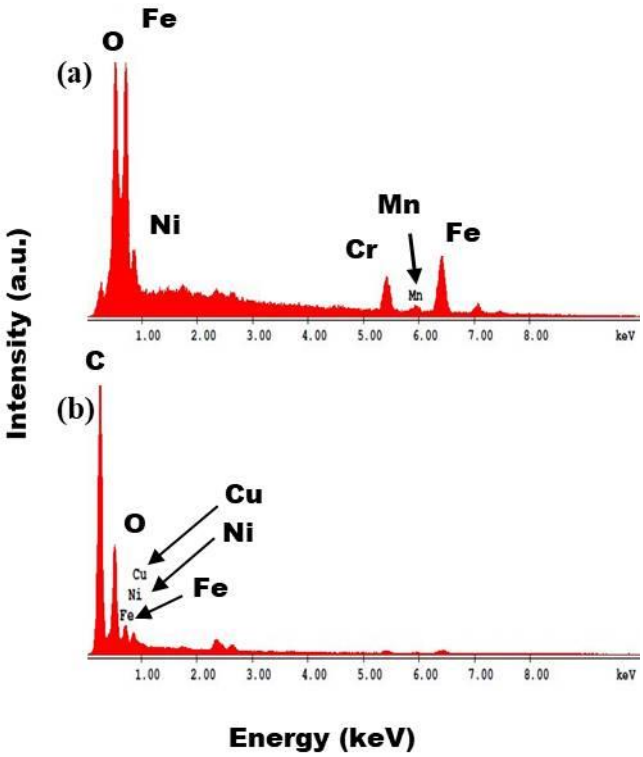

Figure C.3: EDS data were analyzed for stainless steel after air plasma exposure at (a) plasma footprint region, (b) burned surface region.

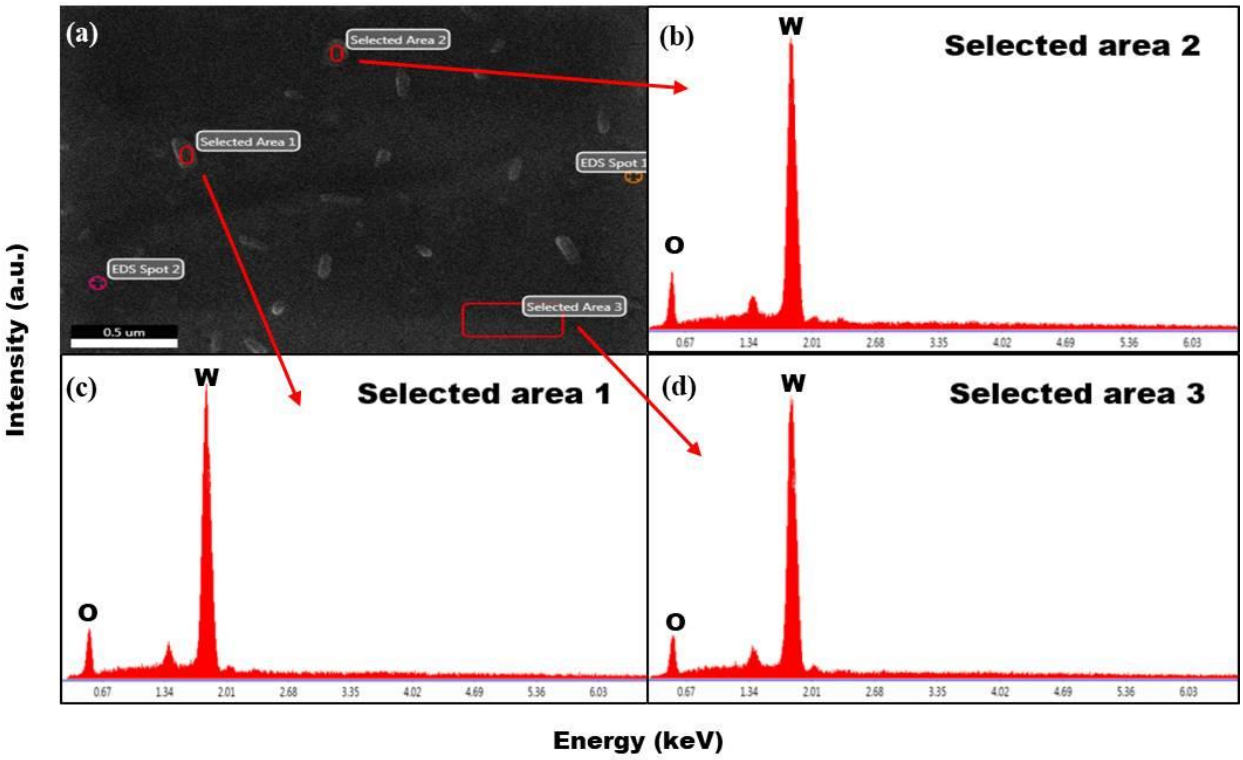

Figure C.4: An EDS example of tungsten sample after 10 minutes exposure was collected from (a) scanning region at (b) rod region, (c) another rod region, and (d) background bulk tungsten.

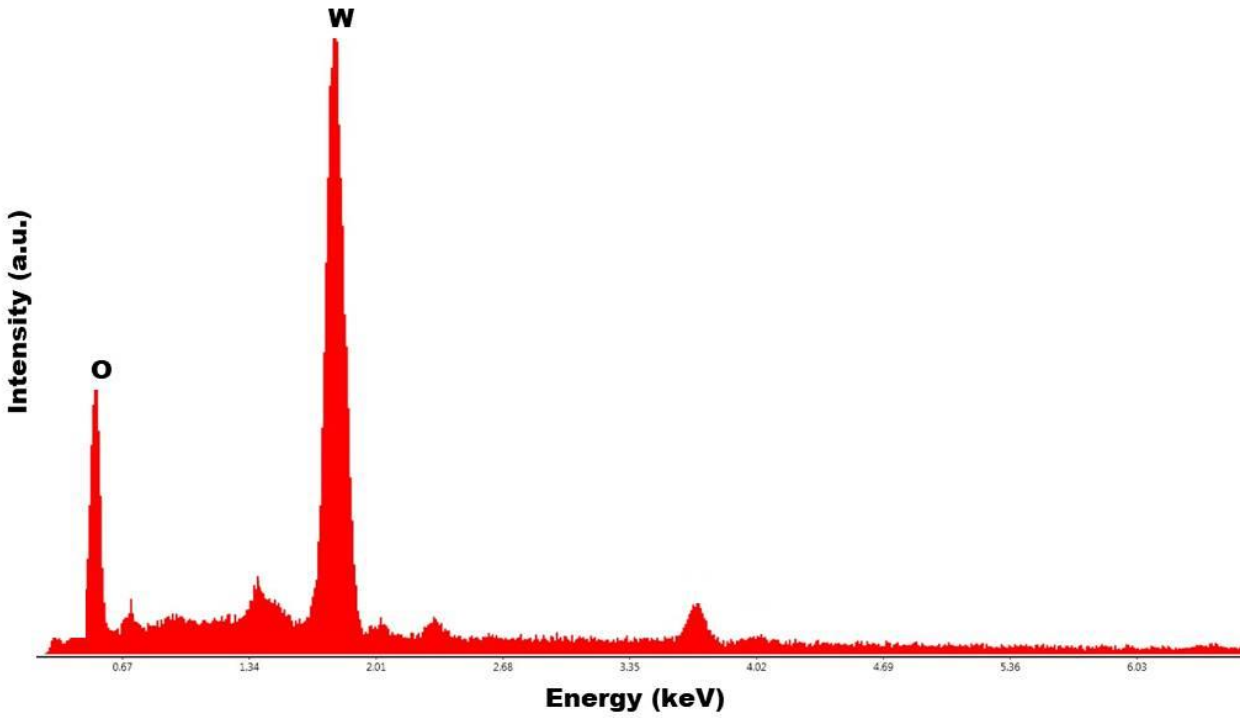

Figure C.5: EDS was collected on the tungsten fuzz after 30 minutes helium plasma exposure in air.